



Development of an Ionized Physical Vapor Deposition System for Superhard  
Amorphous Carbon Coating

Nopphon Saowiang

A Thesis Submitted in Partial Fulfillment of Requirements for  
degree of Doctor of Philosophy in Physics

May 2022

Copyright of Mahasarakham University

การพัฒนาระบบการทดสอบด้วยไอออนเชิงกายภาพสำหรับการเคลือบคาร์บอนอสัณฐานแข็ง  
ยิ่งยวด

วิทยานิพนธ์  
ของ  
นพพล เสาวเรือง

พูน บณฺฑิต ชีวะ

เสนอต่อมหาวิทยาลัยมหาสารคาม เพื่อเป็นส่วนหนึ่งของการศึกษาตามหลักสูตร  
ปริญญาปรัชญาดุษฎีบัณฑิต สาขาวิชาฟิสิกส์

พฤษภาคม 2565

ลิขสิทธิ์เป็นของมหาวิทยาลัยมหาสารคาม

Development of an Ionized Physical Vapor Deposition System for Superhard  
Amorphous Carbon Coating

Nopphon Saowiang

A Thesis Submitted in Partial Fulfillment of Requirements  
for Doctor of Philosophy (Physics)

May 2022

Copyright of Mahasarakham University



The examining committee has unanimously approved this Thesis, submitted by Mr. Nopphon Saowiang , as a partial fulfillment of the requirements for the Doctor of Philosophy Physics at Mahasarakham University

Examining Committee

.....	Chairman
(Prof. Vittaya Amornkitbamrung , Ph.D.)	
.....	Advisor
( Nitisak Pasaja , Ph.D.)	
.....	Co-advisor
(Asst. Prof. Phitsanu Poolcharuansin , Ph.D.)	
.....	Committee
(Asst. Prof. Artit Chingsungnoen , Ph.D.)	
.....	Committee
(Asst. Prof. Prathan Seevili , Ph.D.)	
.....	Committee
(Assoc. Prof. Paveena Laokul , Ph.D.)	

Mahasarakham University has granted approval to accept this Thesis as a partial fulfillment of the requirements for the Doctor of Philosophy Physics

.....  
(Prof. Pairoit Pramual , Ph.D.)  
Dean of The Faculty of Science

.....  
(Assoc. Prof. Krit Chaimoon , Ph.D.)  
Dean of Graduate School



<b>TITLE</b>	Development of an Ionized Physical Vapor Deposition System for Superhard Amorphous Carbon Coating		
<b>AUTHOR</b>	Nopphon Saowiang		
<b>ADVISORS</b>	Nitisak Pasaja , Ph.D. Assistant Professor Phitsanu Poolcharuansin , Ph.D.		
<b>DEGREE</b>	Doctor of Philosophy	<b>MAJOR</b>	Physics
<b>UNIVERSITY</b>	Maharakham University	<b>YEAR</b>	2022

### ABSTRACT

The purpose of this work is to development and demonstrate that the ionized physical vapor deposition system, which consists of four plasma sources (FCVA, L-ALIS, ALIS and magnetron sputtering) enables to produce of superhard amorphous carbon thin films. The superhard amorphous carbon films was designed based on the multilayer film comprising alternating layers of ta-C layers and a-C:H layers, which the a-C:H layer has been fabricated by L-ALIS source and the ta-C layer have been fabricated by FCVA source. The morphologies, microstructure and mechanical properties of the single layer ta-C, single layer a-C:H and multilayer ta-C films deposited on Si and SUS304 substrate were systematically investigated. Results showed that the plasma biasing and substrate bias technique increases the energy of  $C^+$  ions. This phenomenon overcomes the nucleation barrier and subplantation occurs. The energetically enhanced deposition condition during FCVA facilitates the densification of the single layer ta-C films up to  $3.32 \text{ g/cm}^3$ , leading to an increase in film hardness to 47 GPa. While the single layer a-C:H deposited under intense and highly energetic bombardment of molecular ions has a low  $sp^3$  content leading to density of  $2.2 \text{ g/cm}^3$

The multilayer structure effectively reduced the residual stress and restrained spalling of ta-C film, which frequently occurred in single layer structure. The hardness and elastic modulus of multilayer films increased with increase  $sp^3$  content of ta-C layer. Compared to the SUS304 substrate, multilayer films exhibited much high hardness and very low surface roughness. For the multilayer film alternating of ta-C layer deposited at substrate bias potential  $-80 \text{ V}$  and a-C:H layer (M-3 film) had a high hardness of 37.6 GPa and good adhesion with the substrate. In addition, the high hardness, the multilayer films with good elastic strain to failure and high resistance to plastic deformation and cracking.

**Keyword :** Ionized physical vapor deposition system, Superhard amorphous carbon film, ta-C film, a-C:H film, Multilayer film, Microstructure and Mechanical properties

## ACKNOWLEDGEMENTS

I would like to express, first and foremost, my deepest and most sincere gratitude to my advisor Dr. Nitisak Pasaja and co-advisor Asst. Prof. Phitsanu Poolcharuansin for meticulous guidance on all problems and continuous encouragement throughout my doctoral program. Their counsel was always insightful and presented an experience or a concept to overcome a problem both inside and outside Mahasarakham University (MSU), Thailand. Therefore, is no doubt that without their guidance and persistent support this thesis would not have been possible.

In addition to my advisor and co-advisor, I wish to express special appreciation to the committee members Assoc. Prof. Vittaya Amornkitbamrung, Asst. Prof. Artit Chingsungnoen, Asst. Prof. Prathan Seevili and Asst. Prof. Paveena Laokul, for their insightful questions and comments, helpful discussions, and valuable suggestions, it give me incentive to widen my research in various perspectives.

I am profoundly grateful to collaborators at Mahasarakham University (MSU), Thailand, especially Mr. Egkaphon Pachanok the staff of physics workshop for support and give advice about the hard skills and soft skills in the part of manufacturing the vacuum component. Including the Science Training Center (STS) for gave me access to his laboratory, research facilities, including XRR and XRD analysis.

I am grateful to all colleagues at Technological Plasma Research Unit for their friendly assistance, co-operation, and good friendship during my studies.

It gives me great pleasure to acknowledge the continuous support and assistance of Dr. Sarayut Tunmee, Business Development Division at the Synchrotron Light Research Institute (Public Organization), Mr. Ukit Rittihong, Dr. Narong Chanlek, and for helpful and supporting the characterization part of thin films microstructure by Raman spectroscopy and XPS analysis.

I am profoundly grateful to the Mahasarakham University and Thailand Center of Excellence in Physics (THEP) for financial support in the form of grants and scholarships under Contract ThEP-61-EQP-MSU2

Last but not least, I would like to honestly thank my family: my parents Mr. Sukan Saowieng and Mrs. Panom Saowieng, my elder brother Mr. Wigrom Saowieng and younger brother Mr. Arnon Saowieng for their endless love and continuous support

throughout the writing of this thesis and my life. A Ph.D. thesis would not have been completed and possible without the love and compassion of all of those who are beside me.

Nopphon Saowiang

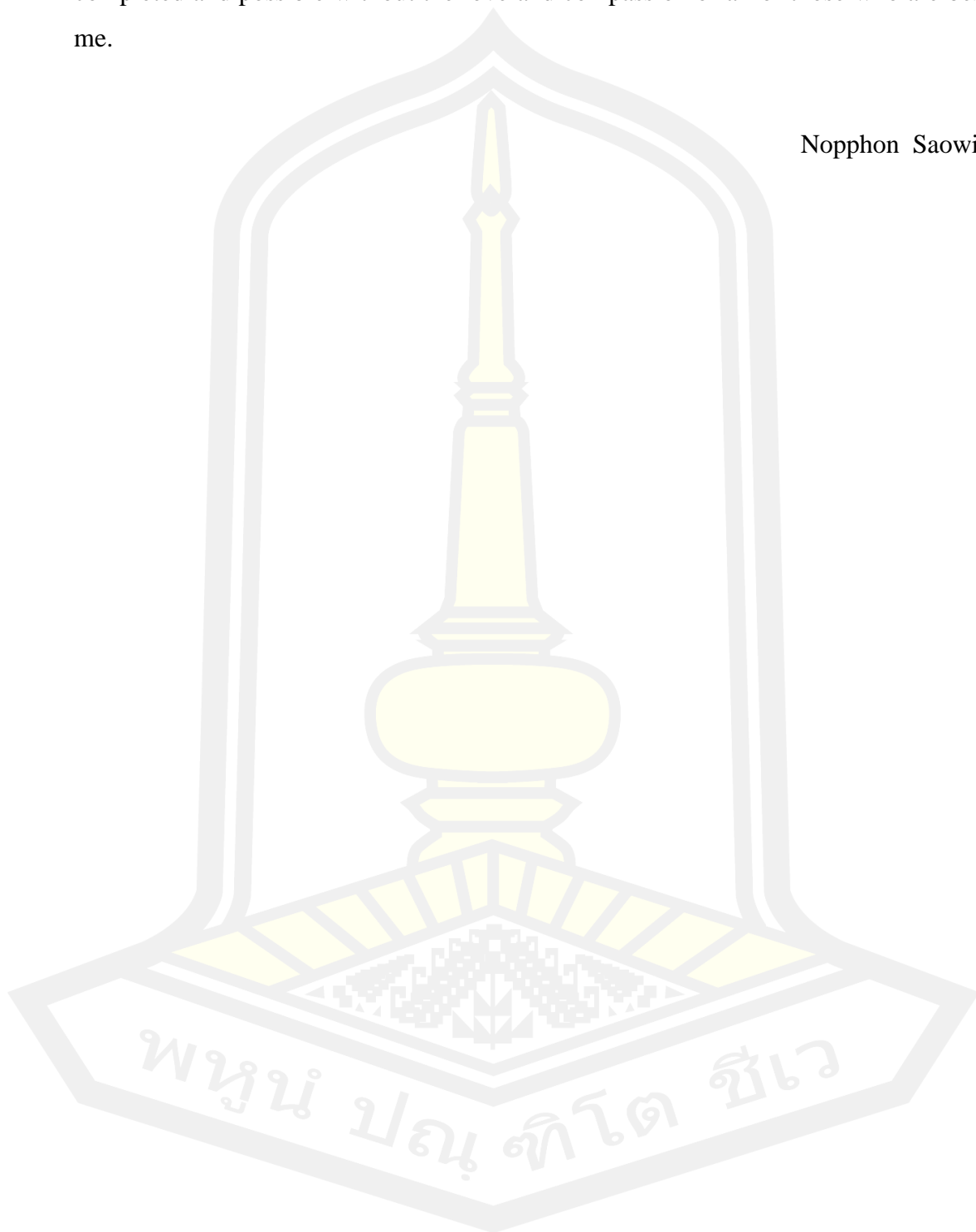


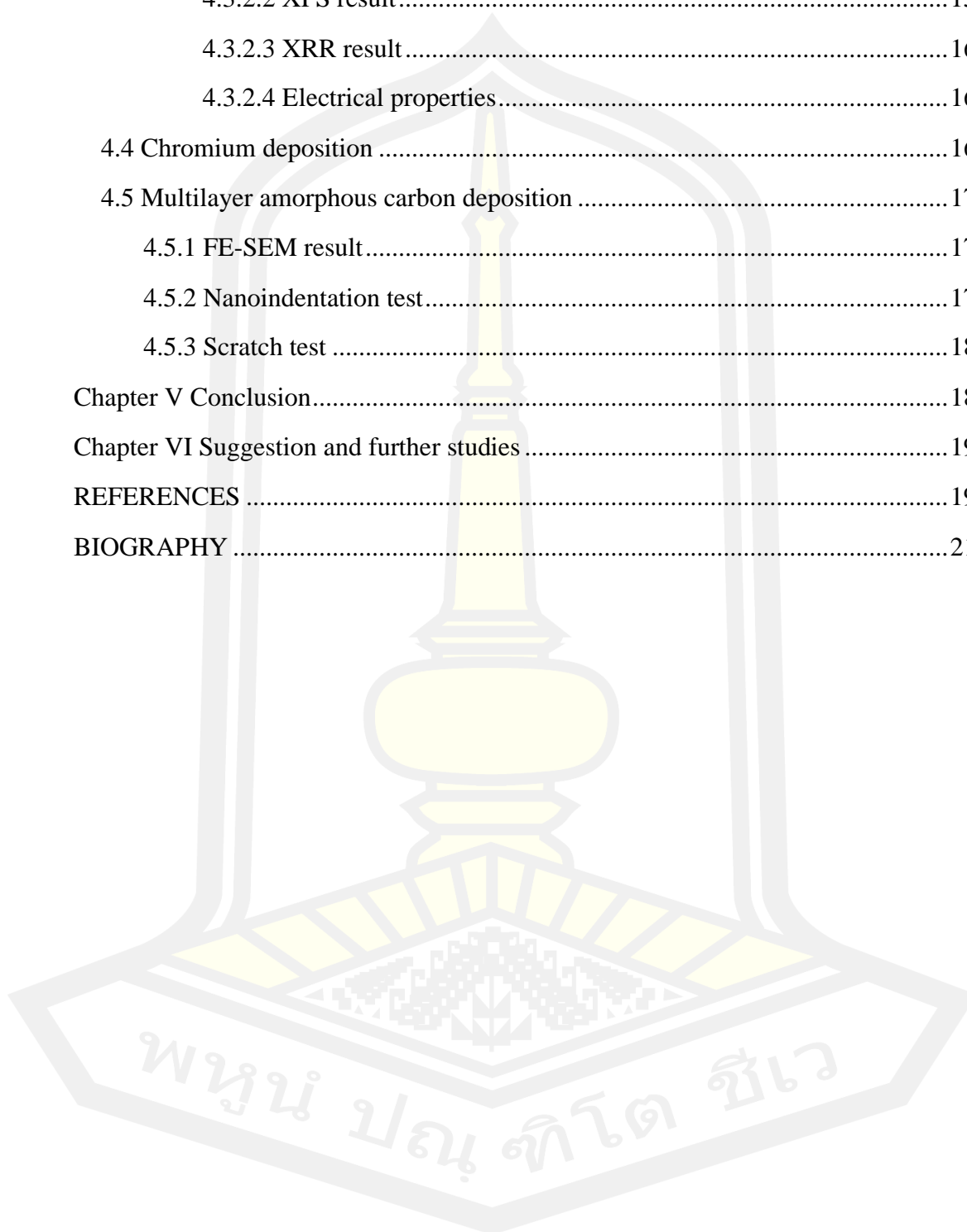
## TABLE OF CONTENTS

	Page
ABSTRACT .....	D
ACKNOWLEDGEMENTS .....	E
TABLE OF CONTENTS .....	G
LIST OF FIGURES .....	K
LIST OF TABLES .....	T
LIST OF ABBREVIATIONS .....	V
Chapter I Introduction .....	1
1.1 Background and motivation .....	1
1.2 Objectives .....	4
1.3 The scope of works .....	4
1.4 The location of the research .....	5
1.5 Anticipated outcomes .....	5
1.6 Outline of the thesis .....	6
Chapter II Literature reviews and theoretical background .....	8
2.1 Literature review .....	8
2.2 Diamond-like carbon .....	12
2.3 Tetrahedral amorphous carbon .....	16
2.3.1 Mechanical properties .....	18
2.3.2 Tribological properties .....	20
2.4 Multilayer DLC film .....	21
2.5 Cathodic vacuum arc .....	28
2.6 Filtered cathodic vacuum arc .....	30
2.6.1 Classic 90° duct filter .....	31
2.6.2 Knee-filter .....	32
2.6.3 Freestanding 90° filter .....	33

2.6.4 S-duct filter.....	34
2.6.5 Freestanding S-filter.....	34
2.7 New filtered cathodic vacuum arc system.....	35
Chapter III Experimental Procedures.....	38
3.1 An ionized physical vapor deposition system .....	38
3.1.1 Vacuum system .....	38
3.1.2 Vacuum component control system .....	39
3.1.3 Plasma sources .....	49
3.1.3.1 Anode layer ion source .....	49
3.1.3.2 Linear anode layer ion source.....	52
3.1.3.3 Magnetron sputtering source .....	53
3.1.3.4 In-house filtered cathodic vacuum arc source .....	56
3.1.3.5 Principle of magnetic filtering .....	59
3.1.3.6 Design of magnetic macroparticle filters.....	60
3.1.3.7 Commercial filter cathodic vacuum arc source .....	61
3.1.3.8 T-shape adapter .....	62
3.1.3.9 Focusing coil .....	66
3.1.4 Pulse forming network .....	67
3.1.5 Plasma and substrate bias power supply .....	71
3.1.6 Substrate holder.....	72
3.1.7 Substrate transfer.....	74
3.2 Retrading filed analyzer probe .....	75
3.2.1 Langmuir probe .....	76
3.2.2 Configuration of the RFA probe design.....	78
3.2.3 Structure of retarding field analyzer.....	78
3.2.4 Analysis of data from the RFA probe .....	81
3.3 Sample preparation.....	82
3.3.1 Silicon wafer preparation .....	83
3.3.2 Stainless steel preparation .....	84

Chapter IV Result and discussion .....	86
4.1 Plasma diagnostics .....	86
4.1.1 RFA probe test.....	86
4.1.2 Ion energy measurement .....	89
4.1.2.1 Plasma biasing technique .....	89
4.1.2.2 Time-resolved ion energy measurement .....	100
4.1.2.3 Substrate biasing technique .....	102
4.1.2.4 Deposition profile.....	106
4.2 ta-C coating.....	109
4.2.1 Plasma biasing technique .....	109
4.2.1.1 Survey of the ta-C deposition.....	109
4.2.1.2 FE-SEM result.....	115
4.2.1.3 AFM result.....	117
4.2.1.4 Raman spectroscopy .....	119
4.2.1.5 XPS result.....	121
4.2.1.6 XRR result.....	125
4.2.1.7 Electrical properties.....	127
4.2.1.8 Nanoindentation test.....	128
4.2.2 Substrate biasing technique .....	131
4.2.2.1 Survey of the ta-C deposition.....	131
4.2.2.2 FE-SEM result.....	135
4.2.2.3 Raman spectroscopy .....	136
4.2.2.4 XPS result.....	138
4.2.2.5 XRR result.....	142
4.2.2.6 Electrical properties.....	144
4.2.2.7 Uniformity of ta-C film .....	145
4.3 a-C:H deposition.....	148
4.3.1 Survey for a-C:H deposition.....	148
4.3.2 a-C:H film properties.....	153

4.3.2.1 Raman spectroscopy .....	153
4.3.2.2 XPS result.....	157
4.3.2.3 XRR result.....	161
4.3.2.4 Electrical properties.....	163
4.4 Chromium deposition .....	163
4.5 Multilayer amorphous carbon deposition .....	171
4.5.1 FE-SEM result.....	175
4.5.2 Nanoindentation test.....	179
4.5.3 Scratch test .....	183
Chapter V Conclusion.....	188
Chapter VI Suggestion and further studies .....	193
REFERENCES .....	195
BIOGRAPHY .....	219



## LIST OF FIGURES

<b>Figure 2.1</b> Cutting tools [54].	10
<b>Figure 2.2</b> The $sp^3$ , $sp^2$ , and $sp^1$ hybridized bonding (modified from [20]).	13
<b>Figure 2.3</b> Structure of (a) graphite and (b) diamond.	13
<b>Figure 2.4</b> Ternary phase diagram of bonding in amorphous carbon-hydrogen alloys [20].	16
<b>Figure 2.7</b> Comparison of the variation of the $sp^3$ fraction with ion energy for ta-C. showing the range of variations possible with the different FCVA filter systems and plasma duct sizes [20].	18
<b>Figure 2.9</b> Variation of nano-hardness of ta-C with $sp^3$ fraction [82].	20
<b>Figure 2.12</b> The effects of a bilayer period on the mechanical properties. (a) Elastic modulus and hardness, and (b) residual stress of WC/DLC coatings for the bilayer period [98].	23
<b>Figure 2.13</b> The ta-C multilayer of alternating high- $sp^3$ -content and low- $sp^3$ -content layers, the $sp^3$ content ratio of the sample is M-1: 51/60, M-2: 44:60, M-3: 36:60, YG6: substrate. (a) Wear rate, hardness and H/E ratio of the samples, (b) Friction coefficient curves against sliding times and (c) Average friction coefficient and wear rate of samples [23].	25
<b>Figure 2.15</b> (a) hardness and average wear rate of the DLC, CrN, CrN/DLC/Cr-DLC. (b) 3D images and cross-sectional profiles of wear tracks sliding with an AISI 440C ball. And (c) SEM images of wear tracks (top view) and EDS mapping results (bottom view) of the coatings, sliding with an AISI 440C ball [34].	27
<b>Figure 2.16</b> Schematic physical model of the emission of particles from the surface of the cathode spot of the arc discharge.	29
<b>Figure 2.17</b> Schematic of the classic 90°-duct filter [112].	32
<b>Figure 2.18</b> Schematic of the 45° Knee-filter [116].	33
<b>Figure 2.19</b> Freestanding 90° filter, operating with the arc current (200 A), Platinum plasma. [112].	33
<b>Figure 2.20</b> Schematic of an S-duct filter [112].	34
<b>Figure 2.21</b> Freestanding S-filter, operating with a pulsed high arc current (1 kA), and Titanium plasma [112].	35



<b>Figure 2.22</b> Photograph of 120° filter with high-current arc source [125].	35
<b>Figure 2.23</b> Schematic sketches of new filter cathodic vacuum arcs. (a) FCVA [23], (b) Y-FAD and (c) T-FAD [125].	37
<b>Figure 3.1</b> Diagram of the ionized physical vapor deposition system.	39
<b>Figure 3.2</b> The graphical user interface of the reactor controller of the main process and control view.	41
<b>Figure 3.3</b> Concept of the control system of a filtered cathodic vacuum arc system.	41
<b>Figure 3.4</b> National Instruments PXI-8108 2.53 GHz Dual-Core Embedded Controller [134].	43
<b>Figure 3.5</b> The LabVIEW diagram for control the pendulum valve (open and close valve).	44
<b>Figure 3.6</b> The LabVIEW diagram for control the pendulum valve (set the position of the valve and set pressure in the deposition chamber).	45
<b>Figure 3.7</b> (a) the NI PXI-2565 [136], (b) diagram of an electrical circuit for use NI PXI 2565 to control the working of the device.	46
<b>Figure 3.8</b> The LabVIEW diagram for close or open the solenoid valve and gate valve.	47
<b>Figure 3.9</b> NI PXI-6251 card and pinout.	48
<b>Figure 3.10</b> The LabVIEW diagram for the setpoint flow rate of the argon gas.	49
<b>Figure 3.11</b> Overview assembly and structure diagram of an anode layer ion source.	50
<b>Figure 3.12</b> Anode layer ions source for substrate cleaning.	51
<b>Figure 3.13</b> The plasma characteristic generated using an ALIS.	51
<b>Figure 3.14</b> Assembly of linear anode layer ion source.	52
<b>Figure 3.15</b> (a) The argon plasma beam generated using L-ALIS with the discharge potential of 1200 V. And (b) the a-C:H film deposited using L-ALIS with the discharge potential of 1200 V and discharge current of 13.5 mA.	53
<b>Figure 3.16</b> (a) Position and polarity of the permanent magnet and (b) magnetic force lines generated by permanent magnets.	53
<b>Figure 3.17</b> Assembly of an unbalanced magnetron sputtering source.	56
<b>Figure 3.18</b> Schematic of triggerless vacuum arc initiation (ion extraction system not shown) [139].	57

<b>Figure 3.19</b> Assembly of the pulsed vacuum arc source.....	59
<b>Figure 3.20</b> The commercial filtered cathodic vacuum arc source. ....	62
<b>Figure 3.21</b> T-shape adaptor for support the commercial FCVA source.....	63
<b>Figure 3.22</b> Assembly of installation of the commercial FCVA source on T-shape adaptor.....	64
<b>Figure 3.23</b> (a) installation of the FCVA source on T-shape adaptor and ionized physical vapor deposition, (b) and (c) carbon rod target scratch and zero adjust system. ....	65
<b>Figure 3.24</b> Installation concept of the focusing coil at the gap of FCVA source and deposition chamber. ....	66
<b>Figure 3.25</b> Installation and operation of the focusing coil. ....	67
<b>Figure 3.26</b> Characteristics of the ta-C film on stainless steel deposited by FCVA source (a) do not have the focusing coil and (b) use the focusing coil. ....	67
<b>Figure 3.27</b> VEECO pulse forming network. ....	68
<b>Figure 3.28</b> The box diagram of the PFN. ....	68
<b>Figure 3.29</b> Schematic showing a 10-stage Type E PFN, output switch, and load. ...	69
<b>Figure 3.30</b> The box diagram of the operating pulsed vacuum arc source. ....	70
<b>Figure 3.31</b> Diagram of Pulsed Forming Network (PFN) and support devices.....	70
<b>Figure 3.32</b> The box diagram of high voltage DC power supply (600 V maximum). 71	
<b>Figure 3.33</b> An electrical schematic of the plasma biasing power supply. ....	72
<b>Figure 3.34</b> An electrical schematic of the substrate bias power supply. ....	72
<b>Figure 3.35</b> SOLIDWORK assembly and photo of the substrate holder.....	73
<b>Figure 3.36</b> Stepper motor driving diagram for substrate holder system.....	74
<b>Figure 3.37</b> Load lock transfer substrate system.....	75
<b>Figure 3.38</b> Model of the magnetic transfer arm. ....	75
<b>Figure 3.39</b> An idealized I-V characteristic of obtained with a collecting Langmuir probe in a cold plasma. ....	77
<b>Figure 3.40</b> An I-V characteristic obtain from a probe for measuring the ion. ....	77
<b>Figure 3.41</b> Model of the front grid for the ion energy measurement probe. ....	78
<b>Figure 3.42</b> Diagram and cross-section of the RFA probe. ....	79
<b>Figure 3.43</b> Characteristic of the grids for the RFA probe. ....	79

<b>Figure 3.44</b> An in-house RFA probe for ion energy measurement in the FCVA deposition.....	80
<b>Figure 3.45</b> Comparison of the unpolished and the polished SUS304. ....	84
<b>Figure 4.1</b> Diagram of RFA probe checking.....	87
<b>Figure 4.2</b> Measured current on the G1, G3, G4, and ion corrector electrodes. ....	87
<b>Figure 4.3</b> Diagram of electron repelling performance.....	88
<b>Figure 4.4</b> Measured current on the ion corrector electrode as a function of electron repelling voltage.....	89
<b>Figure 4.5</b> Diagram of ion energy measurement for plasma biasing technique .....	90
<b>Figure 4.6</b> Trigger and notify signal for ion energy measurement. ....	92
<b>Figure 4.7</b> (a) Arc current signal, (b) arc voltage signal, (c) anode bias current signal, and (d) anode bias potential as a function of anode bias potential. ....	94
<b>Figure 4.8</b> (a) the average I-V characteristic measured by the RFA probe, and (b) kinetic energy distribution function as a function of an anode bias potential. ....	94
<b>Figure 4.9</b> (a) density, (b) mean energy, and (c) flux of the C <sup>+</sup> ions measured using an RFA probe.....	95
<b>Figure 4.10</b> (a) I-V characteristic and (b) floating potential signal as a function of anode bias potential (the G1 of a RFA probe is floated). ....	96
<b>Figure 4.11</b> Kinetic energy distribution function as a function of an anode bias potential for G1 electrode as floated. ....	97
<b>Figure 4.12</b> (a) average floating potential, (b) ion density, (c) mean energy and (d) flux of the C <sup>+</sup> ions measured using RFA probe (G1 as floated). ....	99
<b>Figure 4.13</b> Comparison of the potential profile of the ground and floating surface. ....	100
<b>Figure 4.14</b> Delay signal for time-resolved ion energy measurement. ....	101
<b>Figure 4.15</b> Time-resolved ion energy contour graph as a function of anode bias voltage.....	102
<b>Figure 4.16</b> Diagram of ion energy measurement for substrate bias technique.....	103
<b>Figure 4.17</b> (a) I-V characteristic measurement by RFA probe and (b) kinetic energy distribution function as a function of an anode bias potential. ....	104
<b>Figure 4.18</b> (a) density, (b) mean energy, and (c) flux of the C <sup>+</sup> ions as a function of substrate bias potential.....	106

<b>Figure 4.19</b> The ta-C deposition profile on SUS316 plate (diameter 175 mm). The films deposited by varying anode bias potential.....	108
<b>Figure 4.20</b> The ta-C deposition profile on SUS304 plate (diameter 175 mm). The films deposited by varying substrate bias potential. ....	109
<b>Figure 4.21</b> The ta-C films profile deposition on the sample and substrate holder by varying the anode bias potential (holder is grounded).....	111
<b>Figure 4.22</b> The ta-C films profile deposition on the sample and substrate holder by varying the anode bias potential (holder is floated).....	111
<b>Figure 4.23</b> XRR profiles of ta-C films (a) ground sample and (b) floating sample. ....	112
<b>Figure 4.24</b> Film density as a function of the mean energy of carbon ions. ....	113
<b>Figure 4.25</b> Influence of plasma biasing technique on the deposition rate of ta-C film. ....	114
<b>Figure 4.26</b> The ta-C films on Si substrate deposited by varying anode bias potential, which controls the thickness of 85 nm.....	116
<b>Figure 4.27</b> (a) surface and (b) cross-section of the ta-C film deposited on Si substrate by applied substrate bias potential of +80 V.....	116
<b>Figure 4.28</b> 3D AFM images of ta-C thin films deposited with PFCVA technique combined with plasma biasing technique. ....	118
<b>Figure 4.29</b> The estimated values of the root mean square surface roughness (RRMS) of the ta-C films deposited on the Si substrate as a function of anode bias potential. ....	118
<b>Figure 4.30</b> (a) Raman spectra and (b) double plot of the $I_D/I_G$ ratio and G peak position of the ta-C film deposited with the different anode bias potential.....	120
<b>Figure 4.31</b> Survey spectra of the ta-C films with the thickness of about 85 nm deposited by varying anode bias potential. ....	123
<b>Figure 4.32</b> C1s spectra of the ta-C films with the thickness of about 85 nm deposited by varying anode bias potential. ....	123
<b>Figure 4.33</b> O1s spectra of the ta-C films with the thickness of 80 to 90 nm deposited by varying anode bias potential. ....	124
<b>Figure 4.34</b> $sp^3$ content of the ta-C films as a function of anode bias potential. ....	125

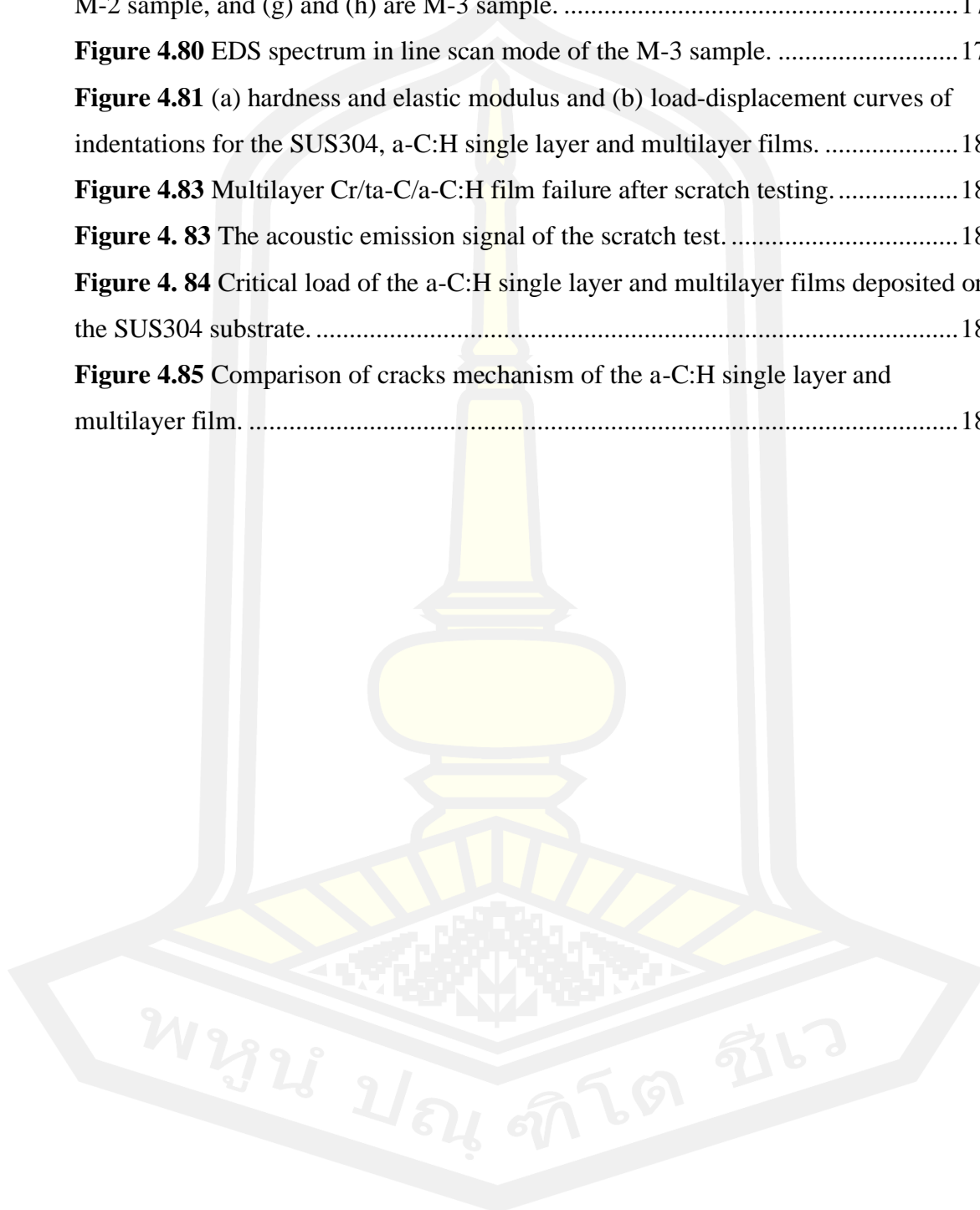
<b>Figure 4.35</b> The XRR profiles of ta-C films deposited on Si substrate by varying anode bias potential.....	126
<b>Figure 4.36</b> (a) thickness of the ta-C films estimated by the period oscillation of XRR curve. And (b) density of the ta-C films deposited on Si substrate as a function of substrate bias potential.....	127
<b>Figure 4.37</b> Electrical conductivity of the ta-C film as a function of anode bias potential.....	128
<b>Figure 4.38</b> (a) hardness and (b) elastic Modulus of the ta-C film as a function of anode bias potential.....	129
<b>Figure 4.39</b> The XRR profiles of ta-C films deposited on Si substrate by varying substrate bias potential (survey study).....	133
<b>Figure 4.40</b> Density and deposition rate of the ta-C films deposited by varying substrate bias potential (survey study).....	133
<b>Figure 4.41</b> The ta-C films on Si substrate deposited by varying substrate bias potential, which controls the thickness of about 90 nm, which label is the substrate bias potential. ....	135
<b>Figure 4.42</b> (a) surface and (b) cross-section of the ta-C film deposited on Si substrate by applied substrate bias potential of -80 V.....	136
<b>Figure 4.43</b> Normalized Raman spectra and of the ta-C films deposited with the different substrate bias potential. The label at tail of spectra is applied substrate bias potential.....	137
<b>Figure 4.44</b> Double plot of the $I_D/I_G$ ratio (black dot) and the G peak position (red square) of the ta-C films deposited on Si substrate with a thickness of about 90 nm. ....	138
<b>Figure 4.45</b> Survey spectra of the ta-C films deposited on Si substrate with the thickness of about 90 nm. The label at the tail of spectra is applied substrate bias potential during the film growth. ....	139
<b>Figure 4.46</b> C1s spectra of ta-C films deposited on Si substrate with a thickness of about 90 nm. The label at the tail of spectra is applied substrate bias potential. ....	140
<b>Figure 4.47</b> O1s spectra of ta-C films deposited on Si substrate with a thickness of about 90 nm. The label at the tail of spectra is applied substrate bias potential.....	141
<b>Figure 4.48</b> The $sp^3$ content of ta-C films as a function of substrate bias potential. ....	142

<b>Figure 4.49</b> The XRR profiles of ta-C films deposited on Si substrate by varying substrate bias potential.....	143
<b>Figure 4.50</b> Thickness of the ta-C films estimated by the period oscillation of XRR curve. And (b) density of the ta-C films deposited on Si substrate as a function of substrate bias potential.....	144
<b>Figure 4.51</b> Electrical conductivity of the ta-C films deposited on Si substrate with the thickness of about 85 nm by varying substrate bias potential.....	145
<b>Figure 4.52</b> Distribution of ta-C film on the substrate holder (grounded).....	146
<b>Figure 4.53</b> The XRR profiles of ta-C films deposited on Si substrate. The label is the position of the sample on a substrate holder. ....	146
<b>Figure 4.54</b> Thickness and density of the ta-C films deposited on Si substrate were estimated by XRR analysis. ....	147
<b>Figure 4.55</b> C1s spectra of the ta-C films deposited on Si substrate. The label is the position of the sample on a substrate holder. ....	148
<b>Figure 4.56</b> Comparison of C1s spectra of the ta-C films deposited on Si substrate at three positions on a substrate holder. ....	148
<b>Figure 4.57</b> Diagram for a-C:H deposition. ....	149
<b>Figure 4.58</b> The a-C:H films deposited on Si substrate by varying discharge potential. ....	150
<b>Figure 4.59</b> XRR profile of the a-C:H films deposited on Si substrate by varying applied discharge potential. ....	152
<b>Figure 4.60</b> Deposition rate of the a-C:H films as a function of applied discharge potential.....	152
<b>Figure 4.61</b> The a-C:H films on Si substrate deposited by varying discharge potential, which controls the thickness of 90 nm.....	153
<b>Figure 4.62</b> Normalized Raman spectra and of the a-C:H films deposited with the different discharge potential. The label at the tail of spectra is applied discharge potential for an anode electrode of an L-ALIS. ....	155
<b>Figure 4.63</b> Double plot of the $I_D/I_G$ ratio (black dot) and the G peak position (red square) of the a-C:H films deposited on Si substrate with a thickness of about 90 nm. ....	156



<b>Figure 4.64</b> Survey spectra of a-C:H films with the thickness of 85 to 90 nm deposited by varying discharge potential.....	158
<b>Figure 4.65</b> C1s spectra of the a-C:H films with the thickness of 85 nm deposited by varying discharge potential. ....	159
<b>Figure 4.66</b> O1s spectra of the a-C:H films with the thickness of 85 nm deposited by varying discharge potential. ....	159
<b>Figure 4.67</b> The $sp^2$ and $sp^3$ content of a-C:H films as a function of discharge potential.....	160
<b>Figure 4.68</b> XRR profile of a-C:H films deposited by varying discharge potential. ....	161
<b>Figure 4.69</b> (a) Thickness and (b) density of a-C:H films on Si substrate deposited by a LAIS.....	162
<b>Figure 4.70</b> Electrical conductivity of a-C:H films deposited on Si substrate by an L-ALIS.....	163
<b>Figure 4.71</b> (a) discharge potential signal, (b) discharge current signal, (c) discharge power signal and (d) average discharge potential as a function of substrate bias potential. The label in the figure is the substrate bias potential. ....	166
<b>Figure 4.72</b> (a) substrate bias current and (b) deposition rate of the Cr films deposited on Si substrate using HiPIMS deposition. ....	167
<b>Figure 4.73</b> The Cr films deposited on Si substrate using HiPIMS deposition by varying substrate bias potential.....	168
<b>Figure 4.74</b> XRD pattern of the Cr films deposited on Si substrate with HiPIMS deposition technique. The label at the tail of the diffraction pattern as substrate bias potential.....	169
<b>Figure 4.75</b> Crystalline size of (110) Cr and (200) Cr structure in the Cr films as a function of substrate bias potential. ....	170
<b>Figure 4.76</b> (a) top surface and (b) cross-section of Cr films deposited at the substrate bias of $-100$ V, the deposition pressure of 0.016 torr, and the HiPIMS average power of 240 W, frequency of 1 Hz, and pulse width of 200 $\mu$ s respectively.....	171
<b>Figure 4.77</b> Assembly cross-section model of the a-C:H single layer and multilayer Cr/ta-C/a-C:H films. ....	173
<b>Figure 4.78</b> Physical characteristics of multilayer amorphous carbon films (Cr/a-C:H/ta-C). The label is the code of the sample.....	175

<b>Figure 4.79</b> The surface and cross section morphology of multilayer amorphous carbon films. (a) and (b) are S-1 sample, (c) and (d) are M-1 sample, (e) and (f) are M-2 sample, and (g) and (h) are M-3 sample. ....	178
<b>Figure 4.80</b> EDS spectrum in line scan mode of the M-3 sample. ....	179
<b>Figure 4.81</b> (a) hardness and elastic modulus and (b) load-displacement curves of indentations for the SUS304, a-C:H single layer and multilayer films. ....	182
<b>Figure 4.83</b> Multilayer Cr/ta-C/a-C:H film failure after scratch testing. ....	184
<b>Figure 4. 83</b> The acoustic emission signal of the scratch test. ....	185
<b>Figure 4. 84</b> Critical load of the a-C:H single layer and multilayer films deposited on the SUS304 substrate. ....	186
<b>Figure 4.85</b> Comparison of cracks mechanism of the a-C:H single layer and multilayer film. ....	187

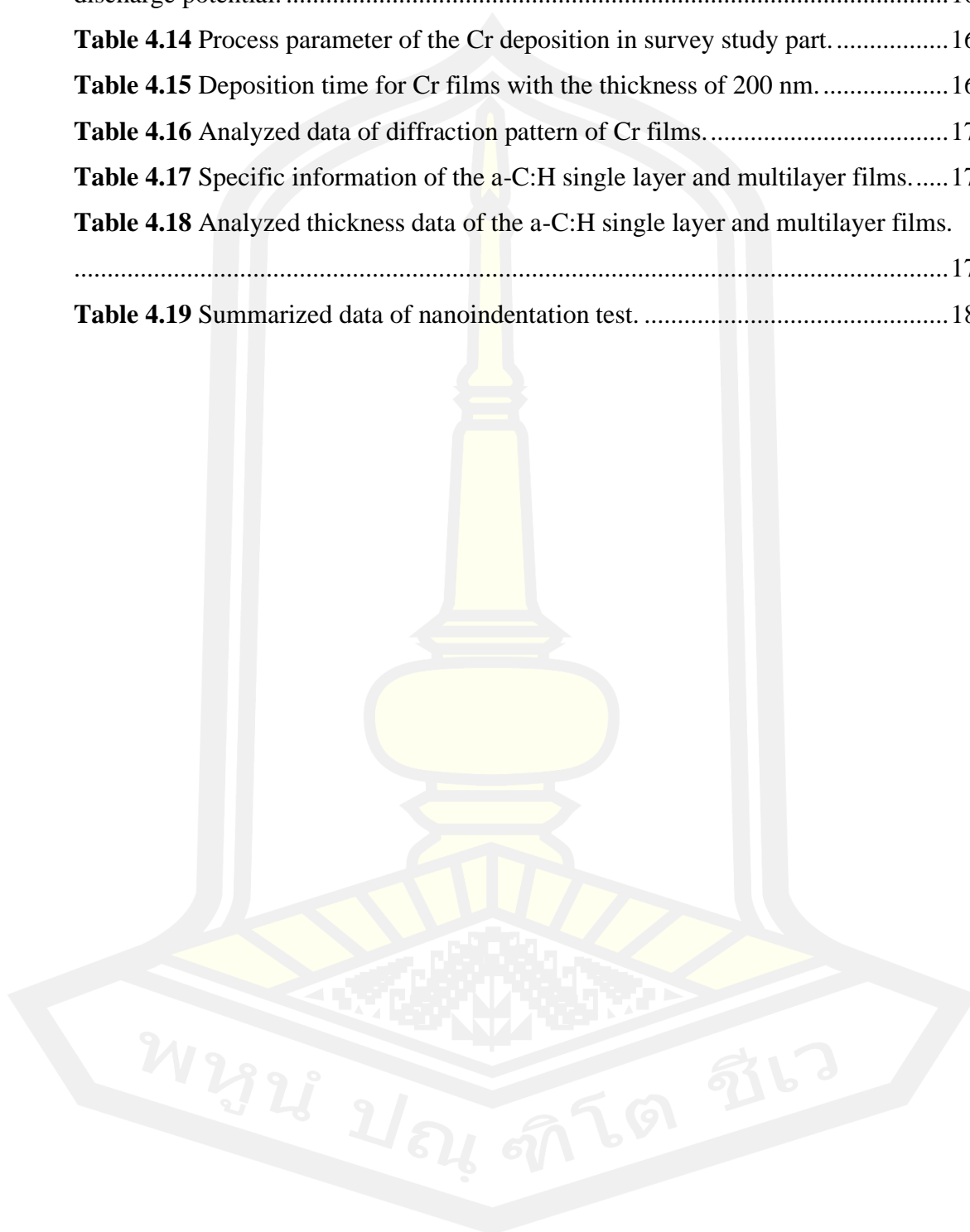




## LIST OF TABLES

<b>Table 2.1</b> Comparison of the coating material properties; Hardness (H), coefficient of friction (COF), Maximum application temperature ( $T_{\max}$ ), and color.....	11
<b>Table 2.2</b> Material hardness classification criteria.....	11
<b>Table 2.3</b> Comparison the properties of carbon-based material.....	15
<b>Table 3. 1</b> I/O interfaces and external connectors of NI PXI-8108 for the control system. ....	43
<b>Table 3.2</b> Specific data of the grids.....	79
<b>Table 4.1</b> Setup parameter of ion energy measurement for ground surface. ....	91
<b>Table 4.2</b> Setup parameter of ion energy measurement for substrate bias technique. ....	104
<b>Table 4.3</b> Process parameter for ta-C deposition on the SUS316 to study deposition profile.....	107
<b>Table 4.4</b> Deposition pulse for the synthesis of the ta-C film with the thickness of about 85 nm.....	115
<b>Table 4.5</b> Analyzed data of Raman spectra; Position, FWHM, area of D and G peak including $I_D/I_G$ ratio. ....	121
<b>Table 4.6</b> The fraction of chemical bonding in the ta-C films deposited by varying anode bias potential.....	125
<b>Table 4.7</b> Summary of estimated mechanical and tribological parameters: indentation hardness (H), elastic modulus (E), H/E, and $H^3/E^2$ ratios. Standard deviations are also listed in this table. ....	130
<b>Table 4.8</b> The z offset position of the substrate holder for synthesis of the ta-C films with the thickness of about 90 nm by varying substrate bias potential. ....	135
<b>Table 4.9</b> Analyzed Raman parameter of ta-C films deposited by varying substrate bias potential. ....	138
<b>Table 4.10</b> The fraction of chemical bonding in the ta-C films deposited by varying substrate bias potential.....	142
<b>Table 4.11</b> Process parameter of a-C:H deposition.....	153
<b>Table 4.12</b> Analyzed Raman parameter data of the a-C:H films. ....	155

<b>Table 4.13</b> The fraction of chemical bonding in the a-C:H films deposited by varying discharge potential. ....	160
<b>Table 4.14</b> Process parameter of the Cr deposition in survey study part. ....	165
<b>Table 4.15</b> Deposition time for Cr films with the thickness of 200 nm. ....	168
<b>Table 4.16</b> Analyzed data of diffraction pattern of Cr films. ....	170
<b>Table 4.17</b> Specific information of the a-C:H single layer and multilayer films. ....	174
<b>Table 4.18</b> Analyzed thickness data of the a-C:H single layer and multilayer films. ....	177
<b>Table 4.19</b> Summarized data of nanoindentation test. ....	183



## LIST OF ABBREVIATIONS

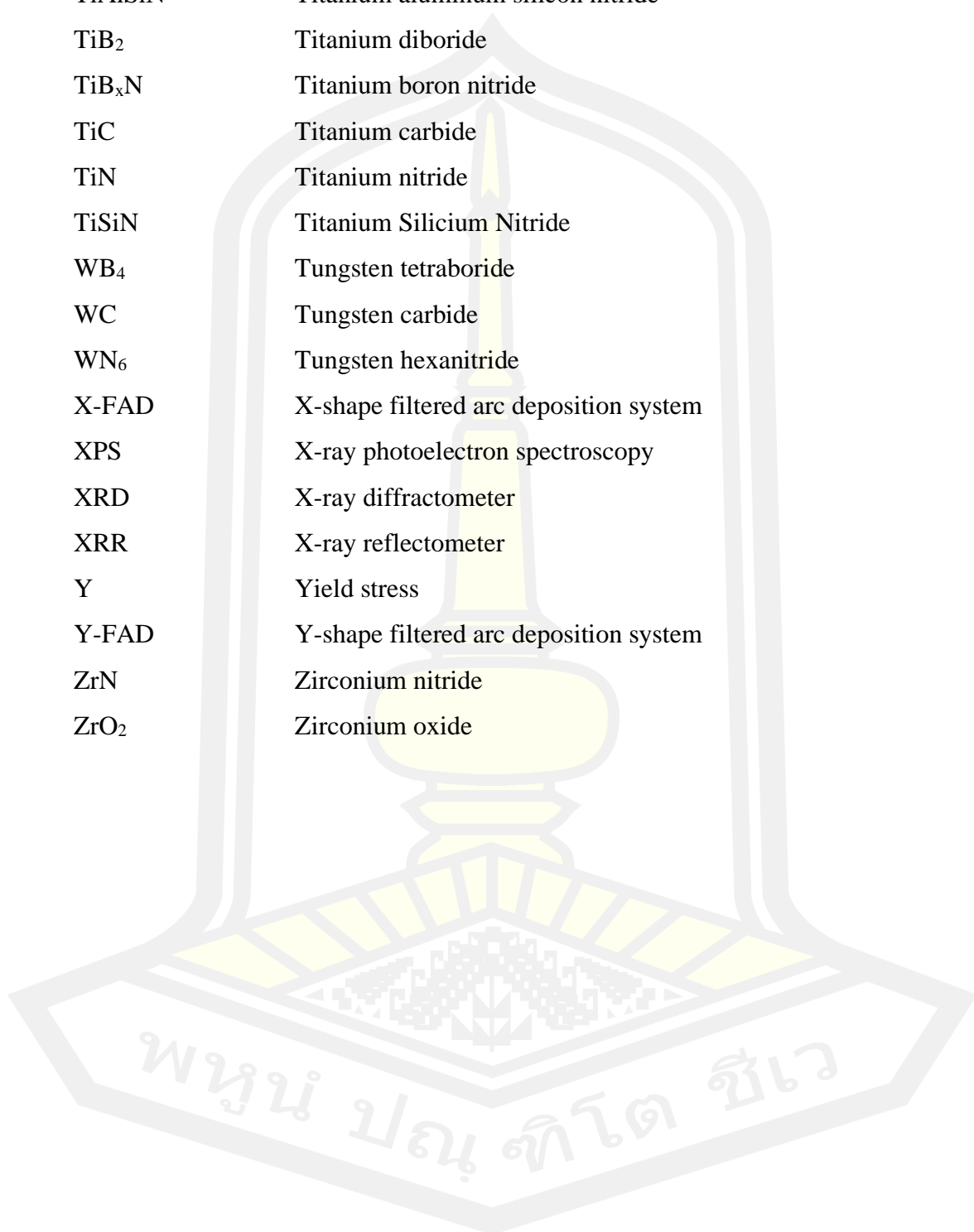
		<b>Unit</b>
$B_x$	Magnetic field in parallel component	Tesla
$I$	The current flowing through a contact point	A
$R$	The resistance of the contact point	$\Omega$
$\rho$	The temperature-dependent specific resistivity of the contact material	K
$A(l')$	The cross-section of the contact point	$\text{mm}^2$
$dl'$	Infinitesimal section of the contact path length	m
$Z$	The impedance of the PFN,	$\Omega$
$N$	The number of stages	
$L$	Inductance	$\mu\text{H}$
$C$	Capacitance	$\mu\text{F}$
$I_p$	Probe current	A
$I_i$	Ion current	A
$I_e$	Electron currents	A
$I_{is}$	Ion saturation current	A
$V_f$	Floating potential	V
$\lambda_{sh}$	Plasma sheath length	m
$M_i$	Mass of $\text{C}^+$ ions	kg
$A_p$	Aperture area	$\text{mm}^2$
$e$	Ion charge	C
$\varepsilon$	Kinetic energy	eV
$\lambda_D$	Debye length	m
$\eta_{system}$	System coefficient	
$F_B$	Lorentz force	N
$v_{\perp}$	Perpendicular speed	m/s

$\chi$	Total transparency of grid electrodes	
$n_i$	Ion density	$\text{m}^{-3}$
$v_i$	Ion velocity	$\text{m/s}$
$\varepsilon_i$	Mean energy of ions	$\text{eV}$
$\Gamma_i$	Ion flux	$\text{m}^{-2}\text{s}^{-1}$
$E$	Electric field	$\text{V/m}$
$f(\varepsilon)$	Kinetic energy distribution function	
$f(v)$	Velocity distribution function	
$I_{arc}$	Arc current	$\text{A}$
$I_{filter}$	Filter coil current	$\text{A}$
$I_{es}$	Electron saturation current	$\text{A}$
$J_i$	Current density	$\text{A/cm}^2$
$k_B$	Boltzmann constant	$\text{J/K}$
$m$	Mass of charge	$\text{kg}$
$n_e$	Electron density	$\text{m}^{-3}$
$q$	Particle charge	$\text{C}$
$r_c$	Gyration radius	$\text{m}$
$t$	Time	$\text{s}$
$T_a$	Temperature of neutrals	$\text{K}$
$T_e$	Temperature of electron	$\text{K}$
$T_i$	Temperature of ion	$\text{K}$
$v$	Charge velocity	$\text{m/s}$
$V_{ab}$	Anode bias potential	$\text{V}$
$V_d$	Discharge potential	$\text{V}$
$V_p$	Plasma potential	$\text{V}$
$V_s$	Substrate voltage	$\text{V}$
$V_p$	Scanning voltage	$\text{V}$
$D$	The gap distance between anode and cathode electrode	$\text{m}$
$B$	The magnitude of the magnetic field	$\text{Tesla}$

$L_c$	Critical load	N
$\sigma$	Sigma bond	
$\pi$	Pi bond	
$A$	Area	mm <sup>2</sup>
a-C	amorphous carbon	
a-C:H	Hydrogenated amorphous carbon	
a-C:H:Me	Metal containing hydrogenated amorphous carbon	
a-C:H:X	Modified hydrogenated amorphous carbon	
a-C:Me	Metal containing hydrogen-free amorphous carbon	
AFM	Atomic force microscopy	
AlCrN	Aluminium chromium nitride or Alcrona	
AlCrTiN	Aluminium chromium titanium nitride	
ALIS	Anode layer ion source	
AlN	Aluminium nitride	
Ar	Argon gas	
Ar <sup>+</sup>	Positive argon ion	
a-Si	Amorphous silicon	
C <sup>+</sup>	Positive carbon ion	
C <sub>2</sub> H <sub>2</sub>	Acetylene gas	
c-BN	Cubic boron nitride	
CFUBMSIP	Close field unbalanced magnetron sputtering ion plating	
CH <sub>4</sub>	Methane gas	
C <sub>m</sub> H <sub>n</sub> <sup>+</sup>	Positive molecular ion of acetylene gas	
CNC	Computer Numerical Control	
CN <sub>x</sub>	Carbon nitride	
COF	Coefficient of friction	
Cr	Chromium	
CrC	Chromium carbide	
CrN	Chromium nitride	
DLC	Diamond-like carbon	

E	Elastic modulus	Pa
EDS	Energy Dispersive X-Ray spectroscopy	
FCVA	Filtered cathodic vacuum arc	
FE-SEM	Field emission scanning electron microscopy	
FWHM	Full width at half maximum	cm <sup>-1</sup>
GND	Ground electrode	
H	Hardness	Pa
H/E	Elastic strain to failure	
H <sup>3</sup> /E <sup>2</sup>	Resistance to plastic deformation	
HiPIMS	High power impulse magnetron sputtering	
I <sub>D</sub>	Area of D peak	a.u./cm <sup>-1</sup>
I <sub>D</sub> /I <sub>G</sub>	Intensity ratio of D peak per G peak	
I <sub>G</sub>	Area of G peak	a.u./cm <sup>-1</sup>
L-ALIS	Linear anode layer ion source	
MEMs	Micro-electromechanical devices	
MS	Magnetron sputtering	
OSC	Oscilloscope	
PECVD	Plasma enhanced chemical vapor deposition	
PFCVA	Pulse filtered cathodic vacuum arc	
PFN	Pulse forming network	
R	roughness	m
RFA	Retrading field analyzer	
RF-PECVD	Radiofrequency plasma enhanced chemical vapor deposition	
SCR	Silicon controlled rectifiers	
Si <sub>3</sub> N <sub>4</sub>	Silicon Nitride	
SMU	Source meter unit	
ta-C	Tetrahedral amorphous carbon	
ta-C:H	Hydrogenated tetrahedral amorphous carbon	
TaN	Tantalum nitride	
T-FAD	T-shape filtered arc deposition system	

TiAlN	Titanium aluminum nitride
TiAlSiN	Titanium aluminum silicon nitride
TiB <sub>2</sub>	Titanium diboride
TiB <sub>x</sub> N	Titanium boron nitride
TiC	Titanium carbide
TiN	Titanium nitride
TiSiN	Titanium Silicium Nitride
WB <sub>4</sub>	Tungsten tetraboride
WC	Tungsten carbide
WN <sub>6</sub>	Tungsten hexanitride
X-FAD	X-shape filtered arc deposition system
XPS	X-ray photoelectron spectroscopy
XRD	X-ray diffractometer
XRR	X-ray reflectometer
Y	Yield stress
Y-FAD	Y-shape filtered arc deposition system
ZrN	Zirconium nitride
ZrO <sub>2</sub>	Zirconium oxide



## **Chapter I**

### **Introduction**

#### **1.1 Background and motivation**

Nowadays, nanotechnology is an emerging field of science that deals with the understanding and development of nanosized (1 nm to 100 nm) devices that have novel properties and functions due to their small size [1], [2]. These devices are used in a wide range of everyday applications, such as agriculture, subsistence, medicine, transportation, communication, etc.

Thin film technology is one of the nanotechnologies. Thin films are layers of atoms or groups of atoms bonded together in a nanometer to micrometer thin layers [3]. They are deposited on a substrate or sample to improve the surface properties of the material such as electrical, optical, mechanical, tribological, etc. Thin film technology has been widely used in the industry for example electronic devices, solar cells, optical displays, cutting tools, magnetic data storage devices, etc. [4].

Cutting tools such as cutting inserts, drills, end mills, taps, dies, and thread milling cutters are very important for the manufacture of metal and non-metallic components for large automotive parts of transport ships, spacecraft, airplanes, automobiles, as well as small parts of microelectronic equipment and others [5]. However, the cutting tools have high friction from contact with the metal sample during the manufacturing working process, which leads to the wear of their, including damage on the surface of the sample, and low quality [6], [7]. Therefore, to reduce the wear rate of cutting tools, the cutting tools are developed to achieve the high hardness and low coefficient of friction by modifying the material, new designs for reducing the contact area (reduce the coefficient of friction), and surface modification by hardening and coating.

Generally, the cutting tool is often coated with nitride and carbide layers such as titanium nitride (TiN), chromium nitride (CrN), titanium carbide (TiC), tungsten carbide (WC), etc., to increase the hardness and thermal stability [6]. Currently, the metal manufacturing industry has focused on the dry manufacturing process. This increases the wear rate of the protective coating due to the thermal expansion mismatch with the substrate, leading to damage of the cutting tool and sample [7].



Therefore, many studies are trying to synthesize the new coating materials, with high hardness, low coefficient of friction, and high thermal stability.

Superhard materials are materials with a hardness greater than 40 GPa [8]–[10], such as diamond, diamond-like carbon (DLC), titanium diboride ( $\text{TiB}_2$ ), titanium boron nitride ( $\text{TiB}_x\text{N}$ ), titanium aluminum nitride ( $\text{TiAlN}$ ), cubic boron nitride (c-BN), tungsten hexanitride ( $\text{WN}_6$ ) and tungsten tetraboride ( $\text{WB}_4$ ), etc. [11]–[16]. Besides, these materials have corrosion resistance, a low coefficient of friction, and high thermal stability. These materials are studied, developed, and coated on cutting tools to reduce the damage, increase their service lifetime, and reduce the cost of maintenance.

Diamond-like carbon (DLC) films belong to amorphous carbon materials (a-C) in a metastable state. The structure consists of a mixed bond of carbon hybridization  $\text{sp}^3$  and  $\text{sp}^2$  [17]. DLC films can be divided into many types depending on the proportion of  $\text{sp}^3$ ,  $\text{sp}^2$  and hydrogen, including doped elements [18]. The  $\text{sp}^2$  carbon hybridization exhibits graphite properties, while the  $\text{sp}^3$  carbon hybridization exhibits diamond properties [19]. Therefore, DLC films have high hardness, low coefficient of friction, wear resistant and chemical inert. Hydrogenated amorphous carbon (a-C:H) have  $\text{sp}^3$  content of about 20 to 60 %, the hydrogen content of about 10 to 50 %, the hardness of 10 to 45 GPa, the density of about 1.5 to 2.4  $\text{g/cm}^3$  [18]. While tetrahedral amorphous carbon (ta-C) has a high  $\text{sp}^3$  content of 70 to 90%, the hydrogen content lower than 20%, the hardness 15 to 60 GPa, the density in the range of 2.7 to 3.2  $\text{g/cm}^3$  [20]–[22], and the coefficient of friction 0.01 to 0.2 [23], [24].

Due to these excellent properties, DLC films have a wide range of applications [25], especially as a hard coating to protect scratches on automotive parts, as a coating layer on cutting tools [26], [27], as a dielectric layer in electronic devices [28], as protective coatings on the recording media and read-write heads of magnetic storage devices to minimize mechanical wear and corrosion [20], [29], [30]. However, the ta-C film has some defects for applied in the industry such as high internal stress, the thermal stability less than the metal nitride [31]–[33].

Decades ago, the interlayer and multi-layer coating designs are gaining great attention in the hard coating industry. X. Sui et.al, [34] study the mechanical and tribological properties of DLC single-layer film, CrN single-layer film, Cr/DLC film,

and CrN/DLC/Cr-DLC multilayer film. The multilayer film has high hardness and low coefficient of friction, due to the combination of the outstanding properties of ceramics and DLC material. However, this work used a chemical vapor deposition technique to prepare the DLC film layer, causing the multilayer film to have a hardness of lower than 10 GPa. While, Wei et.al, [23] prepare the multilayer ta-C film using the filtered cathodic vacuum arc technique with substrate bias to control the ion energy of carbon, which is correlated with the  $sp^3$  bonding. They found that the multilayer ta-C film had the maximum hardness of 59 GPa and the coefficient of friction around 0.04-0.08, due to posing alternately of the ta-C has high  $sp^3$  and low  $sp^3$  layer. Moreover, the film has good adhesion to the substrate because the carbon ions can implantation into the substrate, so the film has a strong bond with the substrate. Therefore, the design of the coating layer, deposition technique, and carbon ion energy is a very important parameter on the structure and properties of the DLC film [35], [36].

From the literature review, the ta-C film has good mechanical and tribological properties, which is suitable for the superhard coating material. This thesis will be developing the ionized physical vapor deposition system for synthesis of the superhard amorphous carbon films. The system consists of the filtered cathodic vacuum arc, magnetron sputtering, anode layer ion source and linear anode layer ion source, which installed in the deposition chamber. Also, the system has a special technique is plasma biasing, in which accuracy controls the ion energy of the carbon. The influence of ion energy of the carbon on the microstructure, mechanical, and tribological properties of the ta-C film was studied. The multilayer film with the alternating of ta-C layer and a-C:H layer was deposited on the silicon wafer and the stainless steel (SUS304) substrate. The morphology and microstructures were performed using scanning electron microscopy (SEM), Raman spectroscopy, x-ray photoelectron spectroscopy (XPS), x-ray reflectometer (XRR). The mechanical and adhesion properties were investigated using nanoindentation and scratch test respectively. The ion energy of carbon measured using a retarding field analyzer probe (RFA probe) works together with the source measure unit (SMU).

## 1.2 Objectives

- Develop an ionized physical vapor deposition system for superhard amorphous carbon coatings.
- Synthesis of the superhard amorphous carbon films by ionized physical vapor deposition system.
- Link the plasma properties to properties of ta-C film deposited using filter cathodic vacuum arc.

## 1.3 The scope of works

- Development of the superhard amorphous carbon coating system under the ionized physical vapor deposition based on these deposition techniques.
  - Filtered cathodic vacuum arc (FCVA) deposition combined with plasma biasing and substrate bias technique for the synthesis of the ta-C film.
  - Linear anode layer ion source for a-C:H deposition.
  - Anode layer ion source for substrate cleaning.
  - Magnetron sputtering for metal deposition (Cr interlayer).
- Development of a control system for equipment mounted on an ionized physical vapor deposition system by using a PXI controller base on the LabVIEW program.
- Focus on the synthesis of the single layer ta-C, single layer a-C:H and multilayer Cr/ta-C/a-C:H films by using an ionized physical vapor deposition system.
- Silicon wafers (P-type, 0.001-0.004  $\Omega\cdot\text{cm}$ ) were used as the substrate for morphology and microstructure characterization. And stainless steel (SUS304) was used as the substrates for multilayer Cr/ta-C/a-C:H films, which investigated the mechanical properties.
- Characterization technique
  - Plasma diagnostic
    - Retarding field analyzer
  - Film characterization
    - Surface and morphology
      - Field emission scanning electron microscopy (FE-SEM)

- Energy-dispersive X-ray spectroscopy (EDS)
- Atomic force microscopy (AFM)
- Microstructure
  - Raman spectroscopy
  - X-ray photoelectron spectroscopy (XPS)
  - X-ray diffractometry (XRD)
  - X-ray Reflectometry (XRR)
- Electrical properties
  - Four point probe
- Mechanical properties
  - Nanoindentation test
- Adhesion properties
  - Scratch test

#### **1.4 The location of the research**

- Technological Plasma Research Unit (SC1-211), Department of Physics, Faculty of Science, Mahasarakham University, Thailand.
- Laboratory Equipment Center (SC1-110), Faculty of Science, Mahasarakham University, Thailand.
- Research instrument center, Khon Kaen University, Thailand.
- Synchrotron Light Research Institute (Public Organization), Thailand.
- National Science and Technology Development Agency (NSTDA), Thailand.
- National Nanotechnology Center (NANOTEC), National Science and Technology Development Agency, Thailand.
- HELMUT FISCHER (THAILAND) CO., LTD.

#### **1.5 Anticipated outcomes**

##### **New Knowledge**

- From this thesis, we will have a hybrid ionized physical vapor deposition system for superhard amorphous carbon coatings. which this system responds with the many deposition materials due to it consists of four plasma sources; FCVA, L-ALIS, ALIS, and MS.
- The concept and experience for the design and fabrication of plasma sources.

- Knowledge about the control system; vacuum devices, vacuum systems and IPVD systems using PXI-controller based on the LabVIEW program.
- Knowledge for the synthesis of multilayer amorphous carbon films between ta-C and a-C:H using FCVA sources combined with L-ALIS.
- Knowledge and production of the hybrid ionized physical vapor deposition system, RFA probe, and DLC films can be applied to the thin film coating industry (magnetic storage industry and manufacturing industry (protective coating on cutting tools)).

#### **New process**

- The synthesis process of multilayer Cr/ta-C/a-C:H films by using the FCVA sources and L-ALIS.
- Time-resolved measurement of ion energy of the  $C^+$  in FCVA deposition with an RFA probe.

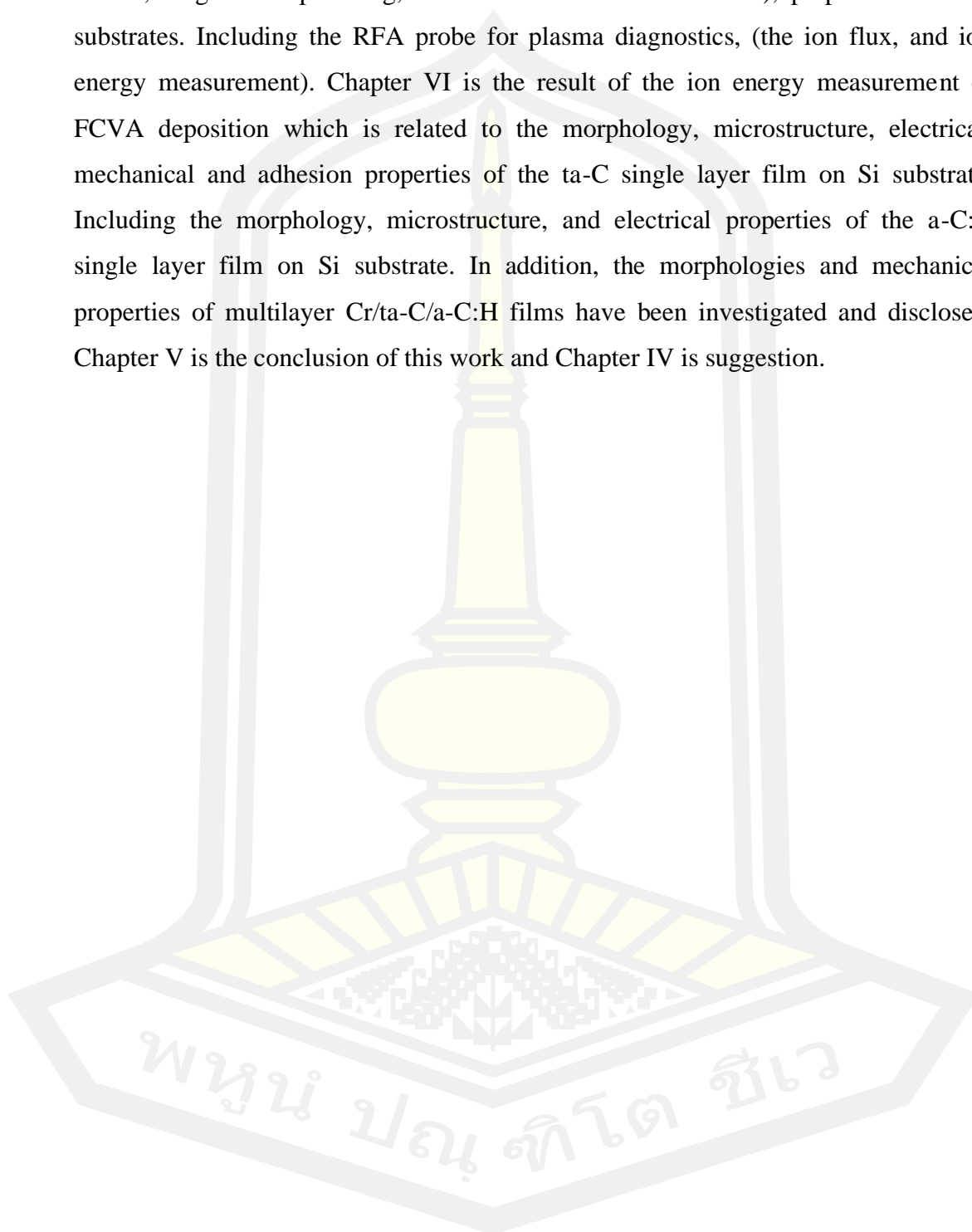
#### **New technology / New technique**

- Ionized Physical Vapor Deposition System
- The RFA probe with excellent performance for plasma diagnostic.
- High hardness amorphous carbon film.

### **1.6 Outline of the thesis**

This thesis has been divided into 6 chapters, which are related to the development of an ionized physical vapor deposition system, ion energy measurement in FCVA deposition, the deposition and characterization of the morphology, microstructure, and mechanical properties of the DLC films were synthesized by an ionized physical vapor deposition system. The introduction to this thesis has already been described in Chapter I, including the background and motivation, objective of this thesis, the scope of the study, the location of the research, and outline of the thesis. The literature reviews and theoretical background in Chapter II provide the superhard coating materials, basic principles and a brief of the DLC films, hydrogenated amorphous carbon (a-C:H), tetrahedral amorphous carbon (ta-C), and multilayer DLC films. In addition, the basic of cathodic vacuum arc and filtered cathodic vacuum arc will give in detail. In Chapter III, there are the experimental detail, which consists of the concept, design and build of the ionized physical vapor

deposition system, plasma sources (anode layer ion source, linear anode layer ion source, magnetron sputtering, and filter cathodic vacuum arc), preparation of the substrates. Including the RFA probe for plasma diagnostics, (the ion flux, and ion energy measurement). Chapter VI is the result of the ion energy measurement of FCVA deposition which is related to the morphology, microstructure, electrical, mechanical and adhesion properties of the ta-C single layer film on Si substrate. Including the morphology, microstructure, and electrical properties of the a-C:H single layer film on Si substrate. In addition, the morphologies and mechanical properties of multilayer Cr/ta-C/a-C:H films have been investigated and disclosed. Chapter V is the conclusion of this work and Chapter IV is suggestion.



## **Chapter II**

### **Literature reviews and theoretical background**

This chapter describes the literature review related to this thesis, in which hard coating material, superhard coating material, and these properties will be compared the advantages and disadvantages. This will lead to the concept and design of an ionized physical vapor deposition system and superhard amorphous carbon films.

#### **2.1 Literature review**

Nowadays, the world has great technological advances. The large-scale manufacturing industry has developed machinery to meet the needs of consumers. And able to produce new technologies efficiently. Automotive parts manufacturing (ships, aerospace, automobiles, airplanes, etc.) including the electronics industry, is a manufacturing industry that is very important to driving global technology. Manufacturing large parts down to micrometer sizes requires efficient forming tools to reduce defects that may occur on the workpiece during the manufacturing process.

Computer Numerical Control or CNC machining is a manufacturing process in which pre-programmed computer software dictates the movement of factory tools and machinery. The process can be used to control a range of complex machinery. With CNC machining, three-dimensional cutting tasks can be accomplished in a single set of prompts [37]. However, the main equipment used for forming the sample is machining tools.

The machining tools is a machine for handling or machining metal or other rigid materials, usually by cutting, boring, grinding, shearing, or other forms of deformation [38]. The cutting tools such as cutting inserts, drills, end mills, taps, dies, and thread milling cutters are the main equipment for the forming of the sample (metals, alloys, plastics, ceramics). The quality of the cutting tools depends on hardness, elasticity, wear resistance, corrosion resistance, etc. Normally, the sample forming process has cooled to reduce heating by pair friction between the cutting tool and sample. Moreover, low thermal conductivity materials resulted in a rapid temperature rise in the cutting zone which enhances tool wear [39]. The use of cutting fluids in the machining process reduces friction between chip and tool. It also helps to carry away the wear debris from the machining zone. However, the use of cutting



fluid is harmful to ecology include human health. Because regulations and management that is not strict about cutting fluids. The used cutting fluid is then released into the environment. Also, these fluids can cause skin and lung diseases among machine operators [40]. So, there is a strong need to shift towards sustainable manufacturing to have both financial and environmental benefits.

In recent years a constant effort has also been made to reduce the use of cutting fluids [40]. Dry machining, which refers to completely avoid the use of cutting fluid in the manufacturing process has several advantages like no health issues to operators, no pollution, etc. [41]–[43]. However, the service lifetime of the cutting tool in it during the dry process is reduced due to the high friction of the cutting tool and sample leading to the failure of the cutting tool [44]. Shokrani et al., 2012 reported that the cost of cutting fluid is about 16% of the total machining cost. And the tooling cost amounts to 4% of the machining cost. It clearly, the cost of a reduction in the tool life than the much lower the costs associated with cutting fluids. Thus, these problems such as diseases to operators and disposal of cutting fluids in an environment-friendly manner can be reduced by adopting dry machining [45]–[47].

To alleviate the drawbacks of the dry machining process, several sustainable techniques in manufacturing have been adopted for cleaner technology production [48]. For enhancing the performance of the dry machining applications, the cutting tools were changed as follow:

- The cutting tools have been designed in different ways to achieve sustainability.
- The development of new cutting tool materials, applying coatings solid layer, and solid lubricants.
- New design of the surface texture to reduce the friction coefficient by decreasing tool-chip and contact length [49]–[53].

Surface coating is the most method to increase the performance and life of cutting tools. In the market, we can see the cutting tools of different colors such as gold, blue, black, gray, brown, etc. These colors have not come from paint technique, but it comes from coating technology. Coating technology was applied to increase the performance and life of cutting tools. The coating material has high hardness, high



thermal stability, low friction coefficient, high corrosion resistance, etc., as shown in **Error! Reference source not found.** The coating materials have different hardness and thermal stability. However, these materials have different applications, which must be used appropriately for the best benefit.



**Figure 2.1** Cutting tools [54].

The hardness level of the coating materials divided into 3 levels as shown in Table 2.2. It can be seen that the materials in **Error! Reference source not found.** such as TiN, CrN, TiC, and TiAlN are hard coating material, which these materials have high thermal stability and rough surface texture. Usually, the physical vapor deposition (PVD) technique is the most of nitride coating. In order to improve durability for mechanical and tribological applications, its were developed into the multilayer coating. Multilayer coating of nitride materials can be divided into 2 categories: isostructural multilayers and non-isostructural multilayers. Isostructural multilayers contain individual layers that have the same crystallographic structure, such as TiN/NbN, TiAlN/ZrN, and TiN/CrN. Nonisostructural multilayers consist of layers with different crystallographic structures, such as TiN/AlN, TiN/TaN, and TiN/CNx, providing a further barrier to dislocation motion [55]. Moreover, superlattice multilayers exhibit significant hardness enhancement [56]–[60]. The hardness of nitride multilayer coatings is 30 to 60 GPa and gradually decreases when working temperatures higher than 500 °C [33], [61], [62].

**Table 2.1** Comparison of the coating material properties; Hardness (H), coefficient of friction (COF), Maximum application temperature ( $T_{\max}$ ), and color.

Coating material	H (GPa)	COF	$T_{\max}$ (°C)	Color
Diamond	100	0.05	-	Transparent
c-BN	50	-	-	-
TiN	24	0.55	400-1300	Gold
TiAlN	28-32	0.5	800	Violet-black
TiB <sub>2</sub>	40-70	-	-	-
TiB <sub>x</sub> N	15 - 25	-	-	-
WN <sub>6</sub>	57	-	1300	-
WB <sub>4</sub>	40	-	1300	-
TiC	30	0.3	-	Black
TiCN	32	0.2	400	Copper
AlTiN	38	0.7	900	Black
AlTiN/Si <sub>3</sub> N <sub>4</sub>	45	0.45	1200	Violet-Black
CrN	18	0.3	700	Silver
AlCrN	28-40	-	1100	Bright-gray
ZrO <sub>2</sub>	8-8.5	-	1000-1500	Gray
TiSiN	40	-	1000-1500	Metallic gold
AlCrN	32	0.6	1000	Blue-Gray
ta-C	35-80	0.02-0.4	200-600	Depend on the thickness
ta-C:H	50	0.02-0.3		
Diamond-like carbon	10-80	0.01-0.5		

**Table 2.2** Material hardness classification criteria.

Classification criteria	H (GPa)
Hard coating	< 40
Superhard coating	40 - 80
Ultrahard coating	> 80

However, nitride coating has a disadvantage in the high coefficient of friction with the rough surface texture. While diamond-like carbon coating has high hardness, low coefficient of friction, and a wide range of properties. Therefore, it has gained a lot of attention from the coating industry.

## 2.2 Diamond-like carbon

Diamond is the metastable, highest density  $sp^3$  phase of solid carbon material. Diamond has excellent properties, such as a high Young's modulus, a high hardness, a wide bandgap, a high thermal conductivity, good biocompatibility, and high carrier mobility as a semiconductor. In general, diamonds can be found in nature. Nowadays, the single crystals of diamond or polycrystalline diamond films can produce, but the production cost is very high. For micromechanical devices and biosensors applications, nanocrystalline diamond films are useful because of their greater smoothness at a lower cost. To reduce the production cost and still the properties of diamond, diamond-like carbon (DLC) material was studied and produced.

Diamond-like carbon (DLC) has a low production cost, can deposit at room-temperature, good mechanical properties, absence of grain boundaries, very smooth, and biocompatibility. This topic will describe the structure, production, mechanical properties, tribology properties, electrochemical properties, and applications of DLC.

Physically, DLC is an amorphous carbon network solid, containing the content of carbon  $sp^3$  hybridization,  $sp^2$  hybridization,  $sp^1$  hybridization, and hydrogen content. Therefore, DLC has high hardness, low coefficient of friction, and chemical inert. From excellent properties, the DLC films have a wide range of applications as protective coatings such as optical windows, magnetic storage disks and read-write head of the hard disks, engine parts, biomedical coatings, food packaging, and micro-electromechanical devices (MEMs).

Normally, carbon forms a great variety of crystalline and disordered structures due to the carbon that can exist in three hybridizations  $sp^3$ ,  $sp^2$ , and  $sp^1$  as shown in Figure 2.2 [63]. In the  $sp^3$  configuration, four valence electrons of the carbon atom are each assigned to a tetrahedrally directed  $sp^3$  orbital, resulting it makes a strong  $\sigma$  bond with an adjacent carbon atom. In the  $sp^2$  configuration as in graphite, three of the four valence electrons of carbon atoms enter trigonally directed  $sp^2$  orbitals, which make

strong  $\sigma$  bonds in a plane. The fourth electrons of the  $sp^2$  atom lies in a  $p\pi$  orbitals, which lies normal to the  $\sigma$  bonding plane. This  $p\pi$  orbital forms a weaker  $p\pi$  bond with a  $\pi$  orbital on one or more neighboring atoms. In the  $sp^1$  configuration, two of the four valence electrons enter  $\sigma$  orbitals, each forming a strong  $\sigma$  bond directed along the x-axis, and the other two electrons enter  $p\pi$  orbitals in the y and z directions.

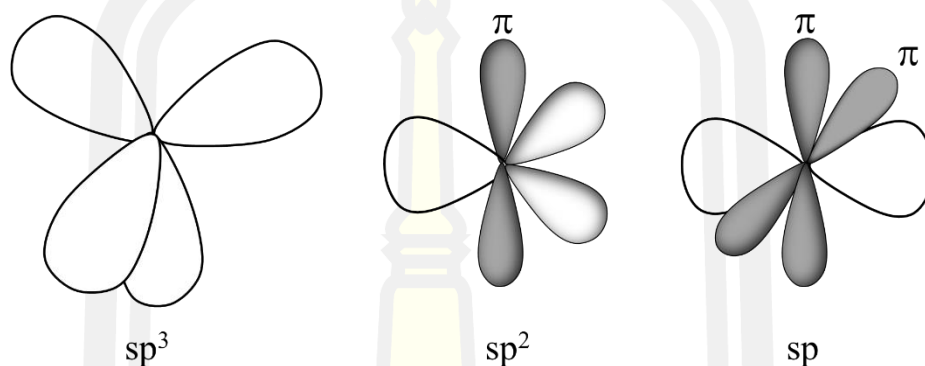


**Figure 2.2** The  $sp^3$ ,  $sp^2$ , and  $sp^1$  hybridized bonding (modified from [20]).

The good physical properties of diamond content in the DLC, derive from its strong  $\sigma$  bonds. Diamond has a tetrahedral structure as shown in Figure 2.3(b) the carbon atom has a strong  $\sigma$  bond. Therefore, it has the largest bulk modulus of any solid, the highest atom density, smallest thermal expansion coefficient, and largest limiting electron and hole velocities of any semiconductor [64]. While the graphite has strong  $\sigma$  bonding and weak van der Waals bonding between the layers as shown in Figure 2.3(a). As the result, it has low hardness. A single graphite plane is a zero bandgap semiconductor.

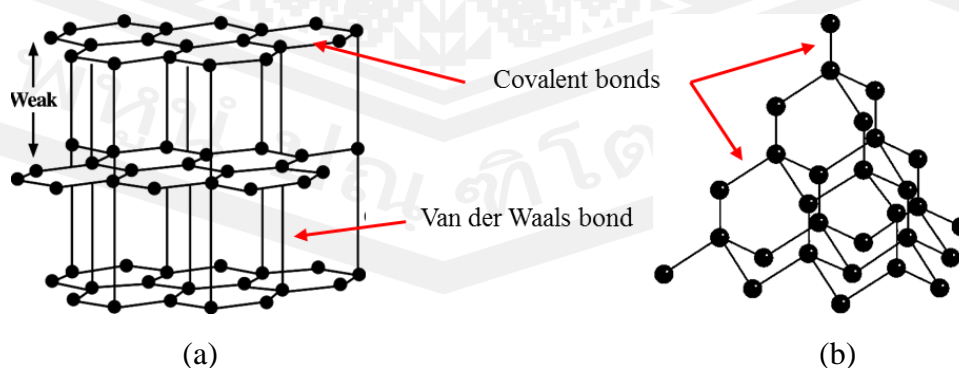


**Figure 2.3** Structure of (a) graphite and (b) diamond.

Currently, the DLC coating has a large variety of carbon-based coating modifications, the types of DLC coatings are as follows [18]:

- Hydrogen free amorphous carbon films (a-C)
- Hydrogen free tetrahedral amorphous carbon films (ta-C) with a high fraction of tetrahedral coordinated  $sp^3$  bonded carbon atoms
- Metal containing hydrogen-free amorphous carbon films (a-C:Me), where the metal often is a carbide forming metal like titanium or tungsten
- Hydrogenated amorphous carbon films (a-C:H)
- Hydrogenated tetrahedral amorphous carbon films (ta-C:H)
- Metal containing hydrogenated amorphous carbon films (a-C:H:Me)
- Modified hydrogenated amorphous carbon films (a-C:H:X), where X is related to non-metal elements such as silicon (Si), oxygen ( $O_2$ ), nitrogen ( $N_2$ ), fluorine (F), and boron (B).

Also, DLC films can be prepared from a variety of processes and the properties of DLC films can be determined by the  $sp^3$  site,  $sp^2$  site, and hydrogen content. A comparison of the properties of carbon-based material prepared different techniques as shown in Table 2.3.

The  $sp^3$  bonding of DLC films confers on it many of the beneficial properties of the diamond itself, such as its high hardness, chemical and electrochemical inertness, and wide bandgap. DLC consists not only of the amorphous carbons (a-C), but also of the hydrogenated amorphous carbon (a-C:H) which a ternary phase diagram as in Figure 2.4, description the relationship between  $sp^3$ ,  $sp^2$ , and hydrogen. These lie in the lower left-hand corner, it consists of many a-Cs with disordered graphitic ordering, such as soot, chars, glassy carbon, and evaporated a-C. On the other hand, in the right-hand corner, if only the hydrogen content we have not found the film. Also, when the  $sp^2$  and  $sp^3$  content increase, it results in the hydrocarbon polymers polyethylene  $(CH_2)_n$  and polyacetylene  $(CH)_n$ , But interconnecting C–C networks cannot form, and only molecules form. And the top of the triangle, when the film has high  $sp^3$  content, the  $sp^2$  and hydrogen content will be decreased and the film has high hardness.

**Table 2.3** Comparison the properties of carbon-based material.

	% sp <sup>3</sup>	% H	$\rho$ (g/cm <sup>3</sup> )	H (GPa)	Technique	Ref
Diamond	100	0	3.515	100	-	
Graphite	0	0	2.267	-	-	
C60	0	0	-	-	-	
Glassy C	0	0	1.3 - 1.55	3	-	
a-C	21 - 51	0	2.3 - 2.7	13 - 23	HiPIMS	[65]
ta-C	80 - 88	0	3.26	80	S bend FCVA	[66]
a-C:H hard	40	30 - 40	1.6 - 2.2	6 - 23	RF-PECVD	[67]
a-C:H soft	60	40 - 50	1.2 - 1.6	16-26	PECVD	[68]
ta-C:H	70	30	2.4	50	Plasma source	[69]
Polyethylene	100	67	0.92	0.01	-	

From Table 2.3, the DLC films can be prepared by many techniques. RF-PECVD and PECVD techniques use hydrocarbon gas as a precursor of carbon atoms such as CH<sub>4</sub>, C<sub>2</sub>H<sub>2</sub>, etc., the existence of hydrogen atoms cannot be avoided. Therefore, the films have low hardness and low friction coefficient. Likewise, the plasma source technique uses hydrocarbon gas to deposit the DLC films. This technique can deposit the ta-C:H film, in which high hardness, low friction coefficient, and good tribological properties because the plasma source can excitability the hydrocarbon gas and generate high plasma density, high ion fraction, and high ion energy, into optimizing condition for deposit the DLC films.

In addition, the DLC films deposited by the magnetron sputtering technique are a hard coating, but low deposition rate because use a carbon target for the precursor of the carbon atom, in which the carbon target has a low sputtering yield. Moreover, the FCVA technique can deposit high density, ultra-hardness DLC films, which meets the objectives of this thesis. Therefore, the next topic will be discussed.



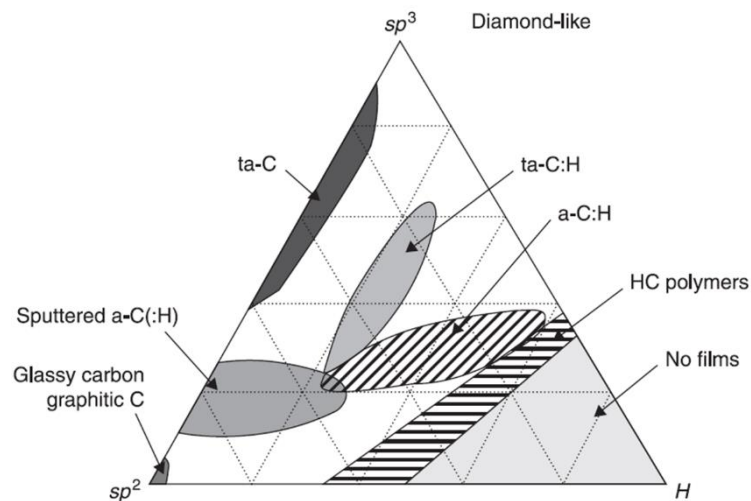


**Figure 2.4** Ternary phase diagram of bonding in amorphous carbon-hydrogen alloys [20].

### 2.3 Tetrahedral amorphous carbon

Tetrahedral amorphous carbon (ta-C) has been studied intensively in the previous decade. Usually, the ta-C is deposited at room temperature. Fallon et al. [70] they were found that the properties of the ta-C film deposited using a 90° filter FCVA as a function of the ion energy of carbon ions, which the  $sp^3$  fraction, density, and stress of the films increase with the increase of ion energy. The ion energy of about 100 eV is an optimized condition for fabricating ta-C film with the highest  $sp^3$  fraction, density, stress, and optical bandgap. In addition, the films become more  $sp^2$ -like at low and high ion energies.

Chhowalla et al. [71] reported that the optical gap of the ta-C film depends on the ion energy. The ion energy of about 100 eV is optimized condition for fabricating ta-C film with the wide optical bandgap. Teo et al. [72] found that optical absorption measurements were affected by the defect in ta-C films (related to surface roughness), in which the bandgap is larger once the defect in the film is removed. Corresponding with the studies of Xu [73], the ta-C films deposited on S-bend arcs with very low microparticle content have wide gaps of around 3.3 eV. It is seen that the optical gap, varies in proportion to the  $sp^3$  fraction. This is expected from the dependence on the  $sp^3$  fraction for all forms of a-C:H, ta-C:H, and ta-C. The bandgap is controlled by the ordering and distortions of  $\pi$  states on  $sp^2$  sites or graphite fraction [74], and this result confirms the findings of Raman that the  $sp^2$  ordering depends in a consistent way on

the  $sp^3$  fraction [75]. The bonding in ta-C film is described as follows. Its network is defined by the connectivity of its  $sp^3$  atoms. They form a network similar to that of a-Si (tetrahedral structure), except that it contains a small fraction of rings (three and four membered), which would be unstable in a-Si [76]. The  $sp^2$  atoms act as defects within this network structure, they forming small clusters with an even number of atoms. The  $sp^2$  clusters tend to be chains (olefinic) rather than aromatic, due to not giving rise to a D peak in Raman is above the vibrational density of states (VDOS) band limit of graphite in UV Raman [75]. The  $sp^3$  network strains and disorder the  $sp^2$  clusters. The bandgap is determined by the size of the clusters and the degree of their disorder.

The sensitive application for example magnetic storage disks, the surface roughness of the ta-C film is an important parameter. The lower value of the roughness and good coverage quality of ta-C and other DLC films is a critical quality for their applications. Marks et al. [76] showed that the surface roughness of ta-C film measured using Atomic force microscopy (AFM) varies in a consistent with the ion energy. The ta-C film deposited with intense and energetic bombardment with the energy of around 100 eV shows that it reaches a minimum roughness and maximum  $sp^3$  content correspond with the report of Lifshitz et al [77], [78]. From these reports, it suggested that ion energy is an important parameter, which determines the microstructure properties of the ta-C film.

However, the properties of the ta-C film prepared by the FCVA technique depend on other factors as well. Figure 2.5 compares the variation of  $sp^3$  fraction of ta-C prepared by different FCVA systems. It is clear that the  $sp^3$  fraction is different for each FCVA system, it indicates that the properties of the films are different. Therefore, the  $sp^3$  fraction in the ta-C film does not depend on only ion energy. Development of the FCVA systems to give ta-C with a higher  $sp^3$  fraction and extends over a wider range of deposition ion energies is a very challenging job.

In addition, for industrial applications, the substrate bias technique is not used to increase ion energy and enhance the properties of ta-C film, using only the plasma self-energy to give the ion energy (self-bias). Xu et al. [79] also found that the energy bandgap of ta-C film increased with a slower growth rate. Therefore, it is clear that the  $sp^3$  fraction is not a single valued function of the ion energy. Generally, the



maximum  $sp^3$  fraction occurs at an ion energy of about 100 eV, except for the data of McKenzie et al. [80].

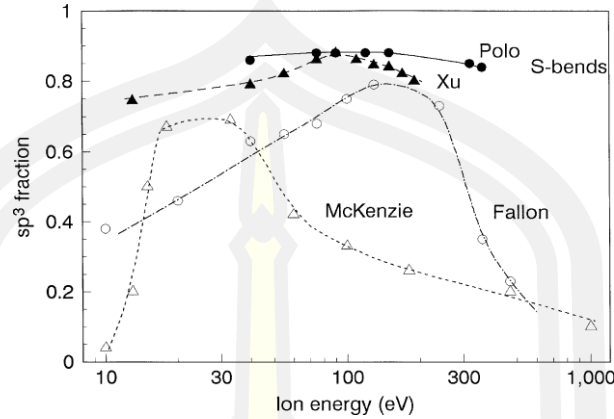


**Figure 2.5** Comparison of the variation of the  $sp^3$  fraction with ion energy for ta-C, showing the range of variations possible with the different FCVA filter systems and plasma duct sizes [20].

### 2.3.1 Mechanical properties

The mechanical properties of DLC are of great importance properties because DLC films as a protective coating [81]. The mechanical properties consist of hardness (H) and elastic modulus (E). Usually, the mechanical properties of DLC films are correlated to their density, chemical composition, and  $sp^3$  content. For example,  $sp^3$ -rich DLC films grown with an energetic ion bombardment were reported to exhibit high hardness, while hydrogenated DLC films exhibit lower hardness, Young's modulus, density, thermal stability, and compressive stress when compared with hydrogen-free DLC films [65]. However, the interpretation of these values is straightforward and can't explain the physical meaning. Therefore, to interpret these values, a theory is needed for their explanation. Hardness is related empirically to the yield stress (Y) and elastic modulus (E) by

$$\frac{H}{Y} = 0.07 + 0.06 \left( \frac{E}{Y} \right) \quad (2.1)$$

For materials with a low Y/E ratio such as diamond and other ceramics, the H/E is 1.8. In which, brittle materials like DLC, yield occurs by bond cleavage. In this case, the yield stress can be calculated by the Orowan approximation [82]. This means

that the yield stress is given by the load to break the bonding, approximating the force curve of a bond by a sine curve. This gives

$$\frac{E}{Y} = \pi \quad (2.2)$$

Combining these equations gives

$$\frac{H}{E} = 0.16 \quad (2.3)$$

The H/E ratio, called elastic strain to failure (rupture), is a suitable parameter for predicting the wear resistance of materials (other than hardness). Materials with high H/E ratio values have better wear and failure resistance (high values of H/E ratio translate into high hardness and low elastic modulus). This parameter can be used to predict whether the films will crack or not under load. According to previous studies, coatings with H/E are considered to be resistant to cracking [83]. Moreover, the  $H^3/E^2$  ratio is a strong indicator of coating resistance to plastic deformation (proportional to the elastic deformation of coatings). This parameter is used for the prediction of shear banding under localized deformation. The films with a high  $H^3/E^2$  ratio can be greatly resistant to plastic deformations.

In conclusion for superhard coating, high hardness and low Young's modulus are desirable to increase the elastic strain to failure and resistance to cracking, allowing the applied load to distribute over an extended layer volume.

The mechanical properties of DLC thin films can be estimated using nanoindenter test . In this technique, a small diamond tip is a pressed forced into the film, and the force-displacement curve is measured. The hardness is defined as the pressure under the tip, given by the ratio of force to the projected area of plastic deformation. Normally, the indentation depth must be limited to a fraction of order 10% of the total film thickness for accuracy (avoid the effect of substrate) [84].

Pharr et al. [85] show the corresponding variation of elastic modulus of ta-C deposited by laser arc as a function of the ta-C density. They found that the elastic modulus steady increases with the increase of film density. Due to the change from  $sp^2$  to  $sp^3$  bonding with increasing density. In addition, for hydrogen-free a-C, the elastic modulus is expected to vary with the bond-density N as  $N^{2/3}$  [82]. Moreover, Shi et al. [86] reported that the hardness increases with the increase of  $sp^3$  content and

the linear trend may be too steep when compared with the equivalent fall in elastic modulus found by Schultrich et al. [87].

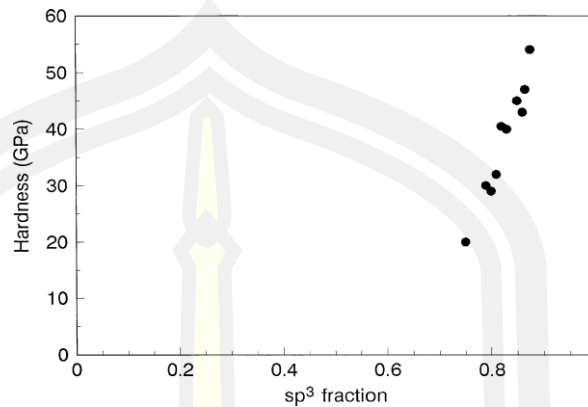


**Figure 2.6** Variation of nano-hardness of ta-C with  $sp^3$  fraction [82].

### 2.3.2 Tribological properties

Tribology of the coating material involves the adhesion, friction, wear, and lubrication of solids in contact. The tribology properties are extremely dependent upon the physical, chemical, and morphology properties of the surface [88]. Tribology properties can be estimated by a ball-on-disk tribometer and pin-on-disk tribometer [21], [24]. This technique uses a ball or a pin for a pair contract with the sample, which a ball or a pin depends on the experimenter required. The data of the coefficient of friction (COF) and wear rate of the sample have been received. During the friction occurs by contact between the ball and film surfaces. The real area of contact is much less than the apparent area of contact so that the real contact pressure is much greater than the average load pressure. The friction force arises from adhesion, deformation, or abrasion at the contact. Adhesive contact dominates for elastic materials with high H/E ratios, in DLC materials. The friction then depends on the transfer layer, which is believed to be graphitic carbon [89].

Normally, DLC films are notable for their low friction coefficients. Many previous studies reported the coefficient of friction of the DLC films has a range of 0.01-0.5 [90]–[93], which depends on the film properties. Ean et al. [94], deposit the ta-C films on the tungsten carbide cobalt by using an FCVA deposition and varying substrate bias potential. They found that the ta-C films deposited under the substrate bias -16 V have a hardness of 65 GPa. But the COF and wear rate is different depending on the condition parameter. The surface roughness is high for the ta-C film

deposited with non-substrate bias, related to the high wear rate. Moreover, the pair contact was damaged and generate the tribolayer, lead to severe corrosion on the surface.

However, ta-C films have some limitations to their practical implications performance for superhard coating on cutting tools are that high residual compressive stress from the complicated cross-linked  $sp^3$  bonds in the films. This introduces to weakly adhesion to the substrate, therefore the thickness of the films has a maximum of 300 to 500 nm depending on  $sp^3$  content. Nowadays, to improve the adhesion of ta-C films on the substrate and increase the thickness of DLC films, the interlayer and doping element methods will be applied. Moreover, multilayer coating is applied to enhance the mechanical, tribological, and corrosion properties of the DLC film.

## **2.4 Multilayer DLC film**

Despite the many advantages characteristic of DLC films, there are some limitations to their practical implications performance for example, high residual compressive stress from the complicated cross-linked of  $sp^3$  bonds and  $sp^2$  bonds, thermal stress from the mismatches of the elastic modulus and expansion coefficient between the DLC films and the substrate give rise to weakly adhesion to the substrate and poor toughness. Especially under harsh cutting with high cyclic fatigue, DLC films with high compressive stress tend to fracture or failure in the initial phase of working, which significantly restricts their cutting application [95]–[97]. Nowadays, many studies aimed to increase the toughness, adhesion strength, tribological characteristics, corrosion and erosion properties of DLC coated cutting tools using various methods. These studies adjusted the  $sp^3/sp^2$  ratio by changing deposition process parameters and designing the film material composition or structure, such as an alternated multilayer design, doping element with metal, un-metal, metal compound and interlayer deposition to improve the mechanical, tribological, corrosion and erosion of DLC films.

From the plastic deformation mechanism of the multilayer architecture, the multiple interfaces constrain the dislocation and defects in crystalline lattices and free volumes in amorphous structures, which contributes to improving the hardness and toughness of amorphous carbon. In addition, the defect being pinned by multi-

interface structures helps to prevent crack formation and propagation under complicated stress fields, where the multilayer interfaces act as barriers to stopping defect coalescence [98], [99]. Previous studies have reported that the multilayer structure design for DLC films provides a decrease of internal stress leading to the overcome the limitation of low thickness, including an increase of hardness, toughness, tribological, corrosion, and erosion properties. However, the properties of multilayer DLC films depend on design (composition of the soft and hard layer, modulation ratio, and interlayer).

Some literature referred to multilayer films alternant layers of DLC/metal nitride such as TiN/a-C:H [100] and TiAlN/DLC [101]. They were found that the incorporation of carbon layers has effective to improving tribological properties. In addition, The number of nitride layers is the main parameter to confine the hardness, COF and wear resistance, these properties were improved with the increase of the number of nitride layers, but the fracture toughness decreased.

The mechanical and tribological performances of the novel TiN/a-C:H multilayer coatings strongly depend on the bilayer period and thickness ratio [100]. Among them, the TiN/a-C:H coating with a bilayer period of 125 nm, and the thickness ratio of 1:1 or 1:2 exhibited the optimal properties in hardness, fracture toughness and good adhesion with the substrate, which showed better wear resistance. While the TiAlN/DLC multilayer film [101] obtained at the substrate bias potential of -150 V with a Cr/CrC<sub>x</sub>/CrC transition layer exhibited excellent adhesion (LC = 63 N) with the substrate, which is related to the surface morphology. The smooth surface obtained at a higher substrate bias is leading to intense and energetic ion bombardment, which affected on the diffusion of the adatom, which improves the adhesion. Moreover, adopting the gradually increasing biases and suitable composition of multilayer TiAlN/DLC, is helpful for fabricating the thick TiAlN/DLC multilayer coating (4.5  $\mu\text{m}$ ) without any interfacial failure.

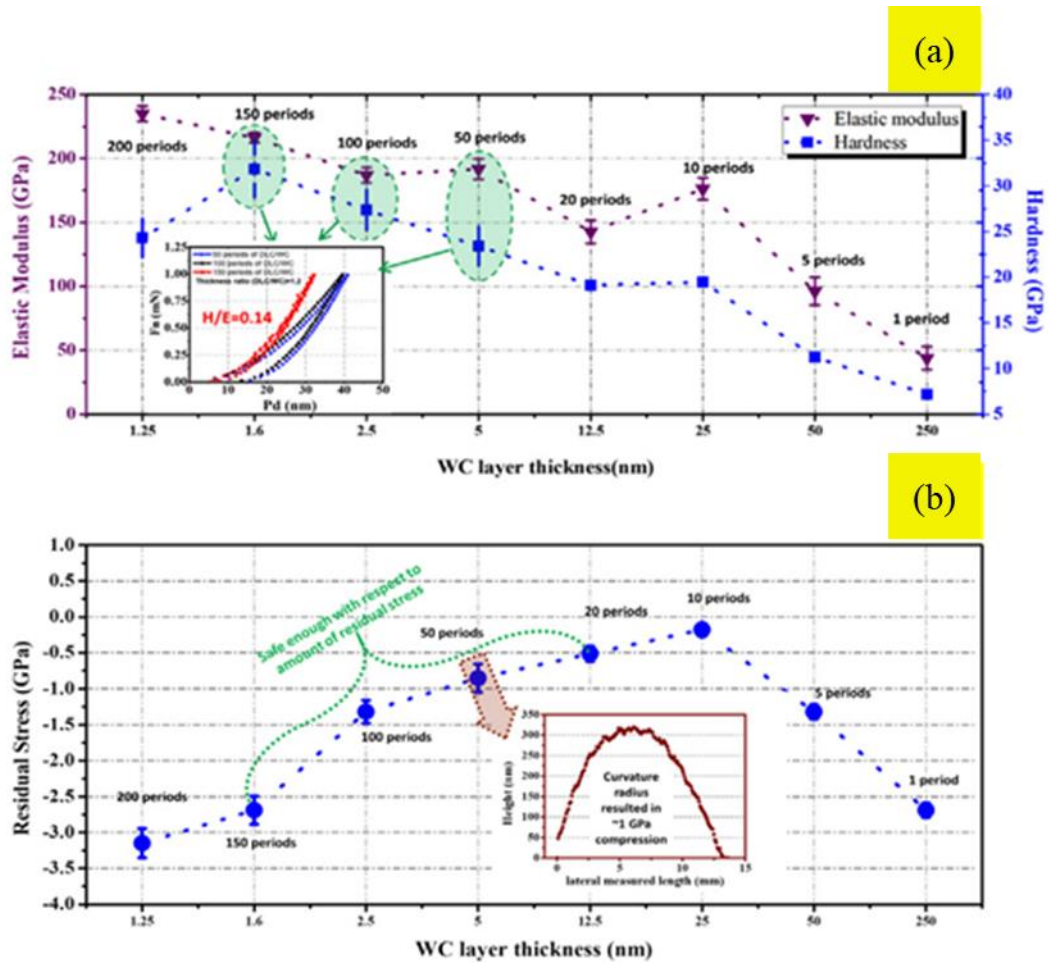


**Figure 2.7** The effects of a bilayer period on the mechanical properties. (a) Elastic modulus and hardness, and (b) residual stress of WC/DLC coatings for the bilayer period [98].

In some studies, the multilayer films composed of alternating layers of DLC/doped DLC and DLC/carbon-containing compounds for example, Ti-DLC/a-C:H [101] and WC/DLC [98], were fabricated to further improve the mechanical properties (hardness and adhesion of film layer/substrate). The Ti-DLC/a-C:H multilayer film shows a lower  $sp^3$  content and a higher  $sp^2$  content compared to the monolayer a-C:H film, which confirms the compressive stress of the multilayer film can be effectively released by an alternating multilayer construction. In addition, the Ti-DLC/a-C:H multilayer film showed super adhesion to the substrate, high toughness, lowest COF and low wear rate, indicate that it has implying an excellent wear resistant performance superior to monolayer a-C:H film,



Nemati et al. [98] introduced a multilayer WC/DLC coating with the combination of superhard coating level (higher than 45 GPa), high H/E ( $\sim 0.15$ ), low compressive residual stress (lower than 3 GPa), and highly resistant wear behavior (wear rate lower than  $10^{-13}$  mm<sup>3</sup>/nm) by optimizing the period number and adopting low-temperature annealing, which can improve the mechanical properties of the multilayer films. This result can be explained by the migration and diffusion of carbon from the WC layer to the DLC layer after annealing at 250 Celsius, which resulted in a rise in the fraction of sp<sup>3</sup> bonds in the DLC layer. Hence, low temperature annealing lower than 400 Celsius, generated an increase in the mechanical properties of the coating through the thermally induced redistribution of carbon. Figure 2.7(a) and (b) showed that the hardness, elastic modulus and residual stress of the WC/DLC multilayer are significantly correlated with the bilayer periods.

Wei et al. [23] reported that the multilayer ta-C films alternating of ta-C high-sp<sup>3</sup>-content and low-sp<sup>3</sup>-content layers were synthesized using FCVA deposition combined with substrate bias voltages alternating. It was found that the M-1 multilayer film has a hardness of 54.6 GPa and elastic modulus of 693.5 GPa. In addition, multilayer ta-C film with optimum period ratio showed lower residual stress (6.2 GPa), a lower wear rate ( $2.87 \times 10^{-7}$  mm<sup>3</sup>/nm) and a lower coefficient of friction (0.06) than that of the single ta-C film. Moreover, the multilayer architecture effectively restricted spalling and peeling of ta-C film, which the wear rate and mechanical properties of the multilayer ta-C films as shown in Figure 2.8

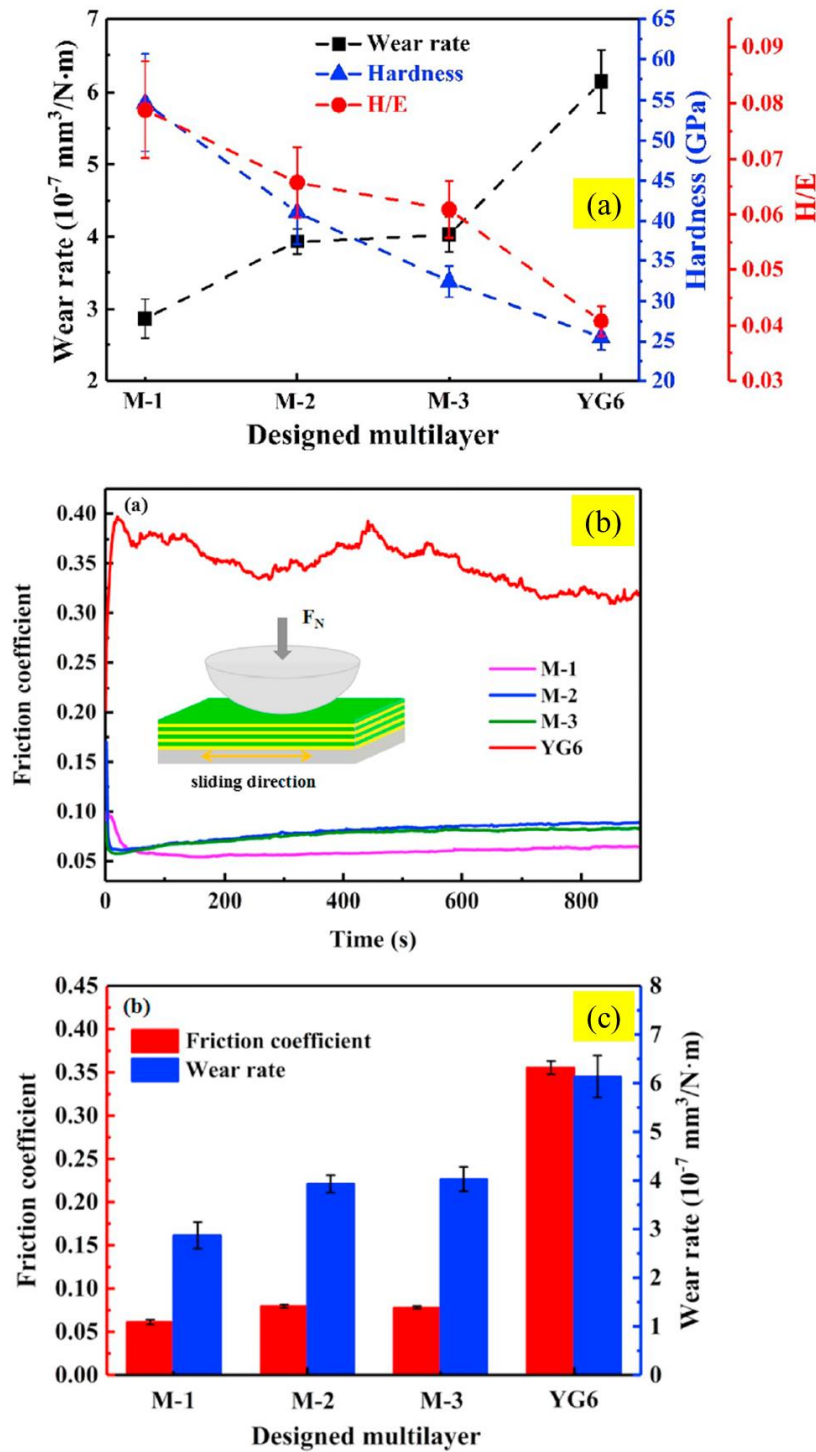
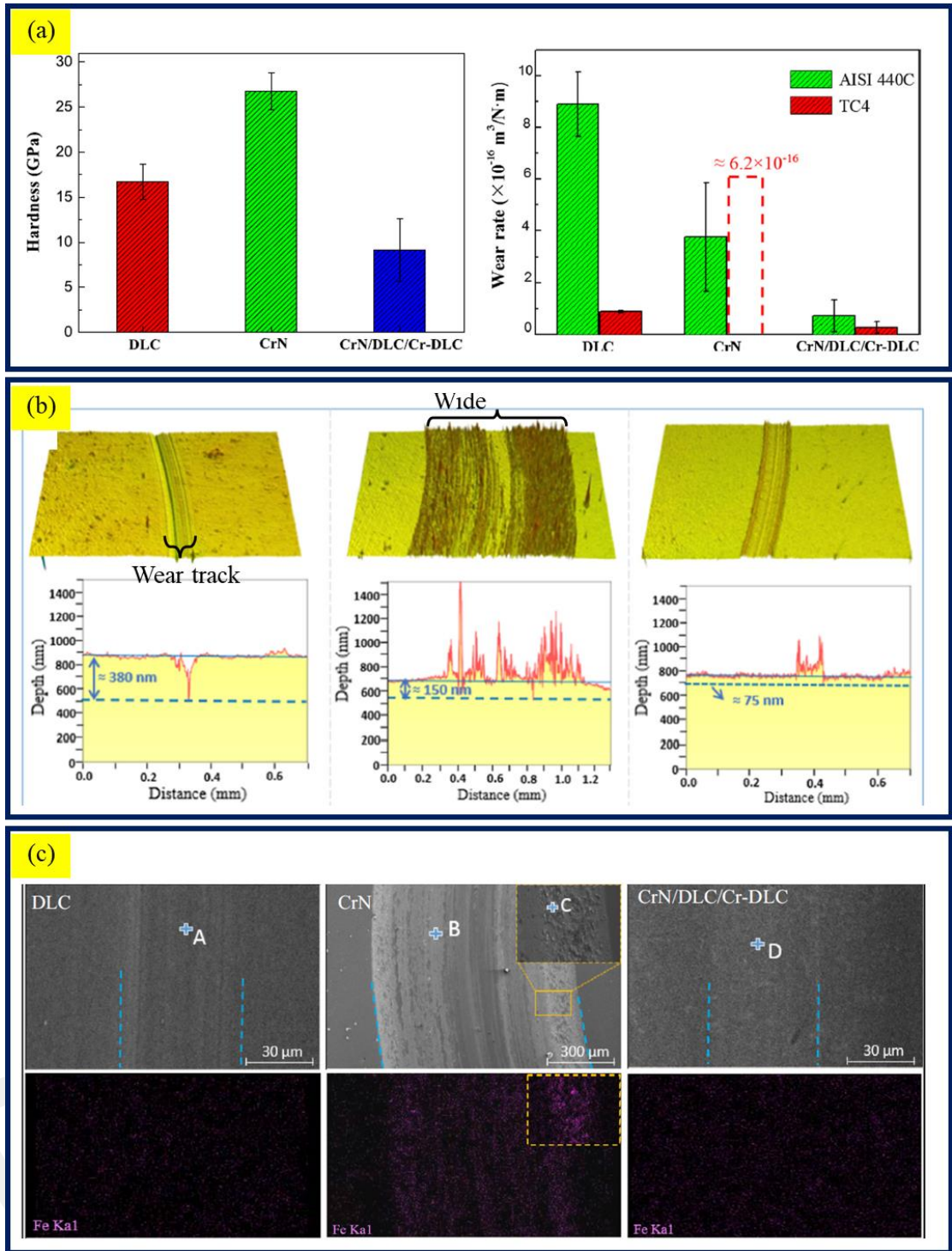


**Figure 2.8** The ta-C multilayer of alternating high- $\text{sp}^3$ -content and low- $\text{sp}^3$ -content layers, the  $\text{sp}^3$  content ratio of the sample is M-1: 51/60, M-2: 44/60, M-3: 36/60, YG6: substrate. (a) Wear rate, hardness and H/E ratio of the samples, (b) Friction coefficient curves against sliding times and (c) Average friction coefficient and wear rate of samples [23].



Lin et al. [102] reported that a multilayer DLC coating comprising alternating hard and soft layers was fabricated using an unbalanced magnetron sputtering system. They were found that the bilayer periods and thickness ratios have affected on the wear rate of DLC coatings, which the SEM morphologies of the wear tracks at an applied load of 80 N, as shown in **Error! Reference source not found.** it was found that the 50% hard multilayer with a bilayer thickness of 61 nm show better toughness and anti-abrasive properties than the monolayer hard DLC coating, especially at a contact load of 3.65 GPa. Under the high load, toughness is crucial to influence the wear resistance, while under the low applied load, the wear rate is highly related to the hardness. The alternating of low-sp<sup>3</sup>-content layers in the multilayer construction contributes to plastic deformation by alleviating the high compressive stress. In addition, the interfaces between the soft and hard layers in the multilayer design provide barriers to reduce the initiation of cracks due to the it was propagation at the interface.

Sui et al. [34] developed the CrN/DLC/Cr-DLC multilayer composite coatings prepared on a plasma-enhanced chemical vapor deposition (PECVD) device with the close field unbalanced magnetron sputtering ion plating (CFUBMSIP) technique. The Cr-containing DLC coating with a transfer layer with a CrN/DLC multilayer, which is characterized by hard Cr layers in combination with lubricant DLC layers. They were found that the CrN/DLC/Cr-DLC multilayer better fracture toughness in the indentation process, in comparison with the single DLC and CrN layer coatings with large cracks and delaminated regions. Moreover, the presence of interfaces in the transfer multilayer structure is conducive to restraining crack propagation. The CrN/DLC/Cr-DLC coating exhibited a low wear rate, which is attributed to the DLC lubricant layer, hard CrN load-support layers and interfaces in crack inhibition. Figure 10 shows the indentation morphologies and 3D images and cross-sectional profiles of wear tracks sliding with an AISI 440C ball. It was found that the wear rate of CrN/DLC/Cr-DLC multilayer coating is  $2.64 \times 10^{-17} \text{ m}^3/(\text{N.m})$ , lower than CrN coating. However, the hardness of the multilayer has a value in the range of 9 GPa, due to the DLC layer deposited using PECVD has a high sp<sup>2</sup> content, which reduces the internal stress but decreases the hardness of the coating as shown in Figure 2.9.



Considering the effects of the multilayer design on the mechanical and tribological properties of the DLC coating can be the conclusion as follows:

- (i) The multilayer DLC films provide an increase in hardness and toughness, decrease in internal stress, and further increases the tribological properties, due to the multi-interface structures.
- (ii) The interfaces of multilayer coating has a role is barriers to defect coalescence, prevent crack formation and propagation under a complicated stress field, which improves the toughness of the coating.
- (iii) Both the bilayer period and the thickness ratio are important parameters to control the performance of the multilayer DLC coating.
- (iv) The  $sp^3$  content in the hard layer important parameter to control the mechanical properties of the multilayer coating.
- (v) The adhesion of multilayer DLC film/substrate depending on interlayer material and deposition process.

The literature review showed that the mechanical properties (hardness) are determined by the properties of the hard layer such as WC layer, TiAlN layer, TiN layer and CrN layer. While the tribological properties (friction coefficient or COF) are determined by the soft layer and the properties of top layer. Therefore, to improve the mechanical properties this thesis focus on the synthesis of multilayer amorphous carbon films alternating of ta-C layer and a-C:H layer or multilayer Cr/ta-C:/a-C:H films, in which ta-C layers deposited using filter cathodic vacuum arc.

## 2.5 Cathodic vacuum arc

Cathodic arc deposition or Arc-PVD is a physical vapor deposition technique in which an electric arc is used to vaporize material from a cathode target. The vaporized material then condenses on a substrate, forming a thin film. The technique can be used to deposit metallic, ceramic, and composite films.

The arc evaporation process begins with the high current and low voltage arc mode on the cathode target that gives rise to a small, leading to a high density and energetic emitting plasma area, this area is called the cathode spot. The arc discharge current at the cathode surface, forming non-stationary locations of extremely high current density (order  $10^{12}$  A/m<sup>2</sup>). The high current density is associated with an

extremely high areal power density (order  $10^{13} \text{ W/m}^2$ ) and extremely high temperature (around  $15000^\circ\text{C}$ ), which in turn provides the conditions for the localized phase transformation from the solid (the cathode material) to a fully ionized plasma [103]. Hence, cathodic arc plasmas contain multiply ionized ions. The ion charge state distributions are enhanced at early discharge times, and they become quasi-stationary for discharge times greater than 100 ms and leaving a crater behind on the cathode surface, then it self-extinguishes and re-ignites in a new area close to the previous crater. This behavior causes the apparent motion of the arc as shown in Figure 2.10.

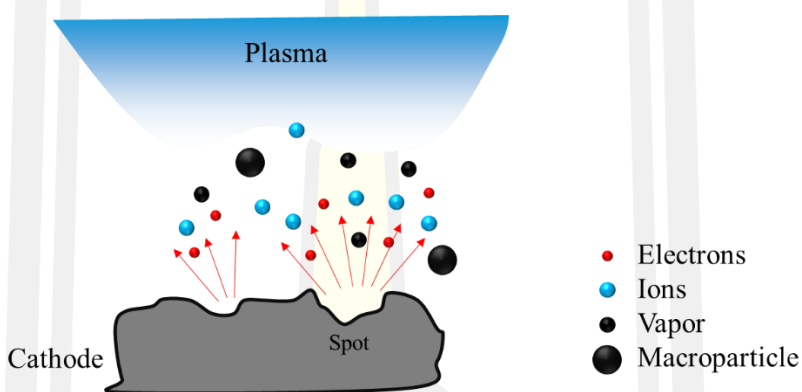


**Figure 2.10** Schematic physical model of the emission of particles from the surface of the cathode spot of the arc discharge.

Brown [104] study the plasma properties and characteristics of 50 cathode elements. The data have been explained in the form of a periodic table of material and plasma properties, it has been shown that ion charge states are different in each material. Also, the ion density can be enhanced by magnetic fields and other methods [105]. Usually, the neutral flux is negligible compared to the ion flux, and therefore the technique name has been changed with a strict physics point of view from “arc evaporation” is “cathodic arc plasma deposition”.

The arc process has an extremely high power density resulting in a high level of ionization (30-100%), in which the multiply charged ions, neutral particles, clusters, and macroparticles (droplets) were generated at the same time. If a reactive gas is introduced to the deposition chamber during the arc process, it can have interactions with the ions (dissociation, ionization, and excitation) and deposit on the substrate into compound films. The plasma produced at cathode spots expands rapidly

into the vacuum ambient. Interestingly, the observed final ion velocities are in the range of  $1.2 \times 10^4$  m/s, almost independent of the cathode material and ion charge state due to electron/ion coupling [106], [107]. The directed ion velocities are supersonic and correspond to approximately 20 eV for light elements and 200 eV for heavy elements. These high ion energies are the major reason for the different film properties obtained by cathodic arc plasma deposition.

One downside of cathodic vacuum arc, the cathode spots are not only the source of fully ionized plasma but also of droplets and debris particles, commonly referred to as macroparticles. Many studies reported the production and size distribution of microparticles, e.g. [108]. Although most reports quote the size range of 0.1 to 10  $\mu$ m and difficult to detect and characterize. The macroparticles are particles that are much larger than ions, atoms, and clusters. Macroparticle prevention or removal is perhaps the most important issue for the future of cathodic arc plasma deposition. The conventional and most successful approach is magnetic filtering to separate the droplets from the coating flux.

Cathodic arc deposition was applied on the coating industrial, to synthesize extremely hard, superhard, and hard films to protect the surface of cutting tools and extend the life of their significance. Hard, Superhard coatings, and nanocomposite coatings such as TiN, TiAlN, CrN, ZrN, AlCrTiN, and TiAlSiN can be synthesized by this technology.

Also, this technology is used quite extensively for carbon ion deposition to create diamond-like carbon films. Because the high density ions are discharged from the cathode surface, single atoms and microparticles are ejected. Thus, this kind of system requires a filter to remove macroparticles from the plasma beam before deposition. The DLC films deposited by filtered cathodic vacuum arc contain an extremely high percentage of  $sp^3$  diamond which is known as tetrahedral amorphous carbon (ta-C films).

## 2.6 Filtered cathodic vacuum arc

It is known that the cathodic vacuum arc will be generated microparticles, causing the defect in the films. To remove this probe, the cathodic vacuum arc was developed by using the filter such as a mechanical filter and magnetic filter.



Therefore, this technique is called “Filtered cathodic vacuum arc or FCVA”. But the design, characteristics, shape, and mechanics of the filter have different depending on the development timeline and purpose of the work.

The basic objective of macroparticle filtering is to prevent line-of-sight of the particle to the substrate and to guide the plasma efficiently to the substrate. For practical applications, the filtering system employed is required to be as efficient as possible. A practical definition of this efficiency is the “system coefficient” ( $\eta_{system} = I_{I,filter} / I_{arc}$ ) which is the filtered ion current normalized by the arc current [109].

The combination of an applied magnetic field (to control electrons) and an electric field (to control ions) is used to induce the plasma to the deposition area. The electrons are magnetized, i.e. forced to spiral along the magnetic field lines due to their gyration radius ( $r_c = -mv_{\perp} / qB$ ) being less than the filter size. On the other hand, the ions have a much larger gyration radius and are unmagnetized but follow the guided electrons in order to maintain a quasineutral state of the plasma. Simple magnetic solenoidal systems have been demonstrated to reduce the macroparticle content in the films. These filters are of the form of a tube with an axial magnetic field. The macroparticles are ejected at low angles to the cathode surface [110], travel in straight trajectories and impact the walls of the tube. Whereas the plasma was bent towards the substrate. The number of macroparticles is reduced by the solid angle occupied by the substrate. In a recent device [111], the application of a magnetic field of 15 mT was found to increase the ionization of metal vapor and macroparticles. The net effect was to produce smoother coatings and the deposition rate is low.

Nowadays, the cathodic vacuum arc is being developed for use in industry, in which the system was installed the different filter coils for different work. The details are as follows.

### 2.6.1 Classic 90° duct filter

To completely eliminate particles by placing the cathode out of sight from the substrate. Most often, the plasma is magnetically guided in curved filters. Electrons and ions in the plasma are ionized from particles based on the huge difference in charge-to-mass ratio. While the plasma can easily be bent, the relatively massive

particles move along almost straight trajectories. Anders [112] introduced a  $90^\circ$  duct filter as shown in Figure 2.11. The duct filter consists of a curved tube which is surrounded by magnetic field coils generating a curved axial field, the  $90^\circ$  duct can also be considered as a quarter magnetic torus. To reduce particle transport by multiple reflections inside the duct was inserted baffles. Moreover, they found that biasing the duct positive voltage can improve plasma transport and filter efficiency. This type of filter has been widely used in a cathodic arc over the last decade. This model can be developed and extended to a large system for dc plasma operation (duct length about 1 m), which easily be scaled. Small systems are suitable for pulsed arc operation (duct length about 10 cm) but it shows the same principal features.

However, Storer et al. [113] they found that plasma transport efficiency decreases exponentially with the increase of the length of the filter. For good plasma transport, the duct must be biased about +10 to +25 V concerning the plasma, corresponding with the report of Bilek and coworkers [114], who showed that applying a positive bias to a strip electrode that is located near the outer wall of the interior of the duct produces a similar effect. With optimized bias (about +20 V ) and at relatively strong magnetic fields (of order 100 mT ), system coefficients of  $90^\circ$  duct filters as high as 2.5% have been found [115].

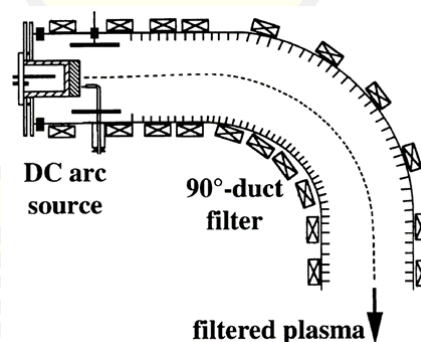


**Figure 2.11** Schematic of the classic  $90^\circ$ -duct filter [112].

### 2.6.2 Knee-filter

To reduce the plasma losses become less for a larger bent angle of the filter, a non-line-of-sight filter that has a relatively small bending angle and is otherwise straight was designed. In this concept the particle reflection is reduced by baffles inserted in the two straight duct sections as in the classic  $90^\circ$ -duct filter. The commercial Knee-filter is designed for d.c. operation.

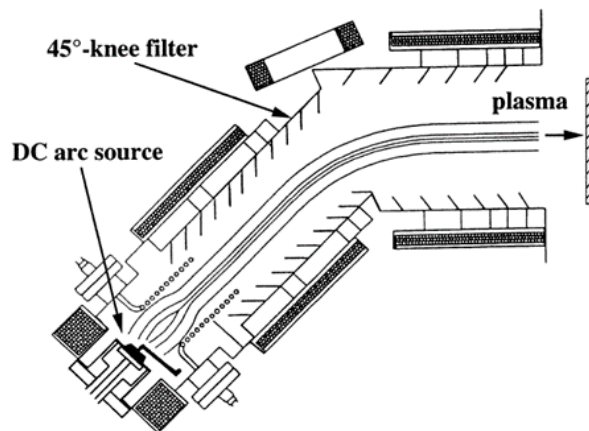


**Figure 2.12** Schematic of the 45° Knee-filter [116].

### 2.6.3 Freestanding 90° filter

From the problem of particle refraction or “bouncing” in the classic 90°-duct filter. There is still a non-negligible probability that a particle is transmitted through the filter, although there is no direct line-of-sight. 90° Freestanding or open-architecture filters improve the situation (Figure 2.13). this filter is no duct present, and the magnetic field is produced by only a few turns of a field coil. The current through the filter coil must be high to obtain a magnetic field. Often, the arc current (positive polarity) is conveniently used for this purpose [113], [117]. Particles may either leave the filter through openings areas between the turns of the field coil. However, some macroparticles will be refected from a turn of the filter coil and come to the substrate. Therefore even freestanding filters do not guarantee completely macroparticle-free film deposition.



**Figure 2.13** Freestanding 90° filter, operating with the arc current (200 A), Platinum plasma. [112].



### 2.6.4 S-duct filter

In an effort to further reduce the flux of residual particles, filters have been developed with a bend angle exceeding  $90^\circ$ . For example, bend the filter to  $180^\circ$  or any other large angle [118]. resulting in the plasma losses in such filters become severe, and these filters are suitable for ultrathin-film coating applications only (hard disk drive). It is known that the plasma in a  $90^\circ$  filter is offset from the filter axis, it caused by several reasons such as asymmetry in the magnetic field,  $E \times B$  fields, and action of the centrifugal force. The S-shaped filter (Figure 2.14) was created to compensate for the distortion of the plasma. The S-shaped filter has been carried out with some success, a system coefficient of 0.6% [119]. And the residual particle flux to the substrate was greatly reduced.

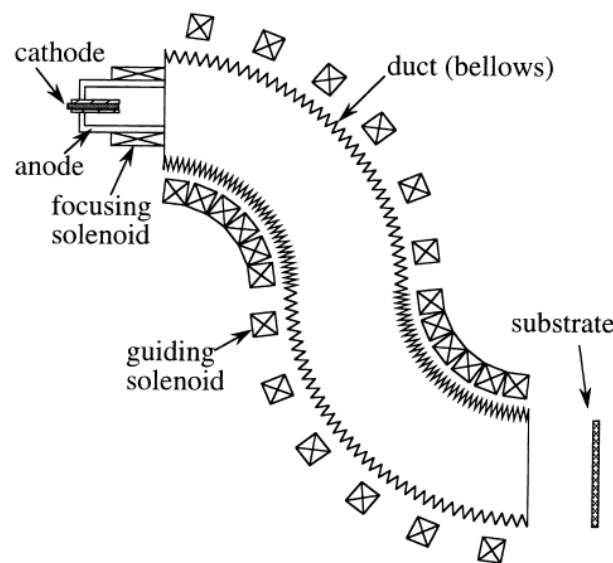


**Figure 2.14** Schematic of an S-duct filter [112].

### 2.6.5 Freestanding S-filter

A freestanding S-filter was developed with the same objective as the freestanding  $90^\circ$  filter. This model is an excellent research tool because it can use for study plasma characteristics (plasma position and plasma density as a function of various parameters) [120]. Figure 2.15 shows a freestanding S-filter with an extremely well-collimated plasma, illustrating the magnetic guiding of the plasma.

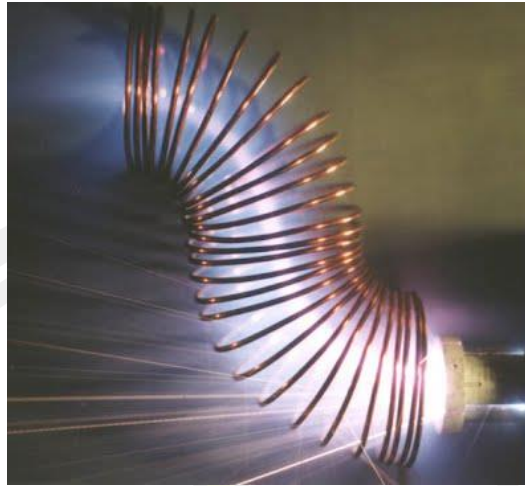


**Figure 2.15** Freestanding S-filter, operating with a pulsed high arc current (1 kA), and Titanium plasma [112].

## 2.7 New filtered cathodic vacuum arc system

In this section, innovative filtered arc systems are described. Figure 2.16 shows the 120° bend filter, which has been developed for preparing ta-C films for the protective top-layer coat on a hard disk system by the IBM group [121], [122]. The vacuum arc plasma is operated in the pulsed high-current mode [108], [123], [124]. In this system, the generation of droplets is suppressed by rapidly chopping the current (reducing the effect of the surface heating), and the droplets are trapped with many baffles placed on the inner wall of the duct during the plasma transport to the exit of the 120° bent duct. Graphite droplets are not simple to filter by using a conventional filter system, since the solid droplets bounce off the duct wall.

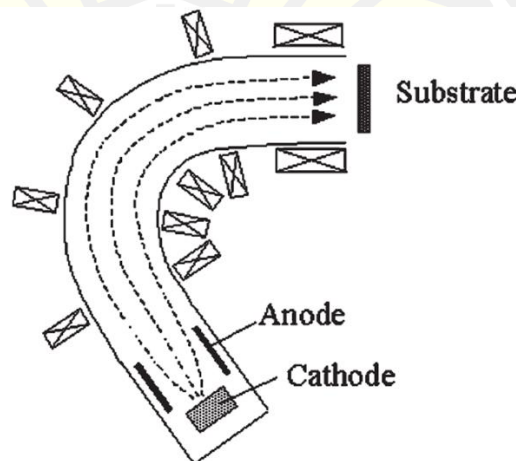


**Figure 2.16** Photograph of 120° filter with high-current arc source [125].

In the past decade, it has been demonstrated that ta-C film is very available as a protective coating on cutting tools for aluminum dry machining [126]. Cathodic arc deposition is the only technique to prepare the ta-C films on an industrial scale. For longer tool life of the cutting tools, the thicker ta-C film is required. Although the DLC, or hydrogen-free DLC, can be prepared on flexible rubber substrates [127], [128]. But, it is difficult for the thick ta-C film to adhere to solid materials, due to its high elastic modulus. Therefore, the interlayer is sometimes introduced between the substrate and the DLC film. In order to prepare thick ta-C with a bonding interlayer, an X-shape filtered arc deposition system (X-FAD) has been designed and developed [129], [130]. Which is an integrated system combining T-FAD [131], [132] and crank-FAD. Figure 2.17(a)-(c) shows schematic sketches of FCVA, Y-FAD, and T-FAD, respectively.

Figure 2.17(b) shows another filtered arc system with Y-shape plasma transporting duct (Y-FAD). The two cathodic arc sources are connected to the Y-duct, which has been developed for two purposes. (i) high-speed deposition with double cathodes. and (ii) to prepare multi-metal composite film and multilayer film, using two different cathodes. Two plasma beams are not easily combined, since their electrical polarities are the same and they tend to remain separate from each other. Therefore, to mix the two plasma beams, a magnet is placed downstream of the Y-duct. The film grows up by incident ions, the films have high density and residual stress.

T-FAD (see Figure 2.17(c)) has been designed particularly for DLC preparation using graphite cathode with the idea is the transportation direction of plasma and the trajectory of droplets (macroparticle) will be separated from each other, using a T-shape filter duct. In T-FAD, the carbon plasma generated between the cathode and the anode is transported with a freestanding  $90^\circ$  filter, in which the droplet travels in a straight direction away from the bend plasma.

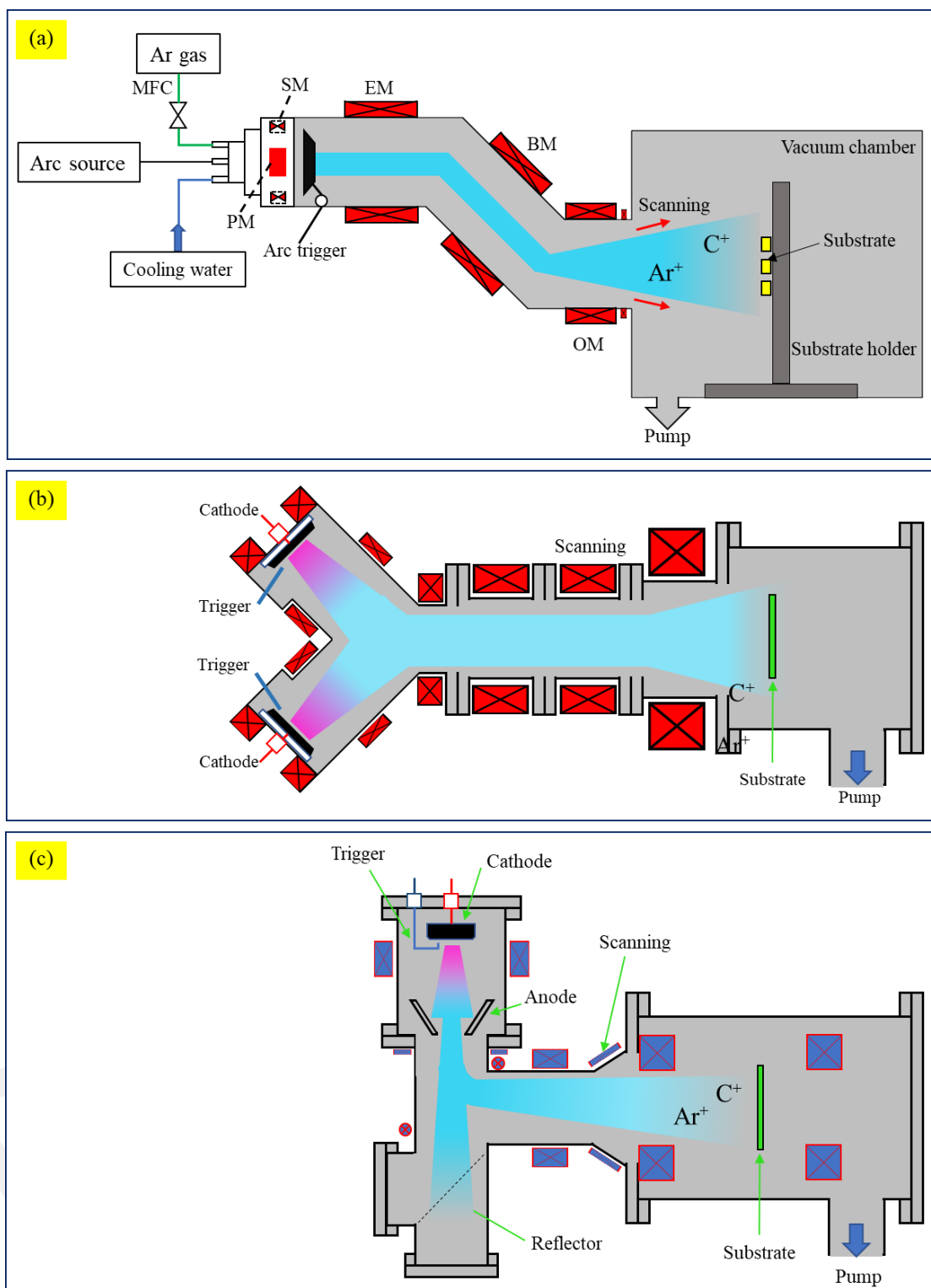


**Figure 2.17** Schematic sketches of new filter cathodic vacuum arcs. (a) FCVA [23], (b) Y-FAD and (c) T-FAD [125].

## Chapter III

### Experimental Procedures

As described in the introduction, the main objectives of this thesis are to develop an ionized physical vapor deposition (IPVD) system for superhard the concept of the multilayer Cr/ta-C/a-C:H film. In order to achieve these goals, the plasma sources for film deposition and ion sources for substrate cleaning have been completely designed, manufacturing, installed on the deposition chamber, operated, and used for thin films deposition.

In this chapter, the main features of an IPVD system are exposed such as vacuum system, vacuum component control, and installation of any component. Along with a brief introduction to the deposition techniques used for the thesis: Filtered cathodic vacuum arc (FCVA), for deposition of ta-C films; anode layer ion source (ALIS), for substrate cleaning; and magnetron sputtering (MS), for the production of the interlayer of the multilayer film. In addition, the concept of ion energy measurement and RFA probe built and the sample preparation will give in detail.

### 3.1 An ionized physical vapor deposition system

The DLC films with the hardness in the range of superhard coating, it can be prepared using the FCVA and the plasma source technique [23], [35]. Therefore, an IPVD system was designed based on the FCVA technique and plasma source. In addition, this system must be responded to many works and applications. Thus, this system was developed in the concept of the hybrid system. The system was divided into seven sections; the vacuum system, the vacuum component control system, the plasma and ion sources, substrate transfer system, gas line, substrate holder system and discharge power supply.

#### 3.1.1 Vacuum system

Figure 3.1 shows a diagram of an IPVD system, the vacuum chamber consists of a 304 stainless steel cylindrical chamber (diameter 600 mm, high 540 mm, volume 113 liters), and the base pressure is a very high vacuum ( $10^{-4}$  Pa measured by the wide range gauge). The vacuum system used o-ring sealings to seal the flanges and the

vacuum devices. The chamber was pumped using a PFEIFFER TMP1001P turbomolecular pump backed by one of LEYBOLD D40B TRIVAC VACUUM PUMP (rotary pump). Also, the copper coil was installed in the import flange of the rotary pump to trap the oil vapor. The pendulum control & isolation valve (VAT, 650 series) was installed between the chamber and the turbomolecular pump to adjust the pumping rate (position control mode) and the pressure (pressure control mode) inside the deposition chamber.

In addition, the side of deposition chamber was installed with four plasma sources (FCVA, L-ALIS, ALIS, and magnetron sputtering), a substrate transfer system and a view port. The substrate holder system was installed at an ISO200 flank in the bottom flank of deposition chamber. The substrate transfer system was installed at port number 8 of deposition chamber, and the pressure in the deposition chamber and load lock chamber is linked by three ways valve.

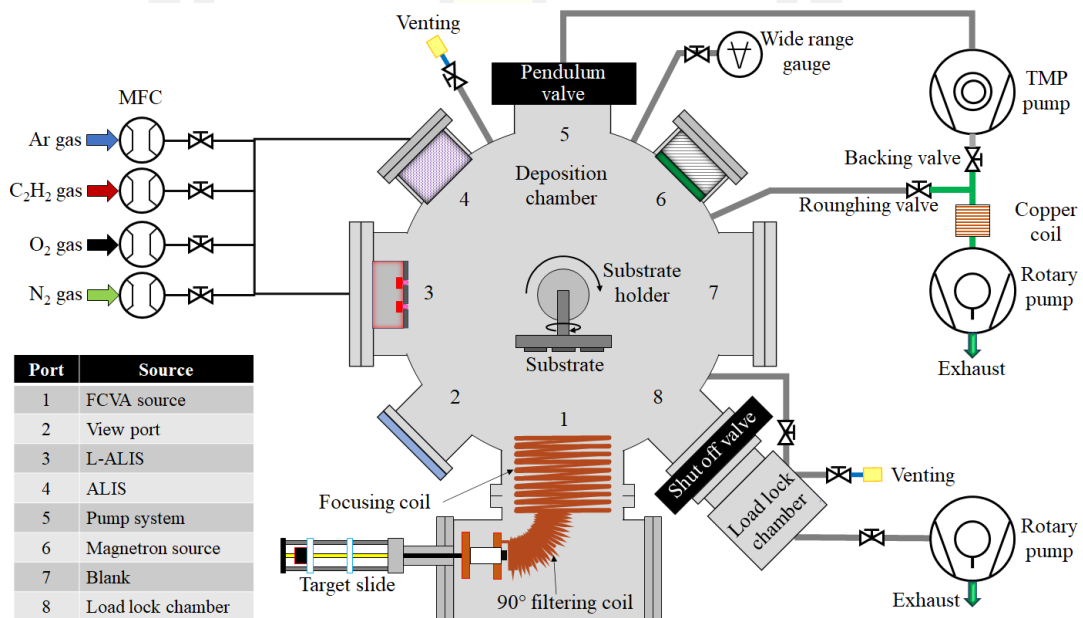


**Figure 3.1** Diagram of the ionized physical vapor deposition system.

### 3.1.2 Vacuum component control system

The vacuum component of an IPVD system was controlled by PXI control. The vacuum device, power supply, mass flow controller, and pressure gauge, it can control by the IPVD control version 7 software based on the LabVIEW program, the control panel of as shown in Figure 3.2. The control program has five zones; the

vacuum control center, gas control, DC power supply control, substrate holder control, and FCVA source control. The software can operate in manual mode. The following equipment and components can be controlled as desired at any time:

- ON/OFF the solenoid valve at the backing valve, roughing valve
- ON/OFF the solenoid valve and key the flow rate value to control the gas flow rate into the deposition chamber.
- ON/OFF the solenoid valve at the wide range gauge to see operating pressure in the deposition chamber. Pressure in the deposition chamber (wide range gauge with the full scale of 1 Pa to  $10^{-6}$  Pa) shows in the numeric displays.
- The operating pressure in the deposition chamber was controlled by the pendulum valve, which has two modes of control: fixed position of the angle valve or pressure regulation.
- All pressure and flow readings are available in real-time updates.
- ON/OFF rotation of the substrate holder and should the port position for cleaning, film deposition and load-unload the sample.

**Safety of the system:**

- When the backing valve shows an open status, the roughing valve is disabled status.
- When the pendulum valve is closed while the turbomolecular pump is running and inside the deposition chamber is high pressure, the pendulum valve is not changing status because it has an interlock.
- The pendulum valve is closed in the case of a power failure. During the load and unload of the sample during venting of the deposition chamber, the pendulum valve is closed and the turbomolecular pump is turned ON. This function is very important to safety the surge of pressure from the atmosphere to high pressure, which directly damages on the blade of the turbomolecular pump.
- The gate valve is closed in the case of a power failure.
- The backing and roughing valve are closed in the case of a power failure, it protects the reverse of the vacuum oil into the deposition chamber.



- The venting valve is closed in the case of a power failure, it protects the air leak into the deposition chamber, in which reduces contamination of moisture and the pumping time for the next experiment.

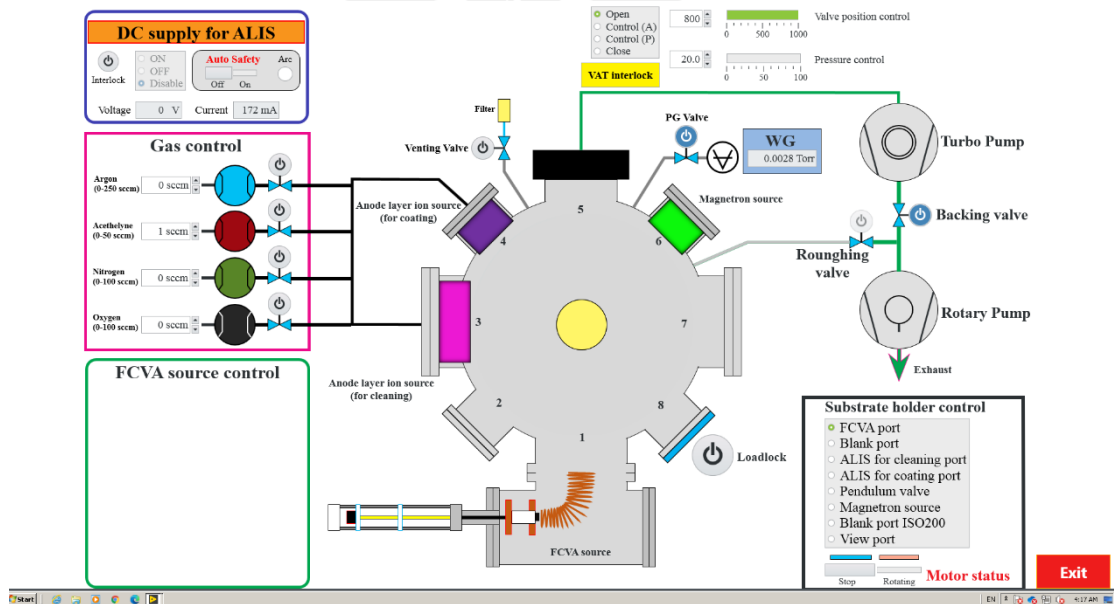


**Figure 3.2** The graphical user interface of the reactor controller of the main process and control view.

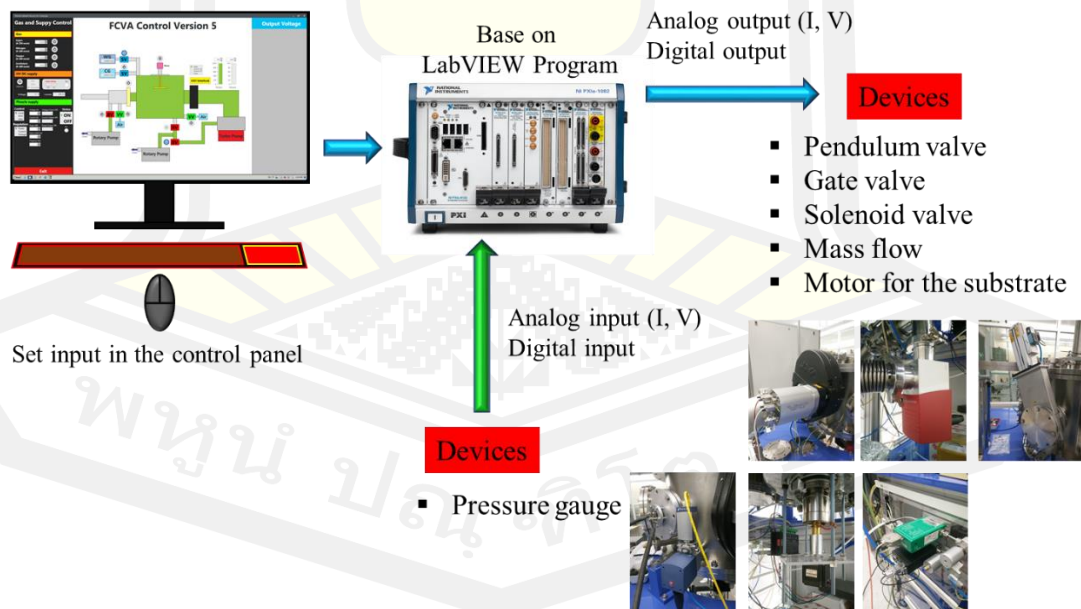


**Figure 3.3** Concept of the control system of a filtered cathodic vacuum arc system.

The control system consists of the monitor, the NI PXI-1042 unit, and the devices. The concept of control as shown in Figure 3.3, the PXI unit is a processor



similar to the CPU, operating by Windows 7. The LabVIEW program is used to control the PXI card. The PXI card has specific options such as generating the analog output, digital output and signal for controlling the devices, detecting analog input and the digital input from the devices. The NI PXI-1042 unit was installed the NI PXI-8108, NI PXI-2565 and NI PXI-6251 card, which has the role as follows:

#### **NI PXI-8108**

The NI PXI-8108 is a modular PC in a PXI 3U-size form factor, consists of the following logic blocks on the CPU module and the I/O module. The CPU module has the following logic blocks:

- Socket 479 CPU is the socket definition for the Intel® Core™ 2 Duo processor T9400.
- The SO-DIMM block.
- The Mobile Intel GM45 Express Chipset connects to the CPU, DDR2 SDRAM, DVI-I video and GPIB.
- The SMB to PXI Trigger provides a routable connection of the PXI triggers to/from the SMB on the front panel.
- The Watchdog Timer block consists of a watchdog timer that can reset the controller or generate a trigger.
- The Chipset ICH9M (I/O Controller Hub) connects to the PCI, USB, SATA, LPC buses, and Ethernet.
- The USB Connectors are connected to the ICH9M chipset.
- The PXI Connector connects the NI PXI-8108 to the PXI/CompactPCI backplane.
- The Super I/O block represents the other peripherals supplied by the NI PXI-8108.
- The NI PXI-8108 has one serial port, and an ECP/EPP parallel port.
- The Gigabit Ethernet connects to either 10 Mbit, 100 Mbit, or 1,000 Mbit Ethernet interfaces.
- The GPIB block contains the GPIB interface.
- The Express Card/34 slot accommodates an Express Card/34 module.
- The SATA block connects a Serial ATA hard drive to the ICH9M.

The NI PXI-8108 uses the LabVIEW program, combine with leading hardware drivers such as NI-DAQmx to provide exceptional control of the hardware. In which, LabVIEW is a powerful and easy-to-use graphical programming, use to acquire data from thousands of different instruments including USB, IEEE 488.2, VXI, serial, PLCs, and plug-in boards. The LabVIEW will be convert acquired data into meaningful results using powerful data analysis routines [133]. Although NI PXI-8108 has many CPU modules and the I/O modules, the control system for FCVA uses some I/O interfaces and external connectors as **Error! Reference source not found.:**

**Table 3. 1** I/O interfaces and external connectors of NI PXI-8108 for the control system.

I/O interfaces	external connectors	Role
USB (four points)	USB 4-pin Series A stacked receptacle	For USB Flash Drive, USB mouse and keyboard
Video	DVI-I (24-pin DSUB)	Connect with the monitor
Serial	COM1 (9-pin DSUB)	Control the pendulum valve
Ethernet	LAN (RJ45)	Connect the internet

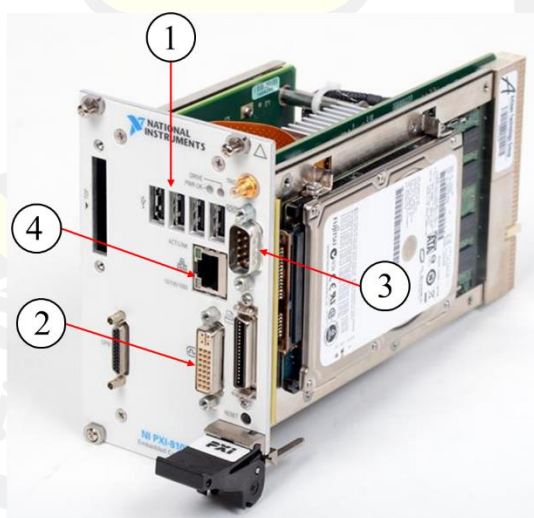


**Figure 3.4** National Instruments PXI-8108 2.53 GHz Dual-Core Embedded Controller [134].

The pendulum valve was controlled by NI PXI-8108 through COM1 (9-pin DSUB). In which the LabVIEW diagram for setting the pendulum valve open, close, set position, and set pressure as shown in Figure 3.5. The concept for controlling the pendulum valve is running as follows:

Open the valve, use the VISA write item for writes the data from a buffer to the device or interface, in which the data is C:0100\r\n, then the data will be through the Sequence Structure (to ensure that a subdiagram executes before or after another subdiagram) into the VISA read item (reads the specified number of bytes from the device or interface and returns the results as string data). After that string data was sending into the VISA write item again to write a new data (O:\r\n where O is open), and the code was sent to read again before sending to the pendulum valve. Is causing the pendulum valve is open.

Close the valve, use the same concept of the open valve, but change the code in the third step is C:\r\n code (C is close). When the data has been written again It will be sent to the pendulum valve to close the valve.

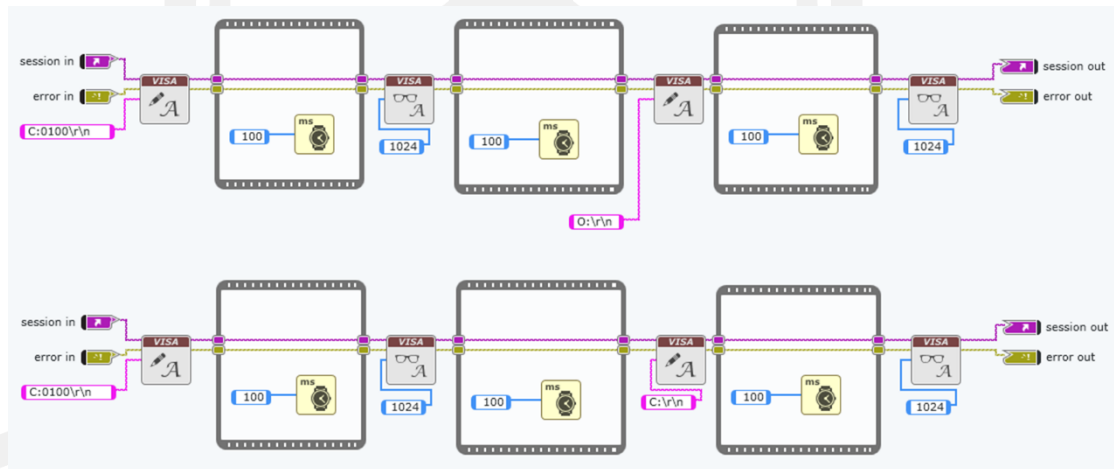


**Figure 3.5** The LabVIEW diagram for control the pendulum valve (open and close valve).

Set the position of the pendulum valve, for controlling the valve position, use the same concept as before. But the input data in the third step with the details as follows: the data divided into 2 sets by use concatenate strings for data integration. Data set 1 is the command for open the valve, and data set 2 is the setpoint of the

valve position. When integration data and the data was written to new data and send to the pendulum valve, the valve position can adjust by the LabVIEW.

Set pressure in the chamber, use the concept similar to the set position of the valve. But initial strings (S:) received from the sensor (capacitance gauge). In addition, the value of pressure must convert the unit in torr, Pa, etc., depending on the user.

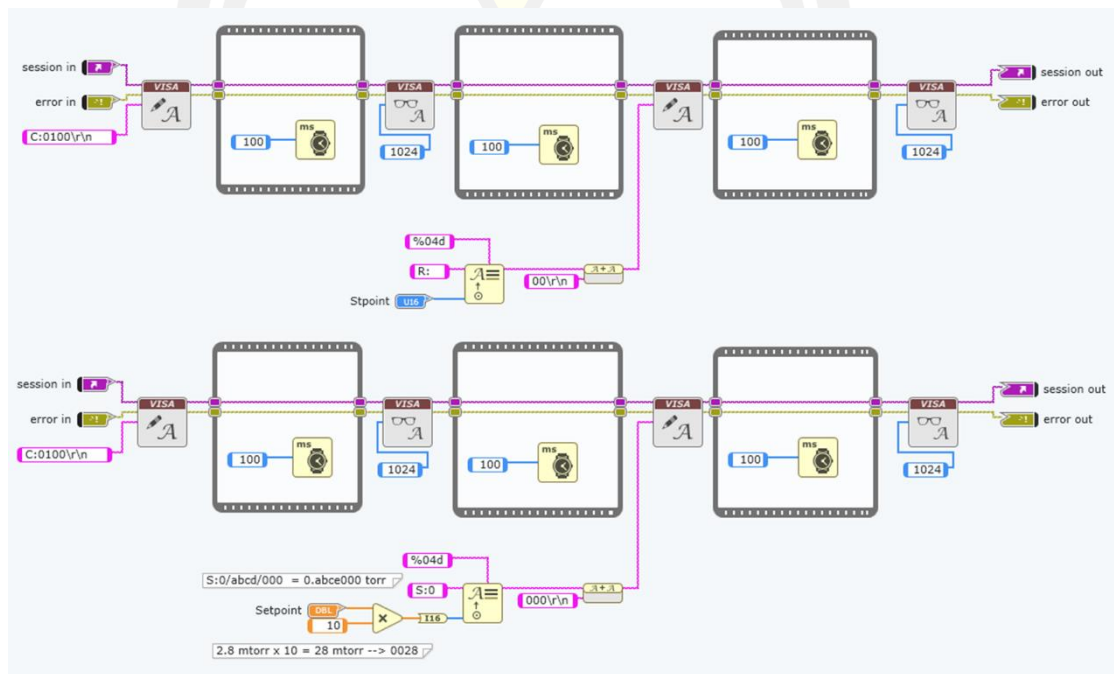


**Figure 3.6** The LabVIEW diagram for control the pendulum valve (set the position of the valve and set pressure in the deposition chamber).

### NI PXI-2565

NI PXI-2565 is the electrical and mechanical relay switch card [135], have 16-channel can see in Figure 3.7(a). It can use the NI-SWITCH driver software for writing the LabVIEW diagram to open or close the relay. The major components of the NI PXI-2565 module are general-purpose relays, relay switch control circuitry, random scanning, PXI bus interface, and triggers.

The concept for operation the relay as shown in Figure 3.7(b). The front side of NI PXI-2565 connects with the source (DC power supply and pulse generator) when the relay switch is closed, the power can transfer to the devices, so the device can operate. On the other hand, when the relay switch is open. on the other hand,

when open relay the circuit is an open circuit causing the device to stop working. The vacuum valve (backing and roughing valve) is the solenoid valve, in which needs 24 VDC power for driven. So, to operate the solenoid valve, the LabVIEW diagram (Figure 3.8), must be consist of NI SWITCH for receiving input power and select the direction of the relay (close relay and open relay). For close relay case, the solenoid valve receives 24 VDC from the power supply, the valve is opened state and the chamber was pumped when the rotary pump is running. On the other hand, when the relay switch is open, the power transfer is stopped, it is causing the solenoid valve is closed state, so the chamber is not pumped.

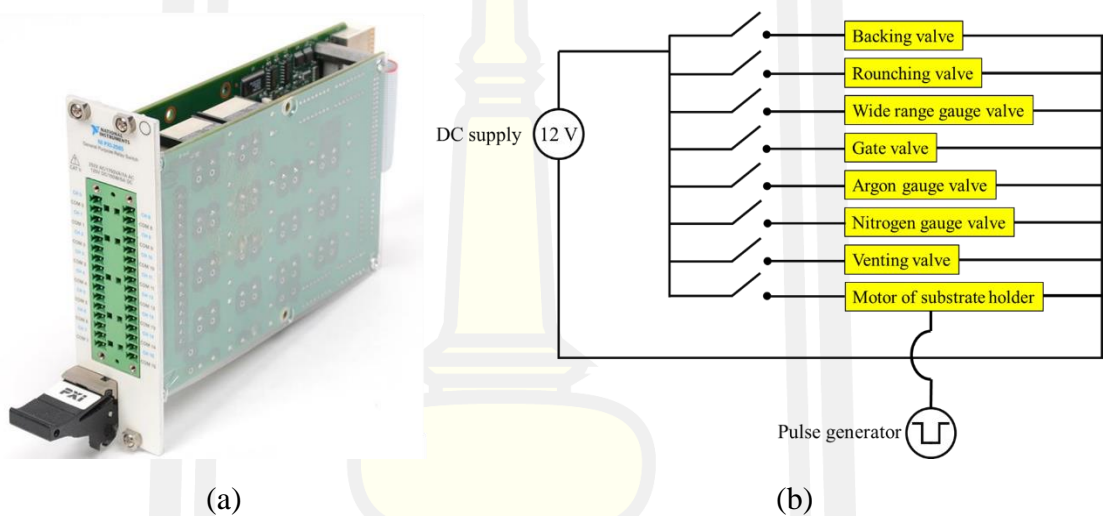


**Figure 3.7** (a) the NI PXI-2565 [136], (b) diagram of an electrical circuit for use NI PXI 2565 to control the working of the device.

A wide range gauge, mass flow controller of Argon and Nitrogen gas and venting valve has the solenoid valve for close or open to connect with the deposition chamber. Therefore, the channel of the relay should be unique. In addition, the gate valve needs 24 VDC to open and close, the gate valve was connected with the relay 24 VDC. While the motor for rotating the substrate uses 24 VDC and square pulse (amplitude 5.0 V) for operation. Therefore, it can the power combined with the 24 VDC power supply to the vacuum devices and any component. But the pulse generator, use the external function generator.

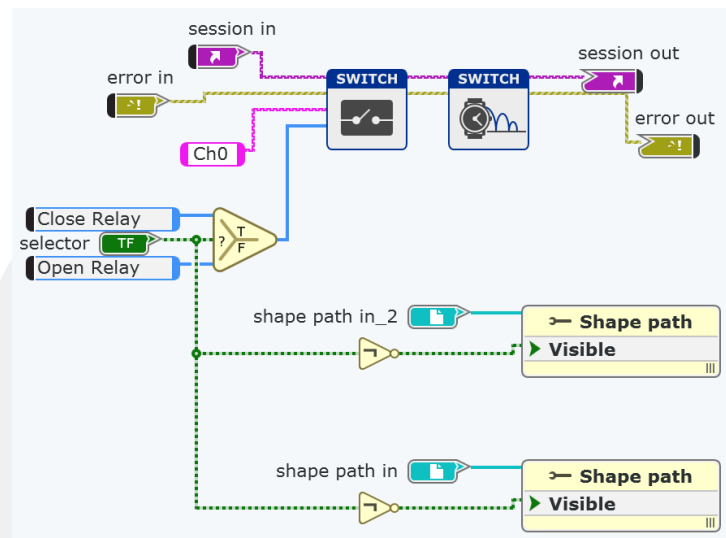


**Figure 3.8** The LabVIEW diagram for close or open the solenoid valve and gate valve.

### NI PXI-6251

NI PXI-6251 is a DAQ card (see Figure 3.9), have a multifunction as follow:

Read the input signal

- Analog input
- Digital input

Generate the output signal

- Analog triggers
- Analog output
- Digital output
- Digital PFI

Trigger

- Analog triggers
- external digital triggers
- device-to-device trigger bus

Generator

- Frequency generator
- power requirements



### Characteristics

- Physical
- Electrical
- Static
- Waveform

NI PXI-6251 uses NI DAQ driver for writing the LabVIEW program to run this card [137]. This can be applied to the setpoint flow rate of the gas and arc frequency. Also, the pressure in the deposition chamber can use analog input to measure the output voltage of a wide range gauge and convert it to pressure by using the equation for each pressure gauge.

The mass flow controller (MFC) has information for control the flow rate is different. In this case of MKS Type 1179B Mass-Flow Controller (for control argon gas) and MKS Type M100B Mass-Flow Controller (for control nitrogen gas), it was controlled by the voltage in the range of 0 – 5 VDC. The voltage received from the analog output function (NI PXI-6251) and use NI DAQ write the voltage output and send to the MFC. The LabVIEW diagram for the setpoint flow rate of the argon gas as shown in **Figure 3.10**. The while loop was used to control ON/OFF of the solenoid valve, the analog output channel ao0 was sent to DAQmx write to determine factor for the flow rate setpoint.

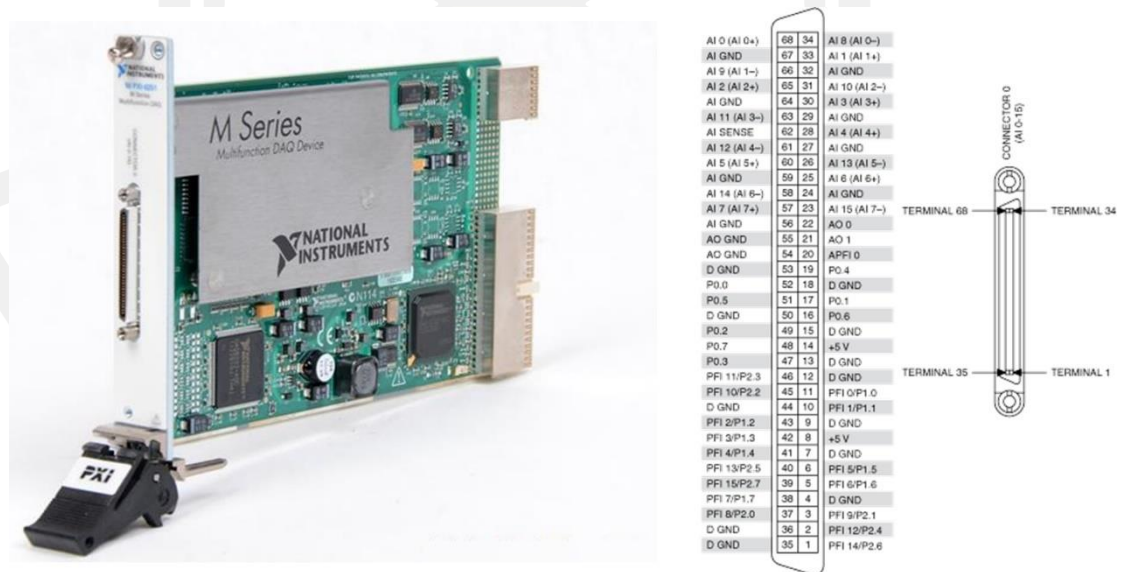


**Figure 3.9** NI PXI-6251 card and pinout.



The factor of setpoint value is 50 due to the 0 - 5 V of MFC as 0 – 250 sccm. Therefore, the setpoint value in DBL Numeric is divided by 50, to order the card to supply voltage in the range 0 – 5 V for MFC. In the case of the MFC being closed, the 0 VDC was auto send to MFC. It indicates that the flow rate of argon gas is zero.

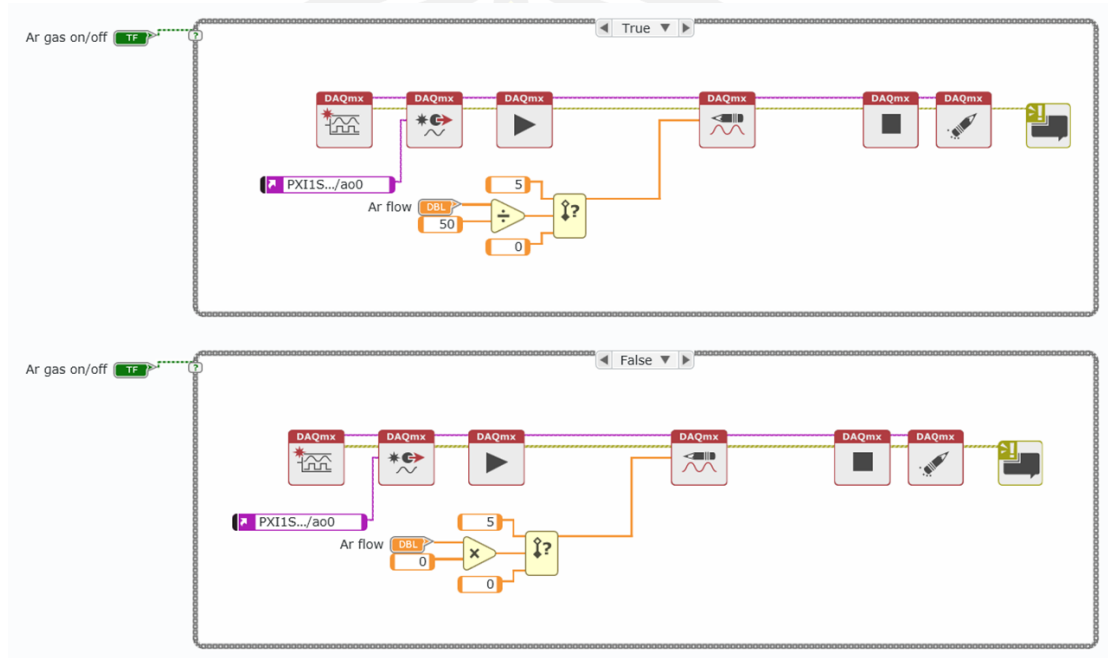


**Figure 3.10** The LabVIEW diagram for the setpoint flow rate of the argon gas.

### 3.1.3 Plasma sources

The plasma source is a very important device for film coating. Each plasma source has its advantages and disadvantages, thus it is designed to be specific to each application to increase efficiency and reduce the wear rate that may occur from misuse. This work focus on an anode layer ion source, linear anode layer ion source, magnetron sputtering, and filter cathodic vacuum arc. The principle and design of these plasma sources will be explained.

#### 3.1.3.1 Anode layer ion source

Anode layer ion source (ALIS) is a physical vapor deposition and cleaning source. The diagram of an ALIS as shown in Figure 3.11, consists of four main parts; anode electrode, cathode electrodes, outer magnet, and inner magnet. This source needs a positive power supply with a high voltage and low current to generate the plasma or ion beam. The principle of an ALIS uses the  $E \times B$  field to trap primary electron, excitation gas and generate plasma on the discharge gap of the cathode, then

the positive ions ( $\text{Ar}^+$  for use argon gas is a precursor) move out from the anode electrode due to the electric force on an anode electrode. Therefore, the ion has kinetic energy around the applied voltage such as the applied voltage of 2 kV, the initial kinetic energy of 2 keV (for the ideal case). However, the ion energy will be decreased with the increase of distance from the anode surface due to collision with other particles. The characteristic of an ion beam generated using an ALIS is a cylindrical beam (tube beam), the thickness of the ion layer depends on the electrode gap design.

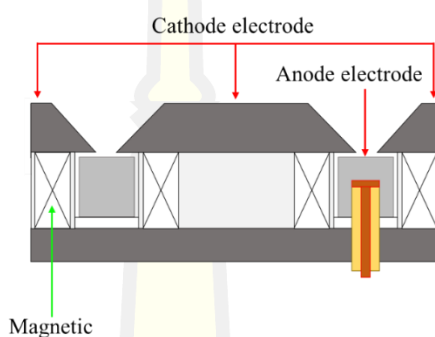


**Figure 3.11** Overview assembly and structure diagram of an anode layer ion source.

An in-house ALIS as shown in Figure 3.12. The base of the ALIS is an ISO100 flange, an anode electrode and the magnetic holder uses stainless steel grad 316. The inner and outer cathode electrodes use stainless steel grad 410 material due to it being ferromagnetic material, the magnetic field between the inner and outer cathode was induced and causes a strong magnetic field in the discharge gap, which is an important condition for generating the plasma. The discharge gap has a diameter of 62 mm.

The anode electrode and base of the source (ground) were separated with the ceramic wisher, the gap distance of both electrodes is 1 mm (less than the mean free part of an electron). So, the ALIS can be applied to a voltage of higher than 2 kV. In addition, an ALIS has a water cooling in at the base of magnetic holder. Therefore, this source can operate for a long time. Moreover, the gas is conveyed directly to the discharge area, which increases the ionization of the gas.

Figure 3.13 shows the plasma characteristic generated using an ALIS. The plasma as a cylindrical beam with a diameter of around the discharge gap diameter. The plasma beam is long and directly ejects on the sample. However, the cylindrical

plasma beam has affected on the uniformity of argon ions cleaning and a-C:H deposition. Therefore, the characteristic of the discharge gap should be changed to a rectangular gap.

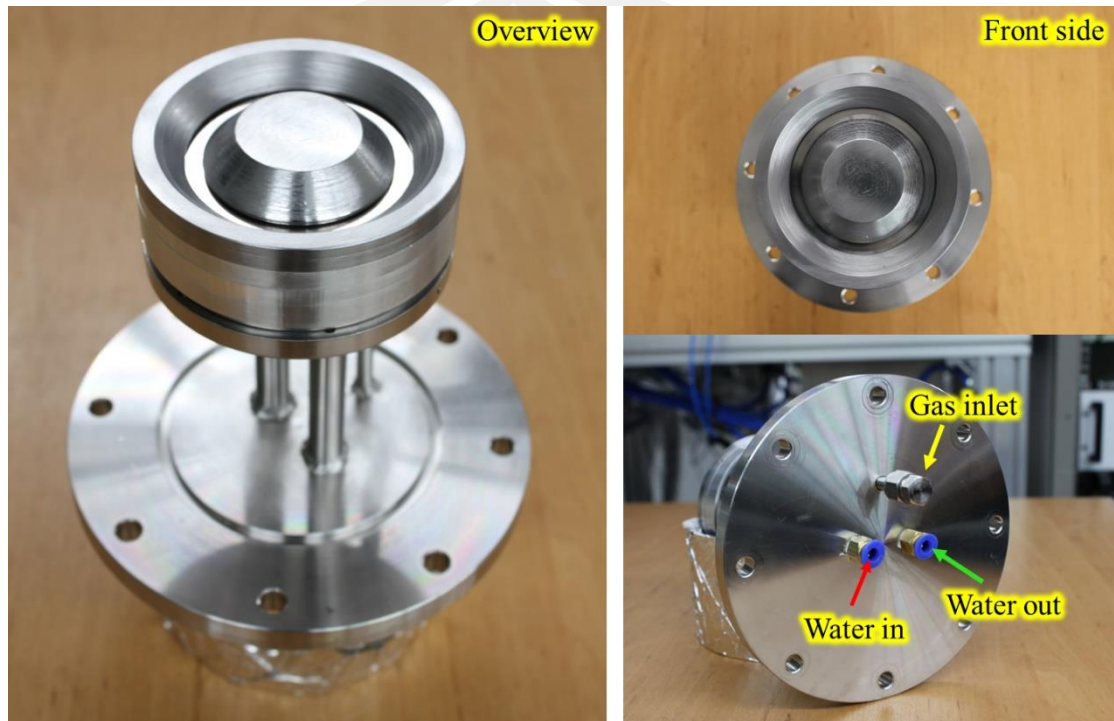


**Figure 3.12** Anode layer ions source for substrate cleaning.



**Figure 3.13** The plasma characteristic generated using an ALIS.

### 3.1.3.2 Linear anode layer ion source

To increase the uniformity of the ion cleaning and a-C:H deposition, an ALIS has upgraded the discharge gap from the cycle to a rectangular gap. Figure 3.14 shows the assembly of the Linear anode layer ion source or L-ALIS. The concept design like an ALIS, the only change is the characteristics of the discharging gap from cycle to rectangular. The discharge gap has a height of 200 mm and a width of 30 mm. Therefore, the plasma beam generated using L-ALIS has a size higher than 200 mm  $\times$  30 mm (height  $\times$  width). The plasma beam characteristic was generated using L-ALIS as shown in Figure 3.15(a). It was found that the plasma beam has a characteristic like the discharge gap (rectangular layer), and ejaculation from the anode electrode with uniformly. Moreover, the uniformity of plasma has directly to the uniformity of the a-C:H film. Figure 3.15(b) shows the a-C:H film on Si substrate and SUS316 holder, it can be seen that the film has a goal color covering the substrate and holder indicates that the film has uniformity.

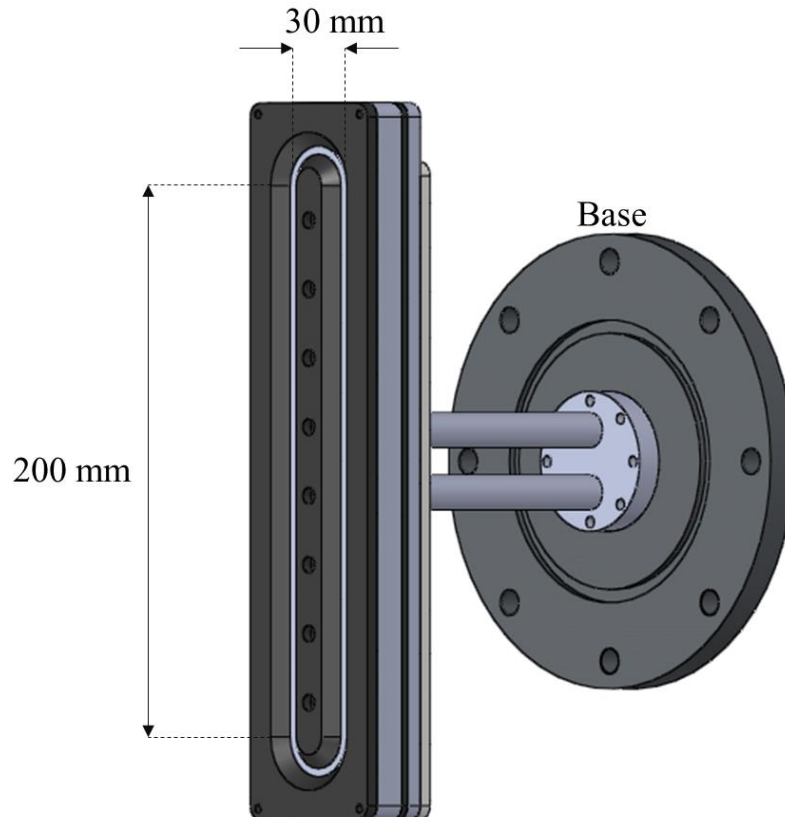


**Figure 3.14** Assembly of linear anode layer ion source.

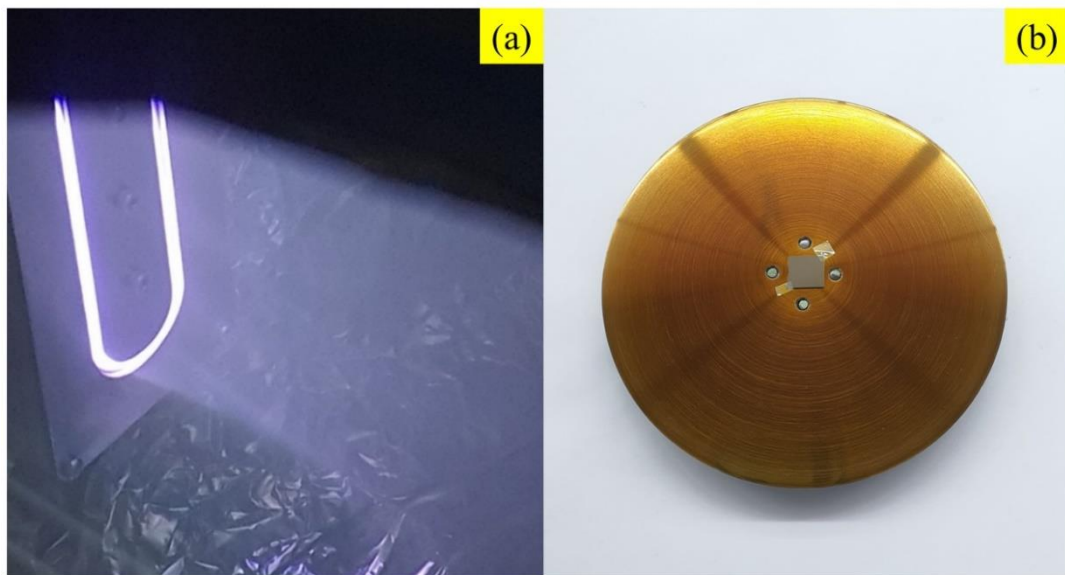


**Figure 3.15** (a) The argon plasma beam generated using L-ALIS with the discharge potential of 1200 V. And (b) the a-C:H film deposited using L-ALIS with the discharge potential of 1200 V and discharge current of 13.5 mA.

### 3.1.3.3 Magnetron sputtering source

Magnetron sputtering is a popular technology for metal and compound material deposition. Nowadays, it was used in wide applications for the manufacturing of innovative products such as magnetic storage disks, flat displays, smart windows, thin-film solar cells, cutting tools, etc., The magnetron sputtering source has the advantages of economic: deposition even on large areas, and the ability to coat very temperature-sensitive plastic substrates.

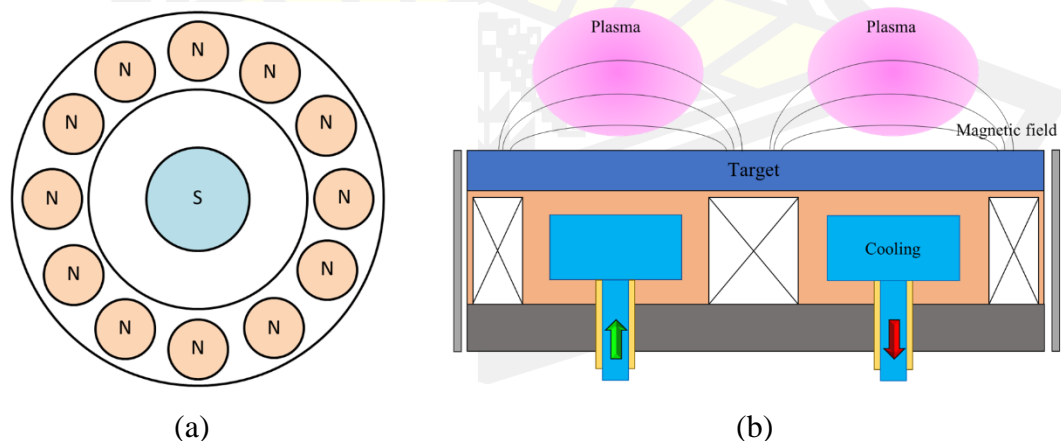


**Figure 3.16** (a) Position and polarity of the permanent magnet and (b) magnetic force lines generated by permanent magnets.



The magnetron sputtering source consists of an important part; the permanent magnet (e.g., NdFeB), it has a role in generating the magnetic field as shown in Figure 3.16(b). Electrons are trapped by the Lorentz force  $F_B = q(v \times B)$ , which reaches a maximum in the area where  $B_x$  (the parallel component to the target surface). It decreases toward the center and the outer areas of the target surface ( $B \parallel v$ ). The trajectories of electrons are obtained by solving the differential equation as follows.

$$m \frac{dv}{dt} = qE + q(v \times B) \quad (3.1)$$

According to Figure 3.16(b), the electrons form a ring-shaped current on the target surface called the 'race track'. Due to the trapping of the electrons in the race track area, the formation of ions is substantially enhanced, resulting in a remarkable drop of target voltage (lower plasma impedance) and a jump in deposition rate. The process pressure can be reduced leading to an increase of the mean free path.

Also, the sputtering yield and deposition rate for different target materials as a function of power density [138]. Generally, the target has three types as follows: pure metal, alloy, and compound target. The size and shape of the target depend on the design of the magnetron source (circular, rectangular and cylindrical). An inherent drawback of the planar magnetron source is the nonuniform erosion (high erosion on the race track region), it causes a nonuniform of film thickness distribution, which is caused by the nonuniform ion current density (ion flux on the substrate). In particular, this holds if the substrate is resting below the magnetron during deposition. Rotation and pass substrate was applied to solve this problem. So, uniformity problems can be easily eliminated. The main advantages of magnetron sputtering are as follows:

- Low thermal sputtered atom to the substrate
- Film good uniformity (rotation and pass substrate)
- Easy to scale up (size of magnetron source)
- Dense films and well-adherent between the films and substrate
- The large variety of film materials available (nearly all metals and compounds)
- The film properties can adjust by the deposition process parameter

With a wide range of applications and excellent properties of the films deposited by magnetron sputtering, the filtered cathodic vacuum arc system will install the magnetron sputtering source on side of the deposition chamber to deposit the interlayer of the superhard amorphous carbon film.

The magnetron sputtering source (see Figure 3.17) has a diameter of 70 mm and a length of 80 mm, and can be moved in the z-axis during the experiment without stopping the vacuum system, consisting of a handle (diameter of 1 inch, length of 300 mm) sealing with ultra torr NW40. The cathode electrode was formed by copper material, Teflon ring for was separated the cathode electrode and handle (ground). The target material (2-inch diameter, 6.0 mm thickness, and cylindrical shape) is placed on top of the cathode electrode, using a stainless steel clamp and M3 male nut to attach the target on the cathode electrode. The permanent magnet was placed is the cycle characteristic under the cathode electrode. The inner permanent magnet and the outer permanent magnet are unbalanced magnetic fields, so this source is an unbalanced magnetron sputtering source. This induces the ion and electron to the substrate more than the balanced magnetron sputtering source, it causing the deposition rate, ion flux, and electron flux to be higher. The cathode electrode and the permanent magnet have been cooled by 17° water, so it can operate for a long time.

For driving the magnetron sputtering source, the pinnacle power supply (ADVANCED ENERGYDC) is used. The pinnacle power supply has 2 functions as follows: DC mode and asymmetric bipolar pulsed mode. For DC mode, the maximum voltage is 1000 V which is sufficient for the sputtering process. In the bipolar pulsed mode, the duty cycle is 10%, frequency, and pulse width can adjust in the range of 0 – 100 kHz and 1.0 – 5.0  $\mu$ s respectively. Moreover, this magnetron source can support high power modes by using high power impulse magnetron sputtering (HiPIMS) power supply.



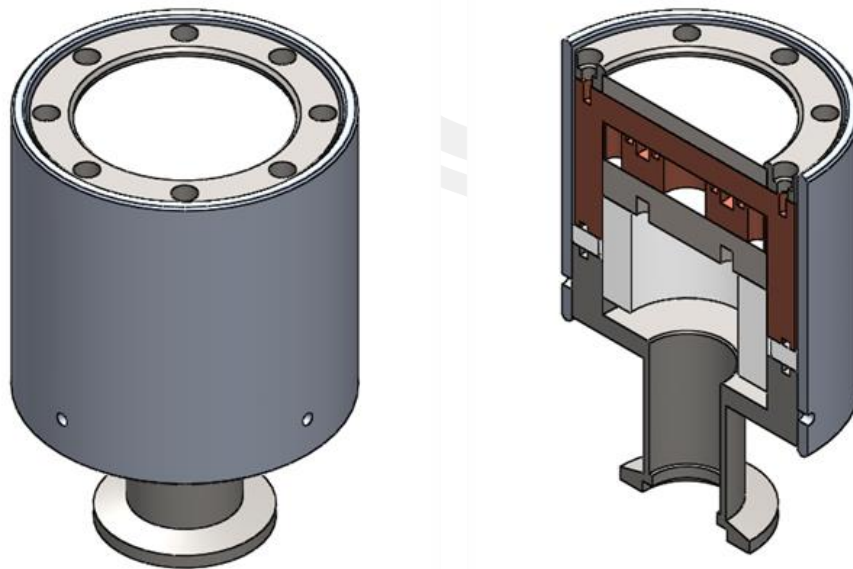


**Figure 3.17** Assembly of an unbalanced magnetron sputtering source.

#### **3.1.3.4 In-house filtered cathodic vacuum arc source**

In this thesis, the cathodic arc source was operated in pulsed mode. This topic will be discussed about the pulsed vacuum arc and filtered cathodic vacuum arc source.

The pulsed vacuum arc is a high-density plasma source arc. For operation in pulsed mode, the process parameters such as pulse width and duty cycle play a very important role. At a low duty cycle, can be applied for temperature-sensitive substrate coating such as plastic sheets. One difficulty that appears with the pulsed operation is the need for rapid arc triggering in all pulsed (1 triggering = 1 pulsed). To avoid this problem, this thesis uses the pulsed vacuum arc source, it doesn't have a mechanical trigger.

The pulsed vacuum arc source was applied to carbon film deposition with a concept of a conductive path between anode and cathode electrode such as a carbon coating on the ceramic provides a means for Joule heating of the coating-cathode interface. This results in rapid plasma formation as soon as the arc voltage is applied to the cathode electrode as shown in Figure 3.18. So, neither a trigger electrode nor a specific electrical trigger pulse generator is required. The method was called “triggerless” arc initiation.

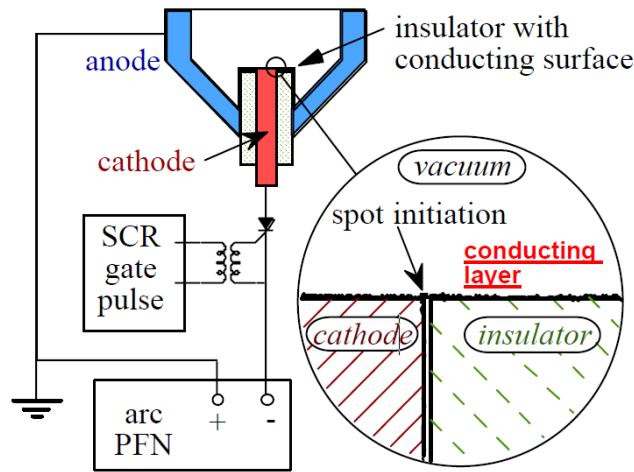


**Figure 3.18** Schematic of triggerless vacuum arc initiation (ion extraction system not shown) [139].

Triggerless arc initiation can be considered as taking the “pencil mark” to the extreme: the pencil mark is well known to aid the occurrence of surface flashover across an insulator in a vacuum. The slightly conducting graphite mark defines the path of lowest resistance and allows the operator to achieve flashover with moderately high voltage (typically of order 10 kV) [140]. As indicated in the inset of Figure 3.18, the current flow between the conducting path and the cathode takes place at only one or a few contact points at the path-cathode interface. As shown in [141], the current density at the contact points can be extremely high (of order  $j = 1 \times 10^{11} \text{ A/m}^2$ ), and hence the power density is also high. The power associated with Joule heating of one contact point can be estimated by

$$dP = IdU = I^2 dU = I^2 \frac{\rho}{A} dl \quad (3.2)$$

where  $I$  is the current flowing through a contact point having a cross-sectional area  $A$ :

$$R = \int \left[ \rho(T(l')) / A(l') \right] dl' \quad (3.3)$$

Where  $R$  is the resistance of the contact point,  $\rho$  is the temperature-dependent specific resistivity of the contact material,  $A(l')$  is the cross-section of the contact point, and  $dl'$  is an infinitesimal section of the contact path length.

For simplicity, we may consider a contact of cylindrical shape with length  $l$  and cross-section  $A = \pi r^2$ . For  $l = 10 \mu\text{m}$  and  $r_1 = 5 \mu\text{m}$  we obtain  $A = 78 \mu\text{m}^2$ , and  $R$

$=6.9 \text{ m}\Omega$ , for tungsten at room temperature, for example. If we further assume that the initial current is of order 10 A, limited by the resistance of the circuit including the conducting path, the current density would be  $j=1.3 \times 10^{11} \text{ A/m}^2$ , and the Joule heating power 0.7 W. The power is concentrated in a small volume of only  $780 \text{ }\mu\text{m}^3$  and the volume power density is  $9 \times 10^{14} \text{ W/m}^3$  in this example. Joule heating increases the temperature of the contact material and its specific resistivity. For most metals, the resistivity increases by one order of magnitude if the temperature rises by 1000 K and is even greater at higher temperatures when phase transitions are taken into account (solid/liquid and metal/dielectric). Thus, the power density also increases by an order of magnitude or more, reaching  $10^{16} \text{ W/m}^3$ , a value known to cause the explosive formation of plasma [142]. It can be concluded that metal plasma can be formed at the cathode with a relatively low voltage (for instance, 500 V) due to the concentration of power in a microscopically small volume.

Because a conductive path between cathode and anode electrode is not only acceptable but required, this arc initiation method is well suited for a vacuum arc geometry in which macroparticles and atoms from the plasma are deposited on the insulator separating the electrodes. Normally, the deposition of conducting and carbon material on the insulator separating the electrodes is beneficial since it “repairs” the conducting path, which is subject to erosion by the action of cathode spots. The repair and erosion process is the balance created after many arc pulses, and the resistance will vary around a steady-state average value.

By using the triggerless arc initiation principle, the requirements for a high-voltage trigger generator, isolation transformer, and trigger electrode are eliminated. However, triggerless triggering does not come for free. In order to precisely specify the instant of arc initiation, the arc power supply needs to be equipped with a switch, which will be discussed in the topic “Pulsed forming network”.

From the triggerless arc initiation principle, the pulsed vacuum arc source was designed by the triggerless model as shown in Figure 3.19. It consists of the graphite rod (diameter 6.35 mm), graphite rod holder (formed by copper material), and anode electrode (formed by stainless 316). The ceramic rod was applied to separate the graphite rod (cathode) and the anode electrode.

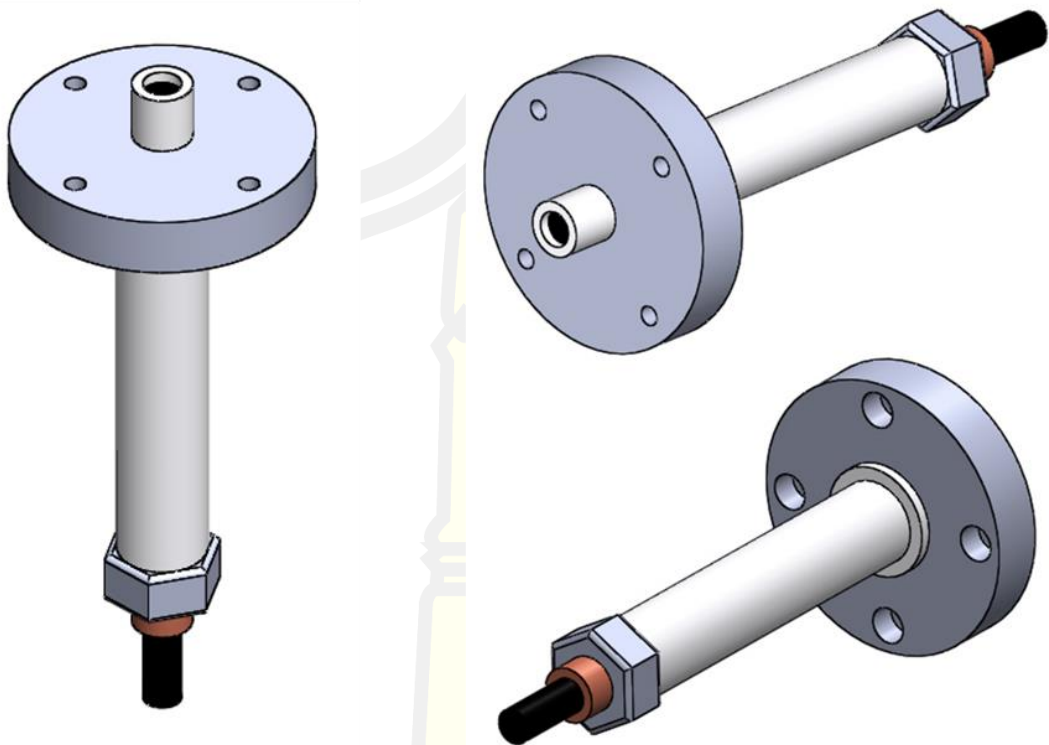


**Figure 3.19** Assembly of the pulsed vacuum arc source.

The resistance between the graphite rod and the anode electrode can reduce by using the pencil mark on the surface of the ceramic. It causes the resistance of about  $400\ \Omega$  (in the range of  $300$  to  $800\ \Omega$ ). However, the resistance between the cathode and anode electrode increased with the increase of operating time due to the ceramic being coated with the carbon film. Therefore, the ceramic should be cleaned when the operating time is 1200 pulsed.

Many previous studies have characteristics of arc plasma and characteristics of DLC film prepared by cathodic arc technique. For DLC coating, the cathodic vacuum arc generated the macroparticle into the defect (droplets, pores, and spikes) on the surface of the films [143], [144]. The defect directly affected on properties and quality of the film leading to a failure during work. So, to reduce the macroparticle, the pulsed vacuum arc source has a filter coil.

### 3.1.3.5 Principle of magnetic filtering

In the presence of an axial magnetic field, the motion of electrons is bound to magnetic field lines. While the electrons spiral around the field lines, they have the collision with another particle. For the magnetic field is bent, such as the field inside a

curved solenoid, electrons follow the curvature. On the other hand, ions are usually not magnetized because their gyration radius are much larger than the gyration radius of electrons and larger than the characteristic size of the filter. Nevertheless, ions are forced to follow the magnetic field lines due to the electric fields between electrons and ions which form if ions are shifted from electrons. The plasma stays macroscopically electrically neutral. Plasma transport along magnetic field lines is therefore a combined magnetic (electrons) and electric (ions) mechanism.

Although, the macroparticles may be slightly charged, but the mass to charge ratio is greater than, which corresponds with electrons and ions density in the plasma. Therefore, macroparticles have high momentum and move along almost straight trajectories part. The important parameter the macroparticle will be separated from the plasma is the plasma, electrons and ions must be separate from the line of the cathode surface. Resulting in, complete macroparticle removal by magnetic filtering would have been accomplished. However, this process causes significant plasma losses and nanoparticle transport by plasma particle interaction. Thus, the plasma density drops when was deviate from the filter coil [145].

#### 3.1.3.6 Design of magnetic macroparticle filters

To reduce the macroparticles on ta-C films, the pulsed vacuum arc source has a bent magnetic filter (a curved solenoid). The filter coil has an open architecture, in which the macroparticles can leave the area of the solenoid filter coil during the plasma generating and transporting. In addition, the advantage of a free-standing magnetic field coil reduces the scattered and sticking to walls of macroparticles. The filter coil is made in the copper tube (diameter 3/16 in, thick 0.5 mm), the coil is 90° curved solenoid, 31 round, the major and minor radius is 150 mm and 29 mm respectively. The coil has the water (17 Celsius) flow inside the copper tube to cool. To build the magnetic field for bending the plasma, a high current is required to flow through the coil. The complete pulsed filter cathodic vacuum arc source is shown in **Error! Reference source not found..** In addition, the pulsed vacuum arc source and filter were installed in the T-shape adapter to protect the macroparticles that come to the deposition chamber. However, an in-house FCVA source has a limitation for ta-C



deposition. The carbon target can't slide and adjust the position during the deposition process, the maximum lifetime for ta-C deposition of about 5000 pulses.

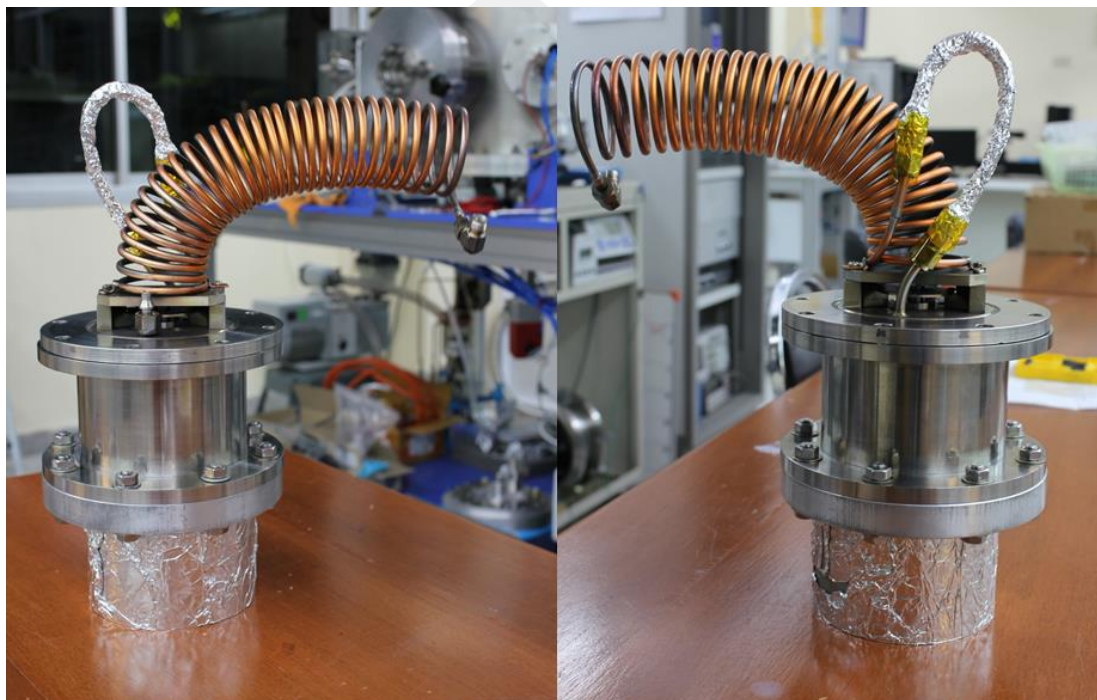


**Figure 1.** Assembly of the pulse filtered cathodic vacuum arc source.

### 3.1.3.7 Commercial filter cathodic vacuum arc source

To operate the plasma and increase the maximum lifetime for ta-C deposition by FCVA source. The FCVA source must be a carbon rod slide and zero sets. Figure 3.20 shows a diagram of the commercial FCVA source. The FCVA source consists of a pulse cathodic arc (triggerless model), cathode electrode, anode electrode, and filter coil. The electrodes have water cooling, it builds up by copper material to increase cooling efficiency. These electrodes were separated from the ground electrode by ceramic. The filter coil is 90° free-standing magnetic field coil, the solenoid has 22 turns, a major and minor radius of 80 mm and 16 mm respectively. Moreover, this source has a sliding target option, indicating that the target can adjust the target position during the arc plasma operation. As a result, the lifetime of arc operation is long (more than 100000 pulses). Therefore, this source can be used to coat thick ta-C films, which is suitable for this work.

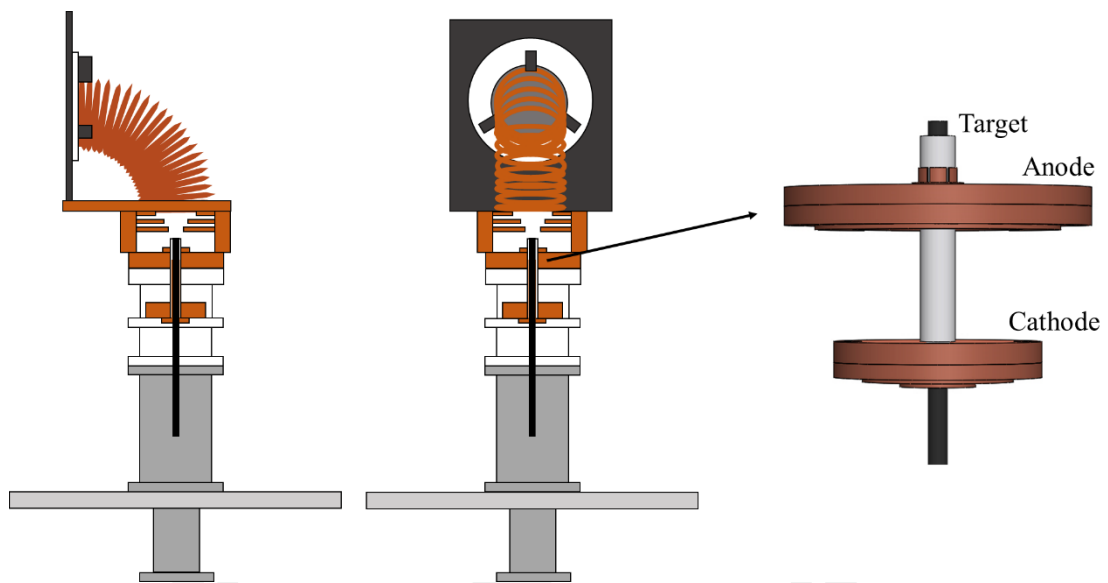


**Figure 3.20** The commercial filtered cathodic vacuum arc source.

#### 3.1.3.8 T-shape adaptor

The nature of the arc, especially the arc of the carbon target, generates the macroparticle. The  $90^\circ$  filter coil can reduce the number of macroparticles. In addition, the structure and design of the FCVA source have affects the efficiency of the microparticles filter. In the literature review, the new design of FCVA deposition such as T-FAD, Crank-FAD, X-FAD and Y-FAD was applied to reduce the contamination of macroparticles on the films. The design of the commercial FCVA source and deposition chamber match the T-shape adaptor. Therefore, to install a commercial FCVA source in an IPVD system, the T-shape adaptor was designed and built.

Assembly of the T-shape adaptor as shown in Figure 3.22, it has three flanges consists of two ISO250 and ISO 00 flanges. The stainless steel grad 316 tube with a diameter of 10 inch and length of 600 mm to use T head and the stainless steel grad 316 tube with a diameter of 8 inch and length of 120 mm to use T-base. All parts use the thick welded process to increase the efficiency of receiving pressure. Due to the high weight of the FCVA source itself.



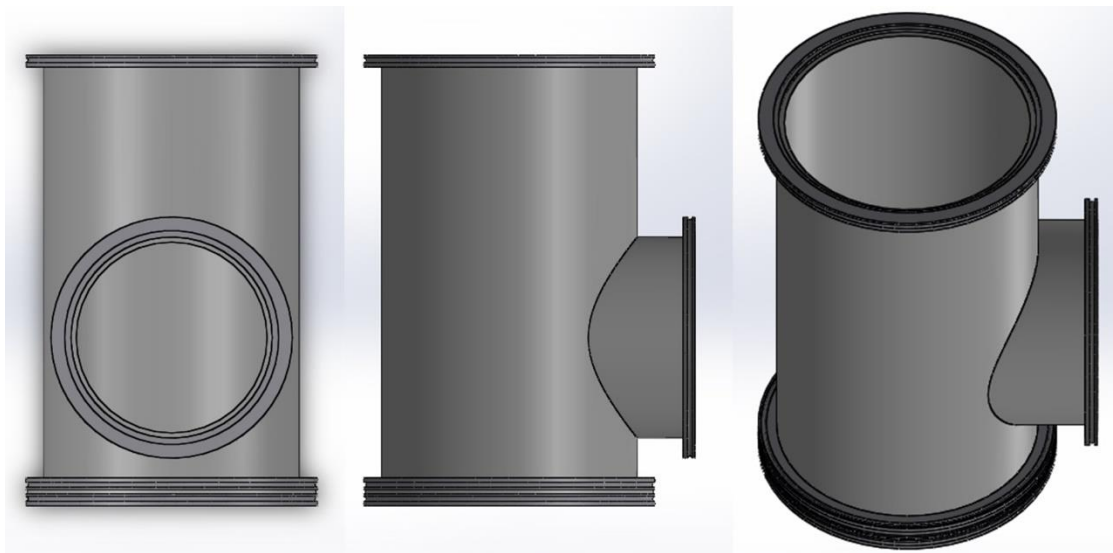


**Figure 3.21** T-shape adaptor for support the commercial FCVA source.

The t-shape adaptor must be matched with the commercial FCVA source. To confirm the size and position of the T-shape adaptor, both assemblies were matched using the mate function in the SolidWorks program. The assembly of the commercial FCVA source on T-shape adaptor as shown in Figure 3.22. It was found that the commercial FCVA source matched with the T-shape adapter. The center of the filter coil has an offset is 20 mm to reduce the plasma loss rate due to the direction of the plasma beam is not perpendicular to the plane of the FCVA cover plate. In addition, the Al plate with a diameter of 200 mm was stuck on the cover plate of the FCVA source to separate the arc chamber and deposition chamber. With this design, the macro particle was filtered by filter coil and blocked by this plate. Thus, the macroparticles during ta-C deposition are decreased.

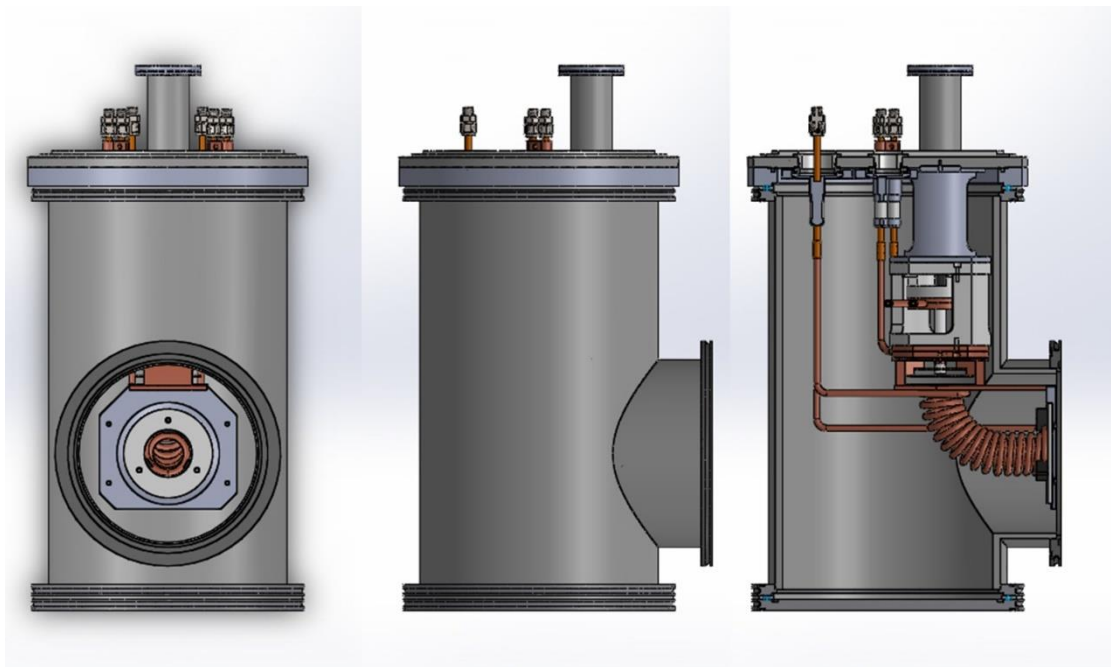


**Figure 3.22** Assembly of installation of the commercial FCVA source on T-shape adaptor.

Moreover, to increase the operating lifetime of the FCVA source and reduce the maintenance cycle, the target slide and zero adjust position option was applied. Figure 3.23(a) shows an overview of commercial FCVA source installation. The T-shape adaptor was installed at port 1 of the deposition chamber. The target slide system was installed at KF70 flange of the FCVA source, which same center as the carbon target rod. To slide the carbon target rod in and out, and target scratch, we use the concept of a CNC controller with the two axes.

The target slide system consists of a stepper motor, T8 lead screw rod, Nuts and 3-axis slide rail with a length of 400 mm. While the target scratch consists of a stepper motor, T8 lead screw rod, Nuts and 2-axis slide rail with a length of 100 mm. The two parts work together efficiently.

The Nema23 stepper motor (J-5718HB4401, 2.5 N.m, 4.4A) is used to turn a lead screw rod or adjust the position of the carbon target rod and scratch blade. The stepper motor was driven by TB6600 and controlled using Candle GRBL Controller. The Candle GRBL software was used to CNC machine control with GRBL source code or G code (X, Y and Z) which is related to the stepper of the motor. The G code is passed to the Arduino Nano 3.0 CH340 USB Driver and CNC Shield V4.0 3-axis

board, to process and convert the G code to pulse data. The pulse frequency and the direction of the pulse determine the rotation or movement of the motor. Therefore, it can work together and work concurrently depending on the working code.

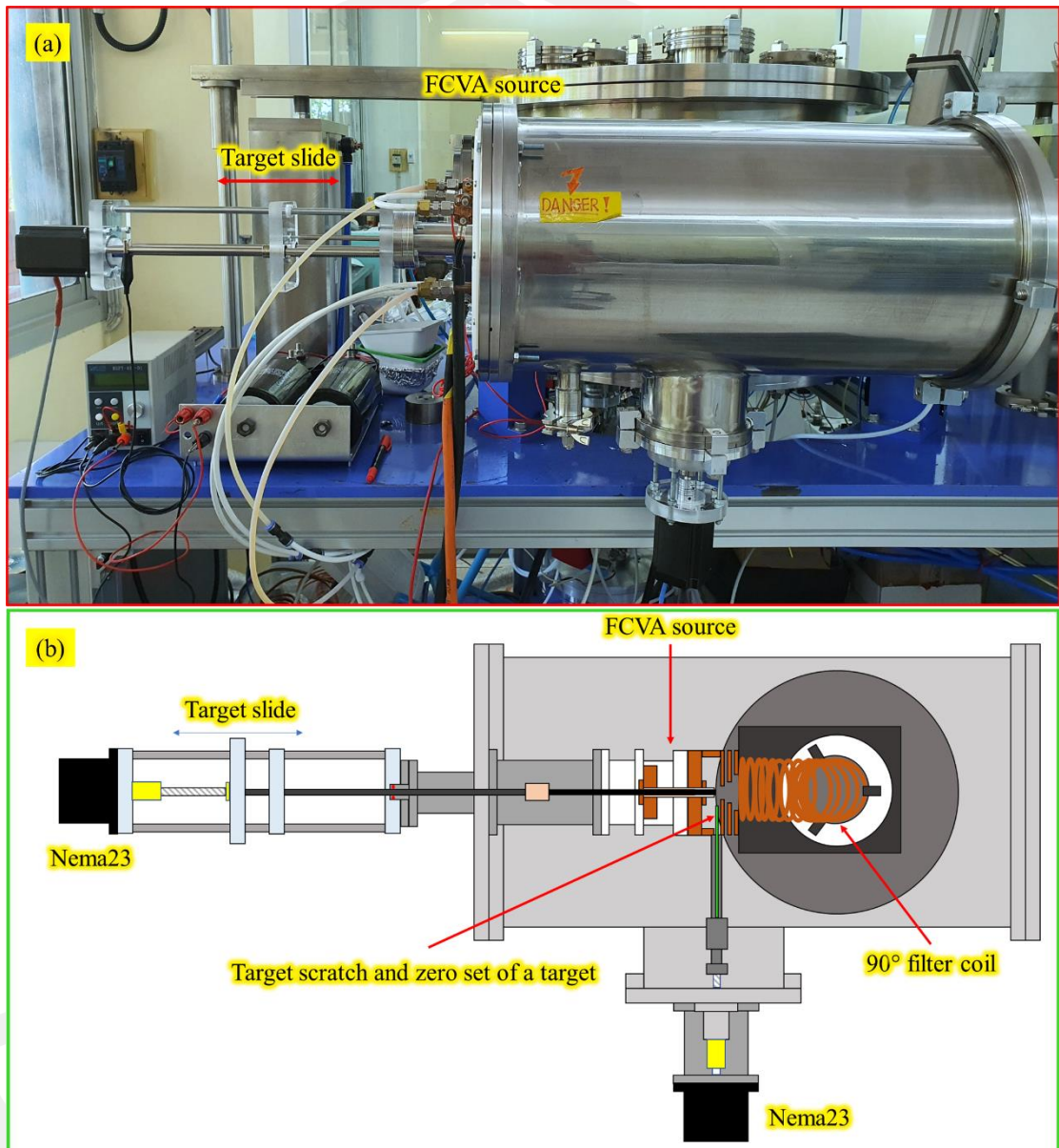


**Figure 3.23** (a) installation of the FCVA source on T-shape adaptor and ionized physical vapor deposition, (b) and (c) carbon rod target scratch and zero adjust system.

### 3.1.3.9 Focusing coil

In order to confine as much plasma to accumulate on the substrate as possible, the focusing coil will be added to the gap between the FCVA source and deposition chamber as shown in Figure 3.24. The focusing coil is made by a copper tube (diameter 3/16 inch, thick 0.5 mm) in solenoid coil characteristic as shown in Figure 3.25. The turn number of a focusing coil is 22 turns, diameter of 130 mm, and a length of 18 mm. The coil has the water with a temperature of 17 Celsius flow inside the copper tube to cooling. Also, the focusing coil contact with the filtering coil by the M4 nut and skull to hold it firmly to prevent falling off during the experiment. To induce the magnetic field to confine the plasma, a high current (positive) from the PFN flowed through the focusing coil. Which the positive current from the PFN into the focusing coil, and then flows into the filtering coil to induce the magnetic field to filter only the plasma used for deposition.

The result of the focusing coil is the plasma was confined and ejected on the sample as seen in Figure 3.25. For the old FCVA source, the ta-C film has a very low deposition rate because the plasma diffuses and non-ejects on the sample. While the FCVA source with a focusing coil can produce the ta-C film with a high deposition rate due to the plasma being focused on the sample.

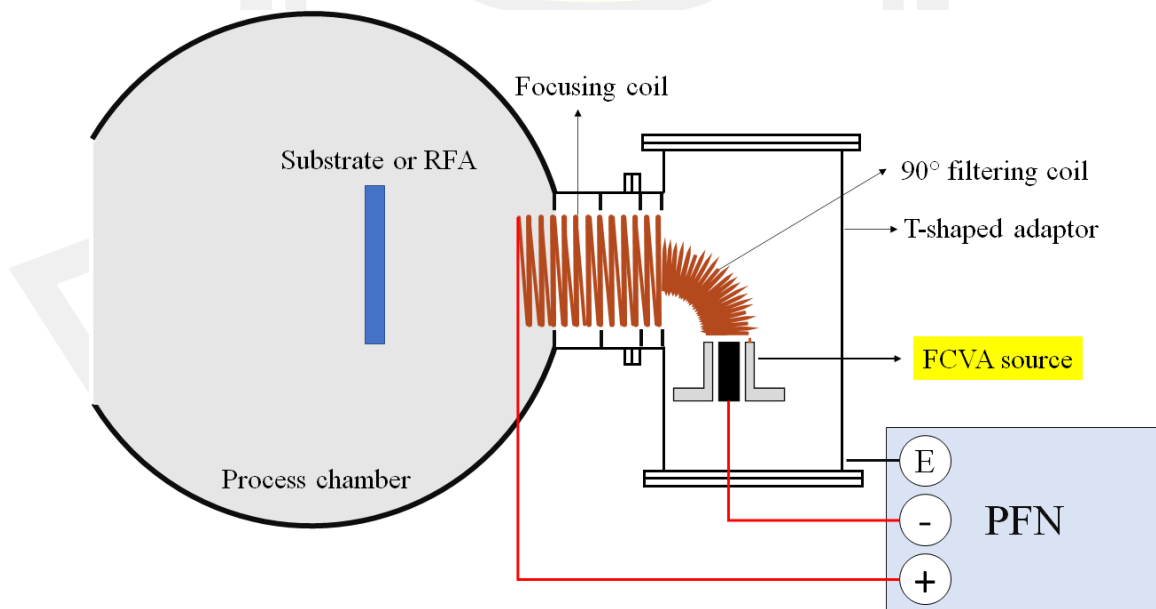


**Figure 3.24** Installation concept of the focusing coil at the gap of FCVA source and deposition chamber.



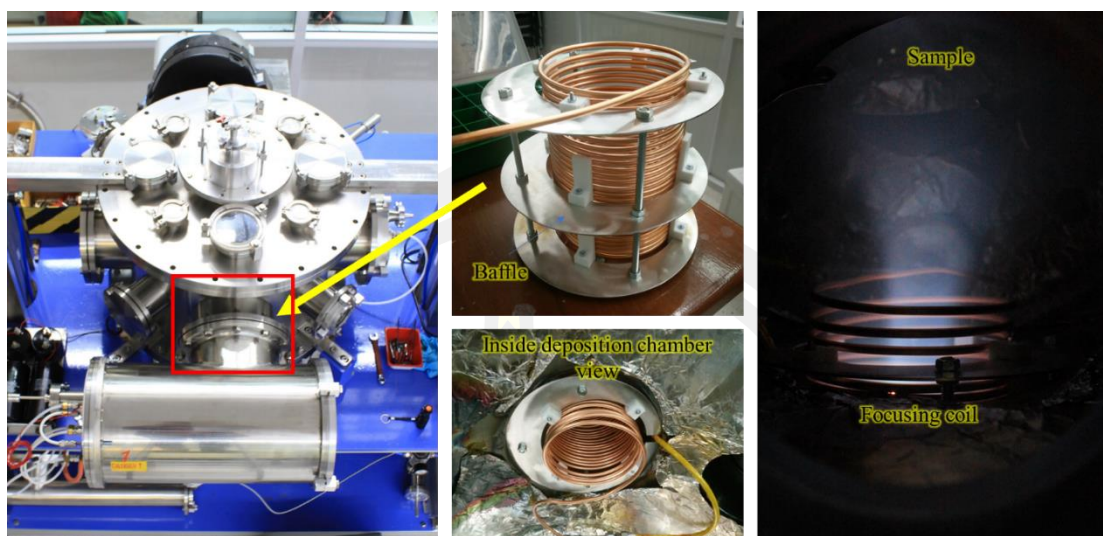


**Figure 3.25** Installation and operation of the focusing coil.

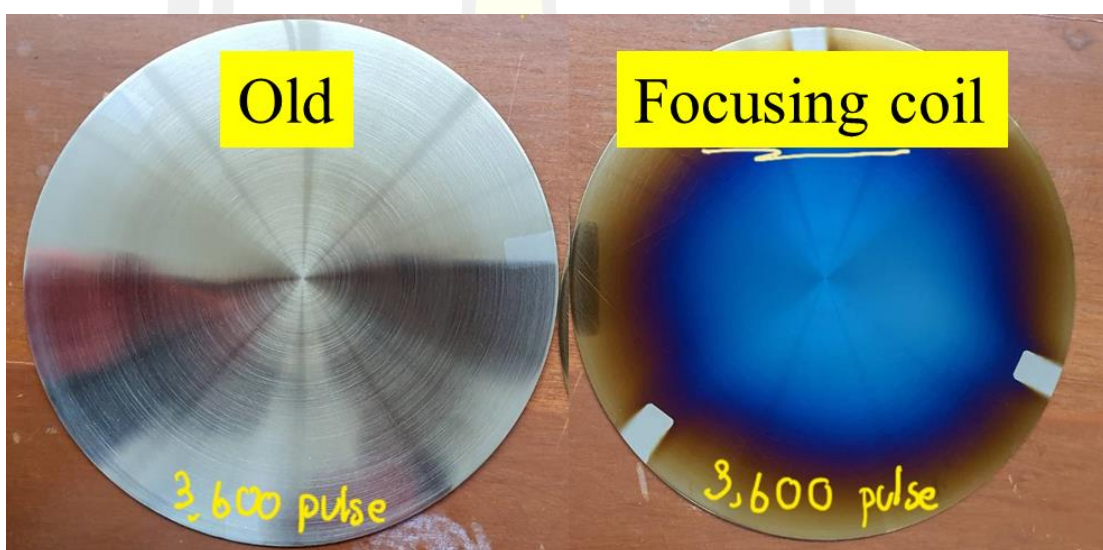


**Figure 3.26** Characteristics of the ta-C film on stainless steel deposited by FCVA source (a) do not have the focusing coil and (b) use the focusing coil.

#### 3.1.4 Pulse forming network

To operate the plasma of the carbon target rod with a high density, the FCVA source was driven by a pulse forming network or PFN. In this work we use the VEECO pulse forming network as shown in Figure 3.27, to operate the commercial FCVA source.



**Figure 3.27** VEECO pulse forming network.

The PFN is an electric circuit that accumulates electrical energy over a comparatively long time and then releases the stored energy in the form of a relatively square pulse of comparatively brief duration. In a PFN, energy storage components such as capacitors, inductors or transmission lines are charged by means of a high-voltage power source, then rapidly discharged into a load through a high-voltage switch. PFNs are used to produce uniform electrical pulses of short duration to power devices such as pulsed lasers, particle accelerators, and high-voltage utility test equipment [146].

The concept of the PFN as shown in Figure 3.28, consists of the charger power supply (1000 VDC maximum), relay, diode, the network of capacitance and inductance, and Silicon Controlled Rectifiers (SCR). The charger power supply will transfer the energy into the LC network to charge the capacitor when the relay is closed. The diode has a role block the reverse current. Charge and discharge were controlled by the SCR, the frequency of charge and discharge was determined from the external trigger.



**Figure 3.28** The box diagram of the PFN.

The LC network of the PFN used radar modulators is the Guillemin Type E network, in which the Type E network capacitance is the same in each mesh and there is mutual inductance between adjacent coils. The squareness of the output pulse is a function of the mesh number. The risetime is determined by the risetime of the first mesh in the network, closest to the load. The pulse width is twice the one-way transit time of the wave.

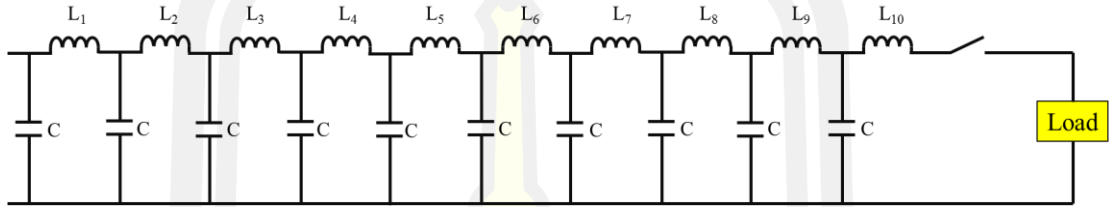


**Figure 3.29** Schematic showing a 10-stage Type E PFN, output switch, and load.

The design of the PFN is very important, especially radar modulators, capacitors, and inductors. The impedance of the PFN is an important parameter because energy transfer from the PFN to the load depends on the impedance of the PFN. If the impedance of the PFN is matched to the load impedance, the energy transfer will be almost completely dissipated in the load (no reflection), and the voltage across the load will be one-half the charge voltage of the PFN capacitors [147]. On the other hand, if the impedance of the PFN mismatch to the load impedance, the energy transfer will be the reflection. The impedance of PFN is calculated as follow:

$$Z_{PFN} = N\sqrt{LC} \quad (3.4)$$

Where  $Z$  is the impedance of the PFN,  $N$  is the number of stages (10 stages),  $L$  is the inductance ( $3.75 \mu\text{H}$ ), and  $C$  is the capacitance ( $100 \mu\text{F}$ ). So, the impedance of the PFN is:

$$Z_{PFN} = 10\sqrt{(37.5 \times 10^{-6}) \times (100 \times 10^{-6})} \quad (3.5)$$

$$Z_{PFN} = 6.0 \text{ ohm} \quad (3.6)$$

The impedance of the plasma depends on many parameters such as arc current, operating pressure, etc. To operate the PFN, the equipment in the box diagram (see Figure 3.30) is required such as the stabilizer and DC power supply for



charging the power during the PFN working. In addition, The PFN needs support devices to operate as shown in Figure 3.31, which consists of the following:

- A pulse generator has a role in the trigger.
- 5 VDC power supply has a role in the open/close gate of the SCR.
- 12 VDC power supply uses drives the fan and open relay of the PFN.

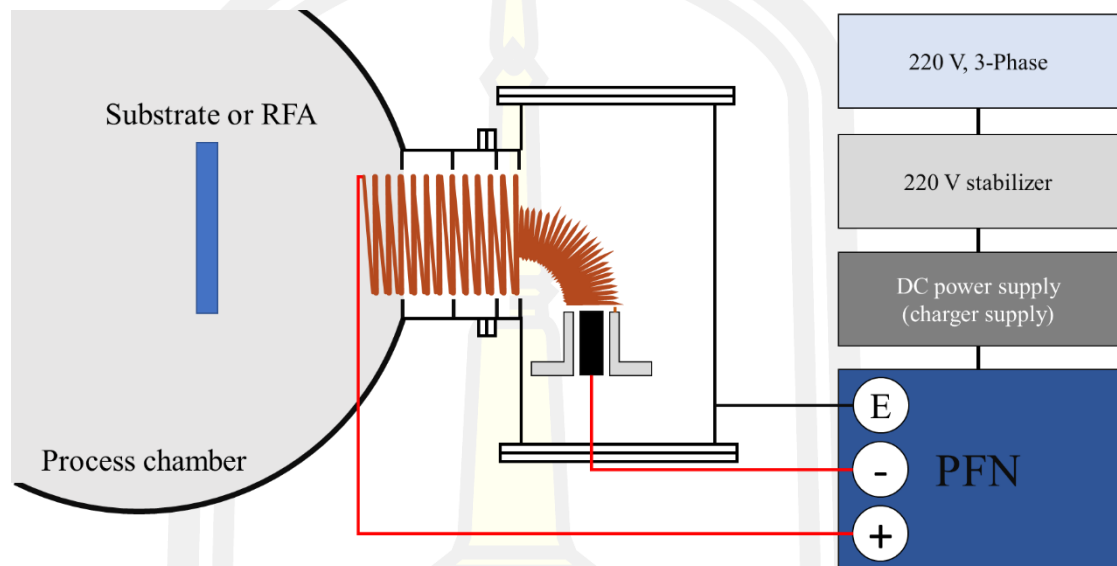


**Figure 3.30** The box diagram of the operating pulsed vacuum arc source.

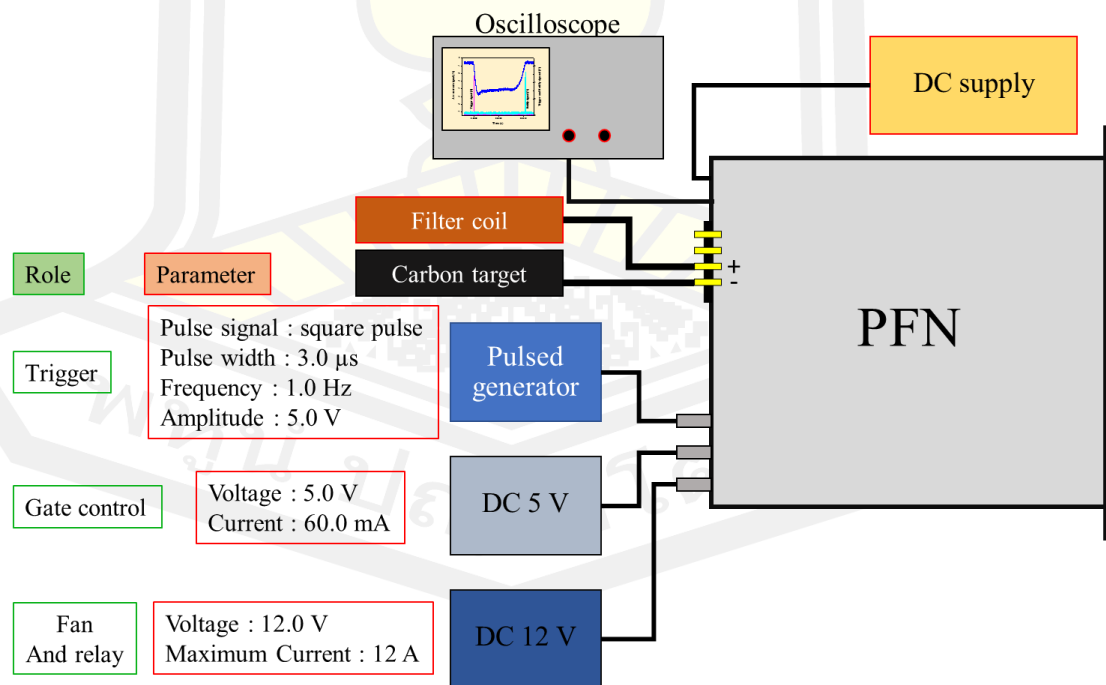


**Figure 3.31** Diagram of Pulsed Forming Network (PFN) and support devices.

However, we still lacked a power supply to drive the PFN, so it was built. The high voltage DC power supply was designed by using the power amp concept as shown in **Figure 3.32**. The amplifier needed the sinewave 10 kHz generator, the sinewave was extended the amplitude by the amplifier and the energy was transferred through the transformer. And then the energy was transferred to the bridge diode, which the negative electrode connects with the resistor (current limit). From the design, this power supply can operate in a long time for the charger voltage lower than -600 V.

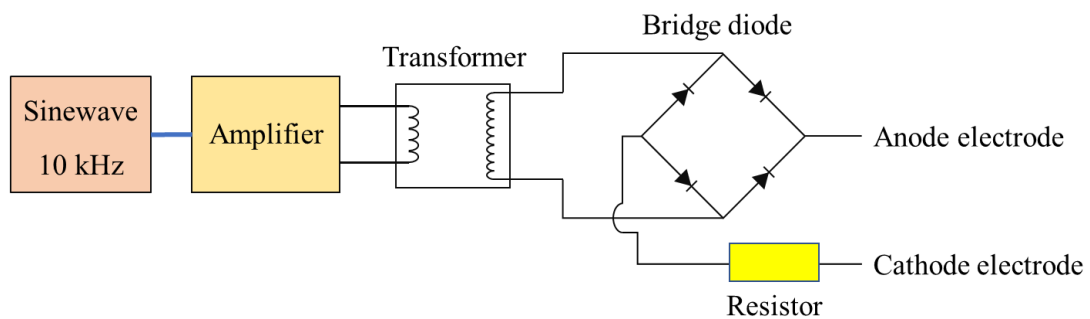


**Figure 3.32** The box diagram of high voltage DC power supply (600 V maximum).

### 3.1.5 Plasma and substrate bias power supply

To increase the ion energy of the depositing ions in ta-C deposition, the plasma biasing and substrate bias technique is required. Therefore, to support the energy to the electrode during the arc process, a high current pulse power supply is required (around 300 V<sub>max</sub>, and 100 A<sub>max</sub>), but its a high value. To reduce the cost of power supply, the DC bias power supply with a capacitor stores energy is one of its many applications would be supplying that energy to a circuit, just like a battery. The upside of capacitors is capable of delivering energy much faster than a battery, which makes them good for applications that need a short, but a high burst of power (pulse).

Therefore, the biased power supply uses the concept of capacitor stores energy, diagram as shown in Figure 3.33 and Figure 3.34. This technique requires is DC power supply (HSPY-400-01, 400 V<sub>max</sub>, 1 A<sub>max</sub>), two capacitors with the capacitance of 100 μF, two capacitors with the capacitance of 1000 μF, and the diodes (120 V, 60 A). The capacitor was parallel-connected with the DC power supply to storage energy in the plasma off (charge) and drive energy in the plasma on

(discharge). While the diode has a role to block the reverse current from the PFN and the plasma.

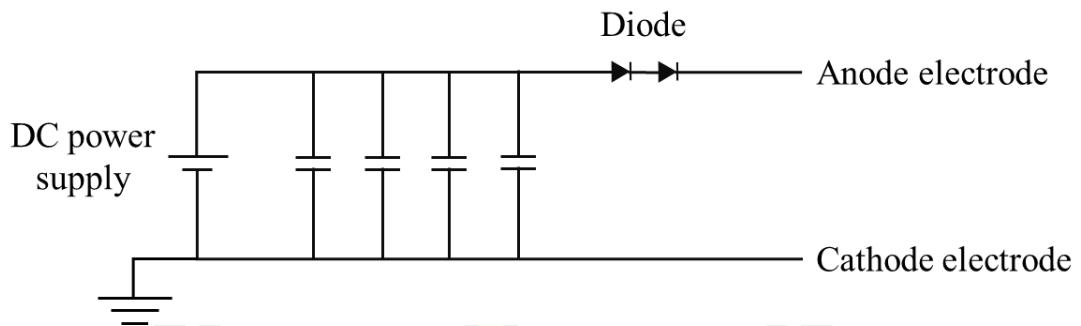


**Figure 3.33** An electrical schematic of the plasma biasing power supply.

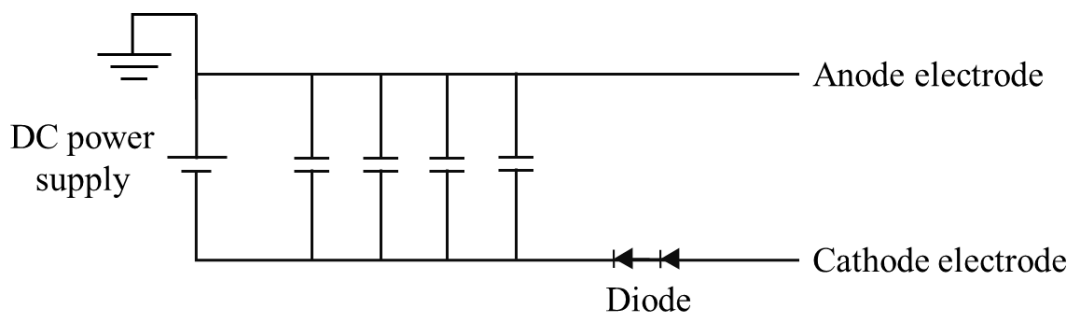


**Figure 3.34** An electrical schematic of the substrate bias power supply.

### 3.1.6 Substrate holder

The substrate holder as shown in Figure 3.35, it was installed at an ISO200 flange in the bottom flange of the deposition chamber (same center as the deposition chamber). The substrate holder can support the 2D and 3D samples with a maximum diameter of 170 mm. To support many studies, the substrate holder is designed independently of the ground electrode. Therefore, this substrate holder has three options for thin film coating state is grounded, floated, and substrate bias. In addition, the position of the sample can adjust in the x-direction (move closer to or away from the source) and the z-direction (shift up or shift down) to control the uniformity of the films.

The substrate holder can be rotated around the x-axis using a nema17 stepper motor (17HS8401S series, 52 N.cm, 1.8A), where the rotation frequency is controlled by the pulse frequency from the generator function.

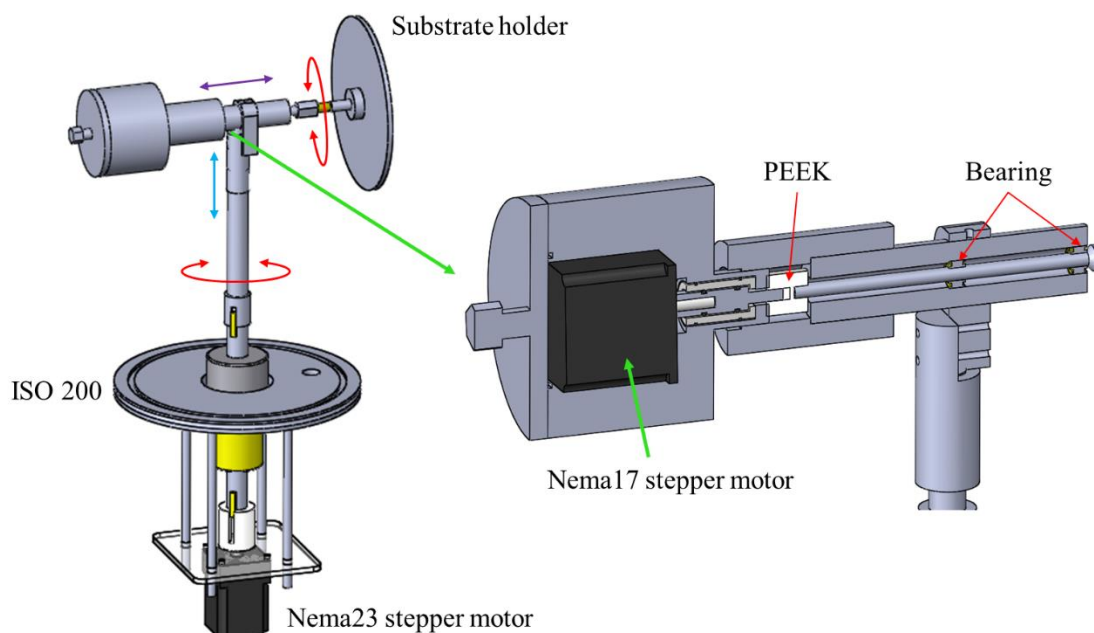


**Figure 3.35** SOLIDWORK assembly and photo of the substrate holder.

Moreover, it can be rotated with  $360^\circ$  around the z-axis, the directional of the substrate holder can determine by a nema23 stepper motor (J-5718HB6401 series, 3.6 N.m, 4A) to select the plasma source or ion source for coating and cleaning sample. The nema23 was driven by TB6600 and controlled using Candle GRBL Controller. Normally, the Candle GRBL software was used to CNC machine control with GRBL source code or G code (X, Y, and Z) which is related to stepper of the motor. The G code is passed to the Arduino Nano 3.0 CH340 USB Driver and CNC Shield V4.0 3-axis board, to process and convert the G code to pulse data. The pulse frequency and the direction of the pulse determine the rotation or movement of the motor.

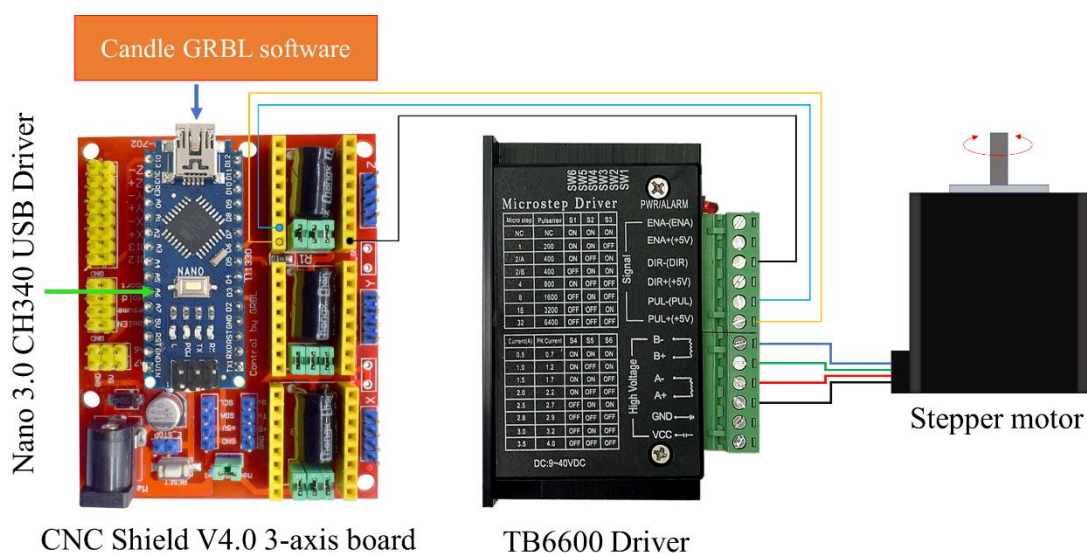


**Figure 3.36** Stepper motor driving diagram for substrate holder system.

### 3.1.7 Substrate transfer

To reduce sample loading time, the substrate transfer system is required. The substrate transfer system as shown in Figure 3.37, consists of a load lock chamber with a diameter of 100 mm, a magnetic load lock transfer arm (600 mm), HV gate valve with the neumatic actuator (VAT, series 091 DN 100 mm) and Rotary vane dual-stage mechanical vacuum pump (Edwards, RV12).

The magnetic load lock transfer arm is the industrial transfer arm. It adopts the magnetic induction principle of outer magnet and inner magnet as shown in Figure 3.38. Thus, it can be able to slide in and slide out of the substrate holder. be able to slide in and slide out.

The sample load-lock system was installed at port number 8 of the deposition chamber, it reduces sample loading time and non-stop the pumping system of the deposition chamber (5 – 10 min for sample loading time). The load-lock chamber was pumped by a rotary pump, the pressure in the load-lock chamber of about 1 Pa, while the base pressure inside the deposition chamber of  $10^{-4}$  Pa. Before opening the HV gate valve, the pressure inside the load lock chamber was adjusted to low pressure by a manual three ways valve (leak valve). It reduces the pressure gradient between the two chambers and reduces the probability of damage to the blade of the turbomolecular pump.

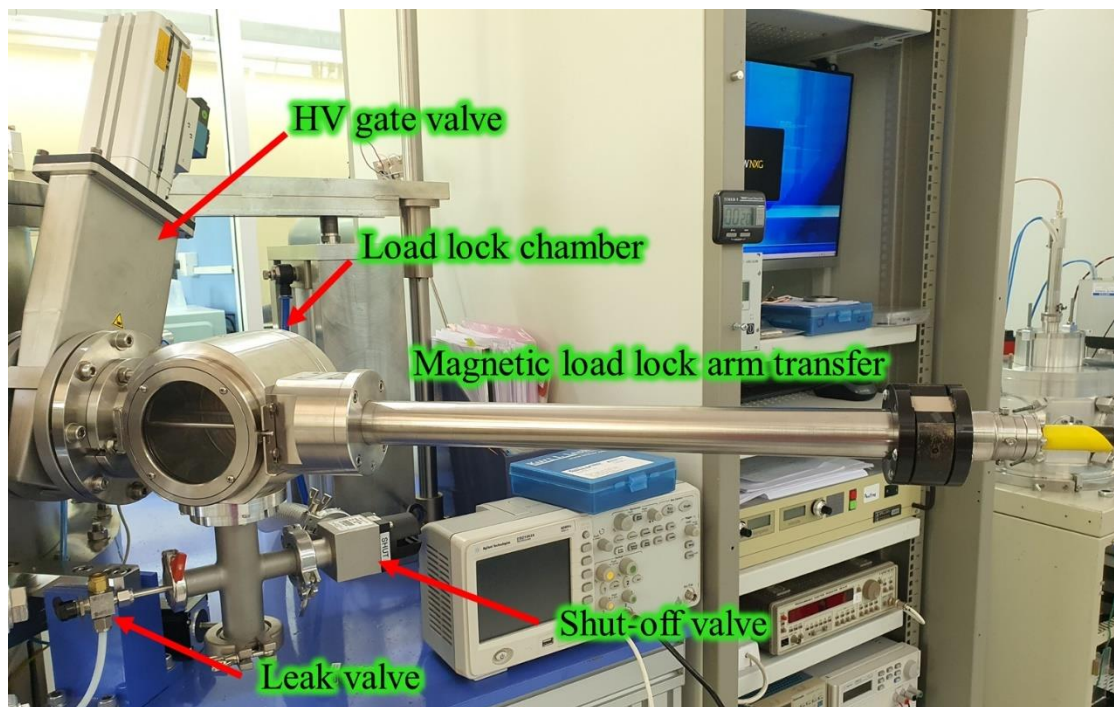


**Figure 3.37** Load lock transfer substrate system.

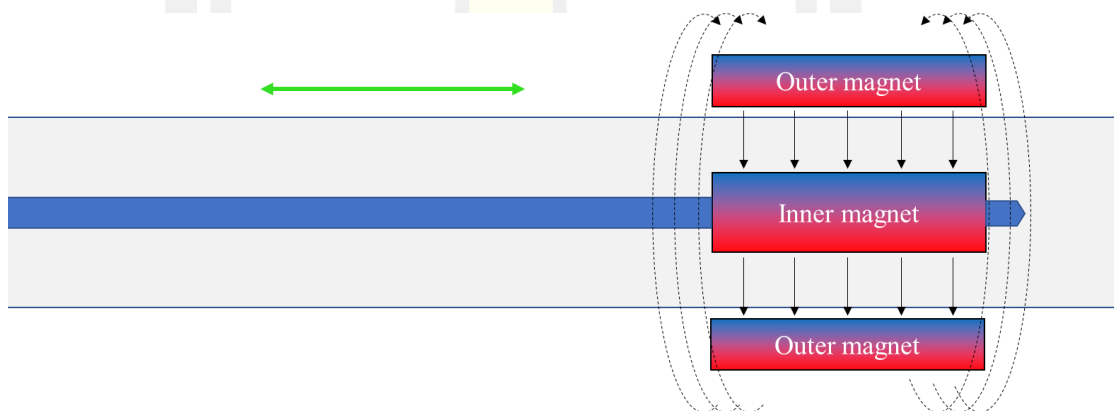


**Figure 3.38** Model of the magnetic transfer arm.

### 3.2 Retrading filed analyzer probe

Plasma diagnostic is the study of interactions between the plasma surface of the substrate, particle-particle, etc. It is an important process of linking plasma parameters with the structure of the DLC film. The ion energy, ion flux, and ion density of carbon directly affect on the properties of the ta-C film. This topic will explain the study of the plasma parameter by using the Retarding field analyzer probe or RFA probe.



### 3.2.1 Langmuir probe

The RFA probe is one of the Langmuir probes. Therefore, the basis of the Langmuir probe is important. Langmuir probe is a simple and conventional instrument for determining the basic characteristics of the plasma [148]. Normally, the Langmuir probe has many designs such as the spherical probe, cylindrical probe, flat probe, double probe, hot probe, and capacitively coupled probe, etc. [149][150]. However, these probes use to study the properties of electrons in the plasma such as electron temperature, electron density, and electric potential [148].

Usually, I-V characteristics of obtained with a collecting Langmuir probe in a cold plasma as shown in Figure 3.39. In order to give a qualitative interpretation, we will consider an idealized non-equilibrium collision less, Maxwellian and unmagnetized plasma. Thus, the collisional mean free paths of all particles are larger than all characteristic lengths ( $\lambda \gg r_p, \lambda_D$ ) and also the electron temperature  $k_B T_e \gg k_B T_i \approx k_B T_a$  is higher than those of ions and neutrals.

I-V characteristic obtains from scanning the potential ( $V_p$ ) at the corrector and measurement the current ( $I_p$ ) at the corrector. The probe current  $I_p = I_i + I_e$  is composed of ion current  $I_i$  and electron currents  $I_e$ . The I-V characteristic is divided into three-zone as follows:

- At the left of point A, the electrons are repelled, while ions are attracted by the probe. The drained ion current from the plasma is limited by the electric shielding of the probe and  $I_p$  decreases slowly. The probe current  $I_p \approx I_{is}$ , where  $I_{is}$  is the ion saturation current.
- At the right of point C, where  $V_p \gg V_{sp}$  the ions are repelled and the electrons are the attracted charges. In this case, the electrons are responsible for the electric shielding of the probe and  $I_p \approx I_{es}$  are called the electron saturation current. At  $I_p = 0$  is the floating potential  $V_F$  (point B) where the contributions of the ion and electron currents are equals.
- At point B-C is a transition region, the electron has kinetic energy to overcome the electrical force from the probe. But the probe potential is less than that of



the plasma potential  $V_p \gg V_{sp}$ . If the electron has a Maxwell-Boltzmann distribution, the electron current increases (exponential decay) with the increase of probe potential.

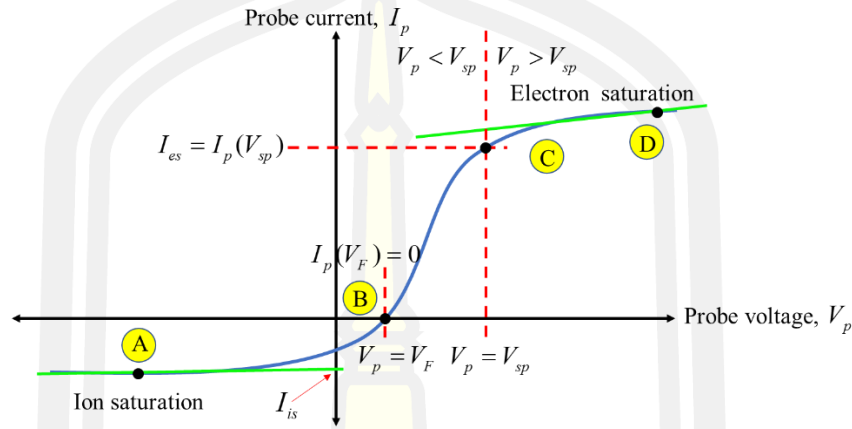


**Figure 3.39** An idealized I-V characteristic of obtained with a collecting Langmuir probe in a cold plasma.

To study the properties of the ion in the plasma and interaction on the substrate surface, the Langmuir probe needs to be modified to repel the electron and only allow the ions on a corrector. In this case, the I-V characteristic is shown in Figure 3.40. Therefore, the probe for this thesis will be a specific design for the measurement of the ion properties (ion flux and ion energy), which are explained in the next topic.

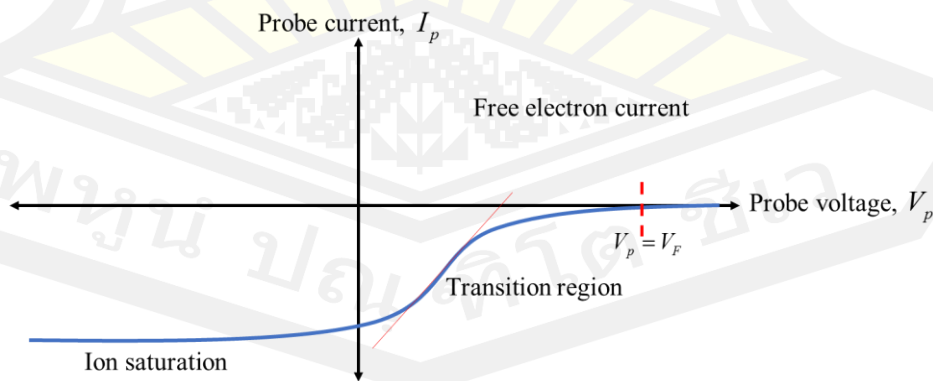


**Figure 3.40** An I-V characteristic obtain from a probe for measuring the ion.

### 3.2.2 Configuration of the RFA probe design

The design of the RFA probe is a very important section due to the probe design related to the performance of ion energy measurement. The consideration of RFA probe design as follows;

- The grid space must be less than the Debye length, to protect the plasma on the front side penetrative to the corrector.
- Grid-to-collector distance must be less than the mean free path of electron ionization collisions. Usually, the plasma sheath on the front of the probe is planar, and the thickness is  $\lambda_{sh}$  was formed nearly with the probe (critical value:  $2\lambda_{sh}$ ). So, if the grid-to-collector distance higher than the mean free path of electron ionization, the plasma can be penetrative and generated in this space.

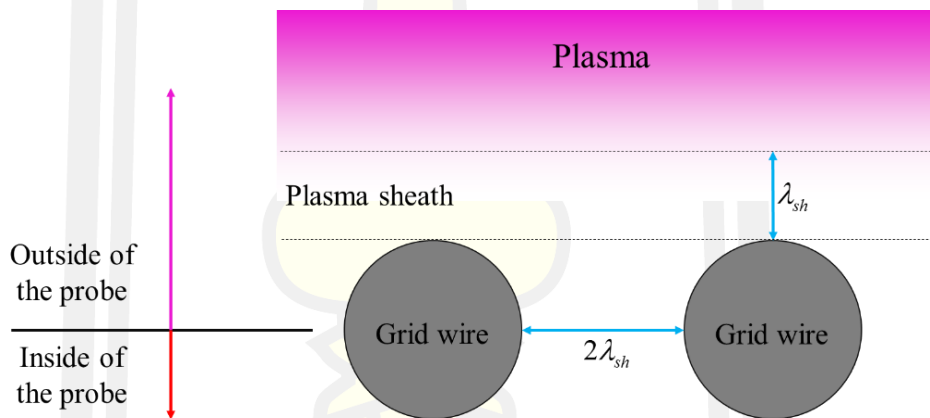


**Figure 3.41** Model of the front grid for the ion energy measurement probe.

### 3.2.3 Structure of retarding field analyzer

The structure of the RFA probe as shown in Figure 3.42. The RFA probe consists of the main components as follows: G1 electrode (use a Ni grid, 200 line/inch), has a role in macroparticle protection. G2 electrode (use Ni grid, 2000 line/inch) has the role is protect the plasma penetrative to the corrector, it connects with the G1 electrode and can select the ground surface or floating surface. G3 electrode (use Ni grid, 600 line/inch) connects with the negative power supply to repel the electrons from the probe and allows ions to move in the ion corrector. G4 electrode (use Ni grid, 600 line/inch) connect with GUARD electrode of SMU to

reduce secondary electrons. Therefore, the probe current is the ion current only. The ion corrector connects with the FORCE Hi of the source measure unit (SMU) for detecting the ion current and scanning voltage.

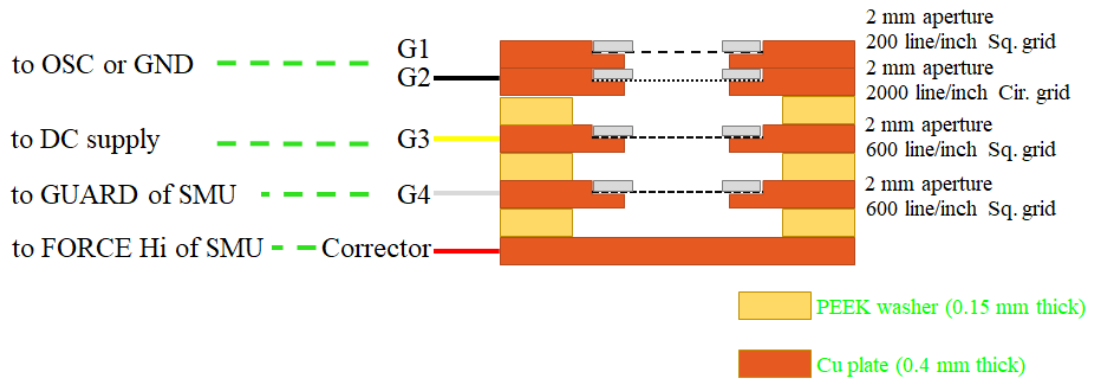


**Figure 3.42** Diagram and cross-section of the RFA probe.

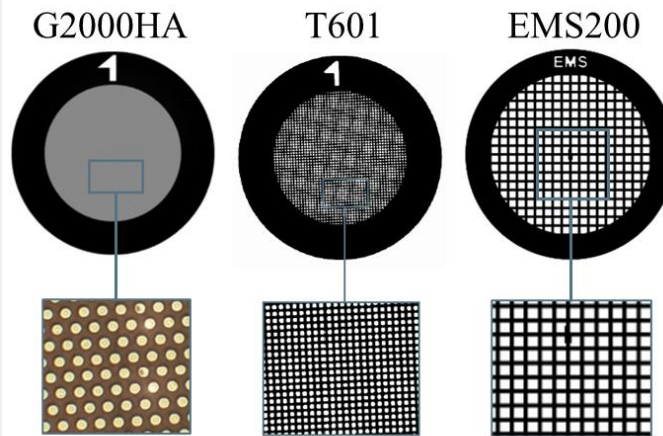


**Figure 3.43** Characteristic of the grids for the RFA probe.

**Table 3.2** Specific data of the grids.

Type	Cat#	Pitch (μm)	Hole (μm)	Bar (μm)	Transparency
200 mesh	EMS200-Ni	125	95	35	0.53
600 mesh (square)	T601-Ni	42	37	5	0.78
G2000HA circular mesh	G2000HA-Ni	12.5	~6.5	~6	0.27

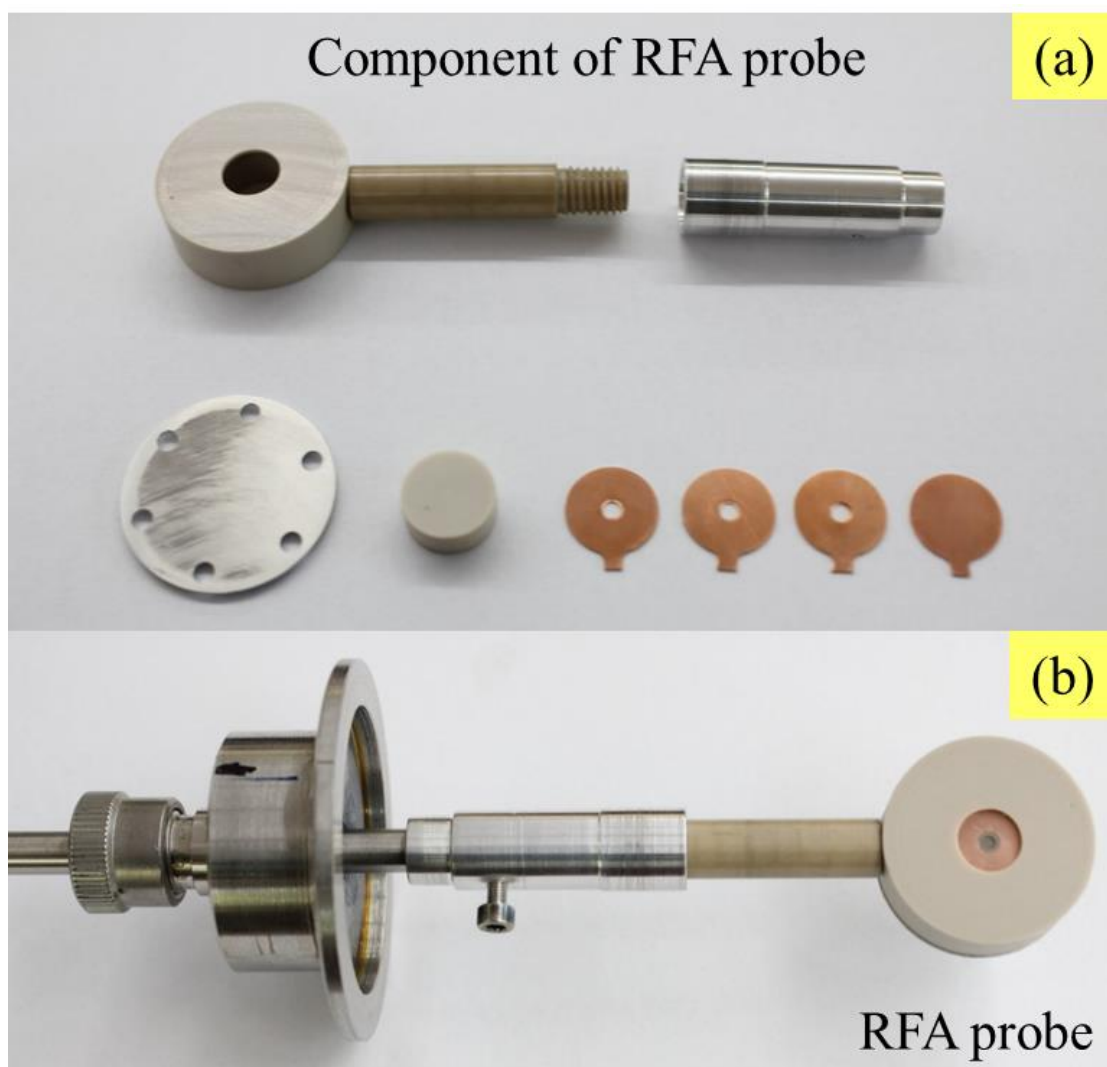


**Figure 3.44** An in-house RFA probe for ion energy measurement in the FCVA deposition.

Figure 3.43 and Table 3.2 show the characteristic and specific data of the grids. It was found that the G2000HA is the circular mesh and thin Ni wire ( $6\text{ }\mu\text{m}$ ), which is extremely fragile. Therefore, for the probe assembling process, a lot of caution is required to avoid damage to it. This will directly affect the ion energy measurement data. In addition, the G2 grid was protected by the G1 grid (EMS200-Ni), which is stronger.

From the ideal and design, the RFA is built to ion energy measurement. An in-house RFA probe as shown in Figure 3.44, consists of eight components; four Cu electrodes, a probe body, a backing plate, the backing plate of the electrode, and a

connector. The body of the probe uses PEEK material to protect the short circuit of the electrodes. The electrodes were separated by a PEEK washer. The RFA probe complete version as shown in Figure 3.44(b). The probe was connected with the handle, which uses stainless steel tube with a diameter of ¼ inch to convey the wires from the outside to the inside of the probe. Besides, the probe is threaded through an ultra-torr vacuum seal to install in the deposition chamber.

### 3.2.4 Analysis of data from the RFA probe

The data received from the RFA probe is I-V characteristics can use calculations and interpretation to find the ion energy distribution function, the kinetic energy of the ion, the ion density, etc. Which has the following process:

1. Smooth the I-V graph to reduce the noise of the measurement.
2. Find the 1<sup>st</sup> derivative of  $I_p$  compare  $V_p$ , it corresponds with the ion velocity distribution function as the equation:

$$f(v) = -\frac{M_i}{ye^2 A_p} \frac{dI_p}{dV_p} \quad (3.7)$$

Where  $M_i$  is the ion mass

$A_p$  is aperture area

$y$  is total transparency of grid electrodes

$e$  is electron charge

3. Plot graph between velocity ( $v$ ) in the horizontal axis and ion velocity distribution function or  $f(v)$  in the vertical axis.
4. The ion density ( $n_i$ ) calculated by

$$n_i = \int_0^\infty f(v)dv = -\frac{M_i}{ye^2 A_p} \int_0^\infty \frac{dI_p}{dV_p} \quad (3.8)$$

5. The average ion velocity  $\langle v \rangle$  by

$$\langle v \rangle = \frac{1}{n_i} \int_0^\infty v f(v)dv \quad (3.9)$$

6. The most population velocity ( $v_{most}$ ), can find from the x-intercept when

$$dI_p / dV_p = 0$$

7. root mean square velocity  $\langle v \rangle^2$ , the ion flux ( $\Gamma_i$ ), and kinetic energy ( $E_k$ ) calculated by

$$\langle v \rangle^2 = \frac{1}{n_i} \int_0^\infty v^2 f(v) dv \quad (3.10)$$

$$\Gamma_i = \langle v \rangle n_i \quad (3.11)$$

$$E_k = \frac{1}{2} M_i \langle v^2 \rangle \quad (3.12)$$

8. Calculate the kinetic energy of ion distribution function  $f(\varepsilon)$  by

$$f(\varepsilon) = \frac{1}{\sqrt{2M_i\varepsilon}} f(v) \quad (3.13)$$

Where  $\varepsilon$  is kinetic energy estimated by  $\varepsilon = eV_p$  for  $C^+$  only and the G1 grid is ground. On the other hand, if the G1 grid is floating,  $\varepsilon = eV_f - eV_p$  where  $V_f$  is floating potential.

9. Plot graph between kinetic energy ( $\varepsilon$ ) in the horizontal axis and kinetic energy of ion distribution function  $f(\varepsilon)$  in the vertical axis.
10. The average kinetic energy of the ion is calculated by

$$\langle \varepsilon \rangle = \frac{1}{n_i} \int_0^\infty \varepsilon f(\varepsilon) d\varepsilon \quad (3.14)$$

From the calculations and interpretation of I-V characteristics, the important plasma parameters were known. Which, these parameters correspond with the superhard coating process, structure, properties, and performance of the superhard coating films.

### 3.3 Sample preparation

The silicon wafer (n-type) and stainless steel (SUS304) will be used as the substrate. This topic will be presented in the sample preparation (cutting, polishing, and cleaning process).



### 3.3.1 Silicon wafer preparation

N-type silicon wafer resistivity 0.001-0.004  $\Omega\cdot\text{cm}$  (with a thickness of  $525\pm 15\ \mu\text{m}$ ) are cleaned by air dry, followed by a deionized water (DI) rinse, followed by acetone clean, followed by methanol clean and DI water and blow-dry. All processes will be made under basic INRF safety certification.

#### Materials needed

- Acetone
- Methanol
- DI water
- Pyrex bath containers
- Beaker 500 ml, 250 ml, and 100 ml
- ULTRASONIC cleaner model UC-5180L
- Safety equipment such as neoprene gloves, safety glasses, mask, and acid apron

#### Silicon cleaning process

1. Use air to blow the silicon sample to remove the microparticles on the surface. Followed by rinsing the DI water through the silicon surface for 10 rounds. And then, blowing hot air.
2. Place the silicon sample in pyrex containers. And then, pour the acetone (50 ml) into a pyrex container and place the pyrex container in the ultrasonic cleaner. Setup the aneling temperature does not exceed 55 degrees Celcius and ultrasonic cleaning time is about 10 minutes. Put on to start and wait for 10 minutes to complete the process. After the ultrasonic stop, dr the acetone out from the pyrex containers into the beaker.
3. pour the methanol (50 ml) into a pyrex container and place the pyrex container in the ultrasonic cleaner. Followed, state the ultrasonic cleaner and wait for 10 minutes. After the ultrasonic stop, pour the methanol out from the pyrex containers into the beaker. And then, pour the methanol (50 ml) into a pyrex container to clean the silicon sample with methanol again. When the complete process, drain the methanol from the pyrex container.

4. pour the DI water (50 ml) into a pyrex container and place the pyrex container in the ultrasonic cleaner. The silicon sample was cleaned in DI water for 3 rounds (10 minutes per round and change the DI water every round).
5. Blow dry with a hot air gun to remove the moisture and store in a desiccator.

### 3.3.2 Stainless steel preparation

Stainless steel grad 304 with the size of 17 mm  $\times$  17 mm and thickness of 5.0 mm are polished with sandpaper number 100 to 5000, then alumina grinding with the aluminum oxide powder with the size of 0.5  $\mu$ m and 0.05  $\mu$ m. The unpolished SUS304 and polished SUS304 as shown in Figure 3.45. The SUS304 sample is polished on all sides, which has a mirror-like shine. In addition, the edge of the sample is chamfered to prevent arcing on the sample during the film deposition.

After the polished process, the SUS4304 samples are cleaned by air dry, followed by a deionized water (DI) rinse, followed by methanol clean and DI water and blow-dry. All processes will be made under basic INRF safety certification.

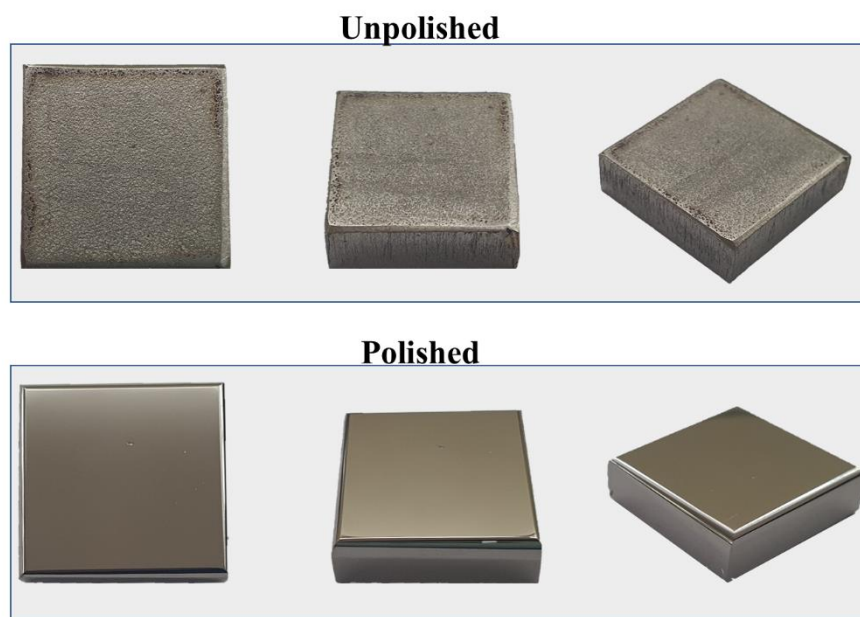


**Figure 3.45** Comparison of the unpolished and the polished SUS304.

#### Materials needed

- Methanol
- DI water
- Pyrex bath containers

- Beaker 500 ml, 250 ml, and 100 ml
- ULTRASONIC cleaner model UC-5180L
- Safety equipment such as neoprene gloves, safety glasses, mask, and acid apron

#### **SUS304 cleaning process**

1. Use air to blow the SUS304 sample to remove the microparticles on the surface. Followed by rinsing the DI water through the silicon surface for 10 rounds. And then, blowing hot air.
2. Place the SUS304 sample in pyrex containers. And then, pour the methanol (50 ml) into a pyrex container and place the pyrex container in the ultrasonic cleaner. Setup the aneling temperature does not exceed 55 degrees Celcius and ultrasonic cleaning time is about 10 minutes. Put on to start and wait for 10 minutes to complete the process. After the ultrasonic stop, pour the methanol out from the pyrex containers into the beaker. And then, pour the methanol (50 ml) into a pyrex container to clean the silicon sample with methanol again. When the complete process, drain the methanol from the pyrex container.
3. Pour the DI water (50 ml) into a pyrex container and place the pyrex container in the ultrasonic cleaner. The silicon sample was cleaned in DI water for 3 rounds (10 minutes per round and change the DI water every round).
4. Blow dry by a air to remove the moisture and stored in a desiccator.

## Chapter IV

### Result and discussion

The purpose of this work is to demonstrate that operation with an IPVD system with the four plasma sources (FCVA, Magnetron sputtering, L-ALIS, and ALIS) enables an energy-enhanced deposition process of superhard amorphous carbon thin films (hardness >40 GPa, very low surface roughness and thickness >1  $\mu\text{m}$ ). The morphologies, structural and mechanical properties of the films deposited on a Si substrate and SUS304 were systematically investigated and linking the film properties with the plasma properties measurement by using the RFA probe. Therefore, this chapter will give in the result of the plasma diagnostics by RFA probe, ta-C deposition, a-C:H deposition, Cr interlayer deposition and multilayer Cr/ta-C/a-C:H deposition including the result of morphologies, structural and mechanical properties characterization of the films.

#### 4.1 Plasma diagnostics

The properties of DLC films such as structural, mechanical, tribological, optical and electrochemical are related to  $\text{sp}^3$  content in the films. Which  $\text{sp}^3$  content can be controlled by the energy of depositing  $\text{C}^+$  ions for non-hydrogenated DLC and  $\text{C}_m\text{H}_n^+$  ions for hydrogenated DLC [20]. Mass spectrometry is popular for ion energy characterization due to it can measure mass-to-charge ratio of ions. However, with the big size, complex component and high price, the other probes such as Langmuir and RFA probes were studied and built for use in laboratories due to their small size and simple structure. Therefore, this topic focuses on ion energy measurement by RFA probe.

##### 4.1.1 RFA probe test

For ion energy measurement in the FCVA system, the RFA probe must be checked the contact between four electrodes (G1, G3, G4, and ion corrector) to ensure that the probe is in a ready-to-use state. The process of probe check as follows:

1. Use the ohmmeter to check the contact of G1, G3, G4, and ion corrector electrodes with the center pin of the BNC connector for each electrode (it must be non-contact).

2. Use the ohmmeter to check the contact ground shield of the BNC connector of G1, G3, G4, and ion corrector electrodes with the ground electrode of the FCVA system (it must be in contact).

3. Then, install the RFA probe in the deposition chamber of the IPVD system and recheck the contact of G1, G3, G4, and ion corrector electrodes.

4. Before the ion energy measurement, the plasma current on G1, G3, G4 and corrector will be measured using OSC as shown in Figure 4.1.

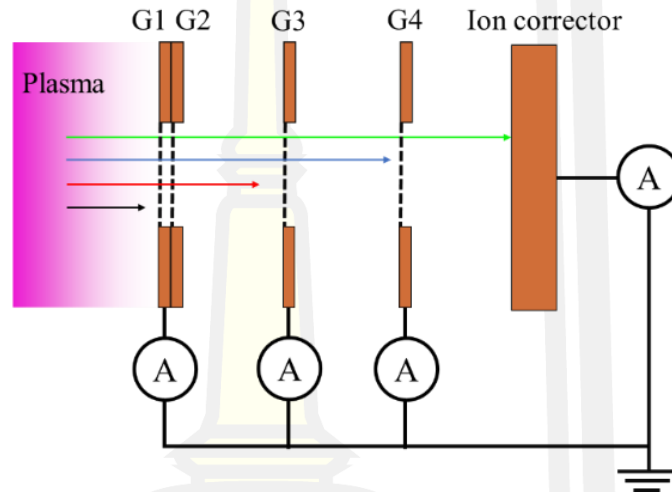


**Figure 4.1** Diagram of RFA probe checking.

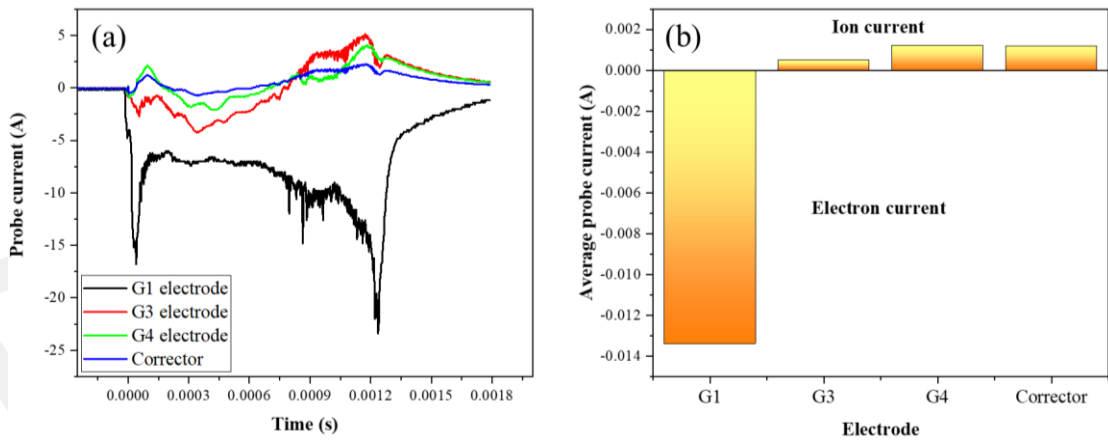


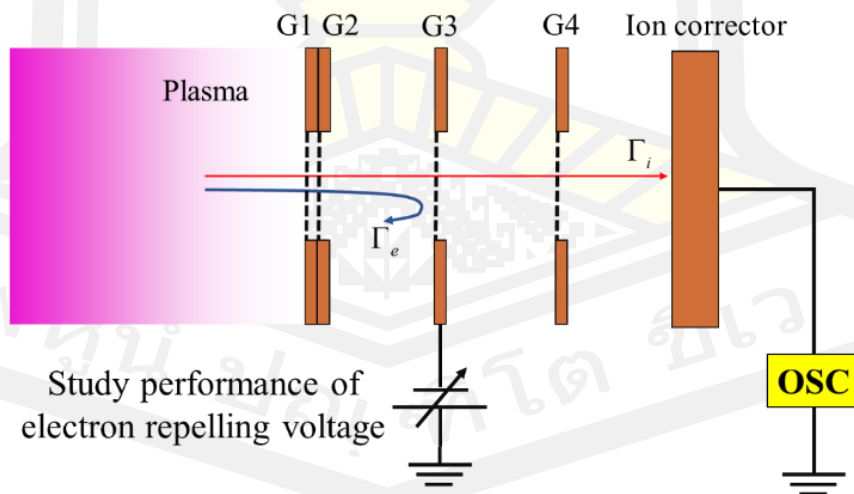
**Figure 4.2** Measured current on the G1, G3, G4, and ion corrector electrodes.

This process uses the arc current 720 A and a repetition rate of 1 pulse/s. The signal of the measured current on G1, G3, G4, and corrector electrodes as shown in Figure 4.2(a). The measured current has a different pulse signal, which average probe current as shown in Figure 4.2(b). It was found that the average probe current at G1

electrode is electron current. The electron current decrease at G3, G4 and corrector, which the ions will be introduced due to the number of particles was reduced by the grid 200 line/inch and grid 2000 line/inch on G1 and G2 electrodes, grid 600 line/inch, in which use for G3 and G4. Moreover, the electron current decreased due to it was absorbed by the front electrode of the measuring electrode. From this process, the RFA probe is ready for the ion measurement process.

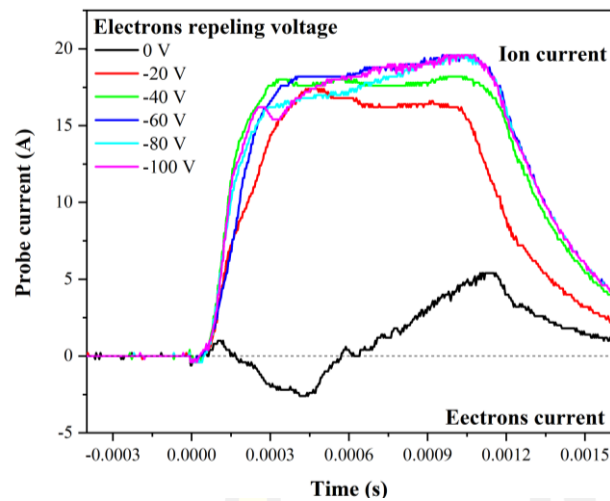
5. Check the performance of electron repelling in the G3 electrode by using a diagram as shown in Figure 4.3. The G1 electrode is grounded, and the ion corrector electrode was connected to OSC for current measurement (probe current). On the other hand, the G3 electrode was connected to the DC negative power supply (HSPY-400-01) for repelling the electrons out from the probe due to only an ion current being required.

Figure 4.4 shows the probe current as a function of applied electron repelling voltage. It was found that for low electron repelling voltage of 0 V to -10 V can't repel the electrons due to the measured current present electron current. On the other hand, for applied electron repelling voltage of -20 V to -100 V, the probe current is an ion current. Therefore, for ion energy measurement the G3 electrode should have been applied a negative voltage higher than -60 V to ensure repelling electrons and allow only the ions to enter the ion corrector electrode.



**Figure 4.3** Diagram of electron repelling performance.





**Figure 4.4** Measured current on the ion corrector electrode as a function of electron repelling voltage.

#### 6. The complete process for RFA probe check

##### 4.1.2 Ion energy measurement

The process parameter for DLC deposition is a very important parameter, such as the ion flux and ion energy of carbon ions during the film growth. In order to study the influence of the ion energy on morphologies, structural, and mechanical properties of the ta-C films deposited using FCVA deposition. This topic will give in detail of ion energy measurement in FCVA deposition combined with plasma biasing technique and substrate biasing.

##### 4.1.2.1 Plasma biasing technique

The plasma biasing technique is one of increasing the energy of depositing ions in the FCVA technique to improve the properties of the film. Andre and Oks (2007) studied the influence of biased plasma potential in the range of 0 V to +30 V on the charge-state-resolved ion energy distribution functions in pulsed vacuum arcs plasma using an electrostatic energy analyzer and a quadrupole mass spectrometer. They found that the ion energy distributions of  $\text{Mg}^+$  and  $\text{Mg}^{2+}$  were broader and shifted to higher energy at the beginning of each arc pulse, indicating that the mean energy of the depositing ions increases [151]. Moreover, Andre et al. used the plasma biasing technique (pulsing bias) to control the growth conditions of ta-C films deposited with pulsed filter cathodic vacuum arcs (PFCVA). They found that plasma

biasing can contribute to the production of ta-C films with a high density of  $3.36 \text{ g/cm}^3$  and  $\text{sp}^3/(\text{sp}^3+\text{sp}^2)$  of  $0.69\pm0.02$  [152]. However, the influence of plasma biasing on the ion distribution function of  $\text{C}^+$  ions, including the structural and mechanical properties of ta-C films prepared with a pulsed filter cathodic vacuum arc, has not been studied. Therefore, this topic presents the setup, measurement, analysis, and discussion of the influence of plasma biasing on the energy of  $\text{C}^+$  ions produced using an IPVD system.

Figure 4.5 shows the schematic diagram of an ion energy measurement in the part of the plasma biasing technique. The RFA probe was connected with the SMU (Keithley 2450) and placed at 15 cm from the focusing coil. The G1 electrode can switch between floating surface or ground surface. The G3 electrode was applied with -80 VDC to repelling the electrons. The G4 electrode contract with the guard of SMU to reduce the secondary electron emission from the ion corrector. And the ion corrector was connected to the SMU to detect the ion current. While the digital delay generator (STANFORD RESEARCH SYSTEM Model DG645) receives a trigger signal from PFN to generate the trigger signal to SMU for determining the aperture time for ion current detection. The ion energy in this part is divided into two parts; (i) measurement of the ion energy of  $\text{C}^+$  ions on the grounded sample, and (ii) measurement of the ion energy of  $\text{C}^+$  ions on the floating sample due to many literature reviews found that the ta-C films deposited on the floating sample have a high density [153].

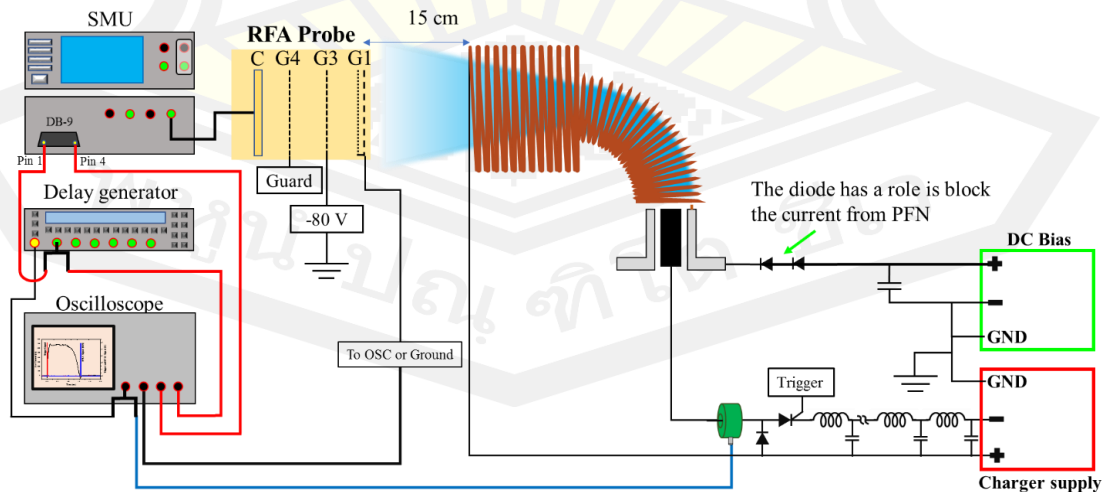


**Figure 4.5** Diagram of ion energy measurement for plasma biasing technique

### Ground surface

In most ta-C film deposition by the FCVA technique, the substrate is grounded due to the FCVA deposition has a high ionization ratio of carbon atoms (90%) and the mean energy of ions has a value in the range of 10 to 40 eV [36], [71]. Which improves the properties of ta-C films to high density and low surface roughness because of intense and energetic bombardment by  $C^+$  ions.

The advantage of the ground surface is support the transition of the charge particle for example electrons, positive ions, and negative ions including molecular ions. It reduces the population of arc process on the films during the film growth. It means that the error of the sample is reduced.

This topic will present the enhanced energy of  $C^+$  ions in FCVA deposition by using the plasma biasing technique, in which the energy of  $C^+$  ions as a function of anode bias potential. The plasma generated parameter, probe setup and SMU setup as shown in Table 4.1.

**Table 4.1** Setup parameter of ion energy measurement for ground surface.

Plasma generated parameter	Value
Operate pressure	Vacuum arc: $2 \times 10^{-6}$ torr
Arc current maximum	720 A
Arc frequency	1 Hz
Pulsed width	1200 $\mu$ s
<b>Probe setup</b>	
Probe distance	15 cm
Probe position	Same center with the focusing coil
G1 grid	Ground
<b>SMU setup</b>	
Scanning voltage range	-20 to +190 V (400 points)
Current range for scan	1 mA
NPLC of SMU	0.05 (Aperture time is 1250 $\mu$ s)

The ion current was detected at the same time with arc plasma operated, the aperture time for ion current detecting of 1250  $\mu$ s, which covers the on-time of plasma

(pulse width 1200  $\mu\text{s}$ ) as shown in Figure 4.6. Therefore, the measured ion current is the average ion current in one are pulsed.

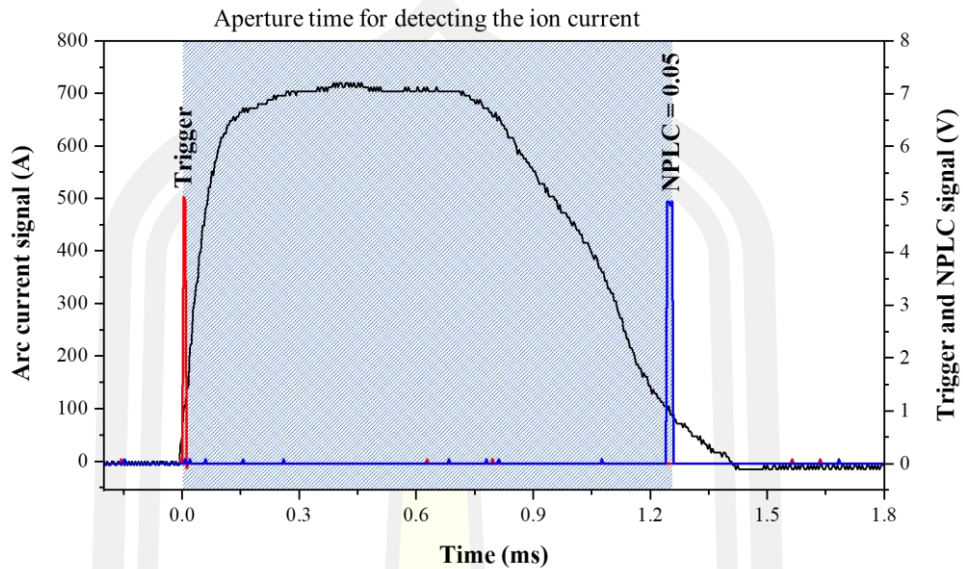


**Figure 4.6** Trigger and notify signal for ion energy measurement.

The data of the arc process is an important parameter, which correlates with the plasma properties. Therefore, the data of the arc process was measured. Figure 4.7 (a) shows the arc current signal measured using a PEARSON CURRENT MONITOR Model 101. The maximum current of about 720 A and the pulse duration of 1450  $\mu\text{s}$ , which is higher than the calculated pulse duration for PFN (1200  $\mu\text{s}$ ). Moreover, to control the maximum arc current at about 720 A, an increase of anode bias potential requires a decrease of charger voltage for PFN from -504 V to -384 V. Figure 4.7(b) shows the arc voltage signal measured using an Agilent model 10076B at the output cathode electrode compared to the ground electrode of the PFN. It can be seen that the arc voltage signals shift up to high positive voltage, but the amplitude is dose not different.

Figure 4.7(c) shows the signal of the anode bias current measured using a PEARSON CURRENT MONITOR Model 101. The amplitude and shape of the signals are significantly different when the anode bias potential increases from 0 V to +70 V, For the anode bias potential higher than +70V, the signals are slightly different. Figure 4.7(d) shows the signals of the anode bias potential as a function of time that were measured using a voltage probe (Agilent Model 10076B). The anode

bias potential signal shows the setpoint or constant value before the FCVA source is discharged ( $t < 0 \mu\text{s}$ ). After FCVA is discharged, the anode bias potential linearly decreases as a function of time with the increase of anode bias potential higher than +20 V. This behavior is due to during the generated plasma, the resistance of the load (plasma) increased, therefore, the bias power supply cannot support full energy to the anode electrode resulting in the anode bias potential being reduced.

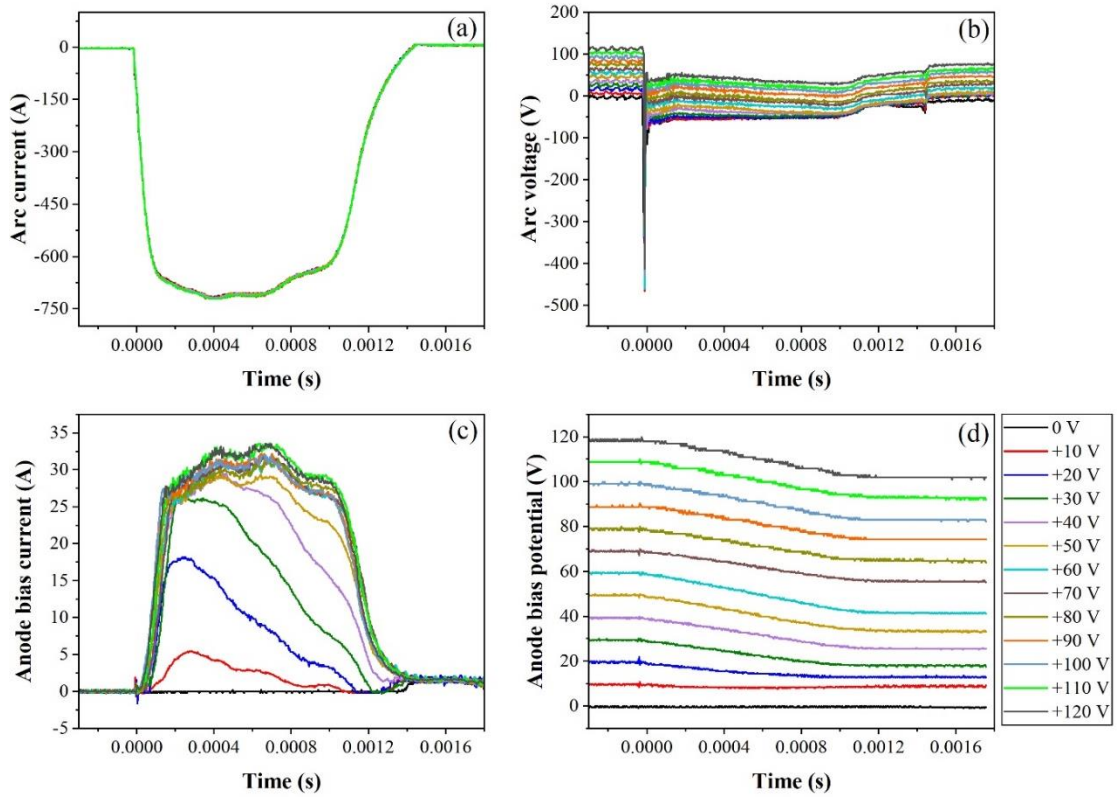
The raw data of the ion energy measurement are present in the I-V characteristic as shown in Figure 4.8(a). The ion saturation current has a value ranging from 12  $\mu\text{A}$  to 40  $\mu\text{A}$  depending on the anode bias potential, and the position of the transition curve of the I-V characteristic shift to a high positive scanning voltage, indicating different plasma properties [154], [155]. In addition, the electron current does not appear, indicating that the RFA probe can effectively reduce the primary electrons from the plasma and secondary electrons in the probe structure. This is an important condition that indicates the accuracy of the probe [156]–[158]. As a result, the measured probe current is only the ion current.

To identify the properties of the ions in plasma (density and mean energy), the I-V characteristics were calculated and transferred to the ion distribution function and the kinetic energy distribution function using as shown in Figure 4.8(b). The characteristic of the kinetic energy distribution function is the Maxwell–Boltzmann distribution, the peak position shifts to higher kinetic energy (shift to the right), and the area under the peak decrease with the increase of anode bias potential. This means that the kinetic energy of the  $\text{C}^+$  ions increases with the increasing the anode bias potential.

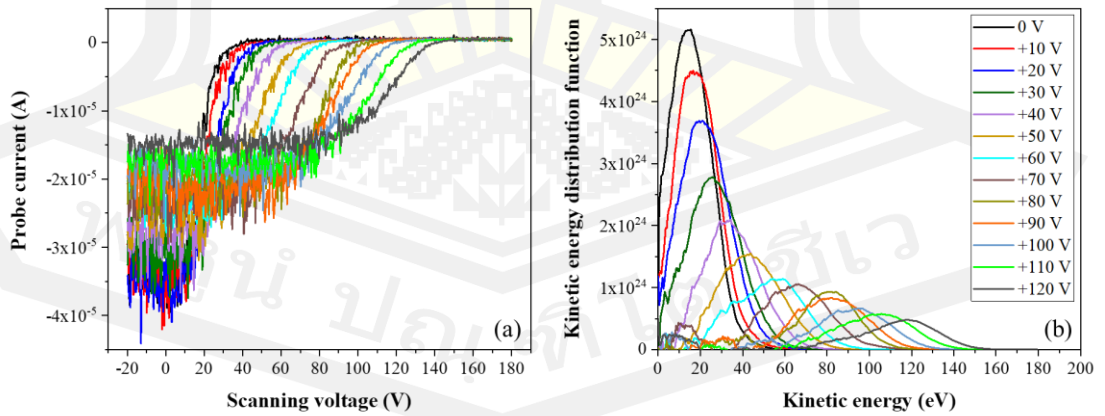
The ion density ( $n_i$ ) was estimated from the area of the velocity distribution function or  $f(v)$ . Figure 4.9(a) shows the ion density as a function of anode bias potential, it was found that the ion density significantly decreases from  $5.12 \times 10^{16} \text{ m}^{-3}$  to  $8.13 \times 10^{15} \text{ m}^{-3}$  with the increase of the anode bias potential from 0 V and +120 V. This can be explained by the electron absorption of the anode electrode. Normally, the ion density in the plasma is equal to the electron density ( $n_i \approx n_e$ ) [159], [160]. Therefore, applying a positive potential to an anode electrode of the FCVA source (including a filtering coil and a focusing coil), the electrons are absorbed by the anode



electrode. As a result, the electron density in the plasma decreases, which means that the ion density also decreases.

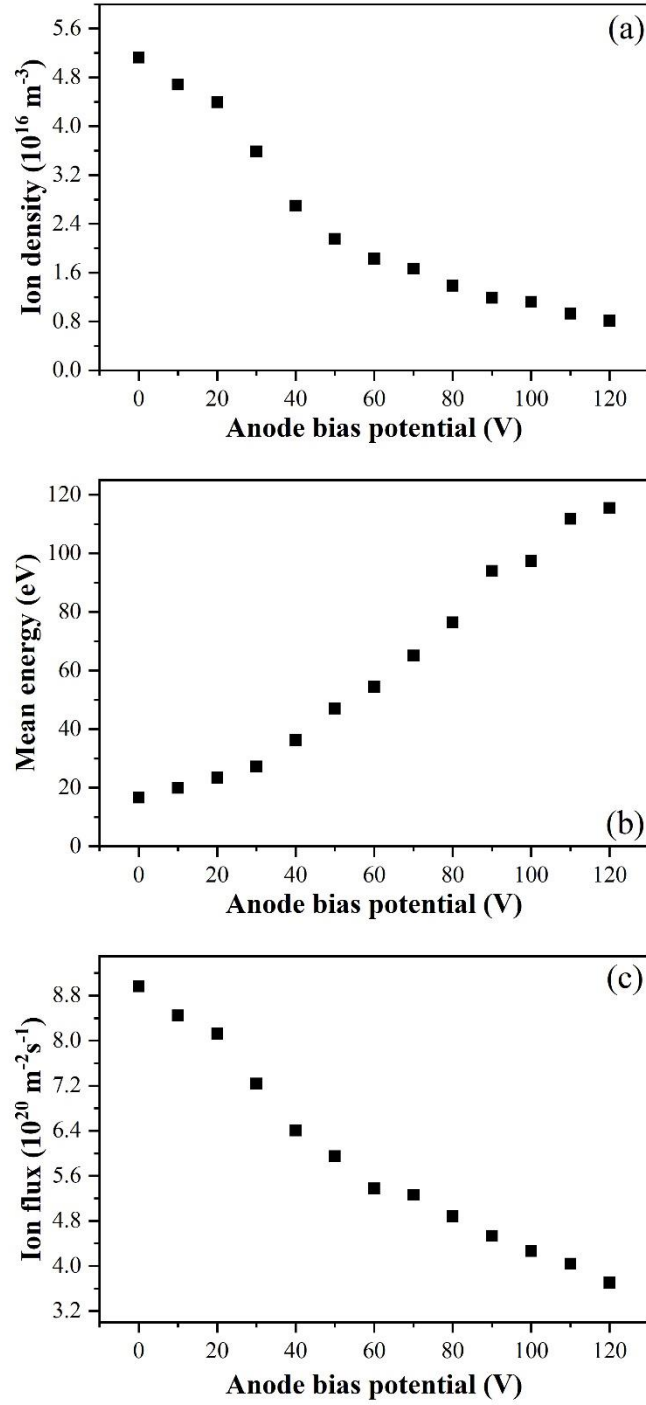


**Figure 4.7** (a) Arc current signal, (b) arc voltage signal, (c) anode bias current signal, and (d) anode bias potential as a function of anode bias potential.



**Figure 4.8** (a) the average I-V characteristic measured by the RFA probe, and (b) kinetic energy distribution function as a function of an anode bias potential.





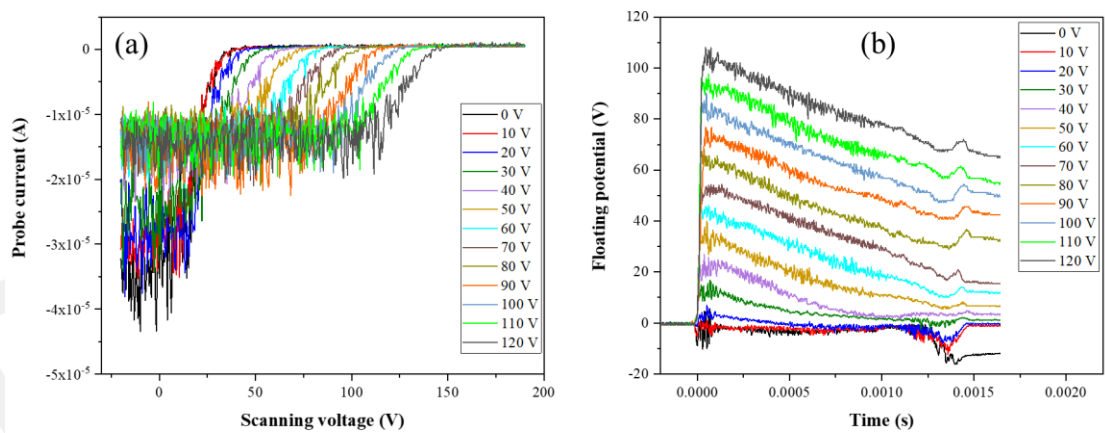
**Figure 4.9** (a) density, (b) mean energy, and (c) flux of the C<sup>+</sup> ions measured using an RFA probe.

Figure 4.9(b) shows the mean energy ( $E_i$ ) of the C<sup>+</sup> ions. The mean energy of C<sup>+</sup> ions increased from 16 to 115 eV with the increasing of anode bias potential from

0 to +120 V. This result can be explained by an increase of the plasma potential when the positive potential was applied to the anode electrode of FCVA source [151]. The mean energy of the  $C^+$  ions coming to the substrate is a summation of the plasma potential ( $V_p$ ) and the floating potential ( $V_f$ ) as the equation  $E_i = e(V_p - V_f)$ , where the substrate is grounded (the floating potential is zero), therefore the mean energy only depends on the plasma potential ( $E_i = eV_p$ ). Therefore, the mean energy of the ion increased with the increasing of applied anode bias potential. Moreover, the flux of  $C^+$  ions during the film growth decreased with the increase of the anode bias potential, as shown in Figure 4.9(c), because the ion flux is directly related to the ion density. In the plasma diagnostics with an RFA probe, it was found that the plasma biasing technique had a significant effect on the ion density, ion energy, and ion flux.

### Floating surface

For the ion energy measurement on the floating surface, the G1 electrode of the RFA probe will be connected using the OCS to detect and monitoring the floating potential signal. To compare the plasma parameter such as ion density and ion energy with the ground surface case, the arc condition is the same as the previous topic.



**Figure 4.10** (a) I-V characteristic and (b) floating potential signal as a function of anode bias potential (the G1 of a RFA probe is floated).

The probe current and floating potential signal as shown in Figure 4.10. The probe current showed that the ion current saturation has the same value as the ground surface case (10 to 40  $\mu$ A), which means that the floating sample is not affected on

the bulk-plasma properties. However, the floating potential signal (see in Figure 4.10(b)) shift to a high positive potential with the increasing of anode bias potential. Indicate that the properties of depositing  $C^+$  ions are different with the increase of anode bias potential.

Figure 4.11 shows the kinetic energy distribution function as a function of anode bias potential. It can be seen that the peak position of distribution shifts up from 20 to 40 eV, which is lower than the ground surface case. Indicate that the kinetic energy of depositing ions income the floating surface lower than the the ground surface.

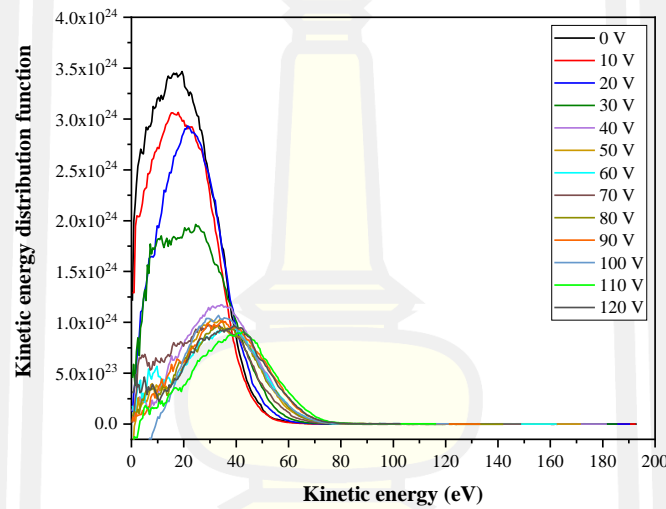


**Figure 4.11** Kinetic energy distribution function as a function of an anode bias potential for G1 electrode as floated.

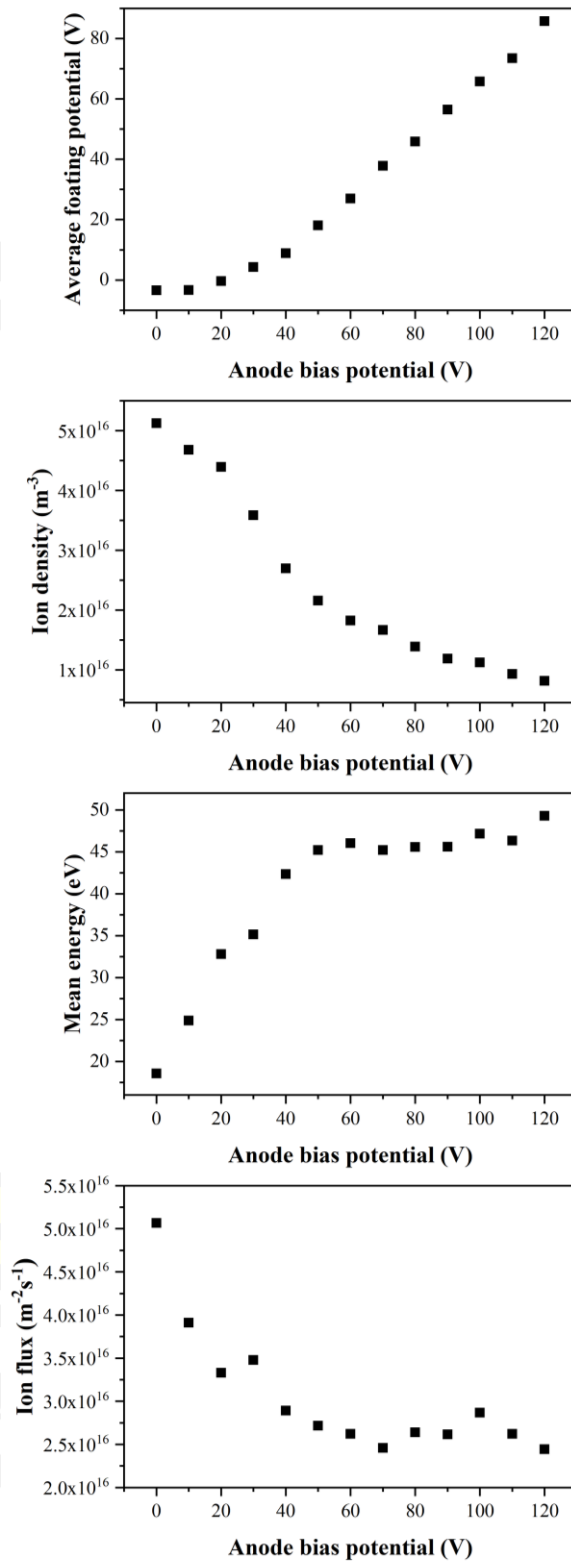
The ion density ( $n_i$ ) was estimated from the area of the velocity distribution function or  $f(v)$ . Figure 4.12(b) shows the ion density as a function of anode bias potential, it significantly decreases from  $5.06 \times 10^{16} \text{ m}^{-3}$  to  $2.4 \times 10^{16} \text{ m}^{-3}$  with the increase of the anode bias potential from 0 V and +120 V. This result can be explained as the same reason with the ground surface case.

Figure 4.12(c) shows the mean energy of the  $C^+$  ions depositing on the floating surface. The mean energy of  $C^+$  ions have two transition zone; (i) for anode bias potential 0 to +50 V, the mean energy increases from 18 to 45 eV with the increase of anode bias potential from 0 V and +50 V and (ii) for the anode bias potential of +60

to +120 V, the mean energy have value in the range of 45 eV to 49 eV. This result can be explained by an increase of the floating potential at the substrate [152], [153]. The mean energy coming to the substrate is a summation of the plasma potential ( $V_p$ ) and the floating potential ( $V_f$ ) as  $E_i = e(V_p - V_f)$ , the average floating potential floating are positive values as shown in Figure 4.12(a). Therefore, even if the initial energy is high, but the sum  $V_p - V_f$  is not different, this indicates that the mean energy of the  $C^+$  on the floating surface is not increase. Moreover, as the same ground surface case, the flux of  $C^+$  ions depositing on the floating surface decreased with the increase of the anode bias potential as shown in Figure 4.12 (d), because the ion flux is directly related to the ion density.

The result of ion energy measurement in FCVA deposition combined with plasma biasing technique for ground and floating surface can be discussed in Figure 4.13. For the ground surface case, the ion energy only dependent on the plasma potential (the second term is zero), in which A. Anders and E. Oks using a hot probe measure the plasma potential, and they were found that the plasma potential increased with the increase of anode bias potential [151]. Which the plasma potential will be introduce the increase of initial energy. Therefore, the mean energy of  $C^+$  ions will be increased with the increase of anode bias potential.

While the floating surface the ion energy of  $C^+$  ions in the plasma sheath as  $E_i = e(V_p - V_f)$ . The plasma potential as the same value of ground surface case (considering from 2<sup>nd</sup> derivative of the I-V characteristic of both experiment). But, the second term of an equation is the floating potential, in which the floating potential is the positive potential value and continues to increase with the increase of anode bias potential. However, although the anode bias or plasma bias technique can increase the initial ion energy (increase plasma potential), but the sum value of  $V_p - V_f$  is slightly different. Therefore, the mean energy of the  $C^+$  ions on the floating surface will be lower than ion energy on the ground surface, as see in Figure 4.13.



**Figure 4.12** (a) average floating potential, (b) ion density, (c) mean energy and (d) flux of the  $\text{C}^+$  ions measured using RFA probe (G1 as floated).

From the result it can conclusion that the plasma biasing technique can enhance the ion energy of depositing ions, but ion density and ion flux decrease with the increase of anode bias potential. Which may be affected on properties of the ta-C films

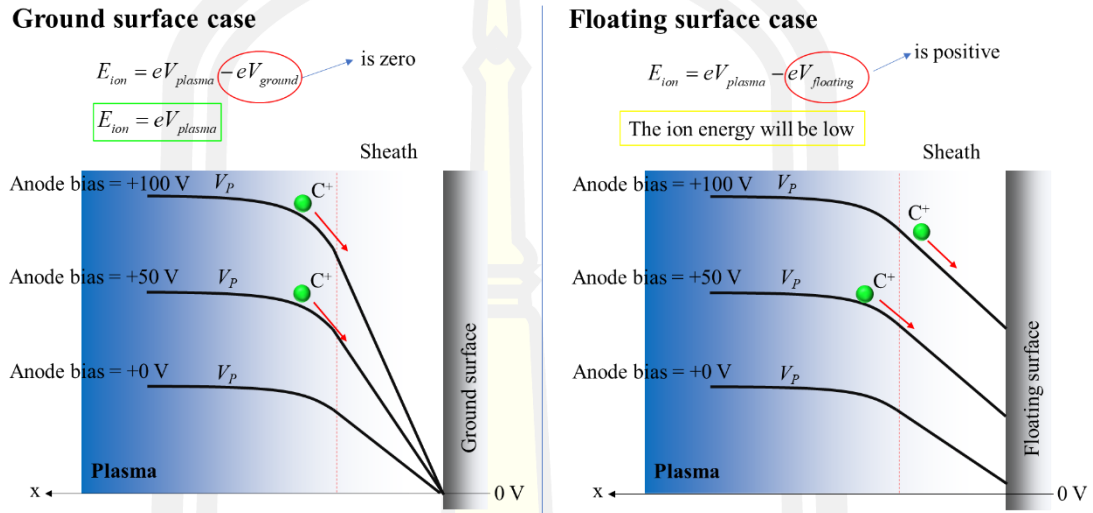


**Figure 4.13** Comparison of the potential profile of the ground and floating surface.

#### 4.1.2.2 Time-resolved ion energy measurement

To study the parameter and behavior of  $C^+$  ions during the plasma operation, the time-resolved technique will be used. In this technique, the delay generator has a role in delaying the trigger time from 0 to more seconds. The NPLC was set of 0.01 correlated to an aperture time of 250  $\mu s$ . The probe setup is the same previous topic, the G1 electrode is grounded. The arc current of about 720 A and repetition rate of about 1 pulse/s. The anode bias potential of 0 V, +30 V, +60 V, +90 V, and +120 V, was applied to an anode electrode of the FCVA source. In the measurement process, the trigger signal was shifted up in step of 100  $\mu s$  to detect the ion current at this time of the arcing process, which covered 0 to 1200  $\mu s$  as shown in Figure 4.14. The raw data of each time and condition were calculated to kinetic distribution function and plotted in a contour graph.



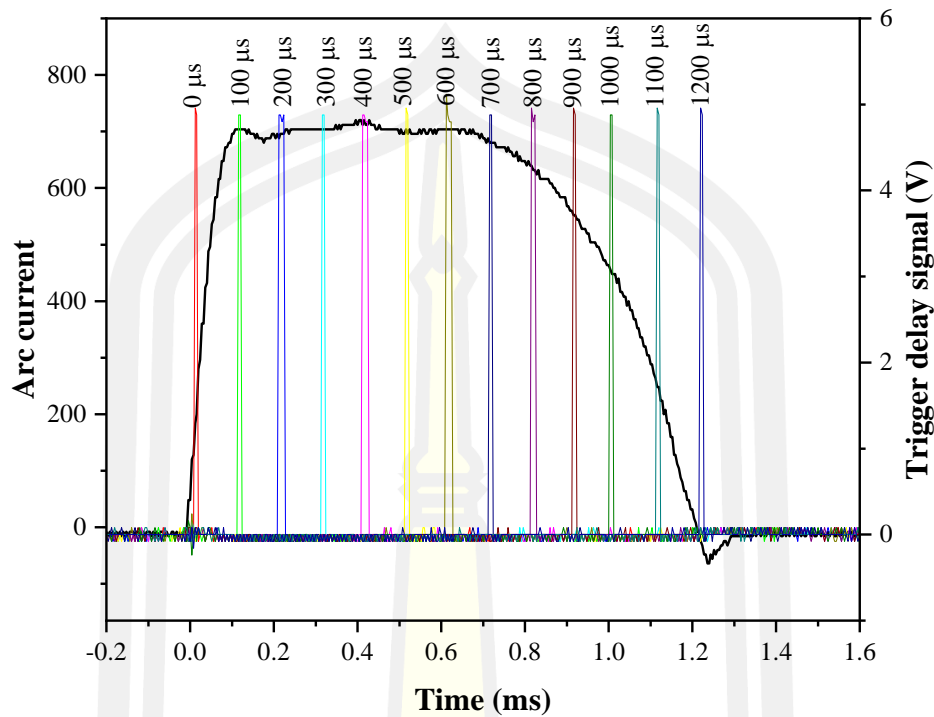


**Figure 4.14** Delay signal for time-resolved ion energy measurement.

The result of the time-resolved ion energy measurement was presented in the contour graph as shown in Figure 4.15, the x-axis is the time, the y-axis is ion energy, and the ribbon bar is the relative ion density. It was found that the population of  $C^+$  ions has ion energy and density different along plasma operating time, which can be observed from the green clusters with different characteristics, positions, and areas. From the analysis, the most population of  $C^+$  ions have mean energy of about 15 eV, 25 eV, 70 eV, 95 eV and 120 eV for applied anode bias potential of +0 V, +30 V, +60 V, +90 V and +120 V respectively. While the maximum ion density shift down to lower plasma operating time, which has maximum density at about 600 to 800  $\mu s$ , and then shift down to 200  $\mu s$  for increasing anode bias potential from 0 V and +120 V respectively. In addition, the observations, the mean energy of the  $C^+$  ions population like a characteristic of the anode bias potential signal (see Figure 4.7(d)). From the time-resolved ion energy measurement technique, it was found that the energy and density on the  $C^+$  ions change with time. This allows us to understand the behavior of depositing ions on the substrate in microseconds.

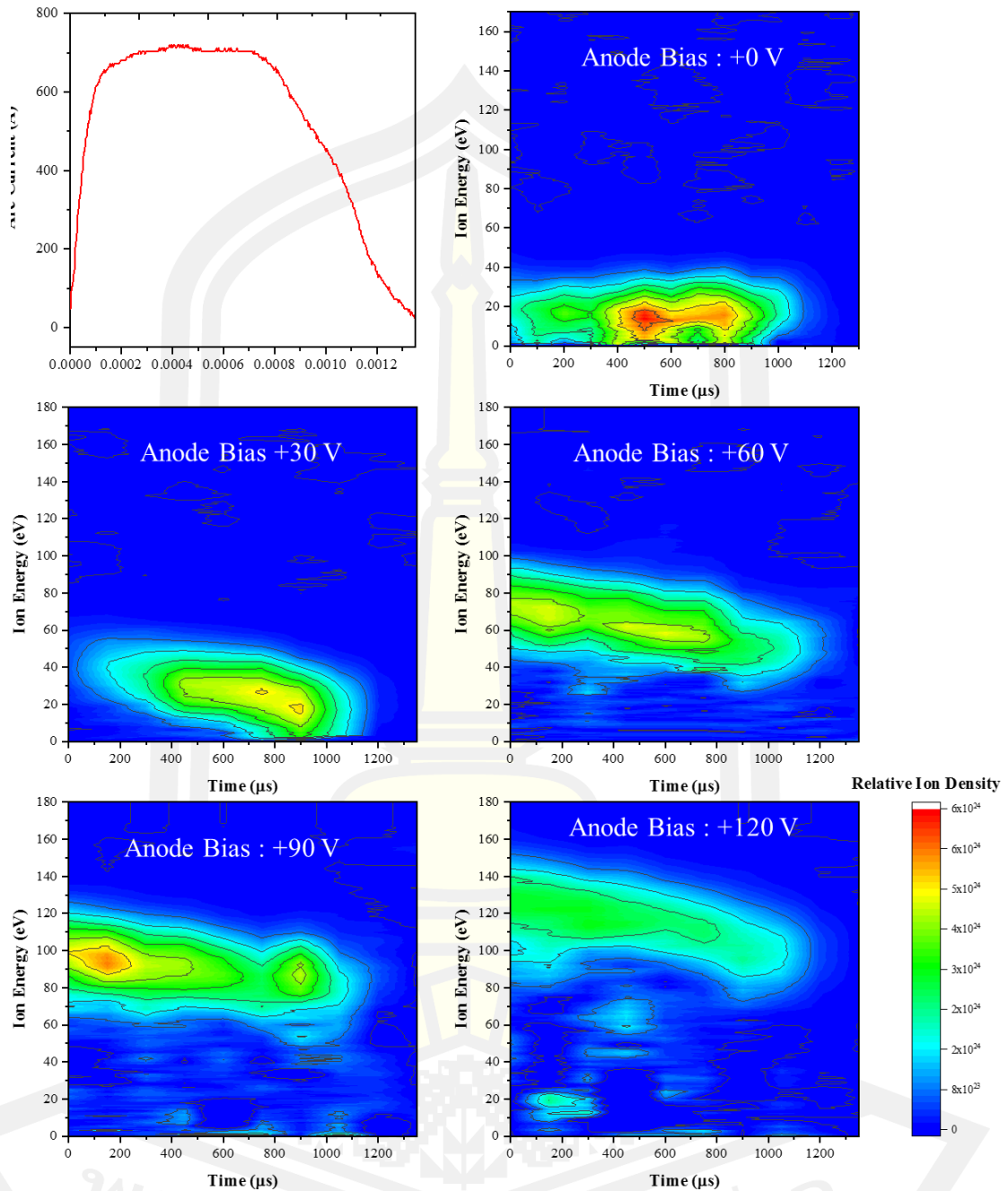


**Figure 4.15** Time-resolved ion energy contour graph as a function of anode bias voltage.

#### 4.1.2.3 Substrate biasing technique

The substrate bias technique is a popular method for improving the properties of films, especially DLC films due to its simple and high performance [17], [161], [162]. Moreover, the ta-C films deposited using FCVA deposition combined with the

substrate bias technique have a high quality such as high density, high hardness, good mechanical properties, and very low surface roughness [163], [164]. Due to the substrate bias technique enhanced the energy of the  $C^+$  ions and subplantation occurs [20], [36]. Therefore, to prove that the substrate bias technique can increase the energy of the deposition ions. This topic will give in detail about ion energy measurement in FCVA deposition combined with the substrate bias technique.

Figure 4.16 shows the schematic diagram of an ion energy measurement in the part of the substrate bias technique. The RFA probe was connected to the SMU (Keithley 2450) and placed at 15 cm from the focusing coil. The G1 electrode is connected to DC negative power supply (HSPY-400-01). The G3 electrode was applied with -80 VDC to repel the electrons. The G4 electrode contract with the guard of the SMU to reduce the secondary electron emission from the ion corrector. And the ion corrector was connected to the SMU to detect the ion current. While the digital delay generator (STANFORD RESEARCH SYSTEM Model DG645) receives a trigger signal from PFN to generate the trigger signal to SMU for determining the aperture time for ion current detection. The ion energy measurement parameter as shown in Table 4.2.

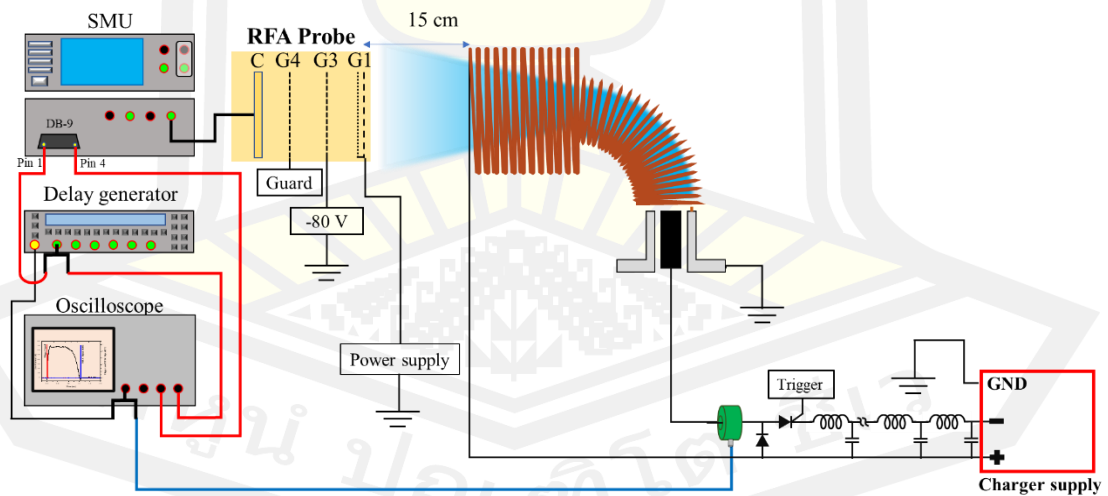


**Figure 4.16** Diagram of ion energy measurement for substrate bias technique.

The I-V characteristic as a function of substrate bias potential as shown in Figure 4.17(a). It can be seen that the ion saturation current has a value in the range of 16 to 40  $\mu A$  depending on the substrate bias potential, and the position of the

transition curve of the I-V characteristic shift up to a high positive scanning voltage, indicating different plasma properties [154], [155]. The electron current in the I-V curve can be not observed, indicating that the applied bias potential on the G1 electrode does not affect on the ion energy measurement performance of the RFA probe.

**Table 4.2** Setup parameter of ion energy measurement for substrate bias technique.

Plasma generated parameter	Value
Operate pressure	Vacuum arc: $2 \times 10^{-6}$ torr
Arc current maximum	720 A
Arc frequency	1 Hz
Pulsed width	1200 $\mu$ s
<b>Probe setup</b>	
Probe distance	15 cm
Probe position	Same center with the focusing coil
<b>SMU setup</b>	
Scanning voltage range	-20 to +190 V (400 points)
Current range for scan	1 mA
NPLC of SMU	0.05 (Aperture time is 1250 $\mu$ s)
<b>Investigated parameter</b>	<b>Substrate bias potential</b>

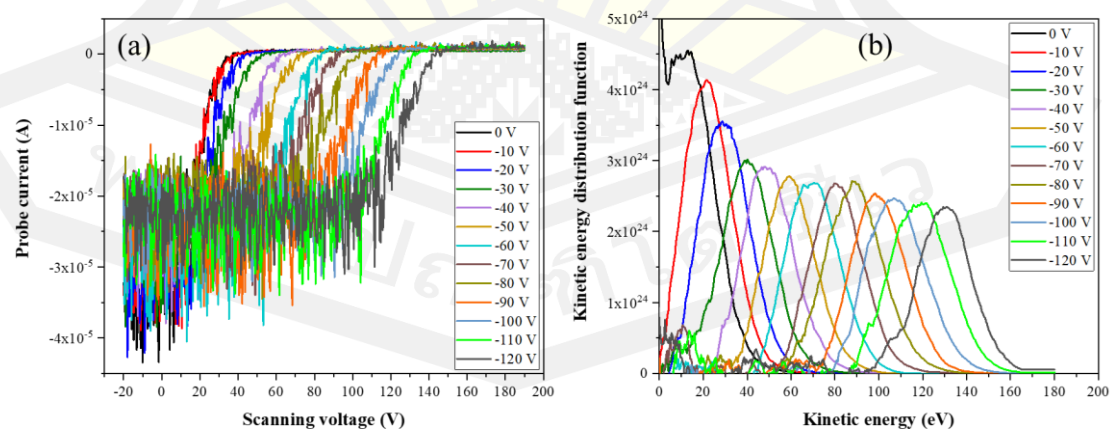


**Figure 4.17** (a) I-V characteristic measurement by RFA probe and (b) kinetic energy distribution function as a function of an anode bias potential.

The kinetic energy distribution function as shown in Figure 4.17(b). The characteristic of the kinetic energy distribution function is the Boltzmann distribution, the peak position starts at about 13.5 eV and the peak position shift up to higher kinetic energy, which means that the kinetic energy of the  $C^+$  ions increases with the increase of the anode bias potential. But the area of the peak of the distribution peak slightly decrease when compared with the kinetic distribution function for the part of plasma bias potential. Indicate that the influence of the substrate bias technique affected on the ion density lower than the plasma biasing technique.

This observation is consistent with the calculated ion densities, which are shown in Figure 4.18(a). The ion density smaller decreases from  $5.6 \times 10^{16} \text{ m}^{-3}$  to  $3.06 \times 10^{16} \text{ m}^{-3}$  with the increase of the substrate bias potential from 0 V and -120 V. Figure 4.18(b) shows the mean energy of the  $C^+$  ions. The mean energy increased from 15 eV to 128 eV with the increase of substrate bias potential from 0 V and -120 V. In the substrate bias technique case, the bulk plasma properties as the same in each substrate bias potential. But the mean energy of the  $C^+$  ions coming to the substrate is a summation of the plasma potential ( $V_p$ ) and the substrate bias potential ( $V_s$ ) as  $E_i = e(V_p - V_s)$ , where the substrate was biased with the negative potential, the mean energy as  $E_i = e(V_p + V_s)$ , Therefore, the mean energy of the ion increased with the increase of substrate bias potential.

Although the ion density will be decreased with the increase of substrate bias potential. But the flux ion tends to slightly increase from  $9.96 \times 10^{20} \text{ m}^{-2}\text{s}^{-1}$  to  $1.36 \times 10^{21} \text{ m}^{-2}\text{s}^{-1}$  with the increase of the substrate bias potential as shown in Figure 4.18(c), because the ion flux as the cross of the density and velocity of the ions, which the ion density in substrate bias case higher than the plasma biasing case, leads to the higher ion flux toward the RFA probe.

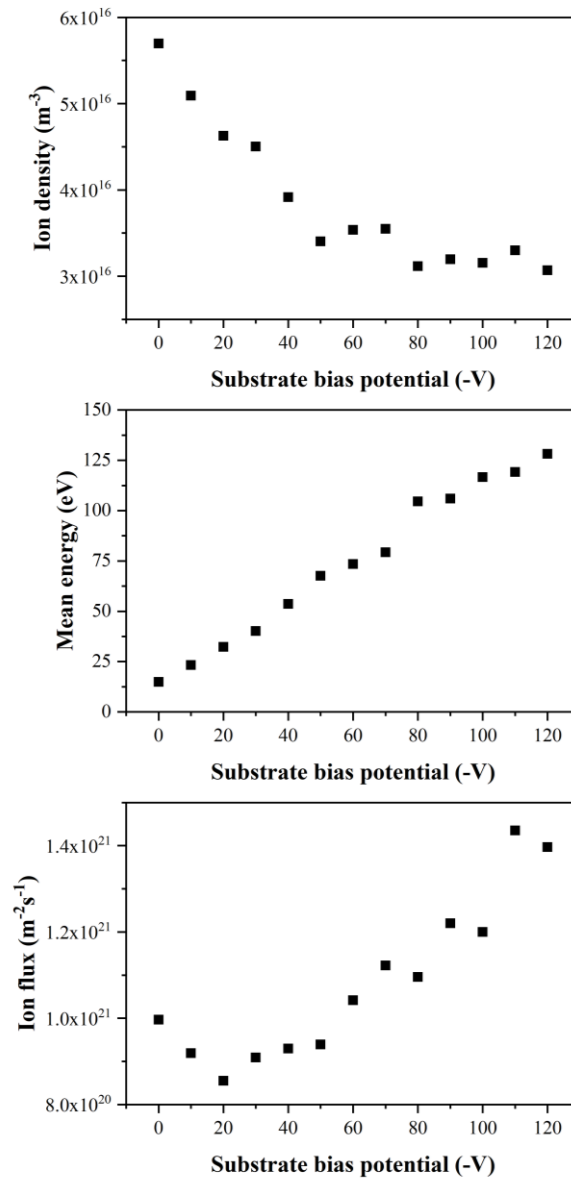


**Figure 4.18** (a) density, (b) mean energy, and (c) flux of the  $\text{C}^+$  ions as a function of substrate bias potential.

#### 4.1.2.4 Deposition profile

In the ion energy measurement section, it was revealed that the plasma biasing and substrate biasing techniques effected on the density, mean energy, and flux of the  $\text{C}^+$  ions. This parameter is directly related to the deposition parameter for example deposition rate and deposition profile. In order to support and confirm the data of ion



energy measurement, the deposition profile of ta-C films will be studied. The influence of plasma biasing and substrate bias techniques are compared.

The ta-C films were deposited on SUS316 substrate with a diameter of 175 mm, the substrate installed at x, y, and z positions is 15 cm, 0 cm, and 0 cm respectively. In the pre-deposition, to improve the adhesion of the film/substrate, the substrate was cleaned by Ar<sup>+</sup> using L-ALIS with the discharge potential and discharge current of +1.4 kV and 8.8 mA. Then the ta-C films were deposited using FCVA deposition, the plasma was generated by applied charger voltage of -504 V to PFN, which related to arc current maximum of about 720 A. Other parameters as shown in Table 4.3.

**Table 4.3** Process parameter for ta-C deposition on the SUS316 to study deposition profile.

Plasma generated parameter	Value
Operate pressure	Vacuum arc: $2 \times 10^{-6}$ torr
Arc current maximum	720 A
Arc frequency	1 Hz
Pulsed width	1200 $\mu$ s
Deposition time	2400 pulses
Substrate	Non-rotate
<b>Investigated parameter</b>	<ul style="list-style-type: none"> <li>• Anode bias potential</li> <li>• Substrate bias potential</li> </ul>

The deposition profile of ta-C films deposited on the SUS316 plate by varying the anode bias potential as shown in Figure 4.19. The ta-C films have the color of blue and brown edges. It can be seen that the anode bias potential has more effect on the deposition rate and position profile, in which the deposition rate has a high ratio for the increase of anode bias potential from 0 to +60 V, while the anode bias potential is higher than +60 V, the color, center and the profiles are very similar. But the substrate bias potential slightly effect on the deposition rate and deposition profile of the ta-C films as shown in Figure 4.20. The color and the center of the film slightly changes. While the angle of the film zone is warped when the increase of substrate bias potential. This result corresponds to the ion energy measurement section. It confirms

that the ion density will be decreased with the increase of anode bias potential leading to a low deposition rate of the films. So it takes a very long time for the synthesis of the ta-C film with a thickness of 200 nm.

However, the deposition rate of the films is still high for the substrate bias technique, its corresponding with the ion energy measurement section. Which the ion density slightly decreases with the increase of substrate bias potential. The decrease of ion density causing by a change of the center of the plasma beam. The RFA probe has a small aperture area, which a diameter of 2 mm, so a slightly change of the center of the plasma beam leads to a very different measurement result.

The plasma diagnostics by the RFA probe found that the plasma properties depend on the process parameter. The plasma biasing and substrate bias technique can enhance the energy of  $C^+$  ions in FCVA deposition. Therefore, the influence of plasma biasing and substrate biasing on the morphologies, structural properties and mechanical properties were investigated in the next part.

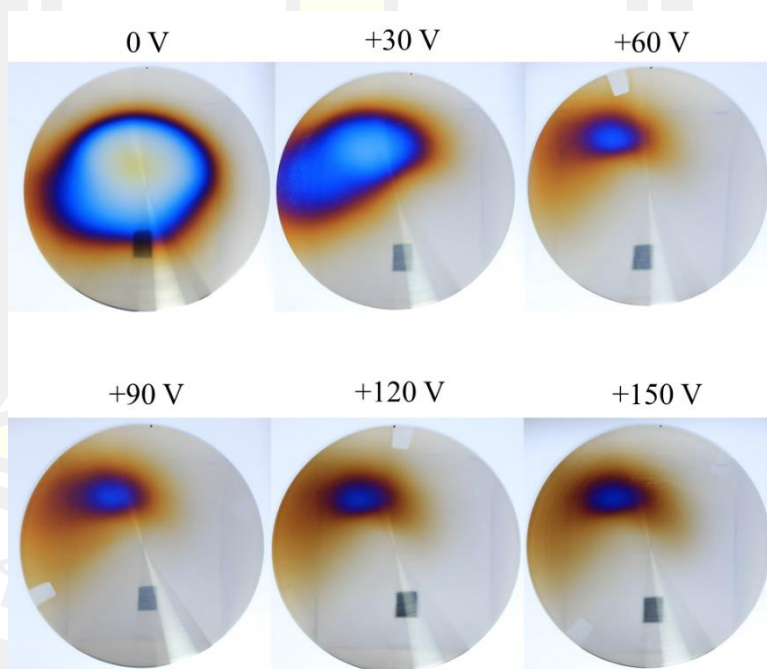


**Figure 4.19** The ta-C deposition profile on SUS316 plate (diameter 175 mm). The films deposited by varying anode bias potential.

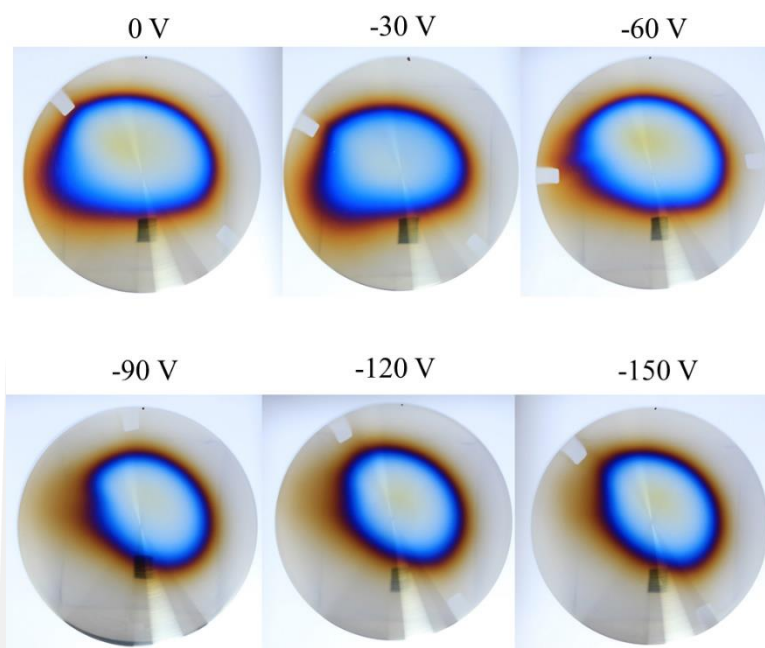


**Figure 4.20** The ta-C deposition profile on SUS304 plate (diameter 175 mm). The films deposited by varying substrate bias potential.

## 4.2 ta-C coating

### 4.2.1 Plasma biasing technique

From the plasma diagnostic, the deposition profile of the ta-C films deposited by varying anode bias potential is different in each condition, in which directly affects on deposition rate, uniformity, microstructure, and properties of the film. A survey study is required, to control these parameters. As a guideline for high quality film deposition.

#### 4.2.1.1 Survey of the ta-C deposition

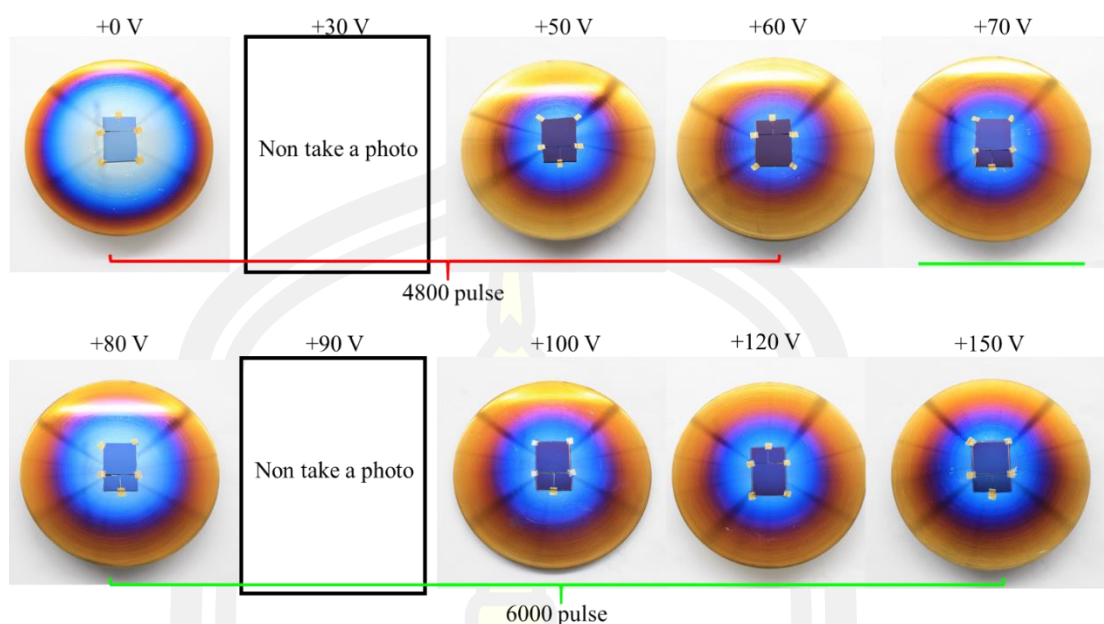
P-type silicon (100) wafers (size of  $2.0\text{ cm} \times 2.0\text{ cm}$ , and  $1.0\text{ cm} \times 1.0\text{ cm}$ ) with a thickness of  $545 \pm 15\text{ }\mu\text{m}$  were selected as substrates and was installed on a substrate holder and loaded in the deposition chamber. The position of a substrate holder has x offset is 15 cm, y and z offset are 0 cm. The Si substrate was cleaned at 10 min by using an anode layer ion source (ALIS) with the discharge potential and discharge current being 1.4 kV and 8.8 mA respectively. The substrate holder rotates around the x-axis as well as the cleaning time. And then, the ta-C film is deposited on the Si substrate by using an FCVA source, the graphite rod with high purity

(99.999%) with diameters 6.35 mm was used as a target. The process parameter as follows.

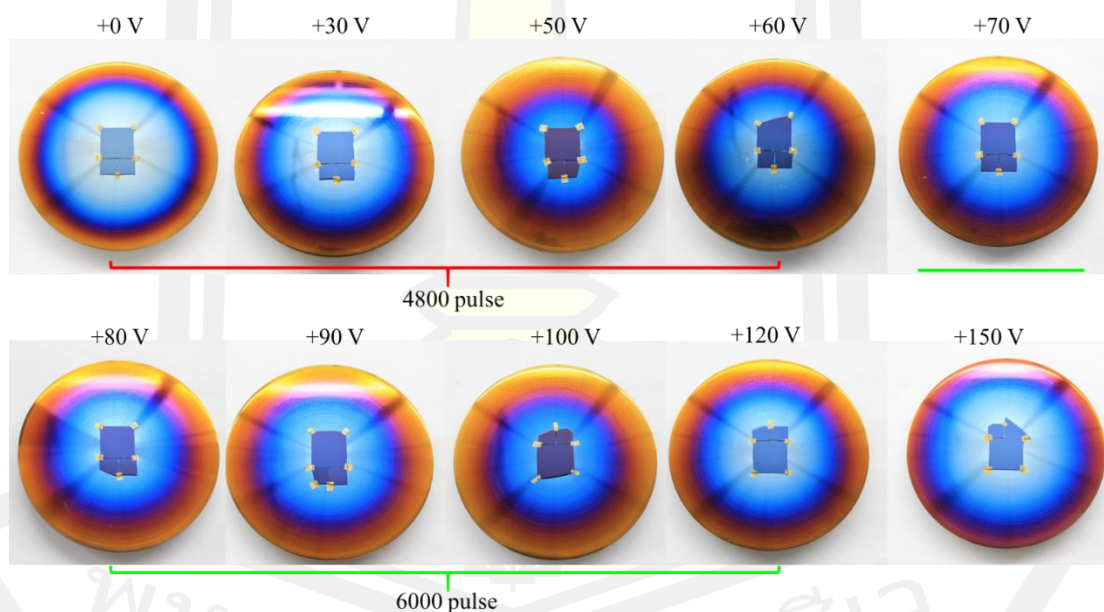
- Operating pressure : Vacuum arc:  $2 \times 10^{-6}$  torr
- Charger voltage : -504 V
- Maximum arc current : -720 A
- Arc frequency : 1 Hz
- Duration time : 1200  $\mu$ s
- Deposition pulse : 4800 to 6000 pulses
- Substrate distance : 15 cm
- Substrate state : holder is grounded and floated
- Study parameter : anode bias potential (0 to +150 V)

Figure 4.21 and Figure 4.22 show the profile of the film on the sample and substrate holder, the number label is an anode bias potential. The blue zone is the thick ta-C film and the yellow zone is the thin ta-C film, in which the diameter of the blue zone decreased with the increase of anode bias potential. It means that the plasma profile has changed and was strongly influenced by anode bias potential. It can be extended by the plasma fluid model, for high density plasma and low energy of the ion, the ions disperse, and the plasma beam will be widened. On the other hand, for high density plasma and high energetic ions, the ions are able to maintain the path of movement and the size of the plasma beam is not different from the size of the primary plasma beam (jet beam).

Moreover, the color of the ta-C film on the Si substrate changed from blue to purple for a sample deposited with anode bias 0 V and +50, +60 V respectively. This means that the thickness of the film trend to decrease with the increase of anode bias potential. This result corresponds with the plasma diagnostic part, the ion density decreased with the increase of anode bias potential, which means that the number of depositing ions and atoms of the carbon decreased leading to a low deposition rate in high applied anode bias potential. Therefore, it is necessary to increase the number of pulses so that the film thickness does not differ much.



**Figure 4.21** The ta-C films profile deposition on the sample and substrate holder by varying the anode bias potential (holder is grounded).



**Figure 4.22** The ta-C films profile deposition on the sample and substrate holder by varying the anode bias potential (holder is floated).

To find the deposition rate of the ta-C film on grounded and floated samples, X-ray reflectometry or XRR is used. The mass densities and thickness of the ta-C films were determined by XRR (Bruker D8 Advance) measurements performed with Cu-K $\alpha$  monochromatic radiation ( $\lambda=0.15406$  nm). The density values were obtained



by fitting the measured XRR data with a simulated XRR curve using the Leptos 7.0 software. X-ray reflectivity was measured in the range of an incident angle,  $2\theta$ , from  $0^\circ$  to  $4.0^\circ$  by a step of  $0.005^\circ$ . Which, the mass densities relate to the critical angle and film thickness relate to the oscillation period of the XRR profile.

Figure 4.23 shows the XRR profiles, the black line is raw data and the red line is the simulation curve; (a) is the ta-C films deposited on the grounded sample and (b) is the ta-C films deposited on the floated sample. The XRR profile presents the critical angle around  $0.5^\circ$ , which shifts to a more critical angle with the increase of anode bias potential. This means that the mass density may be increased with the increase of anode bias potential. Moreover, the oscillation period of the XRR profile is different, which indicated the difference in film thickness.

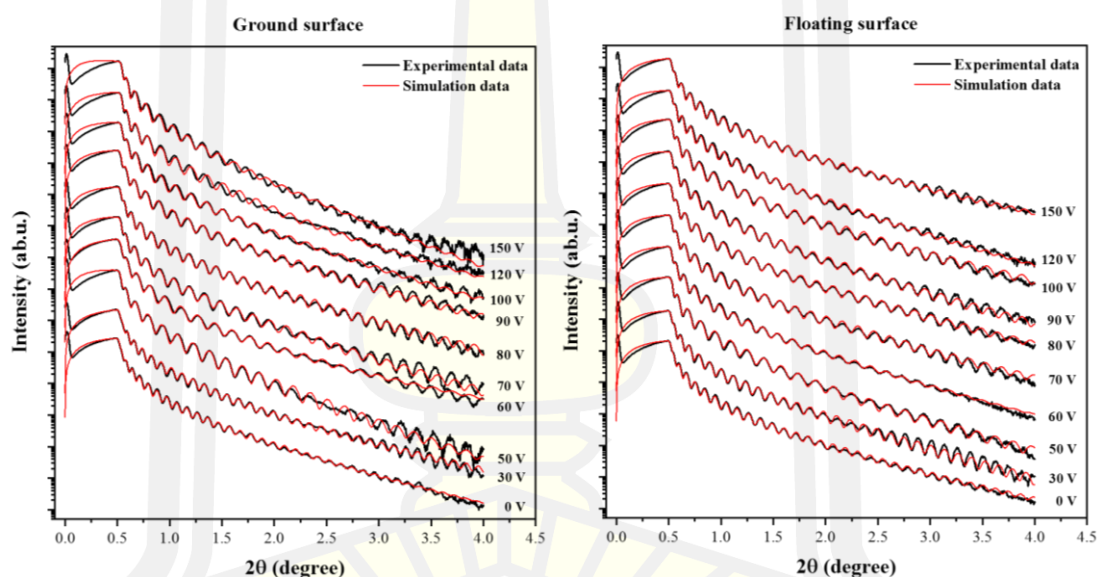


**Figure 4.23** XRR profiles of ta-C films (a) ground sample and (b) floating sample.

Figure 4.24 shows the density of the ta-C film as a function of ion energy. For ta-C film deposited on the ground sample, the density of the ta-C films linearly increases with the increase of the anode bias potential, which a minimum value of  $3.14 \text{ g/cm}^3$  at an anode bias potential of 0 V and a maximum value of  $3.37 \text{ g/cm}^3$  at an anode bias potential of +150 V. For the grounded sample, the film deposited with the energetic ion will be proved overcome of the subplantation threshold, are leading to a significant increase of the film density.

But, for the ta-C films deposited on the floating sample, the density of the films has a maximum value is  $3.27 \text{ g/cm}^3$  (anode bias potential +120 V). Moreover, the mass densities have a cluster distribution in the range of  $3.20$  to  $3.27 \text{ g/cm}^3$  (anode bias potential +50 to +150 V). Due to for the floating sample case, the ion energy of  $\text{C}^+$  ions has a value in the range of 16 eV to 46 eV for anode bias potential 0 V to +150 V. This indicates that the carbon ion energy around 46 eV can't create the subplantation and optimize condition for growing the ta-C film with the high density.

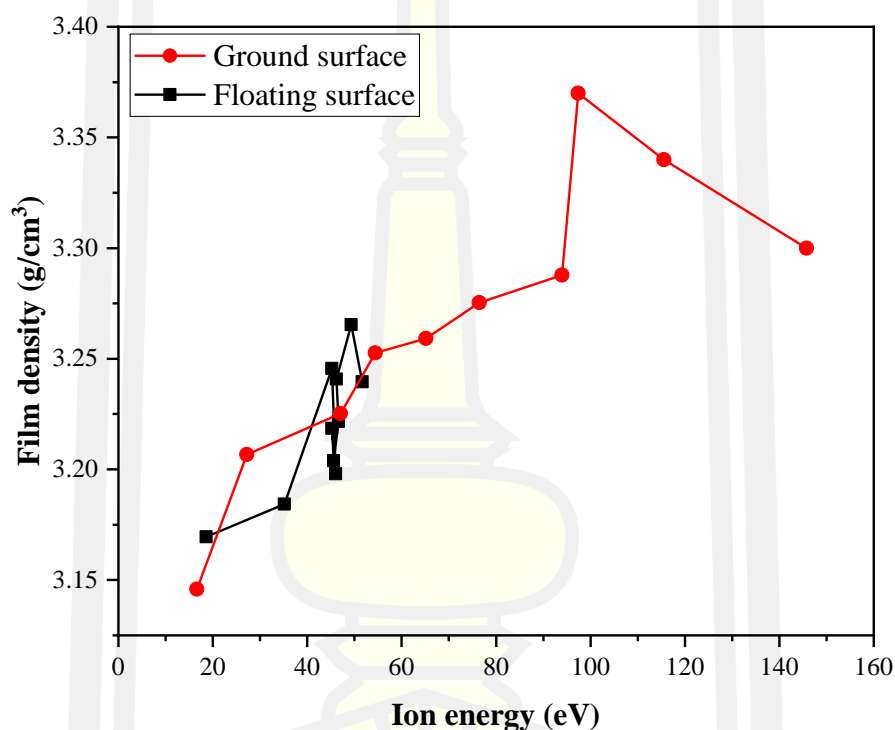


**Figure 4.24** Film density as a function of the mean energy of carbon ions.

Moreover, the deposition rate of the film trend to decrease in exponential decay as shown in Figure 4.25, which looks the same for the grounded sample and the floated sample. The deposition rate of the films decreased from 0.015 to 0.010 nm/pulse with the increase of anode bias potential from 0 to +150 V. This result corresponds with the ion density in the part of plasma diagnostic, the ion density decreased with the increase of anode bias potential. This means that the plasma density decreased, and the number of carbon ions, carbon atoms, and electrons will be decreased, leading to decreasing of the deposition rate of the ta-C film.



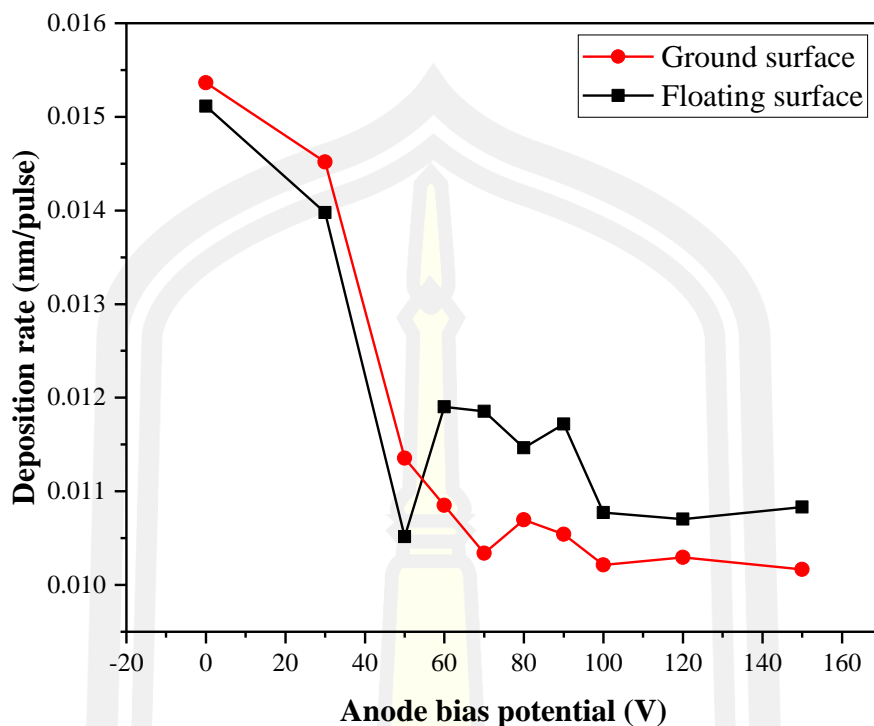


**Figure 4.25** Influence of plasma biasing technique on the deposition rate of ta-C film.

From the survey deposition, the deposition profile of the ta-C films deposited by varying substrate bias potential is different in each condition, in which directly affects on deposition rate, uniformity, microstructure, and properties of the film. To study the influence of anode bias potential on surface morphology, microstructure, and mechanical properties. The ta-C film must be the same thickness.

The Si wafer with the size of 30 mm × 30 mm was installed on a substrate holder and loaded into the deposition chamber. The position of a substrate holder has x offset of 15 cm, y and z offset of 0 cm. The Si substrate was cleaned at 10 min by using an anode layer ion source (ALIS) with the discharge potential and discharge current being 1.4 kV and 8.8 mA respectively. The substrate holder rotates around the x-axis as well as the cleaning time. And then, the ta-C film is deposited on the Si substrate by using an FCVA source, and the graphite rod with high purity (99.999%) with diameters 6.35 mm was used as a target. The process parameter as follows.

- Operating pressure : Vacuum arc,  $2 \times 10^{-6}$  torr
- Charger voltage : -504 V

- Maximum arc current : -720 A
- Arc frequency : 1 Hz
- Duration time : 1200  $\mu$ s
- Substrate distance : 15 cm
- Substrate state : holder and sample is grounded
- Study parameter : anode bias potential

**Table 4.4** Deposition pulse for the synthesis of the ta-C film with the thickness of about 85 nm

Anode bias potential (V)	Deposition pulse (pulse)
0	7257
+30	7331
+60	8482
+80	8547
+90	8554
+100	9141
+120	9208
+150	9276

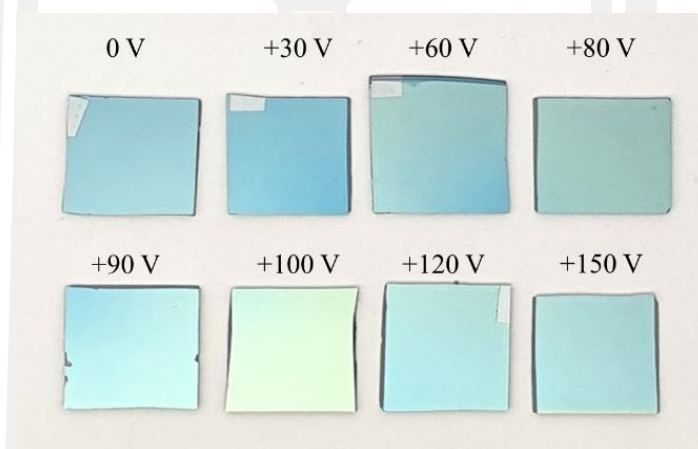
Figure 4.26 shows the ta-C films on Si substrate by varying anode bias potential and controlling the thickness of 85 nm by using deposition pulse are present in Table 4.4. This is the sample with the size of 10 mm  $\times$  10 mm, the color of the film is blue sky, which is the same color for all samples, which indicates that the film thickness is close. The surface morphology, microstructure, electrical properties, and mechanical properties were investigated by AFM, Raman spectroscopy, XPS, XRR, four point probe, and nanoindentation test.

#### 4.2.1.2 FE-SEM result

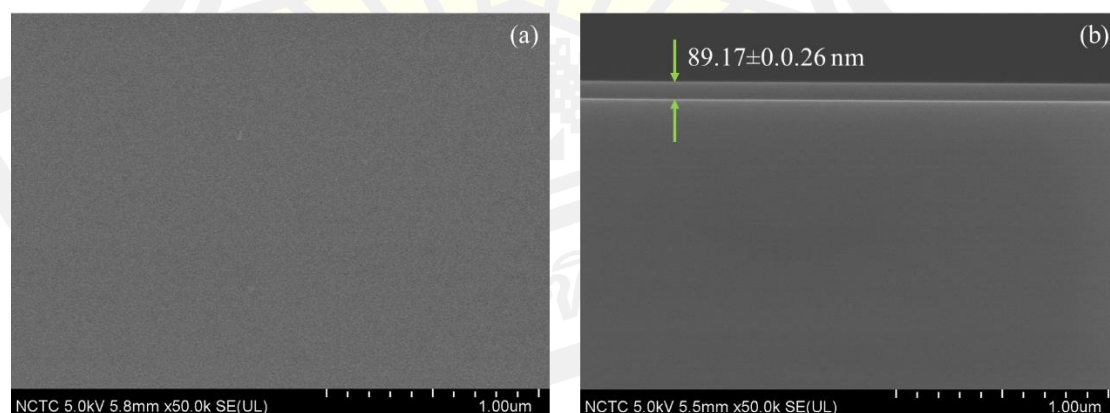
The surface and cross-section morphology of the ta-C film deposited on Si substrate by applied anode bias potential of +80 V, it was characterized by field emission scanning electron microscope (FESEM, Hitachi SU8030) at NSTDA CO., LTD., Thailand.

Figure 4.27(a) shows the surface morphology of the film. The surface of the film is smooth, with free micro pinholes, and macroparticles. That means that the design of the T-shape adaptor and the filtering and focusing coil has performance for filtering the macroparticle of the arc process from the FCVA source. Moreover, anode bias with higher potential does not affect and generate the arc on the anode electrode, which introduces the macroparticle of metal in the anode electrode.

In order to confirm the thickness of the film, the sample was mechanical cracked and investigated the cross-section as shown in Figure 4.27(b). The film has a thickness of 85.17 nm and non-observe the columnar grain, indicating that the film is amorphous characteristic and dense.



**Figure 4.26** The ta-C films on Si substrate deposited by varying anode bias potential, which controls the thickness of 85 nm.



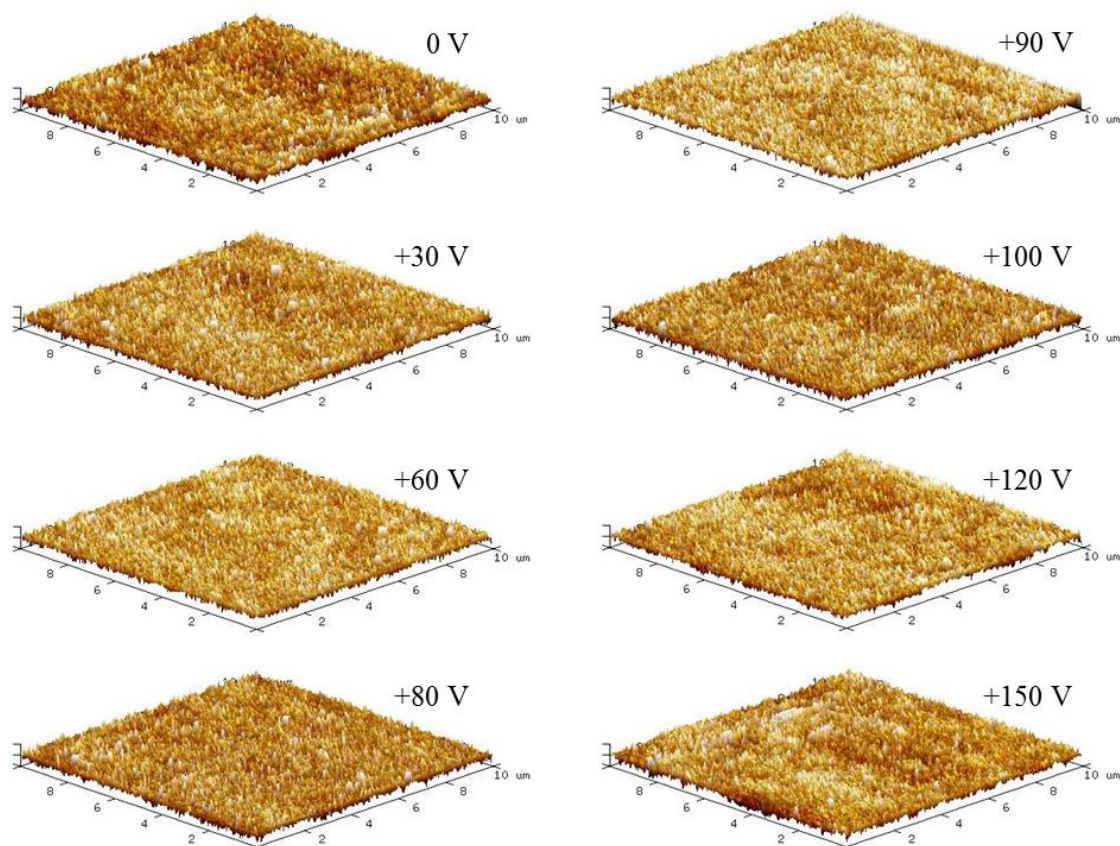
**Figure 4.27** (a) surface and (b) cross-section of the ta-C film deposited on Si substrate by applied substrate bias potential of +80 V.

#### 4.2.1.3 AFM result

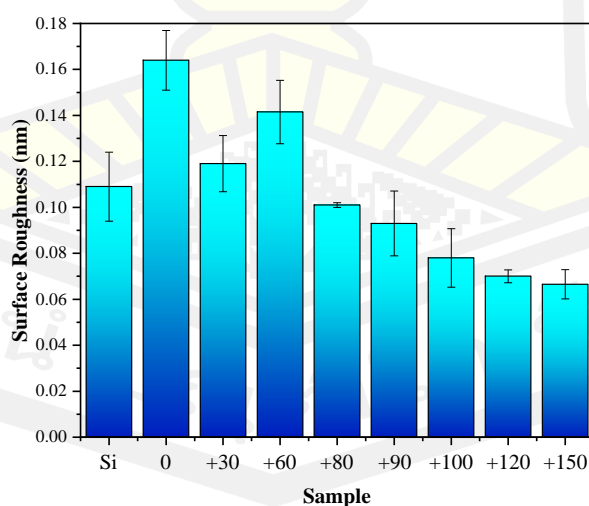
The effect of anode bias potential on the topography of the films was investigated using atomic force microscopy (AFM), using Bruker: Dimesion Icon. For Si wafer and each ta-C sample, the mean value of the root mean square surface roughness (RRMS) value was calculated by scanning two random areas of  $10 \times 10 \mu\text{m}^2$ . Microscope controlling, acquisition, processing, and analysis of the recorded data were done using Nasoscope analysis 2.0 software.

Figure 4.28(a)-(d) shows the 3D AFM images of ta-C films deposited by the plasma biasing technique at an anode bias potential of 0, +60, +100 and +150 V, respectively. AFM inspection of the ta-C films deposited with different mean energies and fluxes of  $\text{C}^+$  ions shows a different topography, revealing a very fine and evenly distributed grain structure of the surface of the film. The ta-C film deposited with an anode bias potential of 0 V (mean energy of 16 eV) exhibits a predominant small columnar grain-like surface morphology as shown in figure 7(a). While the number of small columnar grains was reduced when the anode bias potential increased, as shown in **Error! Reference source not found.**(b)-(d). Although the film growth occurs at low ion flux, the high-energy ion bombardment during the arc pulse interrupts the continuous growth of the columnar grains, resulting in a high density and smooth surface of the ta-C films. The estimated values of RRMS as shown in Figure 4.29. The surface roughness of the ta-C films gradually decreases from 0.164 to 0.067 nm with increasing anode bias potential from 0 to +150 V. For an anode bias potential of +150 V, the RRMS exhibits the lowest value of about 0.067 nm.

The surface roughness and morphology of the ta-C films are related to the significant increase in the mean energy of the  $\text{C}^+$  ions, as shown in **Error! Reference source not found.**(b). The high energetic ion bombardment in the PFCVA combined with the plasma biasing technique leads to increased mobility and diffusivity of the adatoms on the substrate surface, including re-nucleating grains. This result facilitates and reduces the gaps between each column, leading to increasing the density of the nucleation sites and a change in the surface morphology of the film [165], [153].



**Figure 4.28** 3D AFM images of ta-C thin films deposited with PFCVA technique combined with plasma biasing technique.



**Figure 4.29** The estimated values of the root mean square surface roughness (RRMS) of the ta-C films deposited on the Si substrate as a function of anode bias potential.



#### 4.2.1.4 Raman spectroscopy

Most of the structural and mechanical properties of DLC thin films, such as density, hardness, elastic modulus, and stress, are directly correlated to the  $sp^3$  content. Raman spectroscopy is the most popular technique for quantitative estimation of  $sp^3$  content in DLC films because it can be processed quickly without damaging the test sample. The microstructural properties of ta-C films were estimated by using Raman spectroscopy (Bruker, SENTERRA). The laser wavelength of 532 nm was used and pointed into the films (laser power is 12 mW and resolution 9 to 12  $cm^{-1}$ ), measurement in the range of 500 to 2700  $cm^{-1}$ . The Raman spectra were curve-fitted by ORIGIN-2018, which through subtracting background to evaluate the  $I_D/I_G$  ratio, the G peak position, which can tell the trend of the  $sp^3$  contents in the ta-C films. The parameters of Raman spectra such as position, width, and intensity of the D and G peaks ( $I_D/I_G$ ) are closely related to the density, size, and structure of the  $sp^2$  clusters which are, in their turn, closely related to the  $sp^3$  content [166].

The intensity ratio of the D and G peaks or  $I_D/I_G$ , was used for only a qualitative estimation of  $sp^3$  content in the film, due to  $I_D/I_G$  being proportional to the number of rings at the edge of the grain. The G peak is due to resonance of all  $sp^2$  sites, but the D peak is only due to resonance of six-fold rings in the DLC film. Therefore, if  $I_D/I_G$  is decreased, the number of rings per cluster will be decreased, which means that the fraction of chain groups rise in the DLC film [19].

Figure 4.30(a) shows the Raman spectra of the ta-C films deposited with different anode bias potentials. Raman spectra of the ta-C films were first treated with linear background removal and D and G peaks were deconvoluted using two Gaussian functions. The Raman spectra have nonsymmetric Raman intensity distribution in the range 1060-1840  $cm^{-1}$  and centered around 1554  $cm^{-1}$ , which includes the structure information of  $sp^2$  and  $sp^3$  sites, this also confirms the amorphous carbon characteristic of the films [167]. The analyzed data are listed in Table 4.5, the D peak and G peak appears at the position of 1390  $cm^{-1}$  with the FWHM of 173.88 to 237.34  $cm^{-1}$  and 1562.94 to 1579.02  $cm^{-1}$  with the FWHM of 219.70 to 234.69  $cm^{-1}$  respectively.



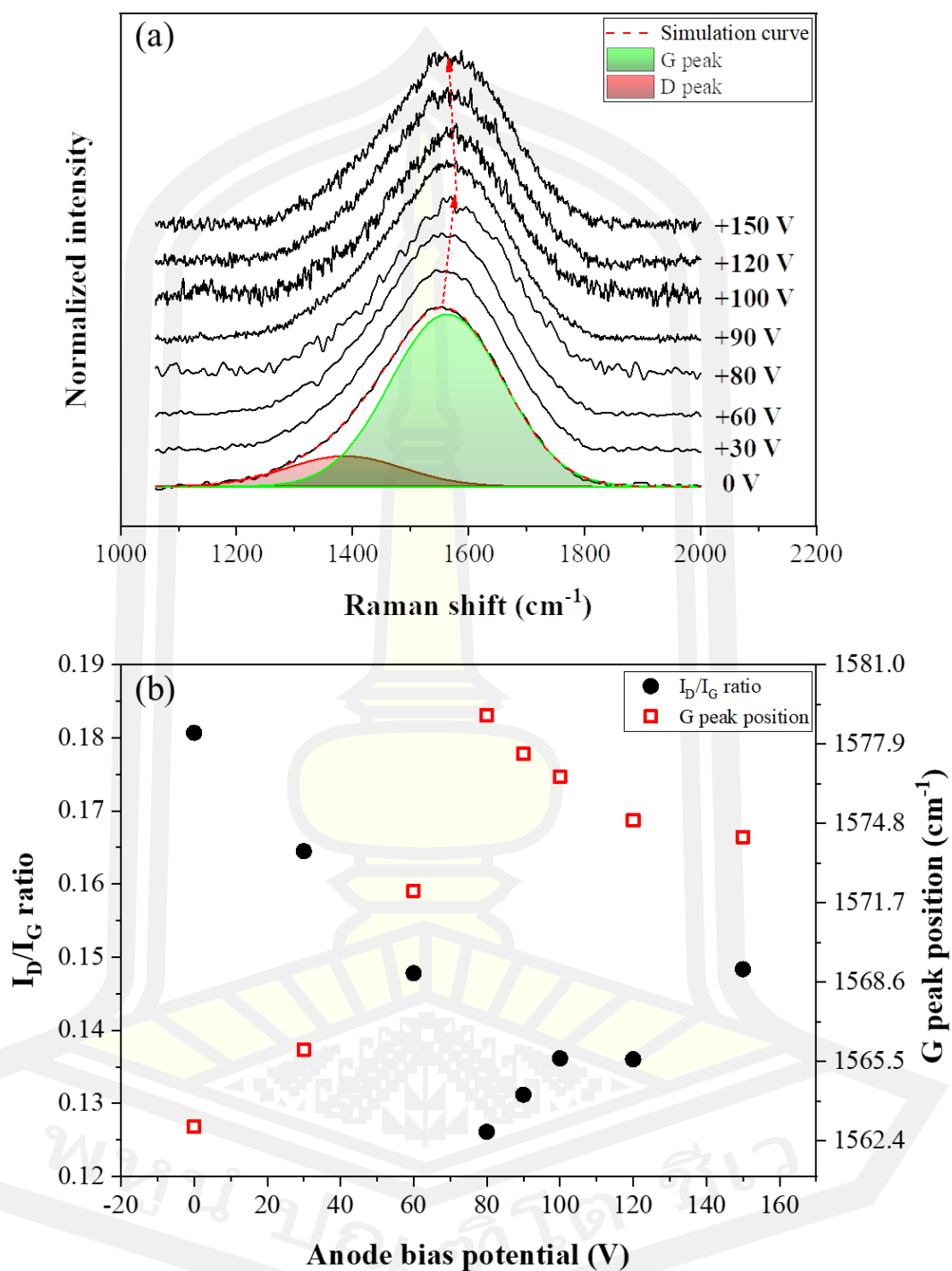


**Figure 4.30** (a) Raman spectra and (b) double plot of the  $I_D/I_G$  ratio and G peak position of the ta-C film deposited with the different anode bias potential.

The values of  $I_D/I_G$  and G peak position are shown in Table 4.5 and plotted in Figure 4.30(b) as a function of the applied anode bias potential. The  $I_D/I_G$  values

decrease from 0.18 to a minimum value of 0.12 with the increase of anode bias potential from 0 to +80 V and then increase again to 0.15 for a film deposited by applied anode bias potential of +150 V. This means that proportional to the number of rings at the edge of the grain decreased with the increasing of anode bias potential from 0 to +80 V and was introduced with higher anode bias potential [168]. While the G-peak position shows the opposite trend with  $I_D/I_G$  ratio. The G peak position significant shift up from 1562.92 to 1579.02  $\text{cm}^{-1}$ , indicating the changes of the  $\text{sp}^2$  configuration from mainly rings to short chain [166], [169]. This can be explained from a three-stage model proposed by Ferrari et al [168]. That means the ta-C films deposited by applied a substrate bias potential +80 V, the film rich  $\text{sp}^3$  content. Therefore, the energy enhanced of  $\text{C}^+$  ions by substrate bias technique during the film growth, as a result in rearrangement of  $\text{sp}^2$  (amorphous carbon) to  $\text{sp}^3$  (tetrahedral amorphous carbon).

**Table 4.5** Analyzed data of Raman spectra; Position, FWHM, area of D and G peak including  $I_D/I_G$  ratio.

$V_{ab}$ (V)	D position ( $\text{cm}^{-1}$ )	FWHM of D ( $\text{cm}^{-1}$ )	G position ( $\text{cm}^{-1}$ )	FWHM of G ( $\text{cm}^{-1}$ )	$I_D$	$I_G$	$I_D/I_G$
+0	1386.63	237.34	1562.94	230.99	15.30	84.70	0.18
+30	1389.00	214.22	1565.95	230.17	14.13	85.87	0.16
+60	1390.00	209.30	1567.26	231.49	12.88	87.12	0.15
+80	1390.00	183.11	1579.02	234.62	11.20	88.80	0.13
+90	1390.00	173.88	1577.52	224.62	11.60	88.40	0.13
+100	1390.00	179.07	1576.61	219.70	11.98	88.02	0.14
+120	1384.08	176.96	1574.92	226.06	11.97	88.03	0.14
+150	1390.00	204.04	1572.77	226.44	12.92	87.08	0.15

#### 4.2.1.5 XPS result

The chemical bonding, chemical states, and electronic structures of the films were determined by X-ray photoelectron spectroscopy (XPS). The XPS measurement was performed using a PHI5000 Versa Probe II, ULVAC-PHI, Japan at the SUT-NANOTEC-SLRI joint research facility, Synchrotron Light Research Institute

(SLRI), Thailand. The monochromatic  $\text{AlK}_{\alpha}$  X-ray (1486.6 eV) was used as an excitation source. All binding energies of the samples were calibrated with the  $\text{C1s}$  peak at 284.8 eV. The data were fitted by using Shirley background subtraction and sub-peak with Gaussian-Lorentzian function.

The XPS measurement is popular for measuring the percentage of atom bonds within the film or material because it can indicate the binding energy of photoelectrons on the film surface. The photoelectron will be generated when X-rays incident the surface of the material. Which, these photoelectrons will be measured kinetic energy by the detector and converted to the binding energy of these photoelectrons, which corresponds with a specific bond in the film surface. Therefore, the XPS will be used to estimate the chemical bonding, chemical states, and electronic structures.

The XPS measurement was divided into two parts: survey scanning and finely scanning. In the case of survey scanning, it is used to measure binding energy in a wide range from 0 to 1400 eV, in which atoms of various elements are present on the film surface. The survey spectra of ta-C films deposited on Si wafer by varying anode bias potential as shown in Figure 4.31, the photoelectrons with the binding energy  $285 \pm 0.5$  eV and  $532 \pm 0.5$  eV can be observed which corresponds to  $\text{C1s}$  and  $\text{O1s}$  respectively [170], [171]. It indicates that the film surface is not contaminated by other elements. In addition, the detection of photoelectrons with the binding energy of 980 and 1220 eV corresponds with O KLL and C KLL respectively [172].

To study the chemical bonding of the carbon atoms, the XPS measurement in finely scan (resolution is 0.05 eV) was used.  $\text{C1s}$  spectra as shown in Figure 4.32, the spectra were background-subtract by Shirley function and then deconvoluted by Gaussian function fitting. The  $\text{C1s}$  spectra were deconvoluted into four peaks located at about  $284.1 \pm 0.2$  eV,  $285.0 \pm 0.2$  eV,  $286.5 \pm 0.3$  eV and  $288.5 \pm 0.3$  eV, which originate from  $\text{C}=\text{C}$   $\text{sp}^2$  bond,  $\text{C}-\text{C}$   $\text{sp}^3$  bond,  $\text{C}-\text{O}$  bond, and  $\text{C}=\text{O}$  bond, respectively [173]. Moreover, one of the finely scan is  $\text{O1s}$  spectra, which indicate the bonds of atoms on the surface of films.  $\text{O1s}$  spectra as shown in Figure 4.33, the spectra were background-subtract by Shirley function and then deconvoluted by Gaussian function fitting. Under the  $\text{C1s}$  spectra presenting the  $\text{C}-\text{O}$  bond and  $\text{C}=\text{O}$  bond at about  $531.4 \pm 0.2$  eV and  $532.5 \pm 0.2$  eV respectively [174], [175]. From the XPS spectra,

metal atoms such as copper, aluminum and stainless steel including the insulating ceramics atoms of the FCVA source not detectable. It means that the FCVA source does not generate the contamination atoms on the films.

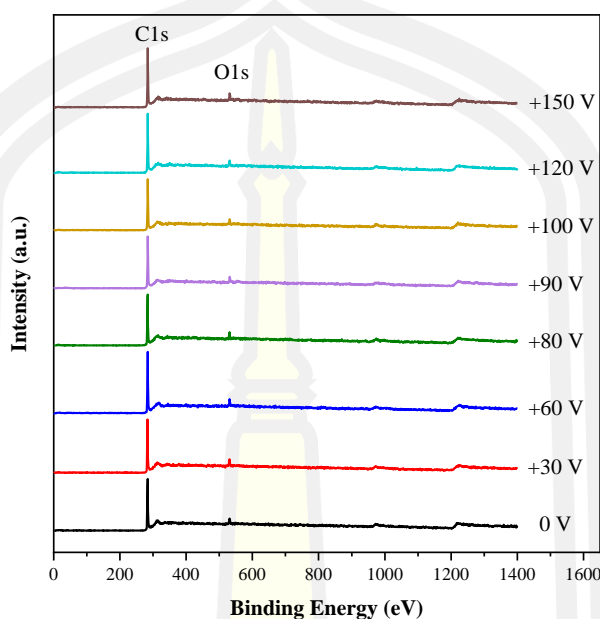


**Figure 4.31** Survey spectra of the ta-C films with the thickness of about 85 nm deposited by varying anode bias potential.

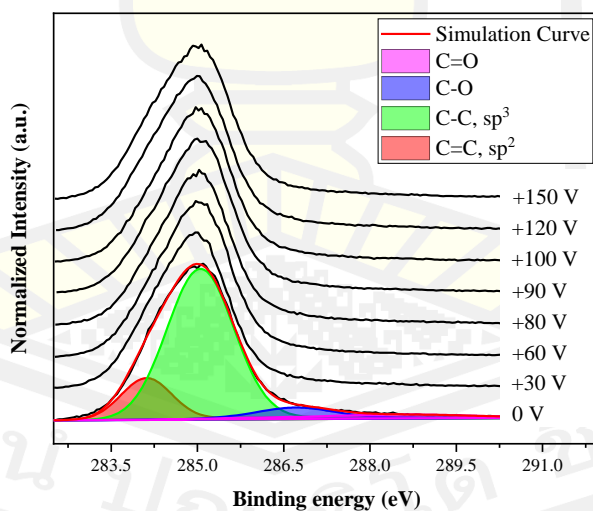


**Figure 4.32** C1s spectra of the ta-C films with the thickness of about 85 nm deposited by varying anode bias potential.

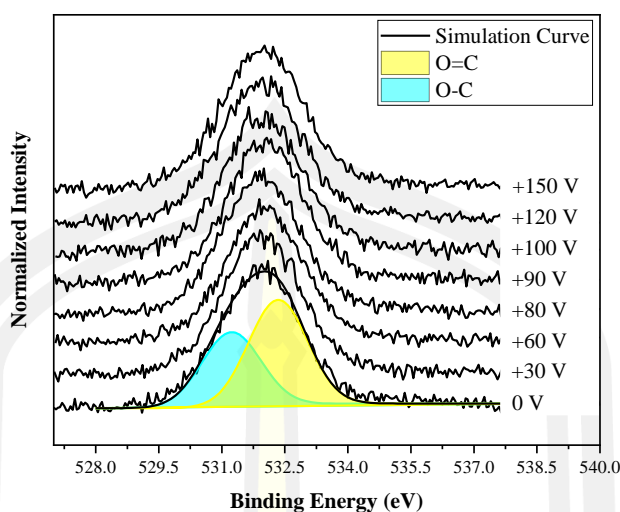


**Figure 4.33** O1s spectra of the ta-C films with the thickness of 80 to 90 nm deposited by varying anode bias potential.

**Table 4.6** shows the composition of C=C or  $sp^2$  bond, C-C or  $sp^3$  bond, C-O bond, and C=O bond. The obtained C-C or  $sp^3$  contents in the ta-C films are further depicted in Figure 4.34. It can be seen that adjusting of the anode bias potential from 0 V to +80 V leads to a monotonic increase in  $sp^3$  content from 75.41% to 83.44%. And decrease to 80.11% again for substrate bias potential higher than +90 V. In addition, the oxygen content on the films slightly different, due to the base pressure in the deposition chamber as the same value.

Raman spectroscopy and XPS test showed that the plasma biasing technique can be enhanced the  $sp^3$  content of the ta-C films. This was described by the densification model of Robertson [20]. For an anode bias potential of 0 V, the mean energy of  $C^+$  ions of 16 eV, it does not have enough energy to penetrate and just sticks to the surface of the film and remains in its lowest energy state with is  $sp^2$  bonded. The anode bias potential is higher than +80 V leads to high  $sp^3$  content in the films due to the mean energy of depositing ions higher than surface penetration threshold energy, this increases the probability to penetrate the surface and enter a subsurface interstitial site during the film growth. This will decrease the poor or pin hole and increase the probability to reform around carbon atoms at the surface of film according to the new structure and density.

**Table 4.6** The fraction of chemical bonding in the ta-C films deposited by varying anode bias potential.

Anode bias potential (V)	C=C ( $sp^2$ )	C-C ( $sp^3$ )	C-O	C=O
0	14.05	75.41	6.54	4.00
+30	16.02	77.25	5.24	1.49
+60	12.21	80.91	4.78	2.10
+80	10.92	83.44	4.37	1.27
+90	11.08	83.01	4.61	1.30
+100	11.61	82.34	4.44	1.61
+120	10.71	81.33	5.99	1.96
+150	13.69	80.11	4.26	1.94

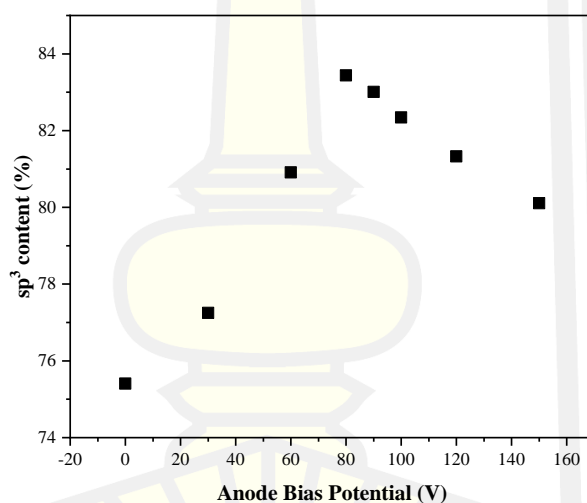


**Figure 4.34**  $sp^3$  content of the ta-C films as a function of anode bias potential.

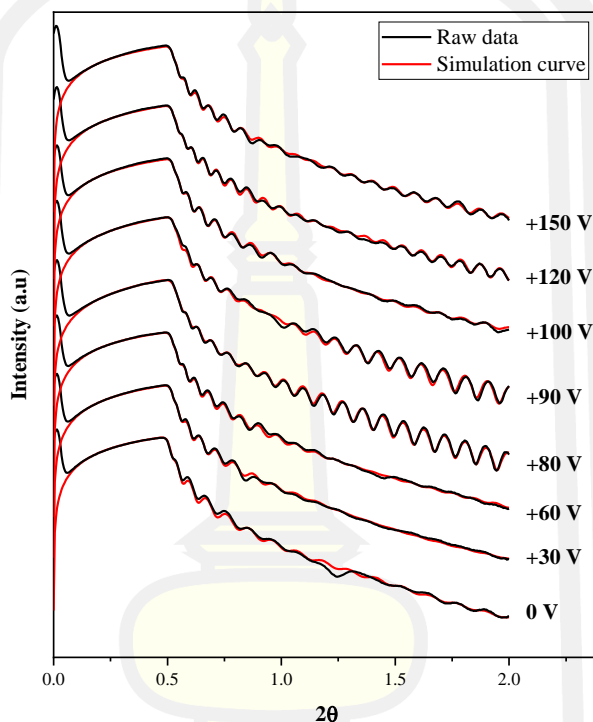
#### 4.2.1.6 XRR result

From Raman spectroscopy and XPS measurement, the ta-C films are high  $sp^3$  content, while for the general case, high  $sp^3$  content leads to a denser ta-C film [164]. To confirm and compare the influence of anode bias potential (ion energy) on the mass density of the films, X-ray reflectometry or XRR was used for estimates the density of the films.

The mass densities of the ta-C films were investigated by XRR (Bruker D8 Advance) measurements performed with Cu-K $\alpha$  monochromatic radiation ( $\lambda=0.15406$



nm). The density values were obtained by fitting the measured XRR data with a simulated XRR curve using the Leptos 7.0 software. X-ray reflectivity was measured in the range of an incident angle,  $2\theta$ , from  $0^\circ$  to  $3.0^\circ$  by a step of  $0.005^\circ$ . Which, the mass densities relate to the critical angle and film thickness relate to the oscillation period of the XRR profile.



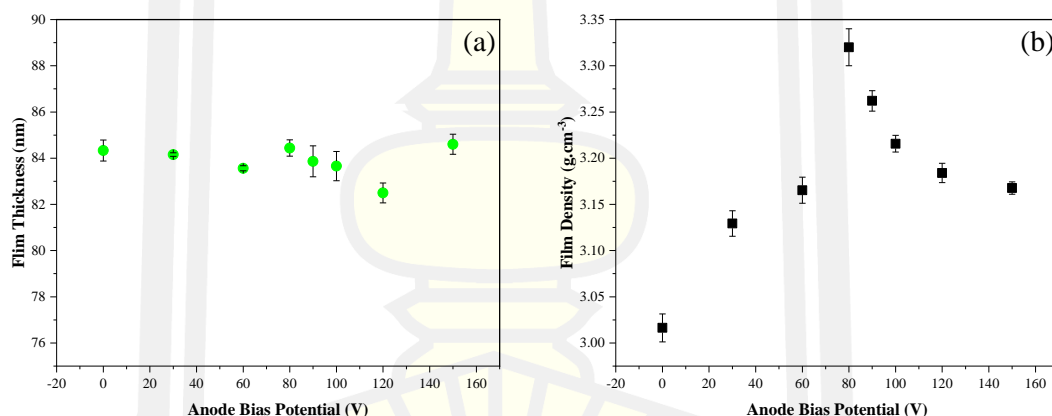
**Figure 4.35** The XRR profiles of ta-C films deposited on Si substrate by varying anode bias potential.

Figure 4.35 shows the XRR profile of the ta-C films deposited on Si substrate by varying anode bias potential and controlling the thickness in the range of 80 to 90 nm. The critical angle is slightly shifted to higher  $2\theta$ , while the oscillation period has the same range, indicating that the film has the same range of films thickness corresponding to the analyzed data as shown in Figure 4.36(a). The thickness of the films has a value in the range of 82.5 to 84.3 nm. Therefore, the density of the films can be compared.

Densities of the ta-C films were calculated using the critical angle for the total external reflection as shown in Figure 4.36(b). It was found that the density of the ta-C films increases with the increase of the anode bias potential, reaching a minimum

value ( $\rho = 3.01 \pm 0.015 \text{ g/cm}^3$ ) and a maximum value ( $\rho = 3.32 \pm 0.02 \text{ g/cm}^3$ ) for the ta-C films deposited by applying an anode bias potential of 0 V and +80 V, respectively. The mass densities are similar to those found by Andre et al [152].

The mass densities of the films were improved by energetic bombardment with  $\text{C}^+$  ions during film growth, which overcame the subplantation threshold, resulting in a significant increase in the density of the films when increasing the anode bias potential was increased from 0 V to +80 V. However, the density of ta-C films deposited with an anode bias potential higher than +120 V decreases. It can be discussed by the thermal spike model, the excess energy of the ion is converted to thermal energy at the point of trajectory and diffuses outward by thermal diffusion in the film structure. This phenomenon creates an expanding front in which all the atoms are inside the film. This allows the atoms to diffuse back to the surface to relax the density of  $\text{sp}^3$  density to the lower  $\text{sp}^2$  density [20].



**Figure 4.36** (a) thickness of the ta-C films estimated by the period oscillation of XRR curve. And (b) density of the ta-C films deposited on Si substrate as a function of substrate bias potential.

#### 4.2.1.7 Electrical properties

An in-house four point probe technique (detect the sheet resistance by using the ohmmeter mode of a dc source meter unit (Keithley 2450) has been used to measure the electrical resistivity and convert to the electrical conductivity of the ta-C films.

Raman spectroscopy, XPS, and XRR test found that the  $sp^3$  content in the ta-C films as a function of ion energy, which control by anode bias potential. The  $sp^3$  content increase with the increase of anode bias potential. It indicates that the  $sp^2$  content in the film decreased. Normally, the electrical properties of the ta-C films are strongly affected by the different possible  $sp^2$  hybridization of the carbon atoms in the ta-C films. Due to in the  $sp^2$ -rich carbon films or graphite like carbon containing of free electrons within the structure. Therefore, the electrical conductivity of the ta-C thin films decreased by 2.5 times  $8.16 \times 10^{-5}$  S/cm to  $2.84 \times 10^{-5}$  S/cm with increasing the  $sp^3$  content from 75.41% to 83.44%. The values of the electrical conductivity indicate an insulator character of the ta-C coating.

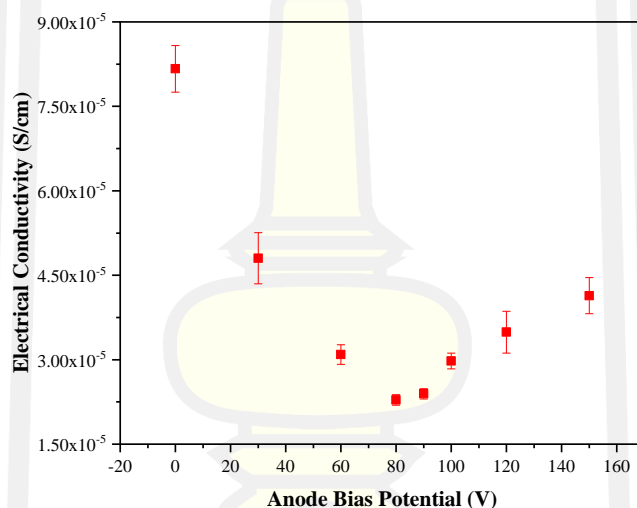


**Figure 4.37** Electrical conductivity of the ta-C film as a function of anode bias potential.

#### 4.2.1.8 Nanoindentation test

The mechanical properties of DLC films such as hardness and Young's modulus are correlated to their chemical composition,  $sp^3$  content, and density [176]. For example,  $sp^3$  rich DLC films grown with an energetic  $C^+$  ion bombardment were reported to exhibit high hardness and compressive stress, while hydrogenated DLC and metal doped DLC films exhibit lower hardness (H), Young's modulus (E), density, thermal stability, and compressive stress when compared with nonhydrogenated DLC films [177]. Hardness is a significant parameter suggesting

mechanical properties, while Young's modulus has also a significant role in wear behavior, in which use estimates the damage of the material or the film under load.

The hardness (H) and elastic modulus (E) of the ta-C films deposited on Si substrate were assessed by instrumented indentation, using Fischerscope HM2000 from NANOTECH (THAILAND) CO., LTD., Thailand, equipped with a diamond Berkovich geometry three-sided pyramidal tip. Before the measurement stage, the tip calibration was performed using quartz, in order to overcome the effect of tip rounding. To avoid the affectation of the substrate on mechanical properties of the ta-C coating response, the load was determined penetration depths lower than 10% of the coating thickness, which maximum loading is 600  $\mu\text{N}$ . A minimum of 5 indentations were performed on each sample, and the results were averaged. The loading-unloading curves were processed using the Oliver & Pharr method.

Figure 4.38(a) shows the hardness of the ta-C films deposited by varying anode bias potentials. The result shows that the hardness of ta-C film increase by increasing the anode bias potential, which the maximum value is  $47.19 \pm 1.67$  GPa were deposited at anode bias potential +80 V. While Figure 4.38(b) shows the elastic modulus of the films, it has the same pattern with the hardness and the maximum value is  $245.35 \pm 3.17$  GPa, it can be extended, the films deposited with the energetic ions (80 to 100 eV) and low ion flux (low heat flux) rich  $\text{sp}^3$  content leading to properties like the diamond.

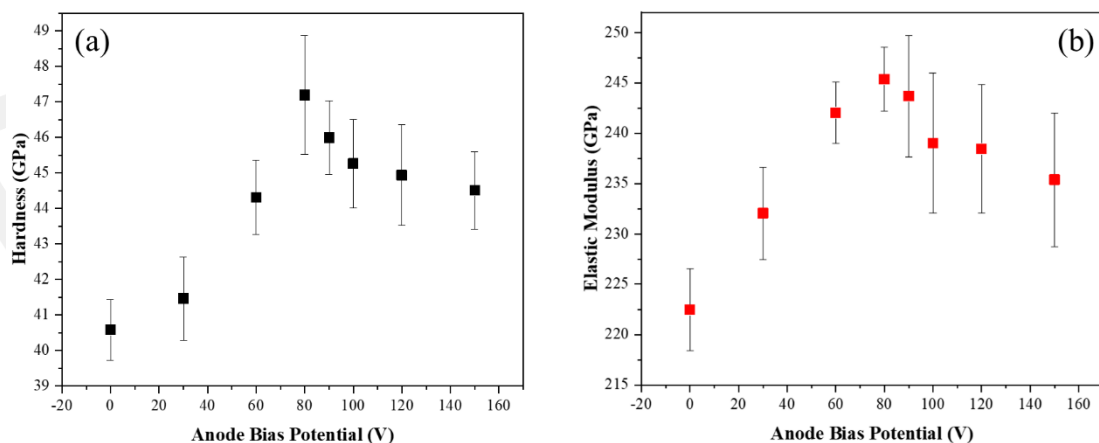


**Figure 4.38** (a) hardness and (b) elastic Modulus of the ta-C film as a function of anode bias potential.

Moreover, another parameter used to predict the wear resistance of film or predicting whether the film will crack or not under load, it is the H/E ratio (elastic strain to failure (rupture)) [32], [33]. The physical meaning of the H/E ratio is the gradual wear of materials, caused by plastic deformation in combination with fracture of material, than by elastic deformation within the material. Materials with a high H/E ratio have a small plasticity index, meaning that their deformation under load is more likely to be elastic than plastic, meaning that the coatings can exhibit improved fracture toughness. According to previous studies, the coatings with  $H/E \geq 0.1$  are considered to be resistant to cracking [180].

While the  $H^3/E^2$  ratio is a strong indicator of coatings resistance to plastic deformation (proportional to the elastic deformation of coatings), This parameter cannot use for predicting the wear and failure resistance of coatings material, but it uses to estimate well their elasticity of coating material [181], [182]. The coatings material with a high  $H^3/E^2$  ratio (high hardness and low values of Young's modulus), it increases the elastic strain to failure and resistance to cracking under the load, in which the applied load to distribute over an extended layer volume. It caused the coating material will be well resistant to plastic deformations.

**Table 4.7** Summary of estimated mechanical and tribological parameters: indentation hardness (H), elastic modulus (E), H/E, and  $H^3/E^2$  ratios. Standard deviations are also listed in this table.

Anode bias potential (V)	H (GPa)	E (GPa)	H/E	$H^3/E^2$
0	41.67±0.32	229.21±2.32	0.182±0.003	1.378±0.059
+30	42.29±2.20	232.78±3.00	0.182±0.008	1.402±0.194
+60	44.31±2.51	234.34±3.32	0.189±0.013	1.600±0.303
+80	47.19±1.67	245.35±3.17	0.192±0.006	1.750±0.172
+90	45.48±1.85	243.14±3.32	0.187±0.007	1.595±0.173
+100	45.16±2.99	238.39±6.54	0.189±0.008	1.626±0.242
+120	44.96±2.82	236.42±6.39	0.190±0.016	1.649±0.385
+150	42.71±2.20	235.03±5.76	0.182±0.013	1.425±0.277

Table 4.7 presents the values  $H/E$  and  $H^3/E^2$  ratios. Analyzing these values, it can be seen that for the ta-C films deposited by the PFCVA technique assisted with the plasma biasing technique, the  $H/E$  and  $H^3/E^2$  ratios increase by increasing the anode bias potential. Which, the films exhibit  $H/E$  and  $H^3/E^2$  ratios higher than 0.1 indicating that the plasma biasing technique allows growing ta-C films with good elastic strain to failure and resistance to cracking and high resistance to plastic deformation which makes them excellent candidates for hard and wear resistance coating applications.

The enhanced mechanical properties are mainly attributed to a high  $sp^3$  content and high density, as a result of an intense and energetic bombardment with carbon ions during the deposition process. In the case of the plasma biasing technique, this bombardment can be controlled through the anode bias potential (positive potential), thus controlling the ion energies and fluxes towards the substrate.

#### **4.2.2 Substrate biasing technique**

From the plasma diagnostic, the deposition profile of the ta-C films deposited by varying substrate bias potential is different in each condition, in which directly affects on deposition rate, uniformity, microstructure, and properties of the film. A survey study is required, to control these parameters. As a guideline for high quality film deposition.

##### **4.2.2.1 Survey of the ta-C deposition**

The Si wafer with the size of 30 mm × 30 mm was installed on a substrate holder and loaded into the deposition chamber. The position of a substrate holder has x offset is 15 cm, y and z offset are 0 cm. The Si substrate was cleaned at 10 min by using an anode layer ion source (ALIS) with the discharge potential and discharge current being 1.4 kV and 8.8 mA respectively. The substrate holder rotates around the x-axis as well as the cleaning time. And then, the ta-C film is deposited on the Si substrate by using an FCVA source with the process parameter as follows.

- Charger voltage : -504 V
- Maximum arc current : -720 A
- Arc frequency : 1 Hz



- Duration time : 1200  $\mu$ s
- Deposition pulse : 3600 pulses
- Substrate distance : 15 cm
- Substrate state : holder and sample is grounded
- Study parameter : substrate bias potential

The ta-C sample was investigated by an X-ray reflectometer or XRR (Bruker D8 Advance) measurements performed with Cu-K $\alpha$  monochromatic radiation ( $\lambda=0.15406$  nm). The thickness and density of the films were obtained by fitting the measured XRR data with a simulated XRR curve using the Leptos 7.0 software. X-ray reflectivity was measured in the range of an incident angle,  $2\theta$ , from  $0^\circ$  to  $3.0^\circ$  by a step of  $0.005^\circ$ . Which, the mass densities relate to the critical angle and film thickness relate to the oscillation period of the XRR profile.

The XRR profile is present in Figure 4.39, this topic focuses on the deposition rate of the film, in which calculated thickness of the film. The thickness of the film corresponds with the oscillation period of the XRR profile, in which is different for each substrate bias potential. The density and deposition rate of ta-C films as shown in Figure 4.40, the density of the films increased with the increase of substrate bias potential. But, this density is not compared due to the thickness of the film is not the same. While deposition rate of the film is divided into two parts; (i) the deposition rate increase with the increase of substrate bias potential from 0 V to -100 V because the depositing  $C^+$  ions were induced by a strong electric field from a substrate holder and change the direction of moving into the center point of a substrate holder, as result the deposition rate higher than. And (ii) the deposition rate decreased with the increase of substrate bias potential from -100 V to -150 V. It can be explained from sputter events on the sample due to higher substrate bias potential leading to high energetic  $C^+$  ions into the film layer and sputter surface of the films. Therefore, the deposition rate of the film will be decreased.

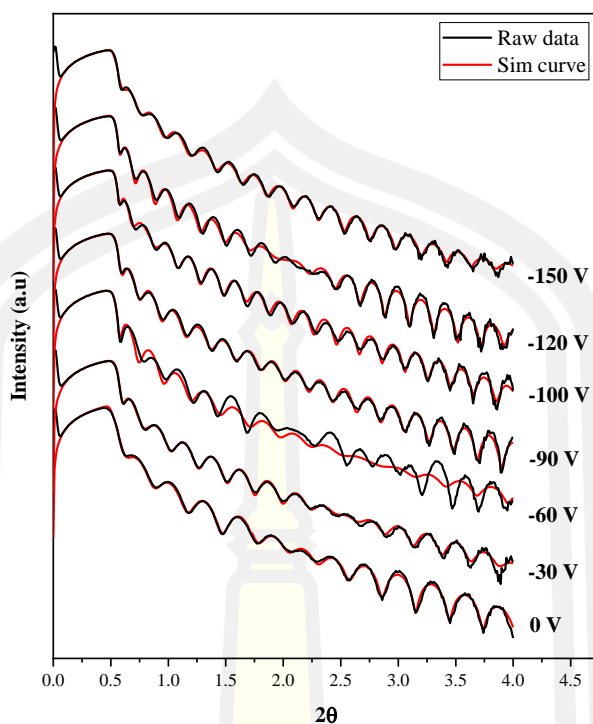


**Figure 4.39** The XRR profiles of ta-C films deposited on Si substrate by varying substrate bias potential (survey study).

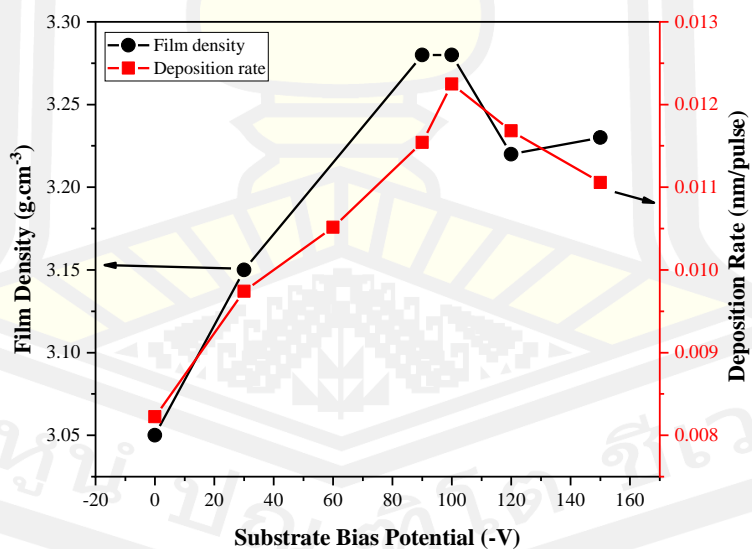


**Figure 4.40** Density and deposition rate of the ta-C films deposited by varying substrate bias potential (survey study).

The survey deposition profile of the ta-C films deposited by varying substrate bias potential shows the non-uniformly and different deposition rates of ta-C films deposition. To study the influence of substrate bias potential on surface morphology, and microstructure, the same thickness must be required.

The Si wafer with the size of 20 mm × 20 mm (3 samples) was installed on a substrate holder and loaded into the deposition chamber. The position of a substrate holder has x offset is 15 cm and y offset is 0 cm. The Si substrate was cleaned at 10 min by using an anode layer ion source (ALIS) with the discharge potential and discharge current being 1.4 kV and 8.8 mA respectively. The substrate holder rotates around the x-axis as well as the cleaning time. And then, the ta-C film is deposited on Si substrate by using an FCVA source, which the graphite rod with high purity (99.999%) with diameters 6.35 mm was used as a target. The process parameter as follows.

- Operating pressure : Vacuum arc,  $2 \times 10^{-6}$  torr
- Charger voltage : -504 V
- Maximum arc current : -720 A
- Arc frequency : 1 Hz
- Duration time : 1200  $\mu$ s
- Substrate distance : 15 cm
- Substrate state : holder and sample are grounded
- Deposition time : 3600 pulses
- Study parameter : substrate bias potential

To control the uniformity of the ta-C films covering the sample area (diameter 10 cm), the z position of the substrate holder must be offset as shown in Table 4.8. The reference position is the center of the deposition chamber.

Figure 4.41 shows the samples with the size of 10 mm × 10 mm of the ta-C films on Si substrate deposited by varying substrate bias potential and controlling the thickness of about 90 nm. The samples have the color is blue sky and the same color tone for all samples, indicating that the film thickness is close. The surface morphology, microstructure, and electrical properties were investigated by FESEM, Raman spectroscopy, XPS, XRR, and four point probe.

**Table 4.8** The z offset position of the substrate holder for synthesis of the ta-C films with the thickness of about 90 nm by varying substrate bias potential.

Substrate bias potential (V)	The z offset position of the substrate holder (mm)
0	-30
-30	-27
-60	-24
-80	-21
-90	-18
-100	-15
-120	-13
-150	-10

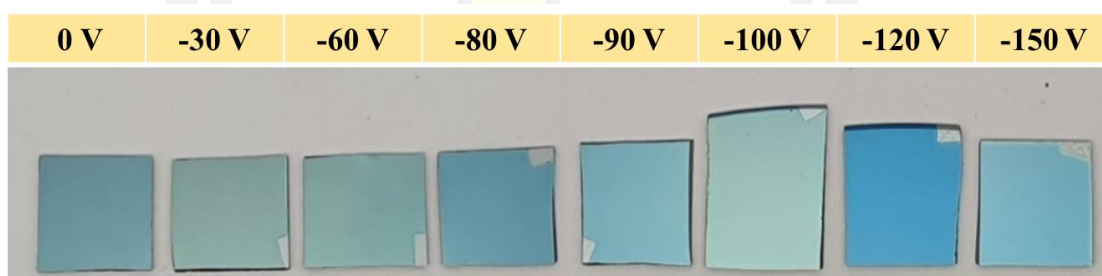


**Figure 4.41** The ta-C films on Si substrate deposited by varying substrate bias potential, which controls the thickness of about 90 nm, which label is the substrate bias potential.

#### 4.2.2.2 FE-SEM result

The surface and cross-section morphology of the ta-C film deposited on Si substrate by applied substrate bias potential of -80 V, was characterized by field emission scanning electron microscope (FESEM, Hitachi SU8030) at NSTDA CO., LTD., Thailand.

Figure 4.42(a) shows the surface morphology of the film. The film surface is smooth, free micro pin hole and the macroparticles. The film thickness was investigated the cross-section as shown in Figure 4.42(b). The film has a thickness of  $92 \pm 0.34$  nm and non-observe the columnar grain, indicating that the film is amorphous characteristic and dense.

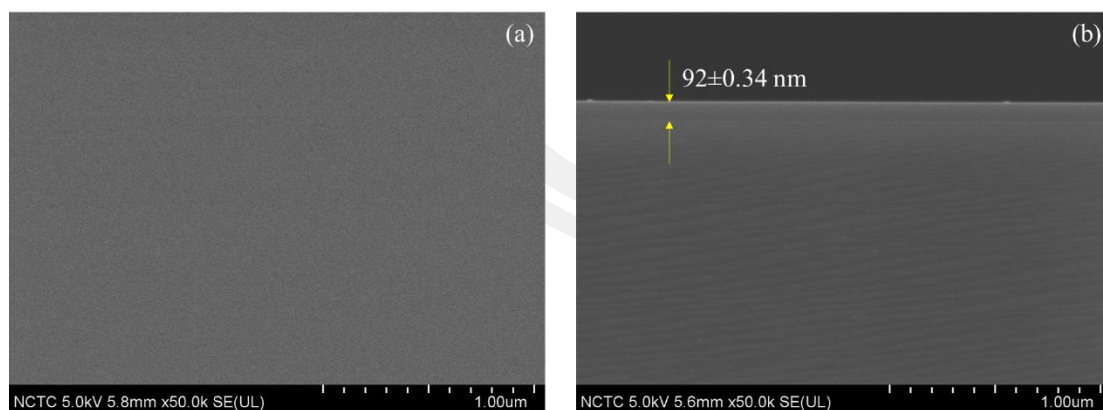


**Figure 4.42** (a) surface and (b) cross-section of the ta-C film deposited on Si substrate by applied substrate bias potential of -80 V.

#### 4.2.2.3 Raman spectroscopy

As the same ta-C films deposited by plasma biasing technique. The microstructural properties of ta-C films of ta-C films deposited using FCVA combined with substrate bias technique were estimated by using Raman spectroscopy (Bruker, SENTERRA). The laser wavelength of 532 nm was used and pointed into the films (laser power is 12 mW and resolution 9 to 12  $\text{cm}^{-1}$ ), measurement in the range of 50 - 2700  $\text{cm}^{-1}$ . The Raman spectra were curve-fitted by ORIGIN-2018 program, which through subtracting background to evaluate the  $I_D/I_G$  ratio, the G peak position, which can tell the trend of the  $\text{sp}^3$  contents in the ta-C films. The parameters of Raman spectra such as position, width, and intensity of the D and G peaks ( $I_D/I_G$ ) are closely related to the density, size, and structure of the  $\text{sp}^2$  clusters which are, in their turn, closely related to the  $\text{sp}^3$  content [166].

Figure 4.43 shows the Raman spectra of the ta-C films deposited with different substrate bias potentials. The Raman spectra of the ta-C films were first treated with linear background removal and the D and G peaks were deconvoluted with two Gaussian functions. The Raman spectra show an asymmetric Raman intensity distribution in the range of 1060 to 1880  $\text{cm}^{-1}$  with a center around 1556  $\text{cm}^{-1}$ , which contains the structural information of the  $\text{sp}^2$  and  $\text{sp}^3$  sites and also confirms the amorphous carbon characteristic of the films [167].

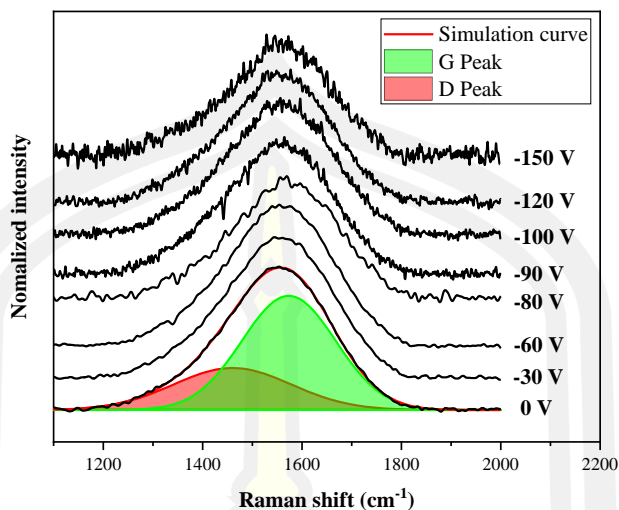


**Figure 4.43** Normalized Raman spectra and of the ta-C films deposited with the different substrate bias potential. The label at tail of spectra is applied substrate bias potential.

The values of  $I_D/I_G$  and G peak position are shown in Table 4.9 and plotted in Figure 4.44 as a function of the applied substrate bias potential. The  $I_D/I_G$  values decrease from 0.46 to a minimum value of 0.29 with the increase of substrate bias potential 0 to -80 V and then increase again to 0.42 for a film deposited by applied substrate bias potential of -150 V. This means that proportional to the number of rings at the edge of the grain decreased with the increase of substrate bias potential from 0 to -80 V and increase again for applied substrate bias potential higher than -90 V. While the G-peak position shows the opposite trend with  $I_D/I_G$  ratio.

The result can be explained by a three-stage model proposed by Ferrari et al [168]. This case uses the model in stage 3 ( $sp^2$  a-C to  $sp^3$  ta-C), decrease of the  $I_D/I_G$  ratio and increase of the G peak position indicate that the changes of the  $sp^2$  configuration from mainly rings to short chain [19], [169]. Which the G peak position in the range of  $1580 - 1600 \text{ cm}^{-1}$  related to the bond length of chains is shorter than that of the rings [183]. That means the ta-C films deposited by applying a substrate bias potential of -80 V, the film rich  $sp^3$  content. Therefore, the energy enhanced of  $C^+$  ions by substrate bias technique during the film growth, as a result in rearrangement of  $sp^2$  (amorphous carbon) to  $sp^3$  (tetrahedral amorphous carbon).



**Table 4.9** Analyzed Raman parameter of ta-C films deposited by varying substrate bias potential.

$V_{sb}$ (V)	D position ( $\text{cm}^{-1}$ )	FWHM of D ( $\text{cm}^{-1}$ )	G position ( $\text{cm}^{-1}$ )	FWHM of G ( $\text{cm}^{-1}$ )	$I_D$	$I_G$	$I_D/I_G$
0	1460.00	280.14	1573.28	222.43	31.64	68.36	0.46
-30	1448.93	243.82	1579.50	218.42	28.36	71.64	0.40
-60	1448.52	242.54	1579.96	218.81	26.86	73.14	0.37
-80	1445.57	235.38	1585.37	219.90	22.54	77.46	0.29
-90	1427.92	225.48	1584.44	216.87	24.30	75.70	0.32
-100	1444.09	239.50	1583.44	221.26	25.99	74.01	0.35
-120	1440.04	234.93	1583.66	214.96	27.29	72.71	0.38
-150	1445.12	252.97	1582.48	205.28	29.54	70.46	0.42

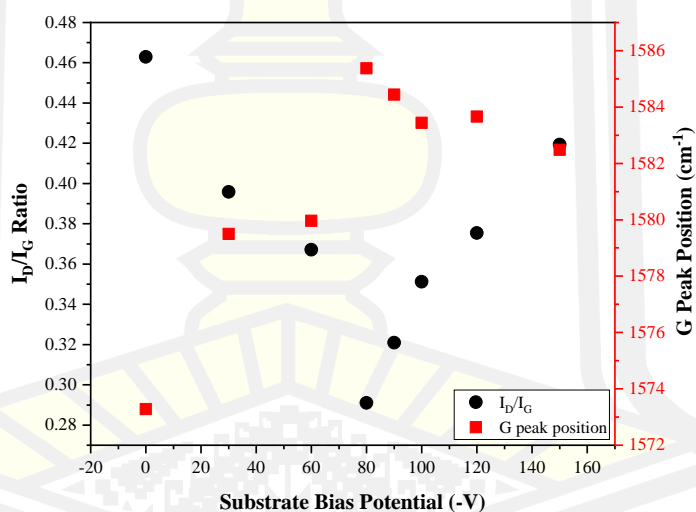


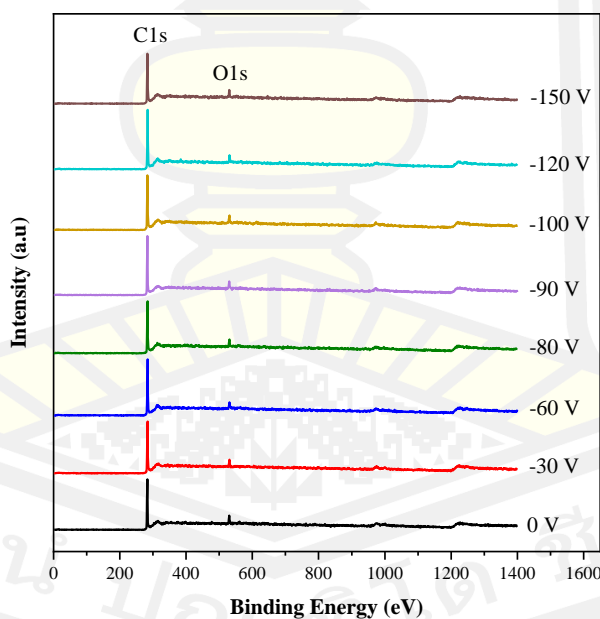
**Figure 4.44** Double plot of the  $I_D/I_G$  ratio (black dot) and the G peak position (red square) of the ta-C films deposited on Si substrate with a thickness of about 90 nm.

#### 4.2.2.4 XPS result

As the same with the ta-C deposited by plasma biasing technique. The chemical bonding, chemical states, and electronic structures of the ta-C films deposited by varying substrate bias potential were determined by X-ray photoelectron spectroscopy (XPS). The XPS measurement was performed using a PHI5000 Versa

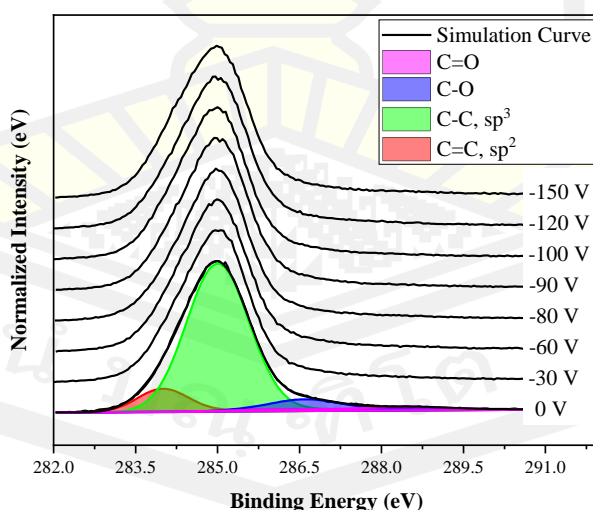
Probe II, ULVAC-PHI, Japan at the SUT-NANOTEC-SLRI joint research facility, Synchrotron Light Research Institute (SLRI), Thailand. The monochromatic  $\text{AlK}_{\alpha}$  X-ray (1486.6 eV) was used as an excitation source. All binding energies of the samples were calibrated with the C1s peak at 284.8 eV. The data were fitted by using Shirley background subtraction and sub-peak with Gaussian-Lorentzian function.

The XPS measurement was divided into parts: survey scanning and finely scanning. The survey scanning mode was used to detect the binding energy of photoelectron in a wide range from 0 - 1400 eV, in which cover the atoms of various elements are present on the film surface. In the survey spectra of ta-C films as shown in Figure 4.45, the photoelectrons with the binding energy at about  $285 \pm 0.5$  eV and  $532 \pm 0.5$  eV can be observed which corresponds to C1s and O1s respectively [170], [171]. It indicates that the film surface is not contaminated by other elements. In addition, the detection of photoelectrons with the binding energy of 980 and 1220 eV corresponds with O KLL and C KLL respectively [172].

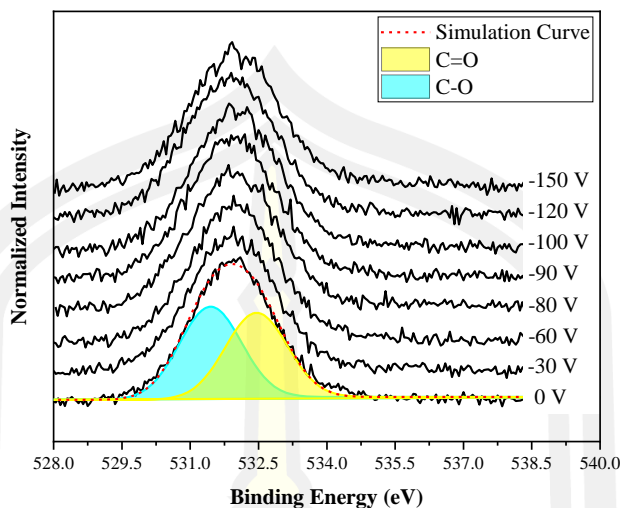


**Figure 4.45** Survey spectra of the ta-C films deposited on Si substrate with the thickness of about 90 nm. The label at the tail of spectra is applied substrate bias potential during the film growth.

To study the bonds of the carbon atoms within the film, the XPS measurement in finely scan was used. C1s spectra as shown in Figure 4.46, the spectra were background-subtract by Shirley function and then deconvoluted by Gaussian function fitting. The C1s spectra were deconvoluted into four peaks located at about  $284.1 \pm 0.2$  eV,  $285.0 \pm 0.2$  eV,  $286.5 \pm 0.3$  eV and  $288.5 \pm 0.3$  eV, which originate from C=C or  $sp^2$  bond, C-C or  $sp^3$  bond, C-O bond, and C=O bond, respectively [173]. Moreover, one of finely spectra is O1s, which indicate the bonds of oxygen atoms on the surface of films. O1s spectra as shown in Figure 4.47, the spectra were background-subtract by Shirley function and then deconvoluted by Gaussian function fitting. Under the C1s spectra presenting the C-O bond and C=O bond at about  $531.4 \pm 0.2$  eV and  $532.5 \pm 0.2$  eV respectively [174], [175]. Which correspond to the observed bonds of C1s spectra. The oxygen on the surface and content of the film is derived from the remaining oxygen atoms in the deposition chamber, which are sensitive to the reaction. When the plasma discharge occurs, these oxygens are also excitation and ionization to the oxygen ions, bonding with carbon atoms and depositing on the substrate. This result showed that the films don't have the contamination of metal atoms, this may be caused by atomic scattering from arcing on the surface of the substrate holder during the film's growth with the higher substrate bias potential (-80 to -150 V).



**Figure 4.46** C1s spectra of ta-C films deposited on Si substrate with a thickness of about 90 nm. The label at the tail of spectra is applied substrate bias potential.



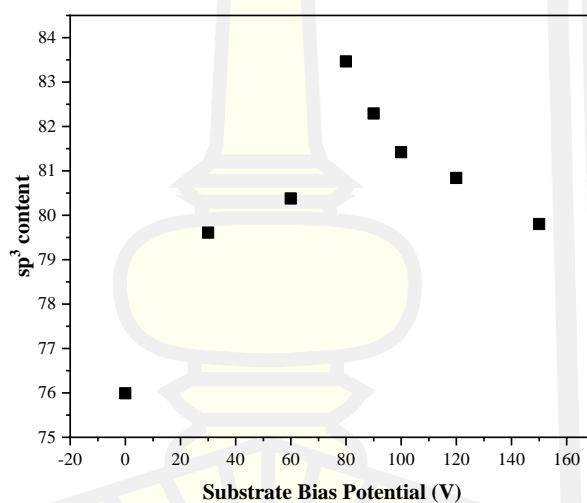
**Figure 4.47** O1s spectra of ta-C films deposited on Si substrate with a thickness of about 90 nm. The label at the tail of spectra is applied substrate bias potential.

Table 4.10 shows the composition of C=C or  $sp^2$  bond, C-C or  $sp^3$  bond, C-O bond, and C=O bond. The obtained C-C or  $sp^3$  contents in the ta-C films are further depicted in Figure 4.48, which clearly shows that adjusting the substrate bias potential from 0 V to -80 V leads to the increase of the  $sp^3$  content from 75.99% to 83.46%. And decrease to 79.80% again for substrate bias potential higher -90 V.

Raman spectroscopy and XPS test showed that the substrate bias technique can be enhanced the  $sp^3$  content of the ta-C films as the same plasma biasing technique. This was described by the densification model of Robertson [20]. For the low substrate bias potential (0 V to -60 V), the ions have low energy (15 eV to 62 eV) and do not have enough energy to penetrate the surface of the film, so they will just stick to the surface and remain in its lowest energy state with is  $sp^2$  bond. The substrate bias potential is higher than -80 V leading to high  $sp^3$  content in the films due to the energy of depositing ions higher than surface penetration threshold energy, this increases the probability to penetrate the surface and enter a subsurface interstitial site during the film growth. This will decrease the poor or pin hole and increase the probability to reform around carbon atoms at the surface of the film according to the new structure and density [20].

**Table 4.10** The fraction of chemical bonding in the ta-C films deposited by varying substrate bias potential.

Substrate bias potential (V)	C=C ( $sp^2$ )	C-C ( $sp^3$ )	C-O	C=O
0	13.42	75.99	7.19	3.40
-30	12.70	79.61	5.23	2.46
-60	11.32	80.37	5.86	2.44
-80	7.71	83.46	5.79	3.04
-90	8.75	82.29	6.23	2.73
-100	10.87	81.42	5.39	2.32
-120	11.03	80.84	4.85	3.28
-150	11.81	79.80	5.69	2.70



**Figure 4.48** The  $sp^3$  content of ta-C films as a function of substrate bias potential.

#### 4.2.2.5 XRR result

The structure of the ta-C films was related to  $sp^3$  content, which controls by applied substrate bias potential. Therefore, the mass density of the ta-C films deposited of Si substrate with the thickness of 85 nm was investigated by X-ray reflectometry.

The process parameter for XRR measurement is the same as the part of the plasma biasing technique. The XRR (Bruker D8 Advance) measurements were performed with Cu-K $\alpha$  monochromatic radiation ( $\lambda=0.15406$  nm), and the reflection

of X-rays were measured in the range of an incident angle,  $2\theta$ , from 0 to  $3.0^\circ$  by a step of  $0.005^\circ$ . The density values were obtained by fitting the measured XRR data with a simulated XRR curve using the Leptos 7.0 software. Which, the mass densities relate to the critical angle and film thickness relate to the oscillation period of the XRR profile.

The XRR profile of ta-C films as shown in Figure 4.49. The oscillation period of the XRR curve is nearly, it means that the thickness of the films is nearly. Figure 4.50(a) shows the thickness of films, it has values in the range of 82.7 nm to 85.2 nm. It indicates that the thickness of the film can be controlled by the process parameter (the offset of z position) due to the center of the deposition profile is not the same position in each substrate bias potential.

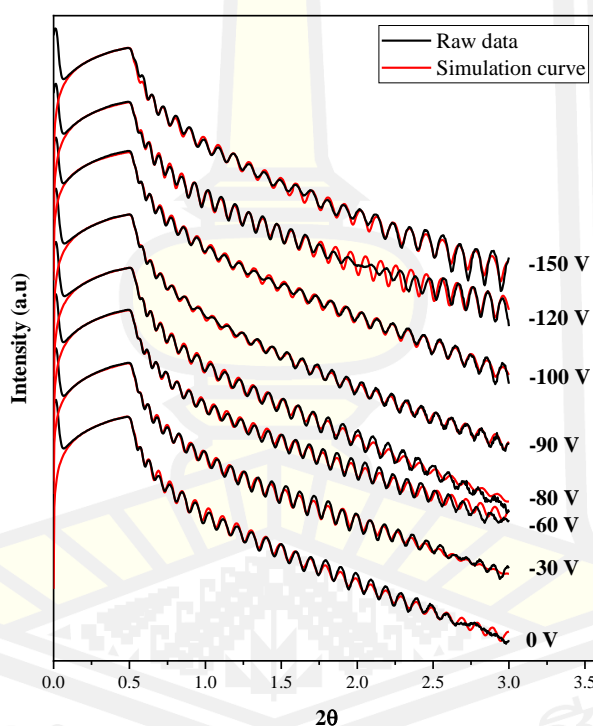


**Figure 4.49** The XRR profiles of ta-C films deposited on Si substrate by varying substrate bias potential.

Moreover, the critical angle of the reflection curve shift up to high  $2\theta$ , related to the increase of density of the ta-C films from  $3.08 \text{ g/cm}^3$  to a maximum value of  $3.28 \text{ g/cm}^3$  with the increase of the substrate bias potential from 0 V to -80 V. And



decrease again for applied the substrate bias potential higher than -90 V during the film growth.

The mass densities are in good agreement with the measured  $C^+$  ion energies, proving that the bombardment of the energetic  $C^+$  ions can overcome the subplantation threshold, resulting in a significant increase in the density of the films with the increase of substrate bias potential from 0 V to -80 V. Which the applied substrate bias potential as -80 V is an optimized condition for inducing the optimize energy of depositing ions leading to a bond rearrangement from the a-C to the ta-C, facilitating the densification of ta-C films. However, the density of ta-C films was decreased for substrate bias potential higher than -90 V. This result can be discussed by the thermal spike model, due to the kinetic energy of depositing ions transfer to thermal energy at the point of trajectory and diffuses outward by thermal diffusion in the film structure. As a result, creates an expanding front in which all the atoms are inside the film. This allows the atoms to diffuse back to the surface to relax the density of  $sp^3$  density to the lower  $sp^2$  density [20].

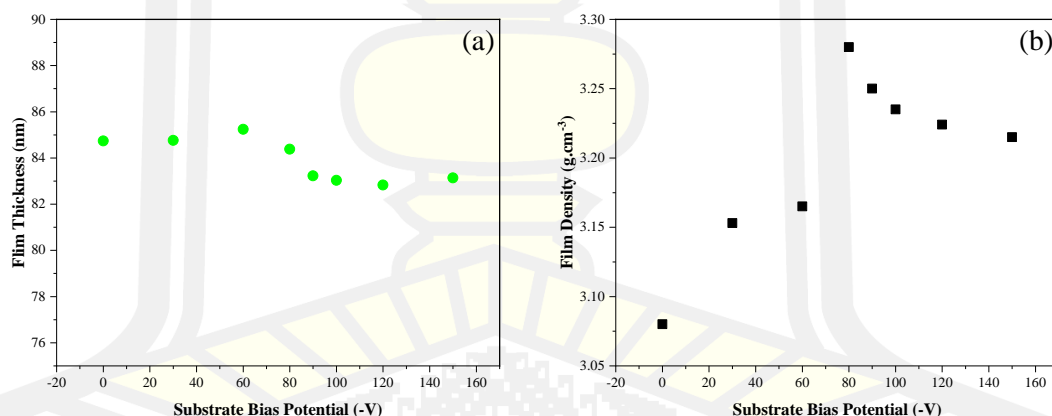


**Figure 4.50** Thickness of the ta-C films estimated by the period oscillation of XRR curve. And (b) density of the ta-C films deposited on Si substrate as a function of substrate bias potential.

#### 4.2.2.6 Electrical properties

From Raman spectroscopy, XPS, and XRR analysis, the  $sp^3$  content in the ta-C films as a function of substrate bias potential, in which  $sp^3$  content increase with the increase of substrate bias potential. It indicates that the  $sp^2$  content in the film decreased. The electrical properties of the ta-C films are strongly affected by the

different possible  $sp^2$  content in the ta-C films. Due to the  $sp^2$ -rich carbon films or graphite like carbon containing of free electrons within the structure. Therefore, the electrical conductivity of the ta-C thin films decreased by two times with increasing the  $sp^3$  content from 75.99% to 83.46%. The values of the electrical conductivity indicate an insulator character of the ta-C coating.

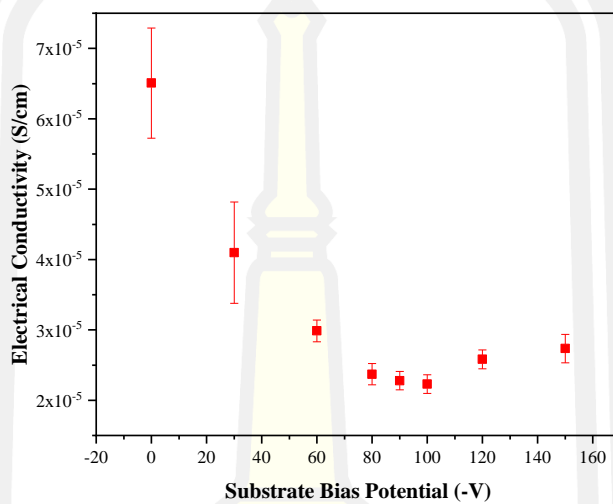


**Figure 4.51** Electrical conductivity of the ta-C films deposited on Si substrate with the thickness of about 85 nm by varying substrate bias potential.

#### 4.2.2.7 Uniformity of ta-C film

The problem for PVD deposition, especially the FCVA technique is the uniformity of the film due to the incident plasma on the sample are the beam characteristic leading to non-uniformity of the film. The system in this work has only one focusing coil, the mechanical technique was used for adjusting the substrate holder position in the z-axis of the system to prove the uniformity of the film. Therefore, this topic will present the result of the ta-C film uniformity.

The Si wafer was placed on the substrate holder at three-point as shown in Figure 4.52, the substrate holder has the offset as -2.5 cm (reference by a center of deposition chamber). The process parameter for ta-C deposition is as follows; the maximum arc current 720 A, repetition rate of 1 pulse/s, and deposition pulse 3600 pulses, in which the substrate holder is always rotated. Figure 4.52 shows the photo of the ta-C films sample on the SUS316 holder. The blue color zone is the ta-C film with

a thickness of 50 nm, which covers samples 1, 2, and 3. To confirm the uniformity of the film, the film was characterized by the XRR and XPS analysis.

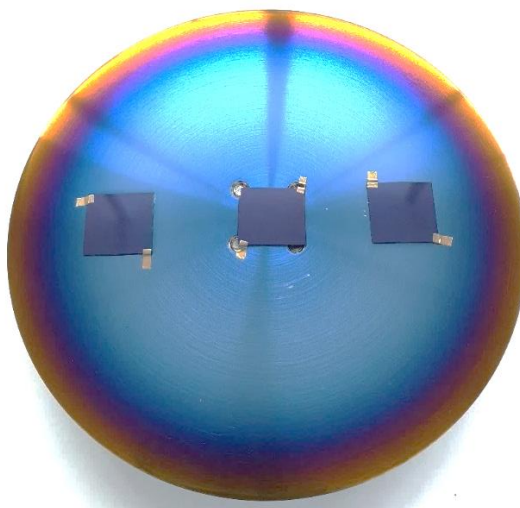


**Figure 4.52** Distribution of ta-C film on the substrate holder (grounded).

Figure 4.53 shows the XRR profile of the ta- C films at positions 1, 2, and 3, it showed that the oscillation curve has the same pattern, indicating that the film has the same properties. The analyzed data as shown in Figure 4.54, the thickness of the films is 49.43 nm, 49.89 nm, and 50.01 nm, while the density of the films is 3.103 g/cm<sup>3</sup>, 3.102 g/cm<sup>3</sup>, and 3.106 g/cm<sup>3</sup> for the sample at position 1, 2, and 3 respectively. Therefore, the thickness and density of the film are uniforms.

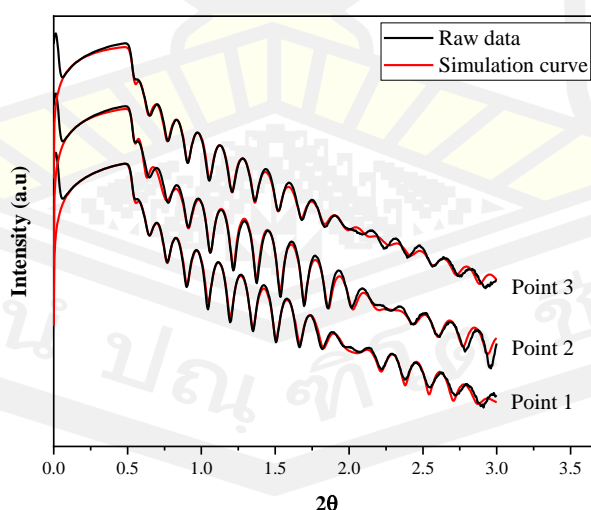


**Figure 4.53** The XRR profiles of ta-C films deposited on Si substrate. The label is the position of the sample on a substrate holder.

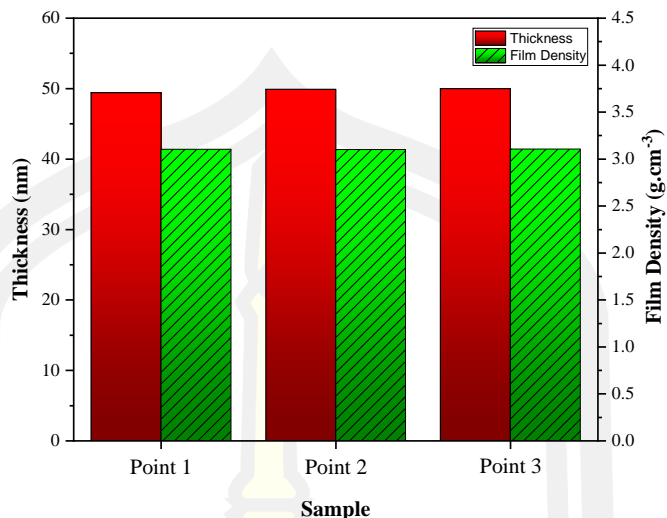


**Figure 4.54** Thickness and density of the ta-C films deposited on Si substrate were estimated by XRR analysis.

Moreover, the chemical bonding at each position was revealed by the XPS test. The C1s spectra of the film at positions 1, 2, and 3 as shown in Figure 4.55, the spectra were background-subtract by Shirley function and then deconvoluted by Gaussian function fitting. The C1s spectra were deconvoluted into three peaks located at  $284.1 \pm 0.2$  eV,  $285.0 \pm 0.2$  eV,  $286.5 \pm 0.3$  eV and  $288.5 \pm 0.3$  eV, which originate from C=C  $sp^2$  bond, C-C  $sp^3$  bond, C-O bond, and C=O bond, respectively [170], [171]. The  $sp^3$  content of the films is 76.72%, 76.54%, and 76.8% for ta-C film positions 1, 2, and 3 respectively. Moreover, the characteristic of the C1s spectra is very nearly, which C1s spectra of ta-C film at three points were plotted in the same y scale as shown in Figure 4.56. The line of spectra are closely overlapped, This means that the films have the same structure, chemical bonds, and the same amount of bonds.

Therefore, the films are uniform, which uniform of the film can adjust by the offset of the substrate holder position. So, for each process parameter (substrate bias potential) must be fine the optimized offset position.

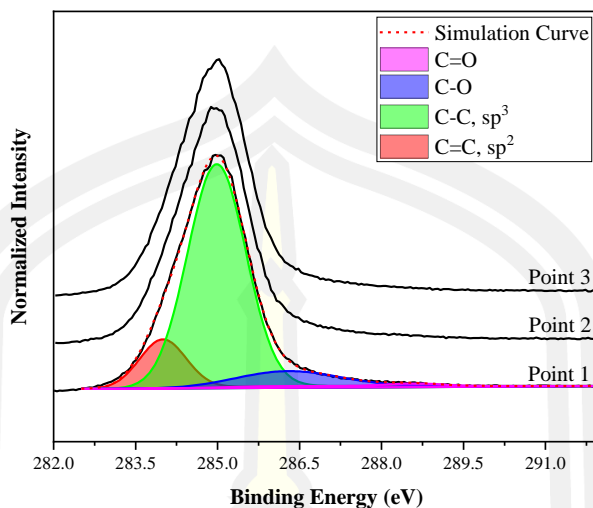


**Figure 4.55** C1s spectra of the ta-C films deposited on Si substrate. The label is the position of the sample on a substrate holder.

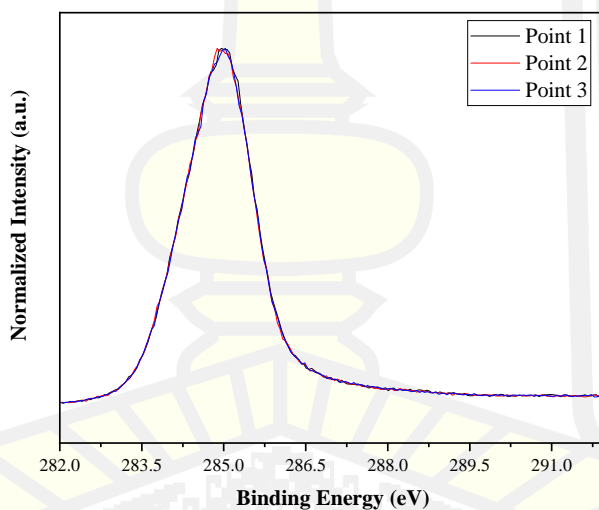


**Figure 4.56** Comparison of C1s spectra of the ta-C films deposited on Si substrate at three positions on a substrate holder.

### 4.3 a-C:H deposition

This topic will be discussed about a-C:H deposition such as the process for a-C:H deposition, process parameter, characteristics of the film, and analyzed result.

#### 4.3.1 Survey for a-C:H deposition

In this work, the a-C:H film will be deposited by a linear anode layer ion source and use the  $C_2H_2$  gas and Ar gas for the precursor of carbon atoms and excited

gas respectively. From the previous study, we know that the plasma beam characteristic generated by the anode layer ions source or linear anode layer ion source is cone circular beam and cone rectangular beam respectively [184]–[186]. In addition, the distribution of the depositing atom and ions depends on applied discharge potential [187], [188]. Therefore, to understand the behavior and process parameter of a-C:H deposition by using a linear anode layer ion source (L-ALIS), Therefore, it is necessary to study in the preliminary first.

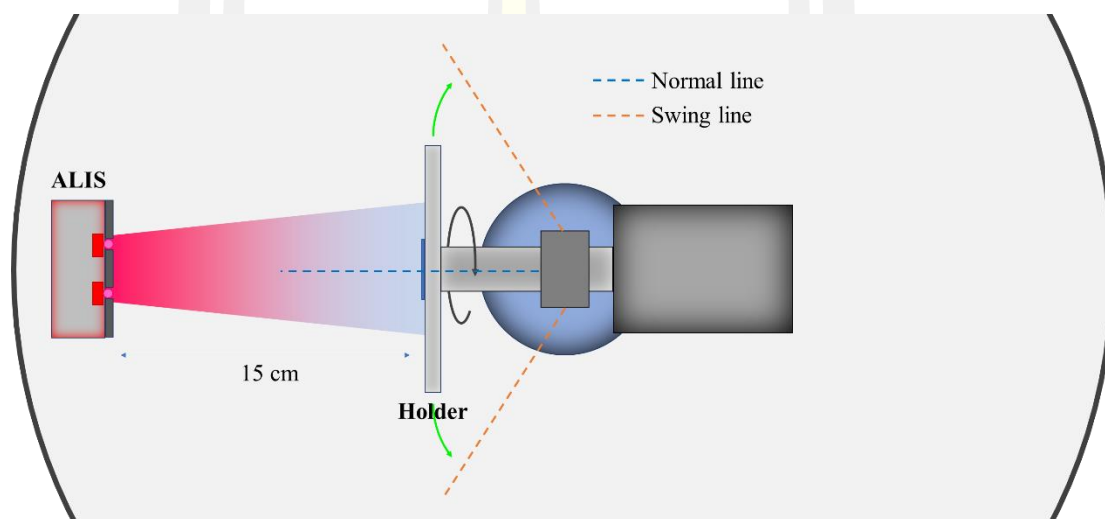


**Figure 4.57** Diagram for a-C:H deposition.

The p-type silicon (100), size 10 mm × 10 mm with a thickness of  $525 \pm 15 \mu\text{m}$  is used as a substrate, it was installed on a substrate holder and loaded in the deposition chamber. The position of a substrate holder has x offset or substrate distance is 15 cm, y and z offset is 0 cm. Before the film deposition, Si substrate was cleaned at 10 min by using an anode layer ion source (ALIS) with the discharge potential and discharge current being 1.4 kV and 8.8 mA respectively to remove contamination and oxide layer on the Si surface. The substrate holder rotates around the x-axis as well as the cleaning time. And then, the a-C:H film is deposited on Si substrate by using an L-ALIS source. The substrate holder is swing mode as shown in Figure 4.57, (the holder swing to 0 is  $\pm 40$  degrees reference with normal line) and the substrate holder life in the rotate state. The process parameter as follows.

- Ar gas flow rate : 10 sccm

- $C_2H_2$  gas flow rate : 30 sccm
- Operating pressure : 0.0024 torr
- Substrate distance : 15 cm
- Deposition time : 10 minuet, 15 minuet for +800 V
- Study parameter : discharge potential 0 to +1600 V

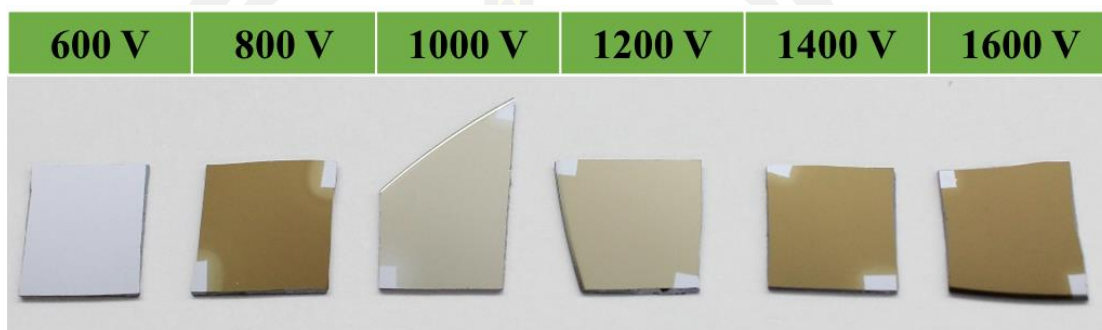


**Figure 4.58** The a-C:H films deposited on Si substrate by varying discharge potential.

The physical characteristics of a-C:H films as shown in Figure 4.58. From the observation, the film has good uniformity due to an ALIS with the size of 30 mm × 200 mm, the plasma beam will be covered the size of the substrate holder. Moreover, it means that the substrate holder system has the performance for controlling the uniformity of the films.

The thickness of the samples was investigated by an X-ray reflectometer or XRR (Bruker D8 Advance) measurements performed with Cu-K $\alpha$  monochromatic radiation ( $\lambda=0.15406$  nm). The thickness and density of the films were obtained by fitting the measured XRR data with a simulated XRR curve using the Leptos 7.0 software. X-ray reflectivity was measured in the range of an incident angle,  $2\theta$ , from  $0^\circ$  to  $3.0^\circ$  by a step of  $0.005^\circ$ . Which, the thickness of the film is related to the oscillation period of the XRR profile.

The XRR profile of a-C:H films are present in Figure 4.59, found that the period oscillation of the XRR curve is narrow down, which means that the thickness of the film increased with the increase of applied discharge potential. Therefore, the deposition rate of the a-C:H film will be increased with the increase of applied discharge potential as shown in Figure 4.60.



It can be explained that for the generating process of the ion beam, electrons are an important parameter to gas ionization and excitation. When gas will be excited and ionized into ion and free-electron, the electrons move to the anode electrode and the ion pushed out from the anode electrode due to the gradient of potential ( $\nabla^2 V$ ). Poisson's equation can explain and use to find the ion current density in the simplest approach, the maximum current density is given by the classical Child-Langmuir law [189]–[191].

$$J = \frac{4\varepsilon_0}{9D^2} \left( \frac{2q}{m} \right)^{1/2} V_d^{3/2} \quad (4.1)$$

Where  $\varepsilon_0$  is the vacuum permittivity,  $D$  is the gap distance between the anode and cathode electrode,  $q$  and  $m$  are the charge and mass of the extracted particle respectively, and  $V_d$  is the applied discharge potential. We can use equation 4.1 to consider the incident ion flux on the surface of sample combined with consideration in conjunction with other plasma physics knowledge as follows.

- Ion current density  $J_i = I_i / A$
- Ion current in the material  $I_i = n_i e v_i A$
- The ion flux at the sample is  $\Gamma_i = n_i v_i$  where  $n_i$  is ion density and  $v_i$  is ion velocity.

The above considerations enable the writing of ion flux equations as

$$\Gamma_i = \frac{I_i}{eA} = \frac{J_i}{e} \propto C \frac{V_d^{3/2}}{D^2} \quad (4.2)$$

Where  $C$  is constance, so the ion flux direct variation with discharge applied or discharge potential. The ion flux is the numbering of bombardment ions on the sample, which is directly proportional to the deposition rate. Therefore, the deposition rate will be increased with the increase of applied discharge potential [192].

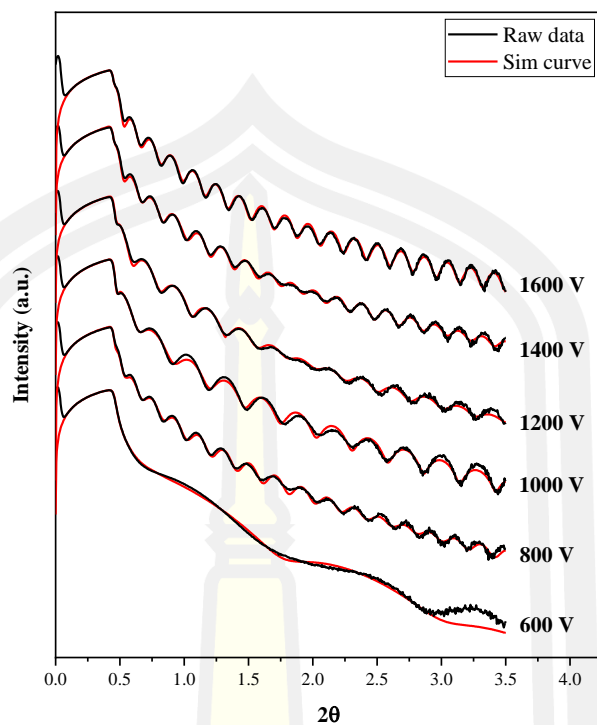


**Figure 4.59** XRR profile of the a-C:H films deposited on Si substrate by varying applied discharge potential.

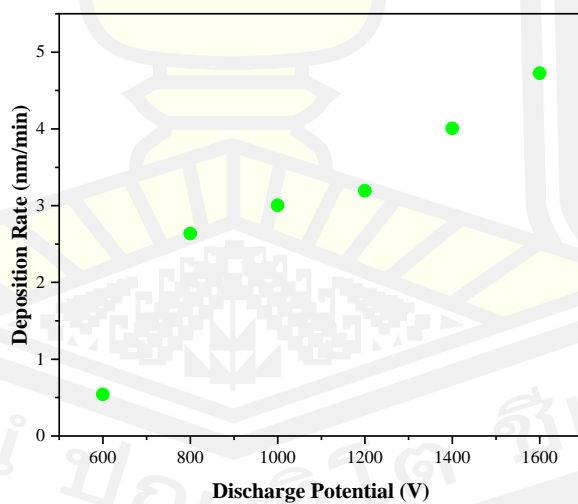


**Figure 4.60** Deposition rate of the a-C:H films as a function of applied discharge potential.

### 4.3.2 a-C:H film properties

From the survey study, the deposition rate of a-C:H films increased with the increase of applied discharge potential. To compare the microstructure of a-C:H films, the thickness of the films must be the same. Therefore, this topic will be given in detail of a-C:H deposition with a thickness of 90 nm. The deposition process is the same as the survey study. But, to control the thickness of the films, the deposition time has changed as shown in Table 4.11.

**Table 4.11** Process parameter of a-C:H deposition

Discharge		Ar (sccm)	C <sub>2</sub> H <sub>2</sub> (sccm)	deposition time
Potential (V)	Current (mA)			
800	8.6	10	30	37 min + 18 sec
1000	10.5	10	30	35 min + 41 sec
1200	12.9	10	30	31 min + 14 sec
1400	14.4	10	30	22 min + 42 sec
1600	16.8	10	30	21 min + 16 sec

Figure 4.61 shows sub of the a-C:H films on Si substrate deposited with a LAIS by varying discharge potential and controlling the thickness of 90 nm by using deposition pulse are present in Table 4.11. The color of the films is blue sky, which is the same color for all samples. It means that the thickness of the films is close. The microstructure, electrical properties, and mechanical properties were investigated by Raman spectroscopy, XPS, XRR, and four point probe respectively.

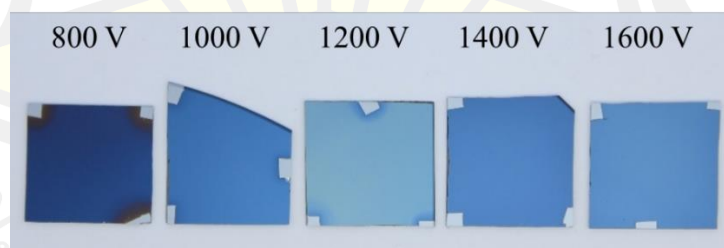


**Figure 4.61** The a-C:H films on Si substrate deposited by varying discharge potential, which controls the thickness of 90 nm.

#### 4.3.2.1 Raman spectroscopy

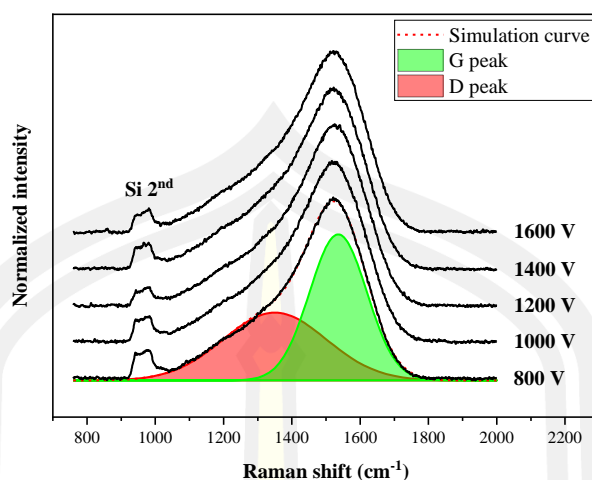
The microstructural properties of a-C:H films were estimated by using Raman spectroscopy (Bruker, SENTERRA). The laser wavelength of 532 nm was used and

pointed into the films (laser power is 5 mW and resolution 9 to 12  $\text{cm}^{-1}$ ), measurement in the range of 50 to 2750  $\text{cm}^{-1}$ . The Raman spectra were curve-fitted by ORIGIN-2018, which through subtracting background to evaluate the  $I_D/I_G$  ratio, the G peak position, which can tell the trend of the  $\text{sp}^3$  contents in the a-C:H films.

In order to describe the microstructure of the a-C:H films it is necessary to discuss the intensity ratio  $I_D/I_G$ , the full width at half maximum of the G-band (FWHM of G peak) and G peak position. These parameters are closely related to the density, size and structure of the  $\text{sp}^2$  clusters, which in turn are closely related to the  $\text{sp}^3$  content in the a-C:H films.

First, it has to be considered, that the  $I_D/I_G$  ratio is a measure of the size of the  $\text{sp}^2$  phase organized in rings [193]. If the  $I_D/I_G$  ratio becomes lower or zero, the  $\text{sp}^2$  phase is organized rather in chains, whereas a higher  $I_D/I_G$  ratio is an indication of an increase of the  $\text{sp}^2$  phase in aromatic rings. Thus, if no D-band is visible, no  $\text{sp}^2$  carbon rings exist in the material [194]. For a-C:H films, a lower  $I_D/I_G$  ratio is connected with higher overall  $\text{sp}^3$  content [166], [194]. However, carbon is  $\text{sp}^3$  bonded in a-C:H films also to hydrogen, an increase in  $\text{sp}^3$  content does not always mean an increase in density, hardness, and other mechanical properties of the films [193], [194].

For a-C:H with hydrogen contents over 25% the overall of  $\text{sp}^3$  content can be increased, which the  $\text{sp}^3$  content is the sum of C–C  $\text{sp}^3$  and C–H  $\text{sp}^3$  bonded [195], [196]. Thus, utilizing the  $I_D/I_G$  ratio only, it is difficult to estimate the bonding regimes in a-C:H films. To investigate the structure of the films in more detail it is necessary to focus also on the FWHM of G peak. The FWHM of the G peak is a key parameter of monitoring structural disorder in amorphous carbon films. This structural disorder of the film arises from the bond angle and bond length distortions. The lower FWHM of G peak is related to a more defect-free and ordered of film structure, while a higher FWHM of G peak is related to an increase in disorder. The effect originates in the higher bond length and higher bond angle in more disordered material [193].



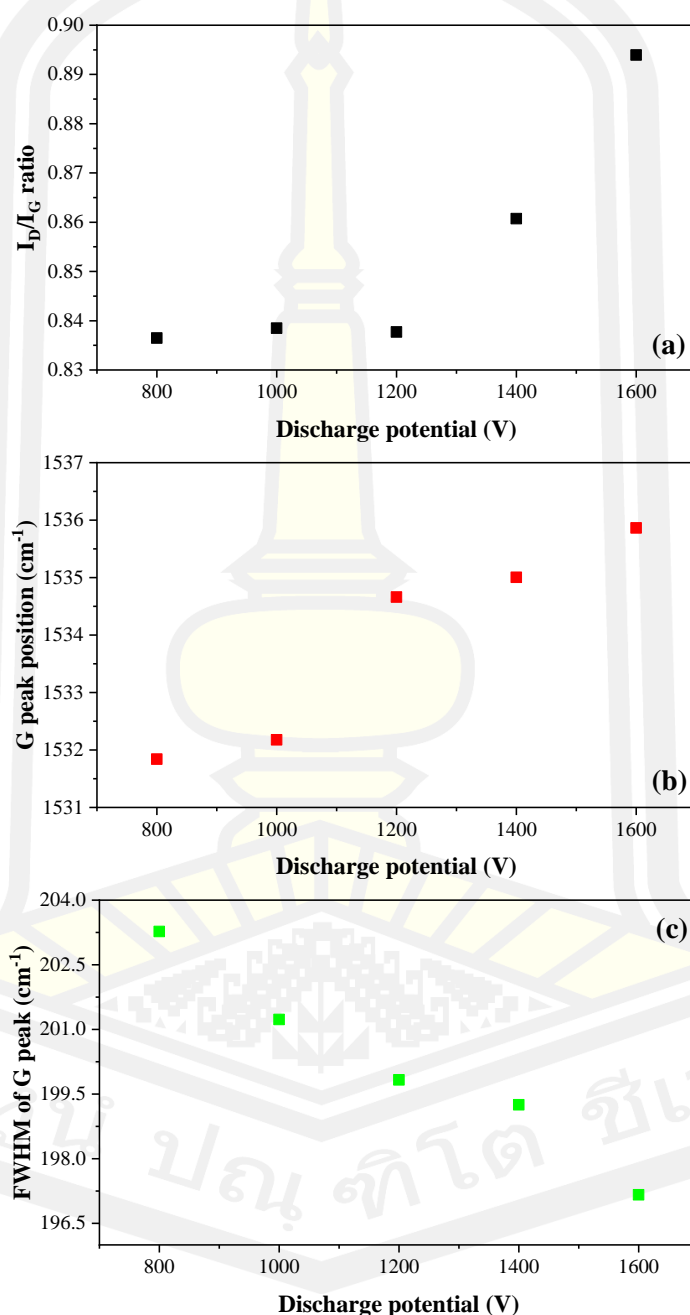
**Figure 4.62** Normalized Raman spectra and of the a-C:H films deposited with the different discharge potential. The label at the tail of spectra is applied discharge potential for an anode electrode of an L-ALIS.

Figure 4.62 shows the Raman spectra of a-C:H films deposited using an L-ALIS by varying applied discharge potentials. The Raman spectra of the films were first treated with linear background removal and the D and G peaks were deconvoluted with two Gaussian functions. The Raman spectra show an asymmetric Raman intensity distribution in the range of 930 to 1800  $\text{cm}^{-1}$  with a center around 1524  $\text{cm}^{-1}$ , which contains the structural information of the  $\text{sp}^2$  and  $\text{sp}^3$  sites and also confirms the amorphous carbon characteristic of the films [167]. In addition, in some spectra found symmetric Raman intensity distribution is centered around 960  $\text{cm}^{-1}$ , which corresponds to the Si 2<sup>nd</sup> order [197], [198].

**Table 4.12** Analyzed Raman parameter data of the a-C:H films.

$V_d$ (V)	D position ( $\text{cm}^{-1}$ )	FWHM of D peak ( $\text{cm}^{-1}$ )	G position ( $\text{cm}^{-1}$ )	FWHM of G peak ( $\text{cm}^{-1}$ )	$I_D$	$I_G$	$I_D/I_G$
800	1350.00	355.00	1531.84	203.27	45.55	54.45	0.84
1000	1350.00	365.00	1532.17	201.23	45.56	54.34	0.84
1200	1352.24	380.00	1534.66	199.83	45.58	54.42	0.84
1400	1341.71	380.00	1535.01	199.25	46.26	53.74	0.86
1600	1347.11	390.00	1535.86	197.16	47.20	52.80	0.89

Table 4.12 and Figure 4.63 shows the analyzed data of Raman spectra as a function of the applied anode bias potential. The  $I_D/I_G$  ratio of the films as shown in Figure 4.63(a), an increases from 0.84 to 0.89, while the G peak position shifts up to a high Raman shift, indicating that an increase of the  $sp^2$  phase in aromatic rings or  $sp^3$  trend to decrease with the increase of discharge potential from 800 V to 1600 V



**Figure 4.63** Double plot of the  $I_D/I_G$  ratio (black dot) and the G peak position (red square) of the a-C:H films deposited on Si substrate with a thickness of about 90 nm.

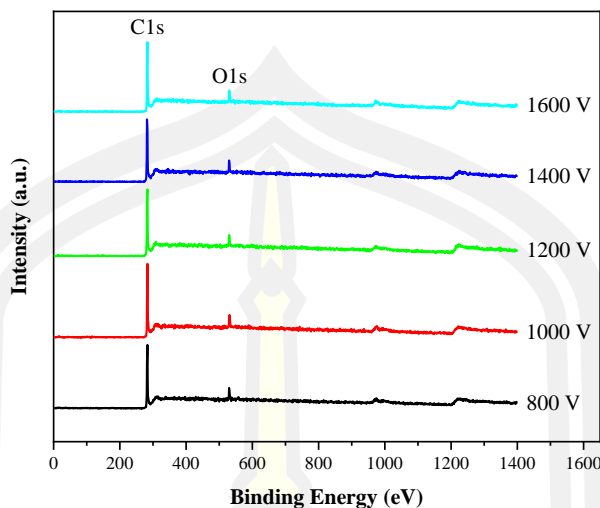
In order to confirm the trends derived from the intensity ratios and G peak position, the FWHM of the G peak is used to reveal information about the structural variance induced by changes in the process parameters. For films deposited at a discharge voltage of 800 V, a FWHM of the G peak of  $203.27\text{ cm}^{-1}$ , which decreases linearly to  $197.16\text{ cm}^{-1}$  for a discharge voltage of 1600 V as shown in Figure 4.63(c). The trends in FWHM of G peak completely confirm the observed behavior that the films at the lowest discharge voltage have increased structural disorder. Indicate that an increase of discharge potential leads to a decrease in disorder (increase  $\text{sp}^2$  phase in aromatic rings), which can here be linked to an increase in  $\text{sp}^3$  content in the films. The high FWHM of G peak of  $203.27\text{ cm}^{-1}$  (fitted with a Gaussian function) for the most disordered film deposited at the lowest ion energy (lowest discharge potential) suggests the classification of the deposited film to the structural class of ta-C:H film [193].

#### 4.3.2.2 XPS result

The chemical bonding and chemical state of a-C:H films were investigated by the X-ray Photoelectron Spectroscopy technique or XPS. The process parameters for XPS as the same as topic 4.2.1. The XPS measurement was divided into two parts: survey scanning and finely scanning. In the case of survey scanning, it is used to measure binding energy in a wide range from 0 to 1400 eV, in which atoms of various elements are present on the film surface. The survey spectra of a-C:H films deposited on Si substrate by varying discharge potential as shown in Figure 4.64, the photoelectrons with the binding energy  $285\pm 0.5\text{ eV}$  and  $532\pm 0.5\text{ eV}$  can be observed which corresponds to C1s and O1s respectively [199]–[201]. In addition, the detection of photoelectrons with the binding energy of 980 and 1220 eV corresponds with O KLL and C KLL respectively [172].

Although, the photoelectrons of other elements cannot be observed on XPS spectra. But the design, structure, and high-discharge potential mechanism of L-ALIS, it have a probability of metal atom (iron, Fe) emission at the cathode electrode of the source and deposition in the a-C:H films. Therefore, to confirm this result must be use any technique of detecting these elements such as an Emission Dispersive X-ray or EDX etc.,

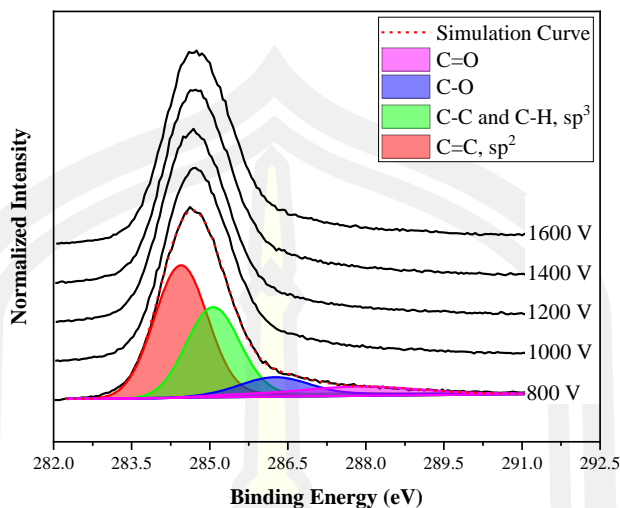




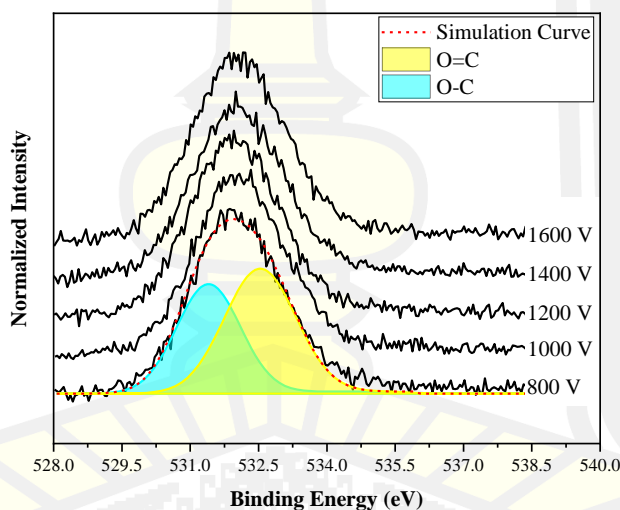
**Figure 4.64** Survey spectra of a-C:H films with the thickness of 85 to 90 nm deposited by varying discharge potential.

The finely scan mode of the XPS measurement was used to study the bonding of the carbon atoms within the film. C1s spectra as shown in Figure 4.65, the spectra were background-subtract by Shirley function and then deconvoluted by Gaussian function fitting. The C1s spectra were deconvoluted into four peaks located at  $284.1 \pm 0.2$  eV,  $285.0 \pm 0.2$  eV,  $286.5 \pm 0.3$  eV and  $288.5 \pm 0.3$  eV, which originate from C=C  $sp^2$  bond,  $sp^3$  bond, C-O bond, and C=O bond, respectively [173]. The  $sp^3$  peak under C1s spectra is the sum of C-C and C-H due to the binding energy are closely of 284.9 eV and 285.1 eV respectively [195], [196]. In addition, the shape of C1s peaks of the a-C:H films are different from the C1s peaks of the ta-C films, indicating that the  $sp^3$  and  $sp^2$  content in the films are different.

Figure 4.66 shows the O1s spectra of the a-C:H films, the spectra were background-subtract by Shirley function and then deconvoluted by Gaussian function fitting. Under the O1s spectra presenting the C-O bond and C=O bond at  $531.4 \pm 0.2$  eV and  $532.5 \pm 0.2$  eV respectively [174], [175]. This result corresponds with the bonds in the C1s spectra.



**Figure 4.65** C1s spectra of the a-C:H films with the thickness of 85 nm deposited by varying discharge potential.



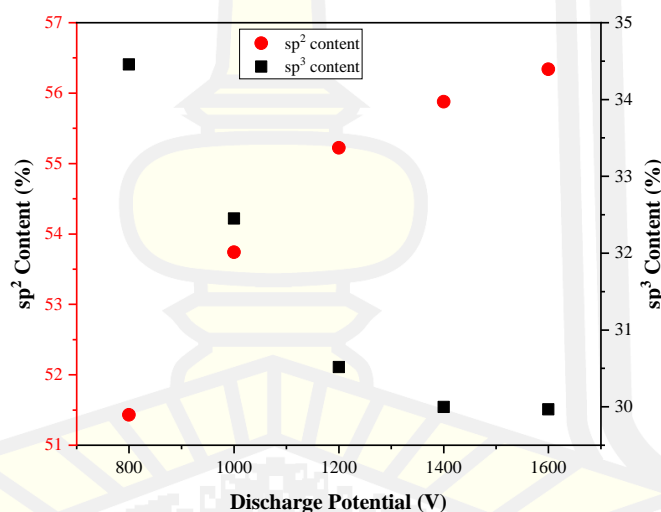
**Figure 4.66** O1s spectra of the a-C:H films with the thickness of 85 nm deposited by varying discharge potential.

Table 4.13 shows the composition percentage of C=C or  $sp^2$  bond, C-C and C-H in  $sp^3$  bond, C-O bond, and C=O bond. The C-O content and C=O content has value in the range of 8.24 to 8.45 % and 5.43 to 5.88 % respectively, in which closely content and non-significant in each the a-C:H films. The obtained C=C or  $sp^2$  and C-C or  $sp^3$  contents in the a-C:H films were plotted with the double y plot as shown in Figure 4.67.

The  $sp^2$  content increased from 51.43 to 56.34 % and  $sp^3$  content decreased from 34.45 to 29.97 % with the increase of the discharge potential, which the content of these bonds significantly related to the discharge potential. This result corresponds with Raman spectroscopy analysis.

**Table 4.13** The fraction of chemical bonding in the a-C:H films deposited by varying discharge potential.

discharge potential (V)	C=C ( $sp^2$ )	C-C, C-H ( $sp^3$ )	C-O	C=O
800	51.43	34.45	8.25	5.87
1000	53.74	32.45	8.38	5.43
1200	55.22	30.52	8.45	5.81
1400	55.88	30.00	8.24	5.88
1600	56.34	29.97	8.26	5.44



**Figure 4.67** The  $sp^2$  and  $sp^3$  content of a-C:H films as a function of discharge potential.

The a-C:H films deposited by an L-ALIS, the films growth under the high flux (in the range of  $10^{16} \text{ m}^{-2}\text{s}^{-1}$ ) [187], [202], which can be discussed from equation 4.2. The flux of depositing ions will be increased with the increase of discharge potential. Moreover, the means energy of depositing is higher than the ions generated by FCVA, magnetron sputtering, PECVD and RF-PECVD. Murmu et al showed that the energy per atom of  $\text{C}_m\text{H}_n^+$  generated by ALIS has a value in the range of 2000 to 7000 eV for

the discharge potential of 8000 V [203]. This result leading to penetration of the depositing ions in the films. But the means energy of depositing ions is higher than the surface penetration threshold energy ( $E_i \gg E_p$ ), the kinetic energy of depositing ions transfers to thermal energy and diffuses over the film surface leading to the relaxation of carbon structure in the films. These results affected on microstructure in a bond rearrangement from  $sp^3$  to  $sp^2$  bonded and introduce the transfers from diamond like carbon (DLC) to graphite like carbon (GLC) [20], which gives rise to a decrease in the local density of the films.

#### 4.3.2.3 XRR result

Raman spectroscopy and XPS measurement show that the a-C:H films are high  $sp^2$  content and low  $sp^3$  content. In order to find the relation between discharge potential and density of the a-C:H film deposited by an L-ALIS, the XRR measurement was used for estimates the density of the films.

The density of a-C:H films were investigated by XRR (Bruker D8 Advance) measurements performed with Cu-K $\alpha$  monochromatic radiation ( $\lambda=0.15406$  nm). The density values were obtained by fitting the measured XRR data with a simulated XRR curve using the Leptos 7.0 software. XRR was measured in the range of an incident angle  $2\theta$  from 0 to  $3.0^\circ$  by a step of  $0.005^\circ$ . Which, the mass densities related to the critical angle and film thickness relate to the oscillation period of the XRR profile.

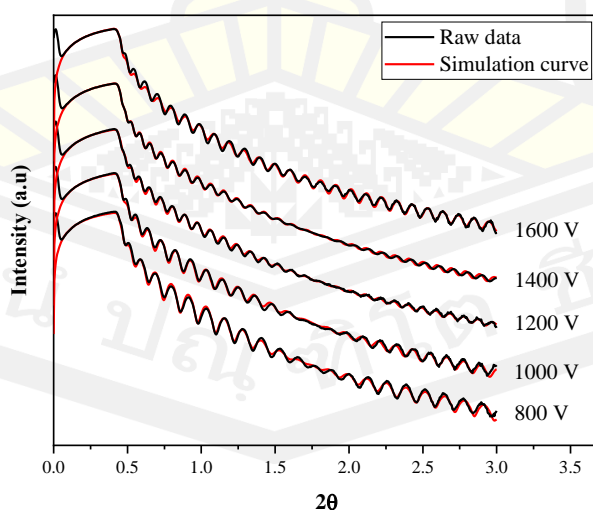


**Figure 4.68** XRR profile of a-C:H films deposited by varying discharge potential.

Figure 4.68 shows the XRR profile of the a-C:H films deposited on Si substrate by varying applied discharge potential and controlling the thickness in the range of 90 nm. The critical angle smaller shift to lower  $2\theta$  with the increase of discharge potential, while the oscillation period has closely period, indicating that the film has the thickness as the same, corresponding to the analyzed data as shown in Figure 4.69(a). The thickness of the films has a value in the range of 85.78 to 90.39 nm. Therefore, the structural properties of the films can be compared. Densities of the a-C:H films were calculated using the critical angle for the total external reflection as shown in Figure 4.69(b). Densities of a-C:H films decrease from 2.31 to 2.22 g/cm<sup>3</sup> with the increase of the applied discharge potential.

This result corresponds with the Raman spectroscopy and XPS analysis due to the density of DLC film related to  $sp^3$  content in the film [20]. Most properties of a-C:H depend on the incident ion energy per C atom [35]. Although the maximum in density for a-C:H can be prepared from acetylene gas [20]. However, the depositing species is molecular ion  $C_mH_n^+$ , which the hydrogen is the main composition. For this reason, the film have complex structure and disorder [20]. Especially the flux and energy of depositing molecular ion is higher than other deposition techniques, leading to thermal heating during the film growth and relaxation of  $sp^3$  density to low  $sp^2$  density.

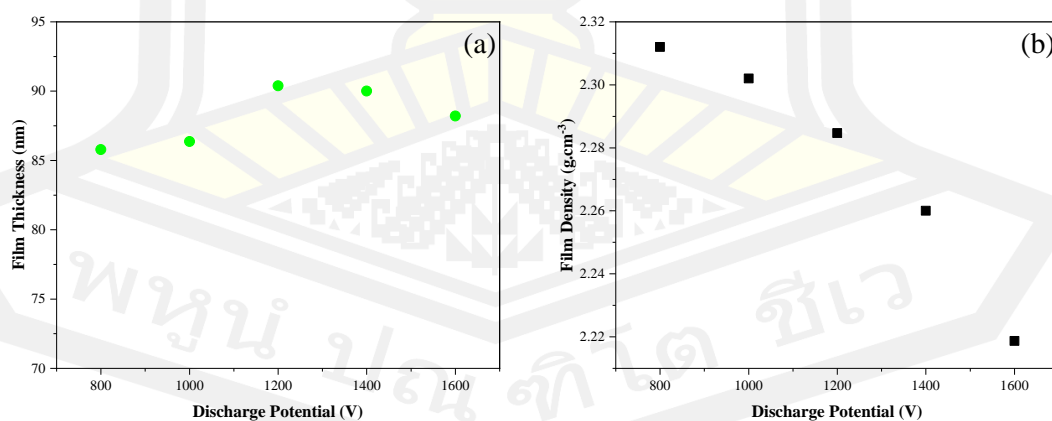


**Figure 4.69** (a) Thickness and (b) density of a-C:H films on Si substrate deposited by a LAIS.

#### 4.3.2.4 Electrical properties

Raman spectroscopy, XPS, and XRR test found that the  $sp^3$  content decrease with the increase of applied discharge potential. It indicates that the  $sp^2$  content in the film increased. Normally, the electrical properties of the ta-C films are strongly affected by the different possible  $sp^2$  hybridization of the carbon atoms in the a-C:H films.

Therefore, to estimate the electrical properties of the a-C:H films, an in-house four point probe will be used. The DC source meter unit (SMU, Keithley 2450) was connected with the probe, which uses ohmmeter mode and 4-wire sensing. For each sample was measured in 20 points. The measured data is sheet resistance, which can calculate to electrical resistivity and electrical conductivity.

The electrical conductivity of a-C:H films is shown in Figure 4.70. Therefore, the electrical conductivity of the a-C:H films increased by 5 times from  $3.0 \times 10^{-5}$  S/cm to  $2.3 \times 10^{-4}$  S/cm with decreasing the  $sp^3$  content from 34.45% to 29.97%. Due to an increase of free electrons in the graphite structure or  $sp^2$  bonded.

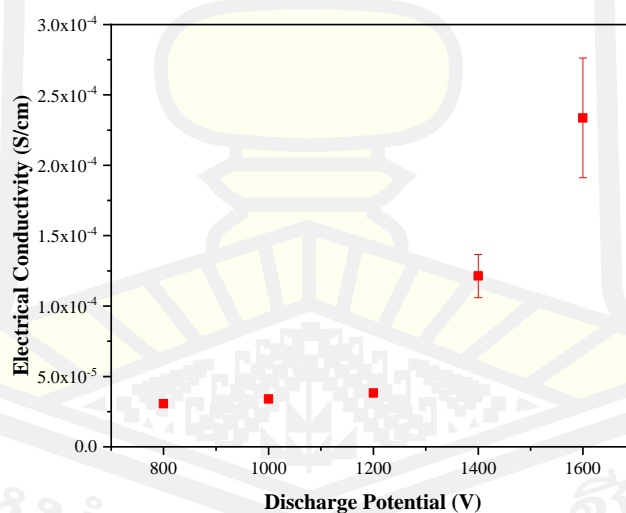


**Figure 4.70** Electrical conductivity of a-C:H films deposited on Si substrate by an L-ALIS.

#### 4.4 Chromium deposition

To increase the adhesion of multilayer amorphous carbon film with SUS304 substrate, the chromium interlayer (Cr) was used. Normally, the magnetron sputtering

technique was used to fabricate Cr films. DC, bipolar, HiPIMS and Bipolar HiPIMS power was applied to the target to generate Cr vapor. HiPIMS and Bipolar HiPIMS techniques are the best for high-quality Cr film deposition (dense and smooth surface) due to the high ionization rate of Cr atoms. The Cr atoms are deposited in the layer by layer leading to a high density and smooth surface with the influence of ion bombardment [204]. Therefore, multilayer amorphous carbon has a Cr layer with a thickness of about 250 nm to improve adhesive properties with the SUS304 substrate. This topic will be given in detail of Cr deposition.

In order to find optimized conditions for Cr interlayer (structure and deposition rate), there should be a survey study. For the survey study, p-type silicon (100), size 10 mm × 10 mm with a thickness of  $525 \pm 15 \mu\text{m}$  is used as a substrate, it was installed on a substrate holder and loaded in the deposition chamber. The x offset or substrate distance is 12 cm (from sample to Cr target on magnetron source), y and z offset is 0 cm. Before the film deposition, the Si substrate was cleaned at 10 min by using an ALIS with the discharge potential and discharge current being 1.4 kV and 8.8 mA respectively to remove contamination and oxide layer on the Si surface. The substrate holder rotates around the x-axis as well as the cleaning time. And then, the Cr film is deposited by a magnetron sputtering source with the process parameter as follows.

- Target material : Cr (diameter 2-inch, purity 99.99%)
- Ar gas flow rate : 100 sccm
- Angle valve position : open 15%
- Operating pressure : 2 Pa
- Substrate distance : 12 cm
- Discharge power :  $P_{\text{avg}} = 240 \text{ W}$ , 1 Hz, 200  $\mu\text{s}$
- Deposition time : 1 minuet
- Study parameter : substrate bias potential ( $V_b$ )

The DC power supply (HSPY-400-01, 400  $V_{\text{max}}$ , and 1  $A_{\text{max}}$ ) was applied to substrate bias potential, which controls the potential of 0 V, -100 V, -200 V, and -300 V. The substrate bias current depending on the applied substrate potential as shown in Table 4.14.



**Table 4.14** Process parameter of the Cr deposition in survey study part.

Sample	Vb		Ar flow rate (sccm)	Deposition time (min)
	V (V)	I (A)		
Cr_HiPIMS_0	0	0	100	1
Cr_HiPIMS_100	-100	0.034	100	
Cr_HiPIMS_200	-200	0.043	100	
Cr_HiPIMS_300	-300	0.055	100	

To study the influence of the substrate bias potential on the deposition rate of Cr films, the process parameter for Cr deposition such as operating pressure and sputtering power is an important parameter. Operating pressure in the deposition chamber is related to the deposition rate, purity, and structure of the films. If the operating pressure is higher than the setpoint value, indicating a system malfunction (micro leak, mass flow controller error), it leads to different plasma properties and film properties (oxygen contamination). Therefore, a system must be controlling the operating as the same value for each experiment, which the ionized physical vapor deposition system has an option for pressure control by adjusting the opening percentage of the pendulum valve into two functions as position control and pressure control.

In addition, the HiPIMS power supply is an in-house HiPIMS power supply. The power, frequency, and pulse duration can adjust to optimize condition for the work. For fabricating Cr films, the average power, frequency, and pulse duration of about 240 W, 1 Hz, and 200  $\mu$ s respectively. Figure 4.71(a) shows the voltage signal measured using an Agilent model 10076B. The maximum amplitude of -885 V and stable voltage of 750 V. Figure 4.71(b) shows the arc current signal measured with a PEARSON CURRENT MONITOR Model 3972. The maximum current amplitude of 26 A and drop into the stable current of about 15 A. The discharge power signal as the cross of voltage and current signal as shown in Figure 4.71(c). For a duration of time, the plasma will be generated with high power of 10 kW. Therefore, the plasma has a high density and high ionization of the Cr atoms, which can be seen in the color of the plasma. In addition, the discharge voltage, discharge current and discharge power signal are non-different shapes and amplitudes. It indicates that the substrate bias

potential does not affect on the discharge power. Which average discharge power has value in the range of 240 W and independent substrate bias potential. This data indicates that the plasma properties as the same for deposited Cr films.

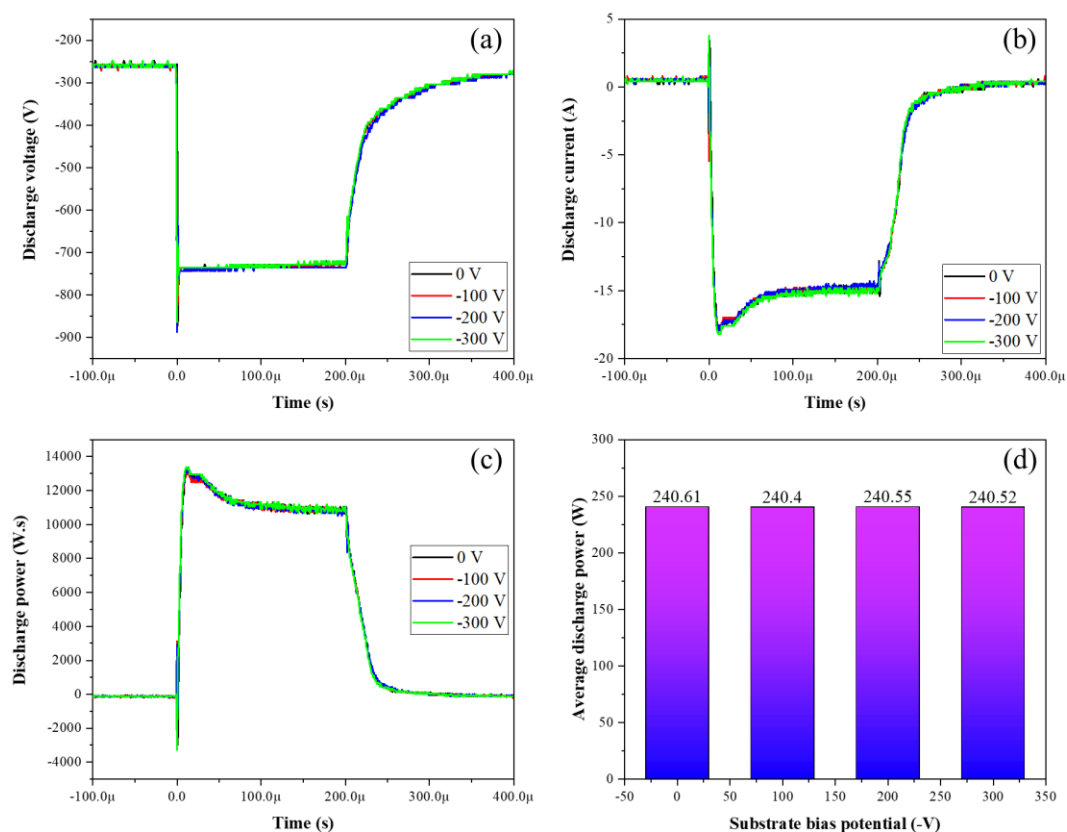


**Figure 4.71** (a) discharge potential signal, (b) discharge current signal, (c) discharge power signal and (d) average discharge potential as a function of substrate bias potential. The label in the flame is the substrate bias potential.

The analyzed data of discharge parameter confirm the properties of plasma as the same. To study the influence of substrate bias on the deposition rate of Cr films. The Cr films was investigated by XRR (Bruker D8 Advance) measurements performed with Cu-K $\alpha$  monochromatic radiation ( $\lambda=0.15406$  nm). XRR was measured in the range of an incident angle  $2\theta$  from 0 to  $3.0^\circ$  by a step of  $0.005^\circ$ . The identifies the thickness of films is related to the oscillation period of the XRR profile. The oscillation period of the XRR profile was obtained by fitting the measured XRR data with a simulated XRR curve using the Leptos 7.0 software. It was found that the deposition rate of Cr films decreased from 0.158 to 0.113 nm/s with the increase of

substrate bias potential from 0 to -300 V as shown in Figure 4.72(b). This result can be explained by the sputtering phenomenon on the substrate during the films growth. The HiPIMS discharge has high plasma density (high electrons density and high ions density), and the ion in plasma consists of argon ions and chromium ions. These ions will be moving to the substrate and form to the film layer. For a lower substrate bias potential, these ions will be induced with the weakly electric field and bombard the film surface with low energy. On the other hand, a higher substrate bias potential induces these ions with a strong electric field or increases the kinetic energy of the ions [205].

The bombardment of energetics positive ions ( $\text{Ar}^+$ ) causes sputtering, which sputtering rate of the film can be considered from substrate bias current due to measured current at substrate holder as the sputtering current, the low sputtering current related to low sputtering rate and high sputtering current related to high sputtering rate [204], [206], [207]. Therefore, the deposition rate of Cr films will be decreased with the increase of substrate bias potential.

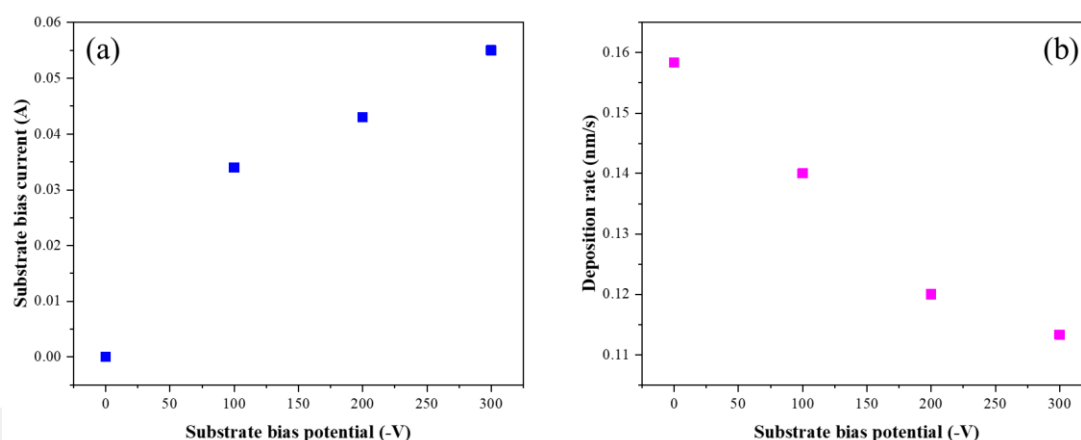


**Figure 4.72** (a) substrate bias current and (b) deposition rate of the Cr films deposited on Si substrate using HiPIMS deposition.

In order to study the influence of substrate bias potential on the structure of Cr films. The Cr films were deposited on Si substrate with the same process parameter as the survey study. The thickness of the films was controlled of about 200 nm, which uses the deposition time as Table 4.15.

**Table 4.15** Deposition time for Cr films with the thickness of 200 nm.

Substrate bias potential (V)	Deposition time	
	Minute	Second
100	21	0
100	23	58
100	27	56
100	29	24

The Cr films with a thickness of 200 nm as shown in Figure 4.73. The color of films is different, the Cr film has the gray metallic color for substrate bias potential of 0 V and shiny metallic color for higher substrate bias potential. This indicates the different structural properties of the films. Moreover, the sample and substrate holder is hot after export from the deposition chamber due to intense and energetic bombardment, the kinetic energy of the ions transfer to thermal energy causing heat at the substrate holder during the film growth.

**Figure 4.73** The Cr films deposited on Si substrate using HiPIMS deposition by varying substrate bias potential.

The crystal structure of the Cr films was analyzed by X-ray diffraction (XRD, Bruker D8 Advance) with Cu-K $\alpha$  monochromatic radiation ( $\lambda=0.15406$  nm). The angle of detector position from the incident X-ray beam ( $2\theta$ ) scanning from 20 to 70° by a step of 0.005°. The crystal structure is related to the FWHM of the diffraction peak at the diffraction line.

The XRD patterns of the Cr films as shown in Figure 4.74. The diffraction peak at 44.5° is presented in all diffraction patterns, which correspond (110) Cr with fcc structure. But diffraction peaks at about 64.2° corresponding (200) Cr with fcc structure are present in the diffraction pattern of Cr film deposited by applied

substrate bias of -200 and -300 V [208]. It indicates that the Cr films deposited by applied substrate bias potential of 0 and -100 V are Cr single crystals, while the applied substrate bias potential of -200 and -300 V introduce the recrystallization of the Cr atoms leading to Cr polycrystalline structure.

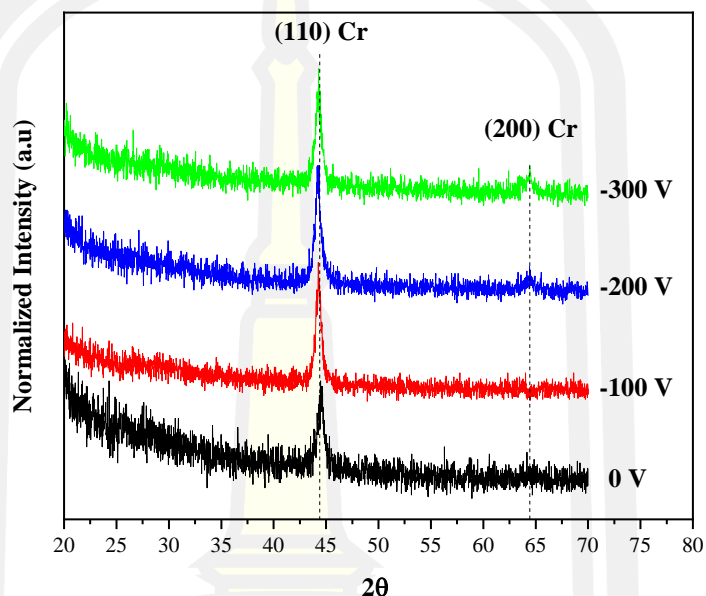


**Figure 4.74** XRD pattern of the Cr films deposited on Si substrate with HiPIMS deposition technique. The label at the tail of the diffraction pattern as substrate bias potential.

Figure 4.75 and Table 4.16 show the crystalline size of (110) Cr and (200) Cr structure in the Cr films, calculated by the Scherrer equation. The grain size of (110) Cr increases from 0.17 to 0.182 nm with the increase of substrate bias potential from 0 to -100 V and decreases again to 0.166 nm for substrate bias potential higher than -200 V. While the grain size of (200) Cr increases from 0.127 to 0.162 nm with the increase of substrate bias potential from -200 to -300 V.

In addition, an increase of substrate bias potential causes a significant shift of (110) Cr to the lower  $2\theta$  value, while (200) Cr shifts up to a higher  $2\theta$  value. Similar changes of the preferred orientation have been found on titanium nitride films [209]–[213]. This result can be concluded that applying substrate bias potential increases the substrate temperature with the intense and energetic ion bombardment leading to high

mobility and high higher kinetic energy of adatoms leading to epitaxial growth of fine grain structure and recrystallization to new structure [209]–[213]. Moreover, shifting of the peak position to lower  $2\theta$  values, usually indicates the formation of compressive stresses [204]. Therefore, the Cr films deposited with the higher substrate bias potential have high compressive stress.

**Table 4.16** Analyzed data of diffraction pattern of Cr films.

Substrate bias potential (V)	$2\theta$		FWHM (110) (°)	FWHM (200) (°)	crystalline size of (110)	crystalline size of (200)
	(110)	(200)				
0	44.51	-	22.25	-	0.17	-
-100	44.28	-	22.14	-	0.18	-
-200	44.23	64.43	22.11	1.57	0.17	0.13
-300	44.21	64.54	22.14	1.30	0.17	0.16

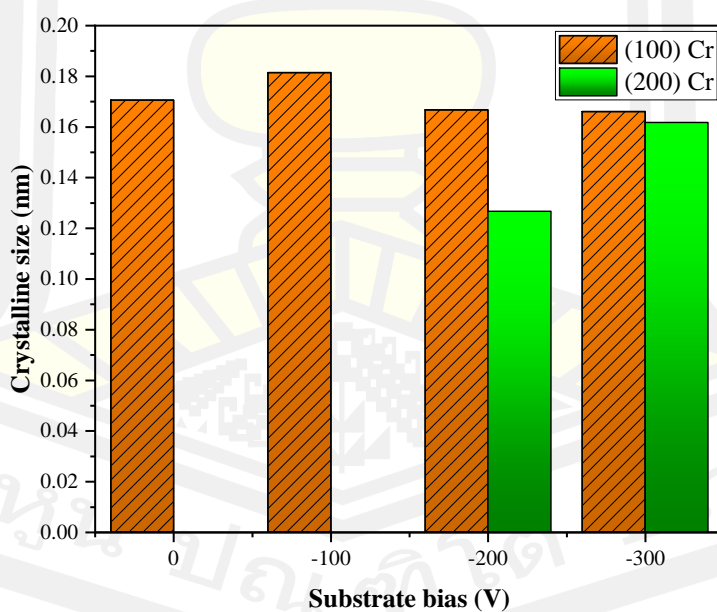


**Figure 4.75** Crystalline size of (110) Cr and (200) Cr structure in the Cr films as a function of substrate bias potential.

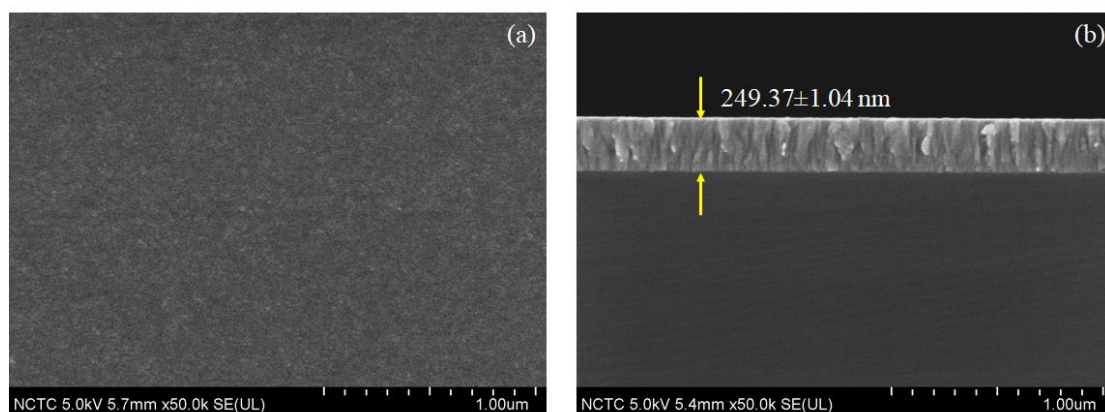


**Figure 4.76** (a) top surface and (b) cross-section of Cr films deposited at the substrate bias of  $-100$  V, the deposition pressure of 0.016 torr, and the HiPIMS average power of 240 W, frequency of 1 Hz, and pulse width of 200  $\mu$ s respectively.

The surface and cross-section morphology of the Cr film deposited on Si substrate by applied substrate bias potential of  $-100$  V, was characterized by field emission scanning electron microscope (FESEM, Hitachi SU8030) at NSTDA CO., LTD., Thailand.

Figure 4.76(a) shows the top surface morphology of the film. The film has smooth surfaces and free macroparticles. Moreover, the edge of grain is not present, indicate that the film has a fine grain structure corresponding with the XRD result. Figure 4.76(b) shows the cross-section of the film. It can be found that the film has a dense granular column structure and a thickness of  $249.37 \pm 1.04$  nm. This reveals that applying substrate bias potential effectively enhances the kinetic energy of incident ions and subsequent mobility of adatoms, which introduce the dense Cr films and smooth surface.

#### 4.5 Multilayer amorphous carbon deposition

The aim of this work is the superhard amorphous carbon films, it's very challenging, due to the DLC film with the hardness in the range of superhard coating having high internal stress. Moreover, if coating thickness is higher than 1  $\mu$ m, special techniques must be used to reduce the residual stress in the film layer and maintain high hardness including good adhesion to the substrate. Interlayer deposition, doping elements, and multilayer structure are effective methods to reduce the residual stress of DLC film. However, element doping introduces non-homogeneous distribution of



the doped atoms. Many works of literature have elucidated that the multilayer DLC alternating hard and soft layers could remarkably reduce stress and hardness in the range of superhard coating [204]. To achieve the goals of this work, the multilayer amorphous carbon film with the structure of alternating ta-C (hard) and a-C:H (soft) layers will be synthesized. This idea corresponds with the performance of an FCVA system, which can variety of DLC film coatings, including ta-C, a-C:H, and a-C:H:Me. Therefore, this topic will be given the detail of the preparation morphologies and mechanical properties of multilayer amorphous carbon (Cr/ta-C/a-C:H) films compared with a-C:H single layer film (700 nm).

Topic 4.2 showed the properties of ta-C films as a function of ion energy, which controls by anode bias potential and substrate bias potential. However, ta-C films deposited by the plasma biasing technique have a lower deposition rate. Therefore, the ta-C layers in multilayer films were prepared using FCVA deposition combined with the substrate bias technique to improve the mechanical properties of the multilayer films. This topic will be given the detail of the preparation morphologies and mechanical properties of a-C:H single layer and multilayer films, which preparation process as follows.

The SUS304 and p-type silicon (100) with a resistivity of 0.40 ohm.cm were used as the substrate. The Si substrate has been cleaned by the standard process with acetone, methanol, and DI water, while for SUS304 use methanol and DI water in an ultrasonic to remove organic contamination. And the substrate was installed on a grounded substrate holder. The pre-deposition, surfaces of the substrate were cleaned by argon ions generated using ALIS with the applied discharge potential and discharge current of 1.4 kV and 8.8 mA respectively, to remove the native oxides formed on surface of the substrate and increase the adhesive of the film layer with the substrate.

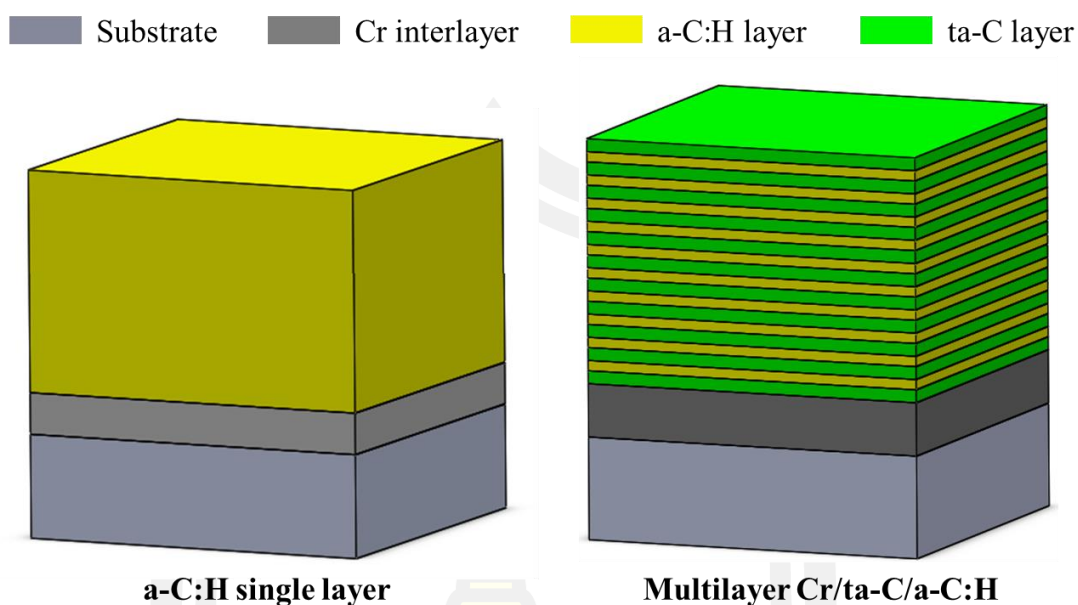


**Figure 4.77** Assembly cross-section model of the a-C:H single layer and multilayer Cr/ta-C/a-C:H films.

Model of the a-C:H single layer and multilayer films as shown in Figure 4.77. Normally, the performances of the multilayer system could be tailored by regulating components of adjacent layers. To improve the adhesion of the film-substrate, the Cr film with a thickness of 250 nm was deposited on the substrate for use as the interlayer.

The Cr interlayer was deposited by a HiPIMS technique. The average power of 140 W was applied to the Cr target for generating vapor of the Cr atoms. The substrate bias potential of -100 V was applied during the film growth.

The a-C:H single layer with a thickness of 700 nm was deposited using an L-ALIS with the discharge potential of +1200 V under a working pressure of 0.13 Pa, in which uses argon gas (99.999%) and acetylene gas (99.99%) with a flow rate of 10 sccm and 30 sccm respectively. The deposition time of 4 hours. The substrate has a swing coating mode to control the uniformity of the films.

The multilayer films consist of ta-C layers alternated with a-C:H layers with many 22 layers. The first layer contacted with the interlayer was set as the ta-C layer with a thickness of 50 nm deposited using FCVA deposition and applied substrate bias potential of -200 V to improve the film-interlayer-substrate adhesion. The a-C:H layers were deposited using an L-ALIS with the discharge potential of +1200 V under

a working pressure of 0.13 Pa, in which uses argon gas and acetylene gas with a flow rate of 10 sccm and 30 sccm respectively. The deposition time for a-C:H layer of 15 minutes and 40 seconds, and the substrate holder has a swing coating mode. While the ta-C layers were deposited using FCVA deposition, and the charger voltage of -504 V was applied to PFN for operating the FCVA source. Which generate stable arc pulses had a current amplitude of 720 A, a pulse duration of 1200  $\mu$ s, and a repetition rate of 1 pulse/s. The number of deposition pulses for the ta-C layer of 2400 pulses. To investigate the influence of  $C^+$  ions energy on the mechanical properties of multilayer films, the substrate bias potential of 0, -60, -80, -100 and -120 V was applied during the ta-C layer growth.

Table 4.17 shows the detail of multilayer films, the modulation ratio of the ta-C and a-C:H layers were set as 1:1 and the modulation period was about 50 nm. In addition, the ta-C layer was always selected as the top layer for wear protection. The top ta-C has high hardness could provide high load carry capacity and contribute to long wear life. The multilayer thickness was determined higher than 1000 nm.

**Table 4.17** Specific information of the a-C:H single layer and multilayer films.

Sample	ta-C layer		a-C:H layer		Thickness ratio (nm)	Film Thickness (nm)
	Substrate bias potential (V)	sp <sup>3</sup> content	Discharge potential (V)	sp <sup>3</sup> content		
S-1	-	-	1200	30.52	-	700
M-1	0	75.99	1200	30.52	50:50	>1000
M-2	-60	80.37				
M-3	-80	83.46				
M-4	-100	81.42				
M-4	-120	80.84				

The physical characteristics of a-C:H single layer and multilayer films on the SUS304 substrate as shown in Figure 4.78. In each condition, all 5 samples were produced at the same time. From the observation, it was found that the a-C:H single layer film has black color and gradient color non-observation. While the multilayer

films has green color tone and gradient color non-observation which indicates that the films has uniformity. However, the color of the samples is different, which depend on refractive index of the ta-C top layers.

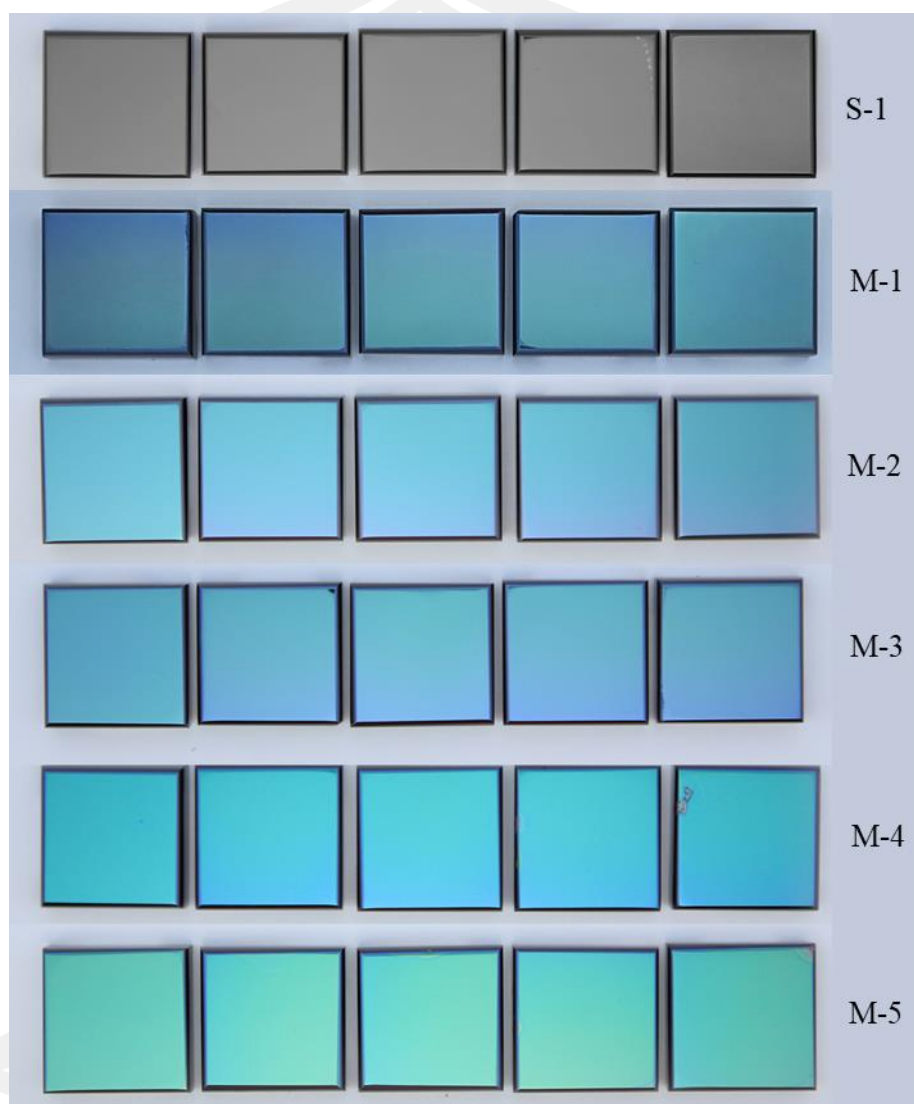


**Figure 4.78** Physical characteristics of multilayer amorphous carbon films (Cr/a-C:H/ta-C). The label is the code of the sample.

#### 4.5.1 FE-SEM result

The surface and cross-section morphologies of the a-C:H single layer and multilayer films were observed by field emission scanning electron microscope (FE-SEM, Hitachi SU8030) as shown in Figure 4.79. The surface morphologies of S-1, M-1, M-2 and M-3 films deposited on the Si substrate are shown in Figure 4.79 (a), (c),

(e) and (g) respectively. The surface of the films is very smooth, porous and pin-hole free, with grain structure not present, indicating an amorphous characteristic surface. In addition, microscale surfaces are non-significantly different.

The cross-sectional microstructure of S-1, M-1, M-2 and M-3 films deposited on the Si substrate are shown in Figure 4.79(b), (d), (f) and (h) respectively. The thickness of the films was analyzed using the ImageJ program, a minimum of 20 points were performed on each sample, and the results were averaged as shown in Table 4.18. It was found that the a-C:H single layer film contains an a-C:H single layer film with a thickness of  $676.35 \pm 3.58$  nm on a Cr interlayer with a thickness of  $325.66 \pm 2.69$  nm.

While the multilayer films contain the alternating 22 coating layers of ta-C layers and a-C:H layers, which the first layer as a Cr interlayer with a thickness of  $260 \pm 6$  nm and shows the columnar structure and good adhesion with the substrate. The multilayer film has a well-defined layered composition and a dense uniform structure. In addition, the interface between the multilayers is tightly bonded, and no significant peeling occurs. The darker (yellow) is the a-C:H layer and the brighter (green) is the ta-C layer. The contrast difference is produced by the difference in density between heterogeneous layers with different  $sp^3$  content [23], [214]. The carbon layer of M-1, M-2 and M-3 samples has a thickness of  $1332.54 \pm 4.97$  nm,  $1155.45 \pm 4.48$  nm and  $1165.51 \pm 2.95$  nm respectively. However, M-4 and M-5 films on Si substrate is failure off during the film growth. Due to the higher substrate bias potential leading to micro-arc at the interface of Kapton tap and Si substrate, including the edge of Si substrate. But the M-4 and M-5 films on SUS304 did not peel due to the edge of SUS304 is chamfered in the sample preparation process, which decreases the probability of micro-arc occurring on the sample.

**Table 4.18** Analyzed thickness data of the a-C:H single layer and multilayer films.



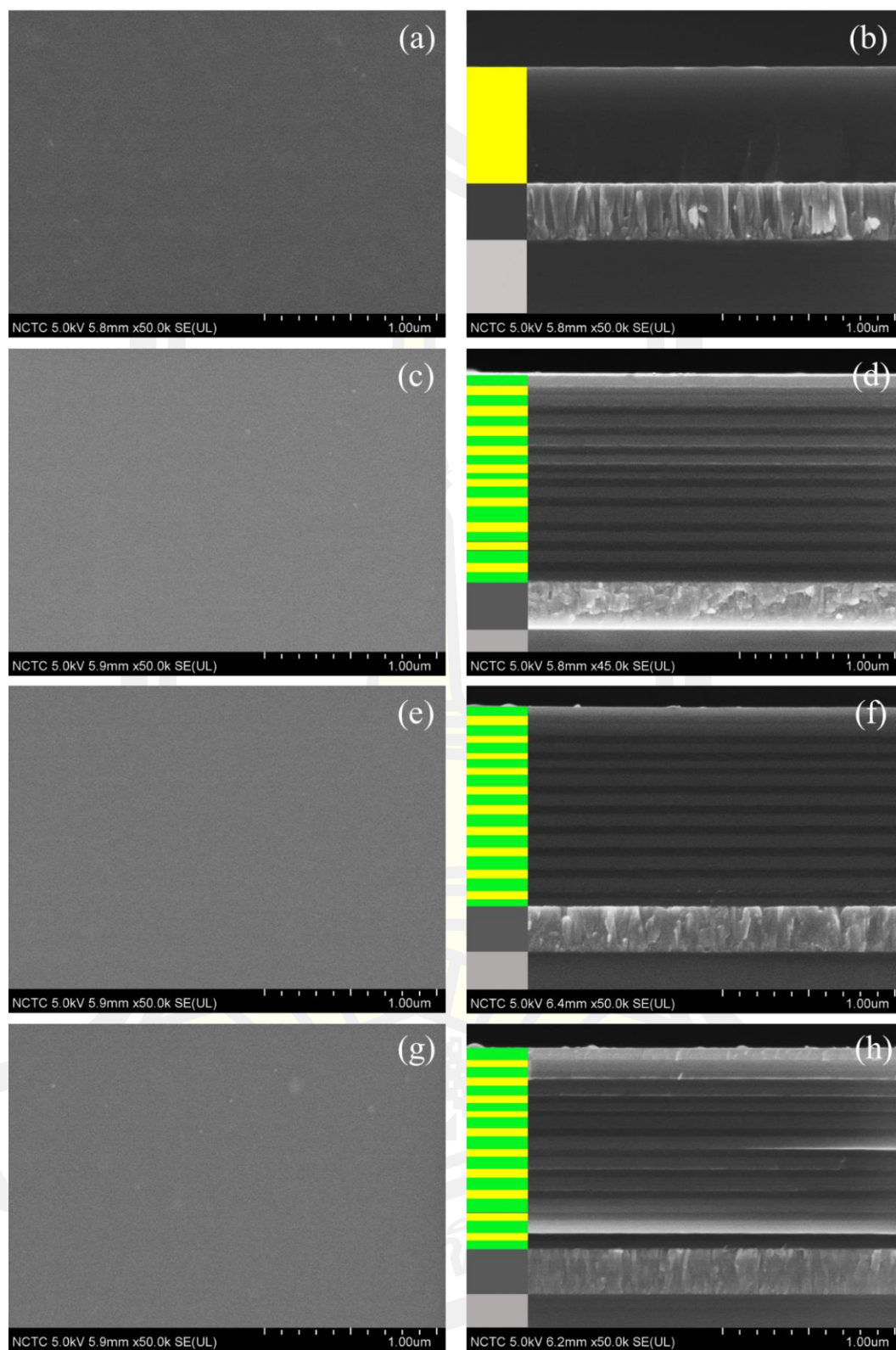
Sample	Thickness (nm)		Film Thickness
	Cr interlayer	Multilayer	
S-1	325.66±2.69	676.35±3.58	1002.00±4.49
M-1	265.72±4.60	1332.54±4.97	1598.26±8.28
M-2	262.39±1.82	1155.45±4.48	1417.84±5.07
M-3	261.21±3.36	1165.51±2.95	1426.72±4.65
M-4			Fail
M-5			Fail

Figure 4.80 shows the element depth distribution of the M-3 film measured using an EDS line scan. It can be found that the film has C, O, and Cr element compositions. The carbon element composition appears at the scanning depth of about 0 to 1200 nm. In addition, the carbon element composition in the film changes with the alternating changes of the ta-C layer and the a-C:H layer. At the scanning depth of about 1200 nm presented intensity of the Cr element, which corresponds to the Cr interlayer. While the intensity of oxygen element increased with the increase of scanning depth and higher composition at the Cr interlayer due to the Cr interlayer deposited using operating pressure of 2 Pa, the oxygen composition in the deposition chamber will be increased. Therefore, this oxygen will be discharged, reacted, and deposited during the Cr layer growth.





**Figure 4.79** The surface and cross section morphology of multilayer amorphous carbon films. (a) and (b) are S-1 sample, (c) and (d) are M-1 sample, (e) and (f) are M-2 sample, and (g) and (h) are M-3 sample.



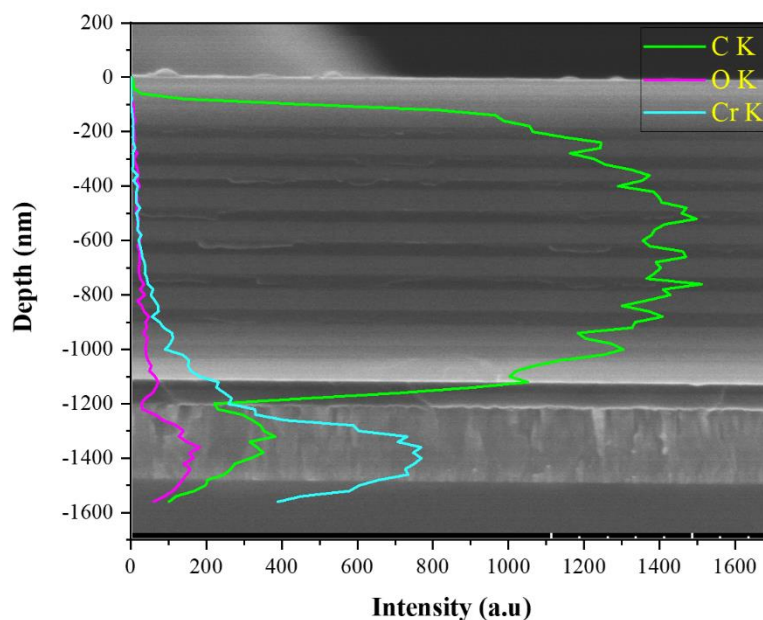


**Figure 4.80** EDS spectrum in line scan mode of the M-3 sample.

#### 4.5.2 Nanoindentation test

The mechanical properties of multilayer DLC films such as hardness and Young's modulus are correlated with their composition,  $sp^3$  content, density, and modulation ratio [23], [215]. For example, DLC multilayer film with the alternation of the ta-C hard layer and ta-C soft layer exhibit high hardness and compressive stress [29]. The DLC multilayer with the alternation of hydrogenated DLC/metal-doped DLC films exhibits lower hardness (H), Young's modulus (E), density, thermal stability, and compressive stress [214], [216]–[218]. While the DLC multilayer film with the alternation of metal nitride/DLC and metal carbide/DLC films exhibit high hardness (H), Young's modulus (E), density, thermal stability, compressive stress and low adhesion with the substrate [98], [219], [220].

Hardness is a significant parameter suggesting mechanical properties, while Young's modulus has also a significant role in wear behavior, in which use estimates the damage of the material or the film under load [221]. The hardness (H) and elastic modulus (E) of the multilayer films deposited on the SUS304 substrate were estimated by instrumented indentation, using a Hysitron: TI Premier, which is equipped with a three-sided pyramidal diamond tip in Berkovich geometry. Before the measurement stage, the tip calibration was performed using quartz, in order to

overcome the effect of tip rounding. To avoid the affectation of the substrate on the mechanical properties of the ta-C coating response, the load was determined to penetration depths lower than 10% of the coating thickness, which maximum loading is 10 mN. A minimum of 5 indentations were performed on each sample, and the results were averaged.

The hardness and elastic modulus of the substrate, a-C:H single layer and multilayer films are summarized in Figure 4.81 and Table 4.19. The result shows that the SUS304 has a hardness and elastic modulus of  $4.98 \pm 0.14$  GPa and  $202.09 \pm 4.22$  GPa respectively. The a-C:H single layer has a hardness and elastic modulus of  $22.29 \pm 0.17$  and  $162.11 \pm 2.24$  GPa respectively. While the multilayer films has a hardness and elastic modulus higher than, the hardness and elastic modulus increases from  $32.32 \pm 2.89$  GPa to  $37.61 \pm 0.93$  GPa and  $202.09 \pm 4.22$  GPa to  $300.61 \pm 1.31$  GPa with the increase of the substrate bias potential from 0 V to -80 V. Then the substrate bias potential for the ta-C layer deposition higher than -100 V, the hardness and elastic modulus decrease again to  $36.07 \pm 0.49$  GPa and  $273.34 \pm 2.44$  GPa respectively.

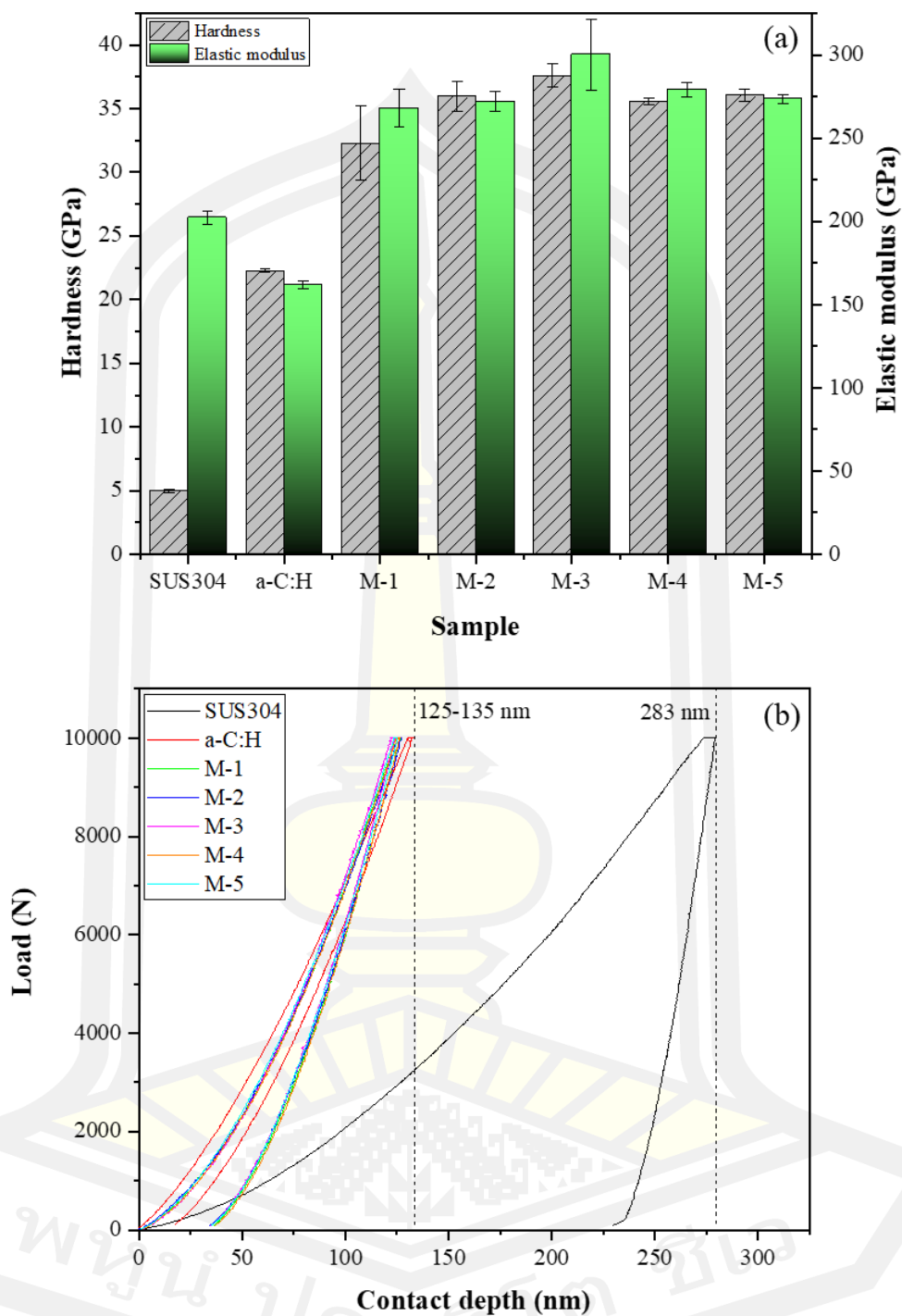
Besides the hardness and elastic modulus, indentation plasticity, defined as the ratio ( $h_p/h_{max}$ ) of the plastic displacement ( $h_p$ ) divided by the total displacement ( $h_{max}$ ), can also be determined from load displacement curves. The plasticity values are tabulated in Table 4.19. It was found that the a-C:H single layer film showed the lowest plasticity of 21.20%, while the multilayer M-3 film showed the highest plasticity of 42.30% and the plasticity decreases with the increase of the substrate bias potential. It implies that the multilayer M-3 film is more capable of resisting plastic deformation.

Figure 4.81 shows the load-displacement curves of indentations for films. The peak load is kept at 600  $\mu$ N. The maximum penetration depth of  $283.39 \pm 4.11$  nm corresponds with the SUS304 substrate. The DLC coating increases the hardness of the substrate, the penetration depth will be decreased, which the a-C:H showed a penetration depth of  $132.26 \pm 1.17$  nm and the multilayer M-3 film showed a penetration depth of  $121.06 \pm 3.35$  nm. The hardness significantly increases from 22.29 GPa to 37.61 GPa, which is  $\sim 68\%$  increase. In a word, the multilayer design with the alternating of the hard-layer (ta-C) and soft-layer (a-C:H) could increase the hardness, elastic modulus and plasticity.

It is clearly that the multilayer film coating can improve the hardness and elastic modulus, which these parameters were controlled with  $sp^3$  content in the film. The a-C:H single layer film has the  $sp^3$  content of about 30%, while the multilayer films have the  $sp^3$  content in the ta-C layer higher than 75% (average  $sp^3$  content higher than 50%). Therefore, the multilayer films will have high hardness. Especially, the applied substrate bias potential of -80 V during ta-C layer deposition in the multilayer film leads to the highest hardness and elastic modulus. Due to the substrate bias potential of -80 V is optimized for deposited ta-C coating rich  $sp^3$  content and diamond-like characteristic.

Moreover, another parameter used to predict the wear resistance of the film or predicting whether the film will crack or not under load, it is the H/E ratio (elastic strain to failure (rupture)). According to previous studies, the coatings with an  $H/E \geq 0.1$  are considered to be resistant to cracking [180]. In addition, the  $H^3/E^2$  ratio is a strong indicator of the resistance of coatings to plastic deformation (proportional to the elastic deformation of coatings), this parameter cannot be used to predict the wear and failure resistance of coating materials, but it is used to estimate the elasticity of coating materials well [181], [182]. The coating material with a high  $H^3/E^2$  ratio increases elastic strain to failure and resistance to cracking under the load or well resistant to plastic deformation.

The H/E and  $H^3/E^2$  ratios as shown in Table 4.19 **Table 4.19**. It showed that the H/E ratios have values in the range of 0.12 to 0.13 and non significantly different, indicating that the a-C:H single layer and multilayer films with good elastic strain to failure and resistance to cracking. The  $H^3/E^2$  ratios have values in the range of 0.42 to 0.63, and the a-C:H single layer film has the lowest  $H^3/E^2$ . While the multilayer films have a higher  $H^3/E^2$  ( $>0.47$ ). Therefore, the multilayer films have resistance to plastic deformation. This result proved that the multilayer films alternating of the ta-C and a-C:H layer have good elastic strain to failure and resistance to cracking under the load because the ta-C layers have a role of absorbing the pressure from the applied load. And the a-C:H layers have a role of distributing the force into the volume of the film. As a result, the coating material will be well resistant to plastic deformation.



**Figure 4.81** (a) hardness and elastic modulus and (b) load-displacement curves of indentations for the SUS304, a-C:H single layer and multilayer films.

**Table 4.19** Summarized data of nanoindentation test.

Sample	H (GPa)	E (GPa)	H/E	H <sup>3</sup> /E <sup>2</sup>	Plasticity (%)	Penetration depth (nm)
SUS304	4.98±0.14	202.09±4.22	0.0247	0.0030	84.98	283.39±4.11
S-1	22.29±0.17	162.11±2.24	0.1375	0.4218	21.20	132.06±1.17
M-1	32.32±2.89	267.94±1.51	0.1206	0.4703	40.08	130.71±4.79
M-2	35.99±1.18	271.88±5.90	0.1324	0.6309	39.49	126.65±1.66
M-3	37.61±0.93	300.13±1.31	0.1253	0.5906	42.30	121.06±3.35
M-4	35.58±0.23	279.16±4.28	0.1275	0.5779	41.60	125.71±0.87
M-5	36.07±0.49	273.34±2.44	0.1319	0.6282	40.32	126.39±0.55

#### 4.5.3 Scratch test

The adhesion of the multilayer films to the SUS304 was assessed by scratch tests using a FISCHER: HM2000 equipped with a Rockwell C Spherical diamond (tip radius 200  $\mu\text{m}$ ). Repeat 3 scratch tests were performed on each sample and the results were averaged. The scratch protocol was progressive linear loading, starting load 0.5 N, final load 20 N, scratch length 5 mm and loading rate 10.0 N/min. the samples were tested at an environment condition: temperature of 28.0  $^{\circ}\text{C}$  and relative humidity of 40.00%. The results of interest were the loads necessary for the occurrence of destructive events: crack formation, partial delamination and total film failure.

The micrographs in Figure 4.82 show the failure of the substrate/coating system when subjected to a scratch test with a progressive linear load of up to 20 N. The behavior of the film subjected to scratch tests can be divided into three groups. The first group is a-C:H single layer film, the crack after 3.1 N of sliding with an arrow shows the buckling spallation. Then at about 3.5 N, the film shows the delamination from the interlayer surface. The second group is multilayer films related to the sample codes M-1, M-3, M-4 and M-5. The crack after 4 N to 6 N of sliding with an arrow shows an angular crack, then the film shows the buckling spallation and coating chipping being generated along the track borders when the applied load is higher than 11 N. But the film did not present the severe crack in radius on surface of the film. And the third group is M-2 film, the top layer of the film is severely delamination from the second layer (the top layer).



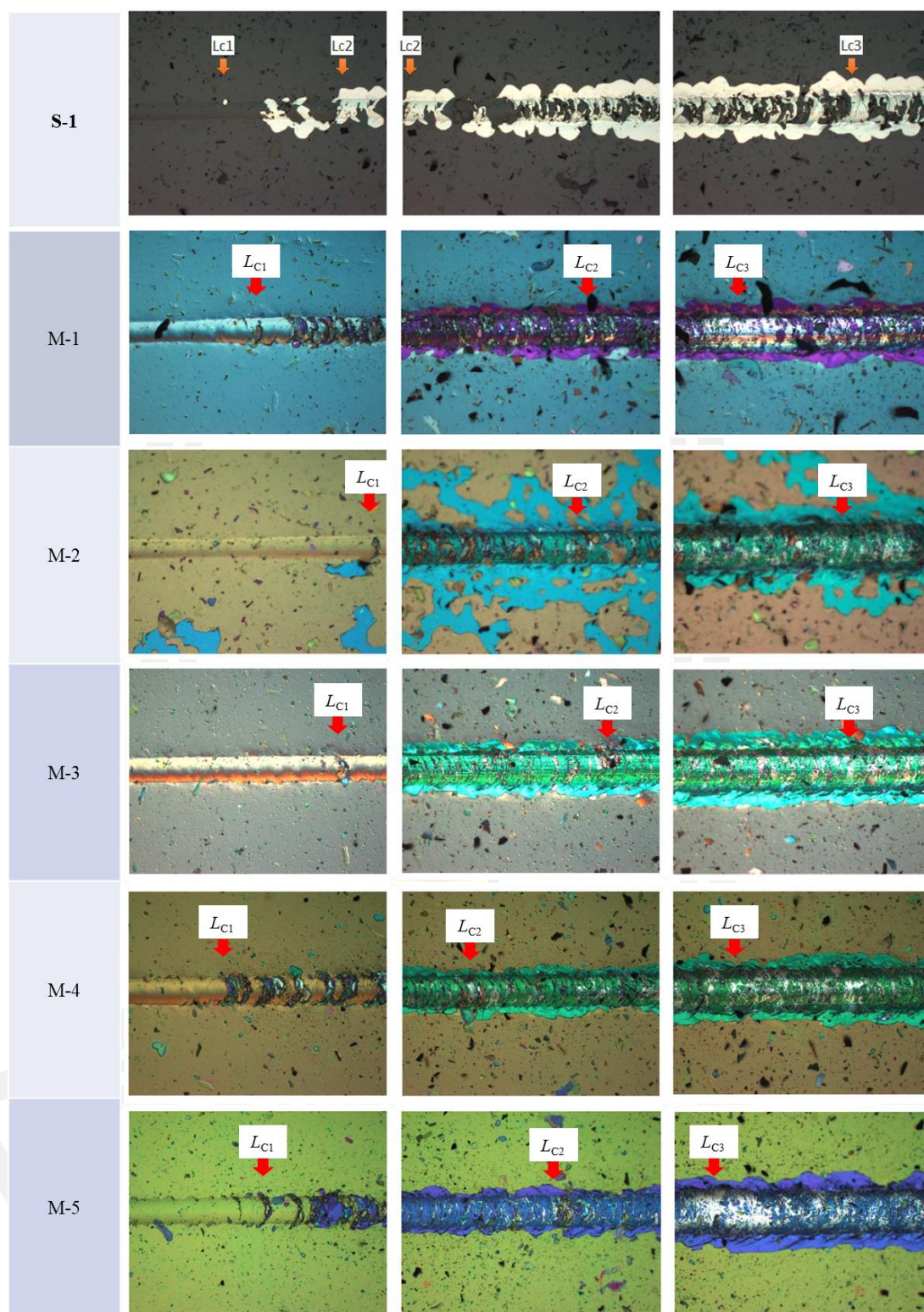


**Figure 4.82** Multilayer Cr/ta-C/a-C:H film failure after scratch testing.

The wear behavior was investigated in the scratch test. The critical load is a strong parameter of total film failure, which is identified by using an acoustic

emission signal during the scratch test combined with wear characteristics on the film. The film consists of three main film layers: substrate, Cr interlayer and carbon layer. Therefore, the adhesive/cohesive failure must be divided into three sections:

- The minimum load of cracking that occurs is called cohesive failure ( $L_{C1}$ ).
- The load of the film beginning to peel off from the Cr interlayer continuously is called adhesive failure ( $L_{C2}$ ).
- The load of the interlayer beginning to peel off from the substrate is called adhesive failure ( $L_{C3}$ ).

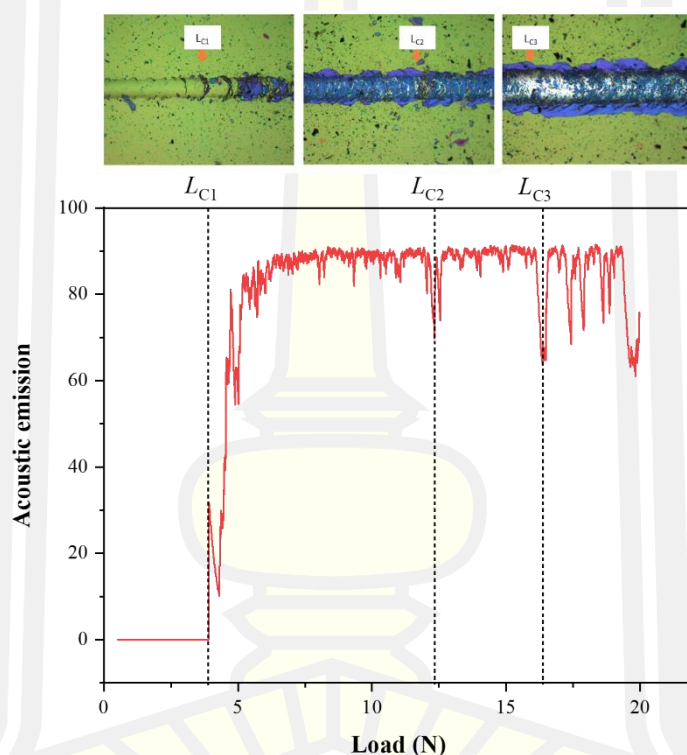


**Figure 4. 83** The acoustic emission signal of the scratch test.

The critical load critical loads of adhesive/cohesive failure of the films as shown in Figure 4. 84. It was found that the critical loads of cohesive failure of the a-C:H single layer films of  $3.16 \pm 0.31$  N and the critical loads of adhesive failure of the films of  $3.53 \pm 0.52$  N. While the multilayer films exhibit the critical loads of cohesive failure in the range of 4.21 N to 6.03 N and the critical loads of adhesive failure of the films of 11.69 N to 13.15 N, which the M-3 film exhibit the highest value of  $13.15 \pm 0.27$  N.



However, the critical loads of adhesive failure of the Cr interlayer on SUS304 have values in the range of 17.54 N to 18.28 N, not depending on the carbon coating layer. This means that the deposition condition of the carbon layer does not affect on properties of the Cr interlayer. Moreover, the similar value of the critical loads of adhesive failure indicates that the deposition process is stable.

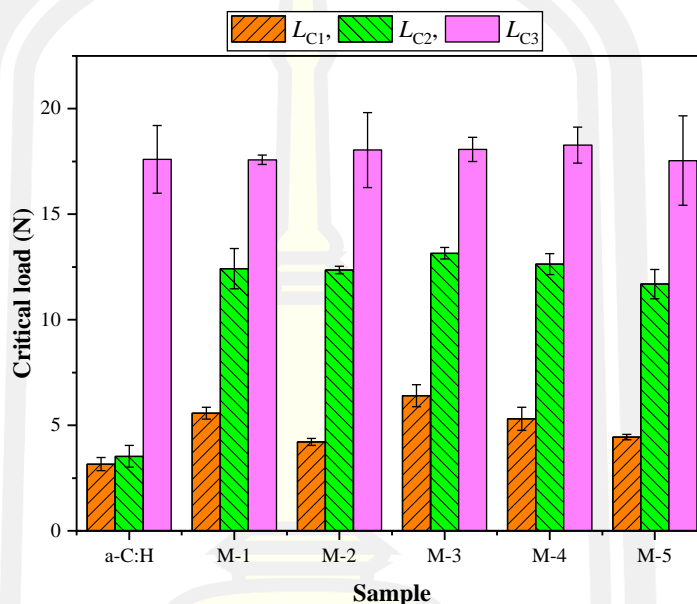


**Figure 4. 84** Critical load of the a-C:H single layer and multilayer films deposited on the SUS304 substrate.

The higher values for the critical loads indicate better adhesive/cohesive behavior of the substrate/coating system. This shows that the adhesive/cohesive of the multilayer film is higher than a-C:H single layer. Due to the a-C:H single layer film having a low  $sp^3$  content, the single layer has a high residual compressive stress from the long and complicated cross-linked  $sp^3$  bonds, including the mismatches of the elastic modulus and expansion coefficient between the DLC and the substrate giving rise to weak adhesion to the substrate and poor toughness as shown in Figure 4.85. While the multilayer film with good elastic strain to failure and high resistance to plastic deformation and cracking from the multilayer architecture, the multiple interfaces restrict the dislocation and defects in crystalline lattices and free volumes in amorphous structures, which contributes to improving the hardness and toughness. In addition, the defect being pinned by multi-interface structures helps to prevent crack

formation and propagation under complicated stress fields, where the multilayer interfaces act as barriers to stopping defect coalescence. The schematic illustration of the stopping cracks mechanism of the multilayer design is shown in Figure 4.85

In addition, the multilayer films exhibit a high value of the critical load ( $L_{CI}$ ), this result indicates that the capacity of load-bearing of the film/substrate system of the film is greater than a-C:H single layer film, leading to potentially superior impact resistance. This result corresponds with the  $H/E$  ratio and  $H^3/E^2$ , in which low values of this ratio are associated with samples that exhibit much greater delamination. Although the values of the  $H/E$  ratio between the a-C:H single layer and multilayer films are relatively close, the relatively better adhesive behavior of the multilayer film can be associated with the higher value of the  $H^3/E^2$  ratio.

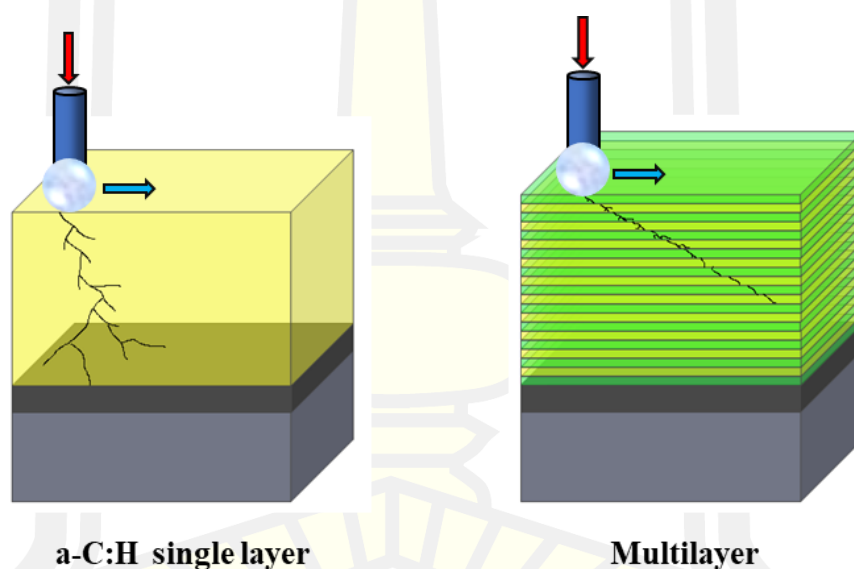


**Figure 4.85** Comparison of cracks mechanism of the a-C:H single layer and multilayer film.

## Chapter V

### Conclusion

The aim of this work is to development of ionized physical vapor deposition system for superhard amorphous carbon coating. The importance conclusion of this Ph.D. thesis has been divided into four parts. (i) the development of ionized physical vapor deposition system, this system was designed in the concept of the hybrid system of physical vapor deposition, which supports the many works and applications. The plasma source consists of an anode layer ion source (ALIS), a Linear-anode layer ion source (L-ALIS), a magnetron sputtering source and a filter cathodic vacuum arc source (triggerless model), which a responsible for substrate cleaning, metal and compound deposition, and ta-C film deposition respectively. These plasma sources were installed on the side of the deposition chamber. The system can be controlled using PXI unit with the NI PXI-8108, NI PXI-2565, and NI PXI-6251card. The control panel on display it is written based on the LabVIEW program, in which the graphic of the panel is related to the actual characteristics of the system. Moreover, the deposition area and uniformity of the film can be controlled by the adjusting directional of the substrate holder, it can rotate and move in two-directional.

(ii) The plasma diagnostics part, the plasma parameter such as ion energy, ion density and ion flux were characterized using an RFA probe. It was found that the initial energy of  $C^+$  ions (generated using an FCVA source) has a value in the range of 15 eV. To improve the properties of the film, the plasma biasing and substrate bias techniques were applied in the FCVA deposition to increase the energy of depositing ions. For the plasma biasing technique, the mean energy of the  $C^+$  ions income to ground surface linearly increases with the increase of anode bias potential, due to the plasma potential will be increased. While the floating surface, the mean energy of the  $C^+$  ions increases from 18 eV to 45 eV with the increase of anode bias potential from 0 V to +50 V, then the mean energy of the  $C^+$  ions enter a steady state for higher anode bias potential because the charges capacitance of ions on the surface lead to the resistance electrical force, then the energy of depositing ions will be decreased. Which can be observed from the floating potential on the surface is positive potential. Although the plasma biasing technique can increase the mean energy of the depositing

ions. But the density of the  $C^+$  ions was greatly reduced from  $5.12 \times 10^{16} \text{ m}^{-3}$  to  $8.13 \times 10^{15} \text{ m}^{-3}$  due to the electrons in the plasma was absorbed by anode electrode of the FCVA source indicate that density of the plasma and ions decrease lead to decreased of ion flux. This affected on the deposition profile and deposition rate of the ta-C films. For the substrate bias potential technique, the mean energy of the  $C^+$  ions linearly increases with the increase of substrate bias potential due to surface potential drops. Moreover, the density of the  $C^+$  ions smaller decrease with the increase of substrate bias potential. It can be explained by the change of center of ta-C deposition area (the center of deposition area is the maximum ion flux which is related to the maximum bombardment of  $C^+$  ions). Therefore, an increase of substrate bias potential leads to an increase of mean energy, but it is not affected on the ion density (high energy high ion flux).

(iii) It is well known that the structure and properties of diamond-like carbon, and in particular the  $sp^3$  content, can be controlled by the energy of  $C^+$  ions. Therefore, in the ta-C deposition, the morphologies, structural, and mechanical properties of the ta-C film deposited using FCVA deposition combine with the plasma biasing and substrate bias were compared. It was found that the ta-C films deposited using plasma biasing technique by applied anode bias potential of +80 V has a very low surface roughness, high  $sp^3$  content of 84%, high hardness of 47 GPa and low electrical conductivity of  $2 \times 10^{-5} \text{ S/m}$ . However, the deposition rate of the film is low. While the ta-C films deposited using the substrate bias technique by applied substrate bias potential of -80 V has a smoother surface, high  $sp^3$  content of 83% and low electrical conductivity of  $2 \times 10^{-5} \text{ S/m}$ . It can be seen that the plasma biasing and substrate bias technique can improve the structural and mechanical of the ta-C films. This was described by the densification model of Robertson [20]. When the energy of the depositing species is higher than the surface penetration threshold energy, the entering atoms penetrate through the surface of the film and subplantation occurs [222]. This leads to a rearrangement of the bonds from  $sp^2$  to  $sp^3$ , resulting in an increase in the local density and hardness of the films. It can conclude that the  $sp^3$  content in the ta-C films can be tailored by controlling energy of the depositing species ( $C^+$  ions).

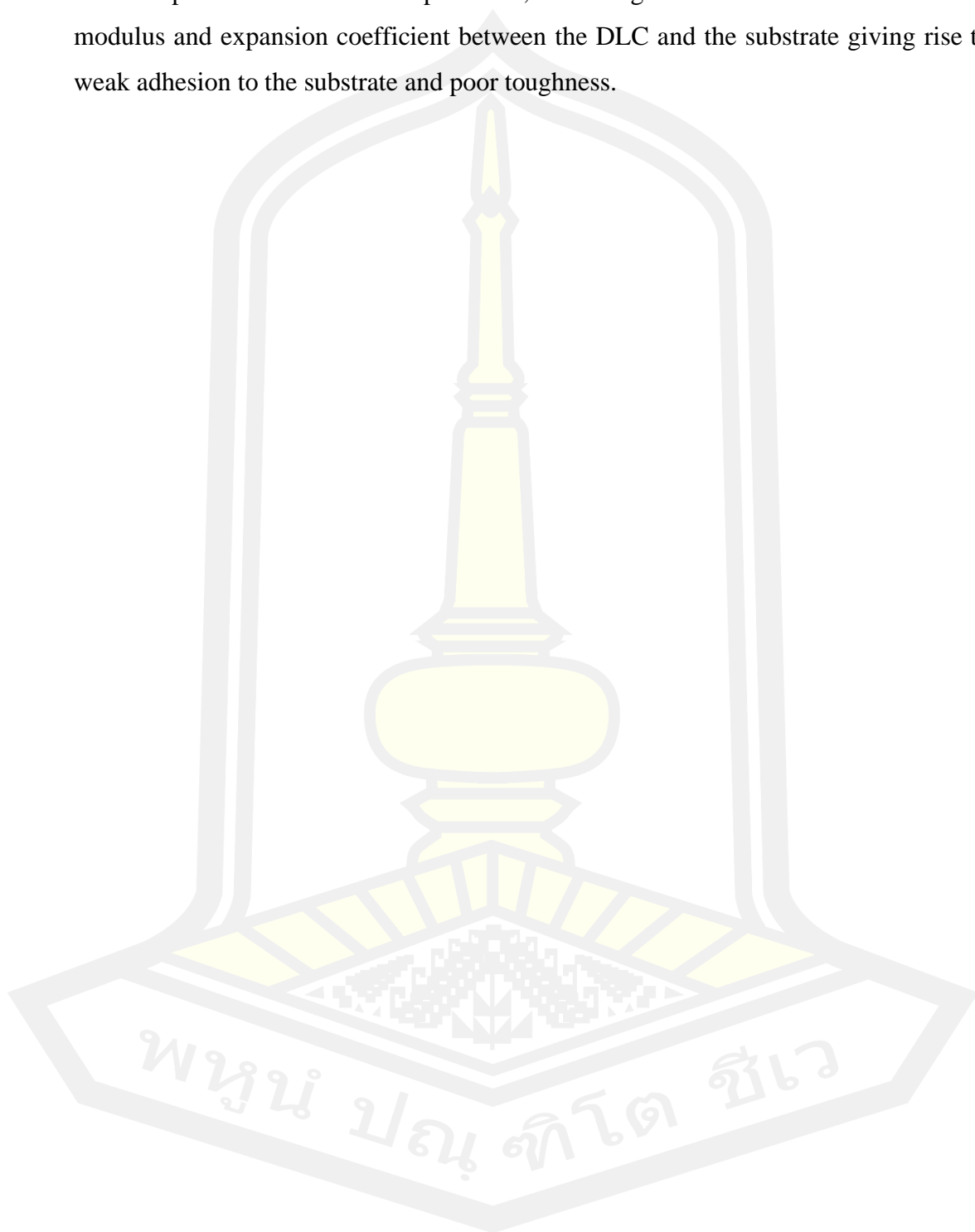
In addition, structural properties of the a-C:H deposited using L-ALIS deposition by varying the discharge potential, were investigated. It was found that the deposition rate of the films increased with the increase of discharge potential, due to the increasing of discharge potential directly affected on  $E \times B$  field in the discharge gap of the L-ALIS. With the higher discharge potential, the electrons were induced with the stronger  $E \times B$  field and moved with the high energy on the discharge gap. As a result, the probability of an ionization rate of the  $C_2H_2$  atoms increases. Therefore, the higher  $C_mH_n^+$  is related to high ion flux and high deposition rate. However, the intense and energetic  $C_mH_n^+$  deposition has more effective in the structure of a-C:H films. The Raman spectroscopy, XPS and XRR analysis found that the a-C:H films has an amorphous characteristic with a higher disorder in the films. The  $I_D/I_G$  has a value in the range of 0.84 to 0.89 for the discharge potential of 800 to 1600 V. In addition, the FWHM of G peak linearly decreased from 203.27 to 197.16  $cm^{-1}$  with the increase of discharge voltage from 800 to 1600 V. The result completely confirm the observed behavior that the films at the lowest discharge voltage have increased structural disorder. Indicate that an increase of discharge potential leads to a decrease in disorder (increase  $sp^2$  phase in aromatic rings), which can here be linked to an increase in  $sp^3$  content in the films that correspond with the XPS test. The XPS test found that  $sp^3$  content (C-C and C-H bonded) decreased from 34% to 30% with the increase of discharge potential. Moreover, the XRR analysis confirms that the decreasing of  $sp^3$  content leads to a decrease of the density of films, which is a decrease from 2.31 to 2.22  $g/cm^3$  with the increase of applied discharge potential of 800 to 1600 V. This result can be discussed by the relaxation model of Ferrari and Robertson [20]. In the nature of L-ALIS discharge, the energy of depositing ions is higher (100 to 1000 eV depending on discharge potential and operating pressure) [ref]. When the energy of depositing ions higher than the surface penetration threshold energy ( $E_i \gg E_p$ ), the kinetic energy of depositing ions transfers to thermal energy and diffuse over the film surface leading to the relaxation of carbon structure, the microstructure in a bond rearrangement from  $sp^3$  to  $sp^2$  bonded and introduce the transfers from diamond-like carbon (DLC) to graphite-like carbon (GLC), which gives rise to a decrease in the local density of the films.

(iv) To produce a superhard amorphous carbon film with a thickness of more than 1  $\mu\text{m}$  on the 304 stainless steel substrates. The multilayer design of alternating of ta-C layer and a-C:H layer was used. The multilayer films consist of Cr interlayer with a thickness of 260 nm and the alternating of ta-C layers and a-C:H layers with a thickness ratio 60 : 50 nm. The a-C:H layers were deposited using L-ALIS by applied discharge potential and discharge current of 1200 V and 13.5 mA respectively. While the ta-C layers were deposited using FCVA deposition by applying charger voltage - 504 V to the PFN, which generates the arc current with a maximum amplitude of about 720 A. The morphologies and mechanical properties were investigated using FE-SEM, nanoindentation tests, and scratch tests. It was found that the multilayer films have a thickness higher than 1000 nm and do not peel on the SUS304 substrate. The SEM image shows the surface of the films very smoother. The cross-sectional image shows the alternating of darker related to a-C:H layers and the brighter related to ta-C layers. The contrast difference is produced by the difference in density between heterogeneous layers with different  $\text{sp}^3$  content. In addition, the hardness of the multilayer films depends on applied substrate bias potential during ta-C layer deposition, in which the M-3 sample has a maximum hardness of 37.6 GPa due to the ta-C layers were deposited using substrate bias of -80 V. Which we are proved that the ta-C films deposited using applied substrate bias potential of -80 V rich  $\text{sp}^3$  content. Therefore, the M-3 films will be had a high hardness and high elastic modulus. Moreover, the multilayer films have high  $H/E$  and  $H^3/E^2$ , it indicates that the multilayer films have good elastic strain to failure and resistance to cracking under the load or well and resistant to plastic deformation.

The scratch test showed that the critical loads of adhesive failure of the a-C:H single layer film of about 3.53 N. While the multilayer M-3 film exhibited the highest critical loads of adhesive failure of the films of about 13.15 N. In addition, the critical loads of adhesive failure of the Cr interlayer on SUS304 have values in the range of about 18 N. This result indicates that the adhesive/cohesive of the multilayer film is higher than a-C:H single layer due to the multilayer film have multiple interfaces, which helps restrict the dislocation and defects in crystalline lattices and free volumes in amorphous structures, leads to the prevents crack formation and propagation under complicated stress fields, which contributes to improving the hardness and toughness.



While the a-C:H single layer film has a high residual compressive stress from the long and complicated cross-linked  $sp^3$  bonds, including the mismatches of the elastic modulus and expansion coefficient between the DLC and the substrate giving rise to weak adhesion to the substrate and poor toughness.



## Chapter VI

### Suggestion and further studies

The future prospects of carbon based-materials, especially DLC films. this thesis has proposed a variety of investigations relating to system and plasma sources design to synthesis ta-C single layer, a-C:H single layer and multilayer amorphous carbon films which it is very much hoped will play an important part in increasing knowledge and providing a good foundation for further research and development in related areas. The ionized physical vapor deposition system with hybrid four plasma sources concept has been responded to be a promising system in developing industrial applications. In addition, the multilayer amorphous carbon film alternating of ta-C layers and a-C:H layers has been proved to be a promising method in developing new materials with exceptional properties in engineering and industrial applications. A specific analytical technique is, however, essential to clearly explain certain phenomena. Furthermore, the improvement of focusing coil of the FCVA source and PFN (for drive focusing coil) is required to achieve a better performance. Further studies, therefore, should be conducted into the following items:

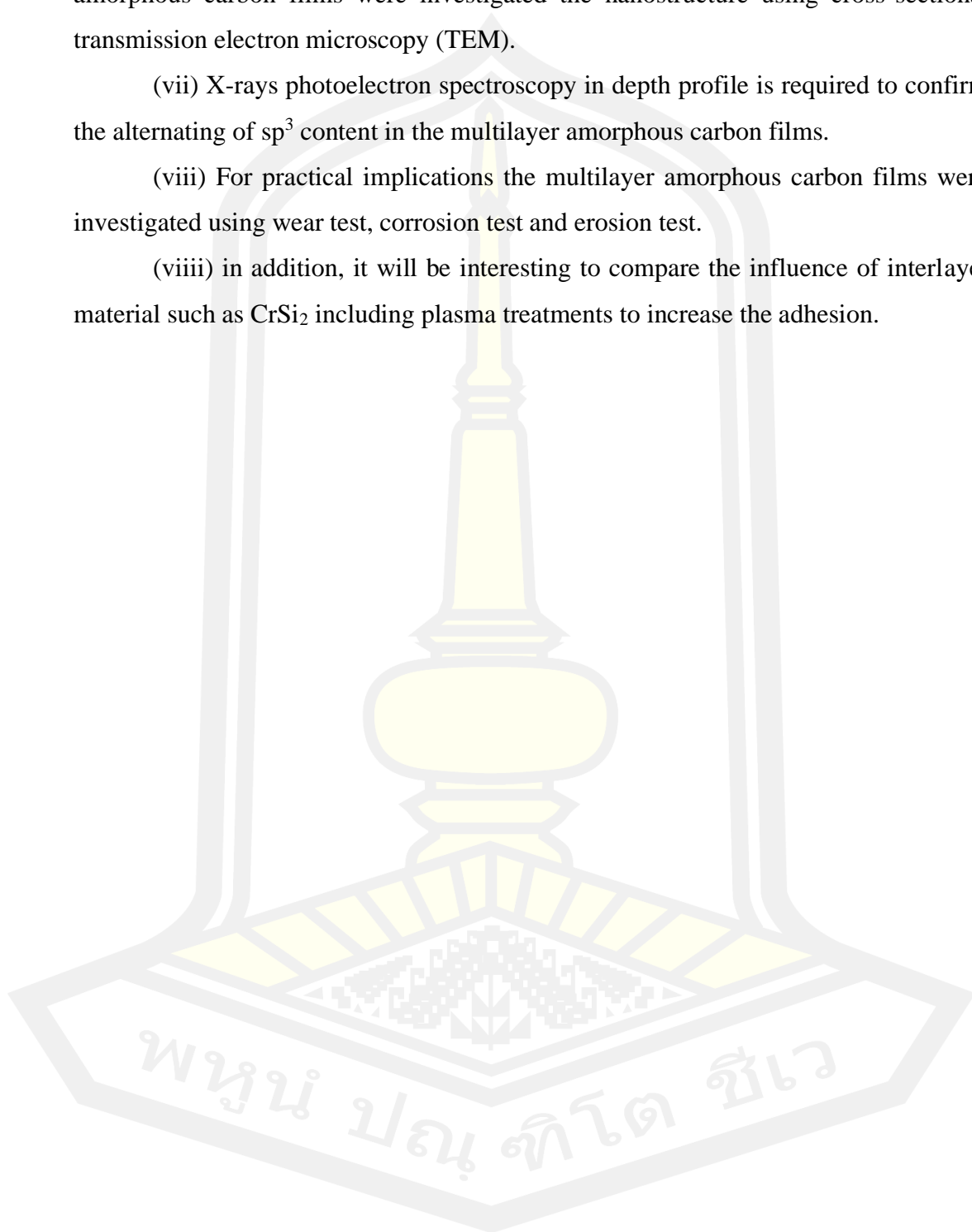
- (i) The magnetron sputtering source should be upgrade to rectangular magnetron sputtering source to support industrial sample.
- (ii) The charger power supply for PFN should be high voltage spec power supply to produce highly density plasma and increase deposition rate of target material and improve properties of the films.
- (iii) The focusing coil of FCVA source should be external induction coil, which install outer the deposition chamber to reduce the influence on the plasma properties.
- (iv) To increase performance of macroparticle filter, the new PFN is requeded for drive only the filtering coil.
- (v) The PXI controller need the new PXI card such as SMU Gard, DMM Gard, and DEQ Gard to increase the data analysis option from the power supply, plasma diagnostic, mass flow controller and PFN.

(vi) The interface of ta-C/a-C:H layers and ta-C/Cr interlayer of the multilayer amorphous carbon films were investigated the nanostructure using cross-sectional transmission electron microscopy (TEM).

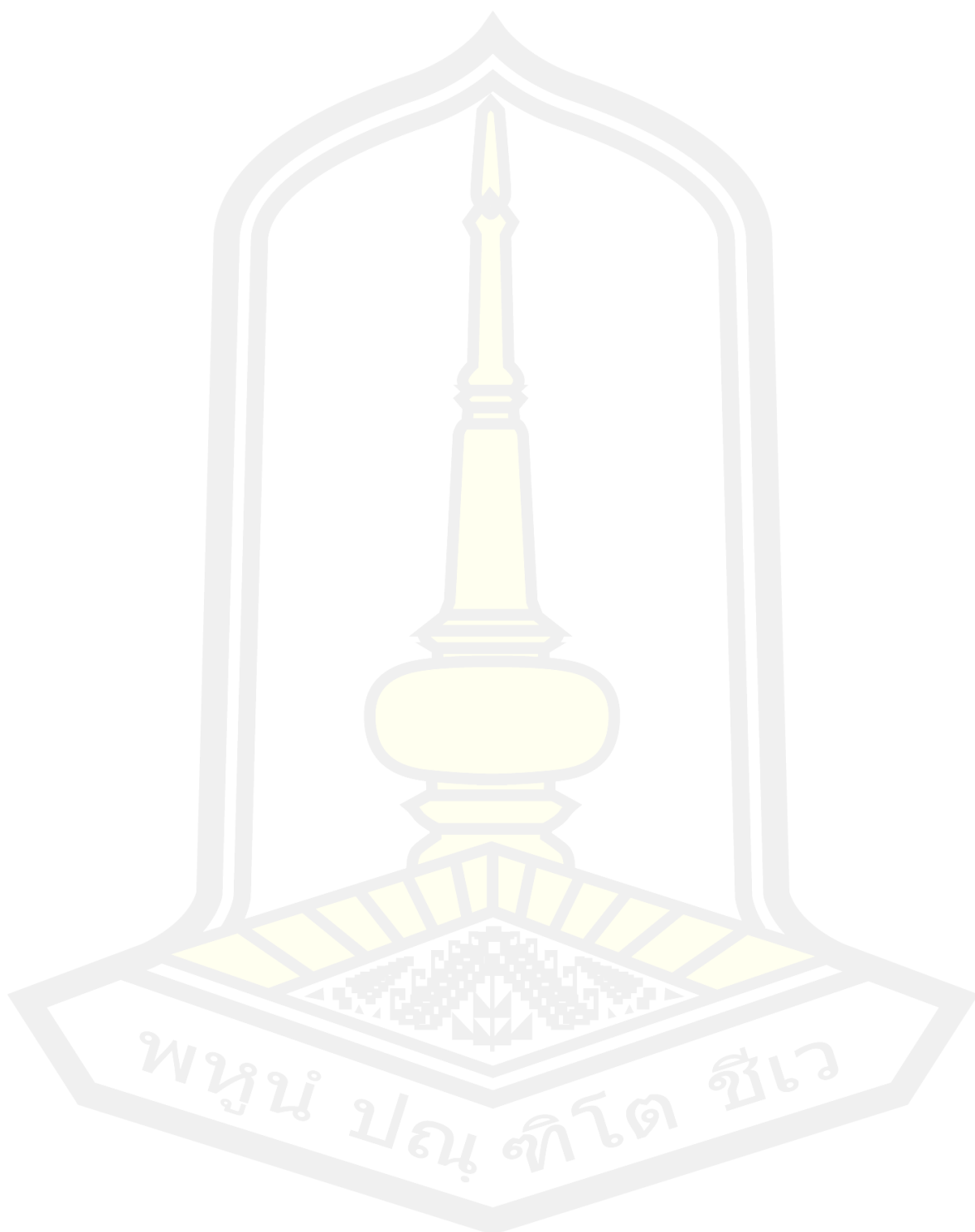
(vii) X-rays photoelectron spectroscopy in depth profile is required to confirm the alternating of  $sp^3$  content in the multilayer amorphous carbon films.

(viii) For practical implications the multilayer amorphous carbon films were investigated using wear test, corrosion test and erosion test.

(viii) in addition, it will be interesting to compare the influence of interlayer material such as  $CrSi_2$  including plasma treatments to increase the adhesion.



## REFERENCES



- [1] R. Lyddy, "Nanotechnology," in *Information Resources in Toxicology*, 4<sup>th</sup> ed., Philip Wexler and Steve G. Gilbert, Ed. Academic Press, 2009, pp. 321–328.
- [2] S. Khare, K. Williams, and K. Gokulan, "Nanotechnology," in *Encyclopedia of Food Microbiology: Second Edition*, vol. 2, Richard K. Robinson, Ed. Elsevier, 2014, pp. 893–900.
- [3] "Thin film," *Wikipedia*. [https://en.wikipedia.org/wiki/Thin\\_film](https://en.wikipedia.org/wiki/Thin_film).
- [4] M. Benelmekki and A. Erbe, "Nanostructured thin films–background, preparation and relation to the technological revolution of the 21<sup>st</sup> century," in *Frontiers of Nanoscience*, vol. 14, Maria Benelmekki and Andreas Erbe, Ed. Elsevier, 2019, pp. 1–34.
- [5] "Cutting tools," *Wikipedia*. [https://en.wikipedia.org/wiki/Cutting\\_tool\\_\(machining\)](https://en.wikipedia.org/wiki/Cutting_tool_(machining)).
- [6] S. George, *Cutting Tools Application*. 2002.
- [7] K. Mylvaganam, Y. Chen, W. Liu, M. Liu, and L. Zhang, "Hard thin films: Applications and challenges," *Anti-Abrasive Nanocoatings Curr. Futur. Appl.*, pp. 544–567, 2014, doi: 10.1016/B978-0-85709-211-3.00021-2.
- [8] A. Fomin, "Superhard titania coatings produced on titanium using induction heat treatment," *Ceram. Int.*, vol. 45, no. 7, pp. 8258–8264, 2019, doi: 10.1016/j.ceramint.2019.01.131.
- [9] Y. Pan, L. Dong, N. Liu, J. Yu, C. Li, and D. Li, "Investigating the influence of epitaxial modulation on the evolution of superhardness of the VN/TiB<sub>2</sub> multilayers," *Appl. Surf. Sci.*, vol. 390, pp. 406–411, 2016, doi: 10.1016/j.apsusc.2016.08.133.
- [10] S. Vepřek, "The search for novel, superhard materials," *J. Vac. Sci. Technol. A Vacuum, Surfaces, Film.*, vol. 17, no. 5, pp. 2401–2420, 1999, doi: 10.1116/1.581977.
- [11] Y. Chung, W. D. Sproul, and S. A. Barnett, "Superhard Coating Materials applications including," *Appl. Phys.*, no. March, pp. 164–168, 2003.
- [12] Y. Z. Hai, "Ion-plating technique and hard coating," *Technical Consultant of Coils Electronic Co., Limited*, pp. 2–3, 2002.
- [13] J. Chrzanowska, L. Kurpaska, M. Giżyński, J. Hoffman, Z. Szymański, and T. Mościcki, "Fabrication and characterization of superhard tungsten boride layers

- deposited by radio frequency magnetron sputtering,” *Ceram. Int.*, vol. 42, no. 10, pp. 12221–12230, 2016, doi: 10.1016/j.ceramint.2016.04.166.
- [14] K. Slipchenko, V. Turkevich, I. Petrusha, V. Bushlya, and J. E. Ståhl, “Superhard pcBN materials with chromium compounds as a binder,” *Procedia Manuf.*, vol. 25, pp. 322–329, 2018, doi: 10.1016/j.promfg.2018.06.090.
- [15] K. Xia *et al.*, “A novel superhard tungsten nitride predicted by machine-learning accelerated crystal structure search,” *Sci. Bull.*, vol. 63, no. 13, pp. 817–824, 2018, doi: 10.1016/j.scib.2018.05.027.
- [16] J. Dong, H. Li, Z. Guo, X. Hao, and D. Chen, “Extraordinary local structure deformation of superhard tungsten tetraboride under compression,” *J. Alloys Compd.*, vol. 817, p. 152989, 2020, doi: 10.1016/j.jallcom.2019.152989.
- [17] C. Li, L. Huang, and J. Yuan, “Effect of  $sp^3$  content on adhesion and tribological properties of non-hydrogenated DLC films,” *Materials (Basel)*, vol. 13, no. 8, 2020, doi: 10.3390/MA13081911.
- [18] K. Bewilogua and D. Hofmann, “History of diamond-like carbon films - From first experiments to worldwide applications,” *Surf. Coatings Technol.*, vol. 242, pp. 214–225, 2014, doi: 10.1016/j.surfcoat.2014.01.031.
- [19] A. C. Ferrari and J. Robertson, “Interpretation of Raman spectra of disordered and amorphous carbon,” *Phys. Rev. B*, vol. 61, no. 20, pp. 95–107, 2000.
- [20] J. Robertson, “Diamond-like amorphous carbon,” vol. 37, pp. 129–281, 2002, doi: 10.1016/S0927-796X(02)00005-0.
- [21] X. Zhang, Z. Yi, T. Zhang, X. Wu, G. Wang, and H. Zhang, “Wear performance of tetrahedral amorphous carbon films prepared by filtered cathodic vacuum arc technique,” *Surf. Coat. Technol.*, vol. 161, pp. 120–124, 2002.
- [22] E. Martínez, J. L. Andújar, M. C. Polo, J. Esteve, J. Robertson, and W. I. Milne, “Study of the mechanical properties of tetrahedral amorphous carbon films by nanoindentation and nanowear measurements,” *Diamond and Related Materials*, vol. 10, no. 2, pp. 145–152, 2001, doi: 10.1016/S0925-9635(00)00461-1.
- [23] J. Wei, H. Li, L. Liu, P. Guo, P. Ke, and A. Wang, “Enhanced tribological and corrosion properties of multilayer ta-C films via alternating  $sp^3$  content,” *Surf.*



- Coatings Technol.*, vol. 374, no. March, pp. 317–326, 2019, doi: 10.1016/j.surfcoat.2019.05.087.
- [24] S. Makowski, F. Schaller, V. Weihnacht, G. Englberger, and M. Becker, “Tribiochemical induced wear and ultra-low friction of superhard ta-C coatings,” *Wear*, vol. 392–393, pp. 139–151, 2017, doi: 10.1016/j.wear.2017.08.015.
- [25] Y. Wang, Y. Ye, H. Li, L. Ji, J. Chen, and H. Zhou, “A magnetron sputtering technique to prepare a-C:H films: Effect of substrate bias,” *Appl. Surf. Sci.*, vol. 257, no. 6, pp. 1990–1995, 2011, doi: 10.1016/j.apsusc.2010.09.040.
- [26] M. Folea, A. Roman, and N. B. Lupulescu, “An overview of DLC coatings on cutting tools performance,” *Acad. J. Manuf. Eng.*, vol. 8, no. 3, pp. 30–36, 2010.
- [27] S. D. A. Lawes, M. E. Fitzpatrick, and S. V. Hainsworth, “Evaluation of the tribological properties of DLC for engine applications,” *J. Phys. D. Appl. Phys.*, vol. 40, no. 18, pp. 5427–5437, 2007, doi: 10.1088/0022-3727/40/18/S03.
- [28] W. I. Milne, “Electronic devices from diamond-like carbon,” *Semicond. Sci. Technol.*, vol. 81, pp. 3–8, 2003, doi: 10.1088/0268-1242/18/3/312.
- [29] C. Casiraghi, J. Robertson, and A. C. Ferrari, “Diamond-like carbon for data and beer storage Carbon,” *Mater. Today*, vol. 10, no. 1, pp. 44–53, 2007.
- [30] A. C. Ferrari, “Diamond-like carbon for magnetic storage disks,” vol. 181, pp. 190–206, 2004, doi: 10.1016/j.surfcoat.2003.10.146.
- [31] D. R. Tallant, J. E. Parmeter, M. P. Siegal, and R. L. Simpson, “The thermal stability of diamond-like carbon,” *Diam. Relat. Mater.*, vol. 4, no. 3, pp. 191–199, 1995, doi: 10.1016/0925-9635(94)00243-6.
- [32] Z. L. Akkerman, H. Efstathiadis, and F. W. Smith, “Thermal stability of diamondlike carbon films,” *J. Appl. Phys.*, vol. 80, no. 5, pp. 3068–3075, 1996, doi: 10.1063/1.363167.
- [33] L. Hultman, “Thermal stability of nitride thin films,” *Vacuum*, vol. 57, no. 1, pp. 1–30, 2000, doi: 10.1016/s0042-207x(00)00143-3.
- [34] X. Sui, J. Liu, S. Zhang, J. Yang, and J. Hao, “Microstructure, mechanical and tribological characterization of CrN/DLC/Cr-DLC multilayer coating with

- improved adhesive wear resistance,” *Appl. Surf. Sci.*, vol. 439, no. 2018, pp. 24–32, 2018, doi: 10.1016/j.apsusc.2017.12.266.
- [35] M. Weiler *et al.*, “Preparation and properties of highly tetrahedral hydrogenated amorphous carbon,” *Physical Review B*, 1996. <http://journals.aps.org/prb/abstract/10.1103/PhysRevB.53.1594>.
- [36] X. Shi *et al.*, “Properties of carbon ion deposited tetrahedral amorphous carbon films as a function of ion energy,” *J. Appl. Phys.*, vol. 79, no. 9, pp. 7234–7240, 1996, doi: 10.1063/1.361440.
- [37] Wikipedia, “CNC machining,” 2002. <https://astromachineworks.com/what-is-cnc-machining/>.
- [38] Wikipedia, “Machine tool.” [https://en.wikipedia.org/wiki/Machine\\_tool](https://en.wikipedia.org/wiki/Machine_tool).
- [39] P. V. Krishna, R. R. Srikant, and D. N. Rao, “Experimental investigation on the performance of nanoboric acid suspensions in SAE-40 and coconut oil during turning of AISI 1040 steel,” *Int. J. Mach. Tools Manuf.*, vol. 50, no. 10, pp. 911–916, 2010, doi: 10.1016/j.ijmachtools.2010.06.001.
- [40] D. J. Ñ, S. Wenlong, and Z. Hui, “Design, fabrication and properties of a self-lubricated tool in dry cutting,” *Int. J. Mach. Tools Manuf.*, vol. 49, pp. 66–72, 2009, doi: 10.1016/j.ijmachtools.2008.08.001.
- [41] N. R. Khalili, S. Duecker, W. Ashton, and F. Chavez, “From cleaner production to sustainable development: the role of academia,” *J. Clean. Prod.*, vol. 96, no. June 2015, pp. 30–43, 2015, doi: 10.1016/j.jclepro.2014.01.099.
- [42] J. A. Ghani, M. Rizal, C. Hassan, and C. Haron, “Performance of green machining: a comparative study of turning ductile cast iron FCD700,” *J. Clean. Prod.*, vol. 85, pp. 289–292, 2014, doi: 10.1016/j.jclepro.2014.02.029.
- [43] W. Lin *et al.*, “A Multi-objective teaching–learning-based optimization algorithm to scheduling in turning processes for minimizing makespan and carbon footprint,” *J. Clean. Prod.*, 2015, doi: 10.1016/j.jclepro.2015.03.099.
- [44] K. Weinert, I. Inasaki, J. W. Sutherland, and T. Wakabayashi, “Dry Machining and Minimum Quantity Lubrication,” vol. 53, no. 2, pp. 511–537, 2004.
- [45] M. Schulze, D. Student, H. Nehler, M. Ottosson, and P. Thollander, “Energy management in industry – a systematic review of previous findings and an integrative conceptual framework,” *J. Clean. Prod.*, vol. 112, pp. 3692–3780,

- 2016, doi: 10.1016/j.jclepro.2015.06.060.
- [46] R. R. Srikant and V. S. N. V. Ramana, "Performance evaluation of vegetable emulsifier based green cutting fluid in turning of AISI 1040 steel-an initiative towards sustainable manufacturing," *J. Clean. Prod.*, vol. 108, pp. 104–109, 2015, doi: 10.1016/j.jclepro.2015.07.031.
- [47] M. F. Rajemi, P. T. Mativenga, and A. Aramcharoen, "Sustainable machining: selection of optimum turning conditions based on minimum energy considerations," *J. Clean. Prod.*, vol. 18, no. 10–11, pp. 1059–1065, 2010, doi: 10.1016/j.jclepro.2010.01.025.
- [48] S. Ghosh and P. V. Rao, "Application of sustainable techniques in metal cutting for enhanced machinability: a review," *J. Clean. Prod.*, vol. 100, pp. 17–34, 2015, doi: 10.1016/j.jclepro.2015.03.039.
- [49] Y. Xing, J. Deng, J. Zhao, G. Zhang, and K. Zhang, "Cutting performance and wear mechanism of nanoscale and microscale textured  $\text{Al}_2\text{O}_3/\text{TiC}$  ceramic tools in dry cutting of hardened steel," *Int. J. Refract. Met. Hard Mater.*, vol. 43, pp. 46–58, 2014, doi: 10.1016/j.ijrmhm.2013.10.019.
- [50] J. Xie, M. J. Luo, K. K. Wu, L. F. Yang, and D. H. Li, "Experimental study on cutting temperature and cutting force in dry turning of titanium alloy using a non-coated micro-grooved tool," *Int. J. Mach. Tools Manuf.*, vol. 73, pp. 25–36, 2013, doi: 10.1016/j.ijmachtools.2013.05.006.
- [51] W. Ze, D. Jianxin, S. Chun, L. Chen, and X. Dan, "Performance of the micro-texture self-lubricating and pulsating heat pipe self-cooling tools in dry cutting process," *Int. J. Refract. Met. Hard Mater.*, vol. 45, no. 238–248, 2014, doi: 10.1016/j.ijrmhm.2014.02.004.
- [52] J. Xie, M. Luo, J. He, X. Liu, and T. Tan, "Micro-grinding of Micro-groove Array on Tool Rake Surface for Dry Cutting of Titanium Alloy," *Int. J. Precis. Eng. Manuf.*, vol. 13, no. 10, pp. 1845–1852, 2012, doi: 10.1007/s12541-012-0242-9.
- [53] Y. Xing, J. Deng, Y. Lian, K. Zhang, G. Zhang, and J. Zhao, "Applied Surface Science Multiple nanoscale parallel grooves formed on  $\text{Si}_3\text{N}_4/\text{TiC}$  ceramic by femtosecond pulsed laser," *Appl. Surf. Sci.*, vol. 289, pp. 62–71, 2014, doi: 10.1016/j.apsusc.2013.10.094.

- [54] “CDBP - CNC Inserts.” <https://www.indiamart.com/proddetail/cdbp-cnc-inserts-17676764230.html>.
- [55] P. C. Patnaik and W. R. Chen, “Advanced Materials and Multifunctional Structures for Aerospace Vehicles,” in *Multifunctional Structures / Integration of Sensors and Antennas*, 2006, no. May, pp. 1–28, [Online]. Available: <https://www.dglr.de/publikationen/2018/480065.pdf>.
- [56] S. Barnett and A. Madan, “Superhard superlattices,” *Phys. World*, vol. 11, no. 1, pp. 45–48, 1998, doi: 10.1088/2058-7058/11/1/34.
- [57] X. T. Zeng, “TiN/NbN superlattice hard coatings deposited by unbalanced magnetron sputtering,” *Surf. Coatings Technol.*, vol. 113, no. 1–2, pp. 75–79, 1999, doi: 10.1016/S0257-8972(98)00825-1.
- [58] Q. Yang, C. He, L. R. Zhao, and J. P. Immarigeon, “Preferred orientation and hardness enhancement of TiN/CrN superlattice coatings deposited by reactive magnetron sputtering,” *Scr. Mater.*, vol. 46, no. 4, pp. 293–297, 2002, doi: 10.1016/S1359-6462(01)01241-6.
- [59] M. S. Wong, G. Y. Hsiao, and S. Y. Yang, “Preparation and characterization of AlN/ZrN and AlN/TiN nanolaminate coatings,” *Surf. Coatings Technol.*, vol. 133–134, pp. 160–165, 2000, doi: 10.1016/S0257-8972(00)00958-0.
- [60] W. D. Sproul, “New Routes in the Preparation Nitride Superlattice Coatings,” *Science.*, vol. 273, pp. 889–892, 1996.
- [61] L. Chen, J. Paulitsch, Y. Du, and P. H. Mayrhofer, “Thermal stability and oxidation resistance of Ti-Al-N coatings,” *Surf. Coatings Technol.*, vol. 206, no. 11–12, pp. 2954–2960, 2012, doi: 10.1016/j.surfcoat.2011.12.028.
- [62] Q. Yang and L. R. Zhao, “Thermal stability of polycrystalline TiN/CrN superlattice coatings,” *J. Vac. Sci. Technol. A*, vol. 21, no. 3, pp. 558–562, 2003, doi: 10.1116/1.1559922.
- [63] J. Robertson, “Advances in Physics Amorphous carbon,” *Adv. Phys.*, vol. 35, no. 4, pp. 37–41, 1986, doi: 10.1080/00018738600101911.
- [64] J. C. Angus and C. C. Hayman, “Low-Pressure, Metastable Growth of Diamond and "Diamondlike" Phases,” *Science.*, vol. 24, pp. 914–921, 1988.
- [65] V. Tiron *et al.*, “Overcoming the insulating materials limitation in HiPIMS: Ion-assisted deposition of DLC coatings using bipolar HiPIMS,” *Appl. Surf.*

- Sci.*, vol. 494, pp. 871–879, 2019, doi: 10.1016/j.apsusc.2019.07.239.
- [66] A. LiBassi, A. C. Ferrari, V. Stolojan, B. K. Tanner, J. Robertson, and L. M. Brown, “Density,  $sp^3$  content and internal layering of DLC films by X-ray reflectivity and electron energy loss spectroscopy,” *Diam. Relat. Mater.*, vol. 9, pp. 771–776, 2000.
- [67] N. Ravi, V. L. Bukhovets, I. G. Varshavskaya, and G. Sundararajan, “Deposition of diamond-like carbon films on aluminium substrates by RF-PECVD technique: Influence of process parameters,” *Diam. Relat. Mater.*, vol. 16, pp. 90–97, 2007, doi: 10.1016/j.diamond.2006.04.001.
- [68] C. Chouquet *et al.*, “Structural and mechanical properties of a-C:H and Si doped a-C:H thin films grown by LF-PECVD,” *Surf. Coatings Technol.*, vol. 204, no. 9–10, pp. 1339–1346, 2010, doi: 10.1016/j.surfcoat.2009.09.016.
- [69] M. Weiler, S. Sattel, K. Jung, H. Ehrhardt, V. S. Veerasamy, and J. Robertson, “Highly tetrahedral, diamond-like amorphous hydrogenated carbon prepared from a plasma beam source,” *Appl. Phys. Lett.*, vol. 64, no. 21, pp. 2797–2799, 1994, doi: 10.1063/1.111428.
- [70] P. J. Fallon *et al.*, “Properties of filtered-ion-beam-deposited diamondlike carbon as a function of ion energy,” *Phys. Rev. B*, vol. 48, no. 7, pp. 4777–4782, 1993, doi: 10.1103/PhysRevB.48.4777.
- [71] M. Chhowalla *et al.*, “Influence of ion energy and substrate temperature on the optical and electronic properties of tetrahedral amorphous carbon (ta-C) films,” *J. Appl. Phys.*, vol. 81, no. 1, pp. 139–145, 1997, doi: 10.1063/1.364000.
- [72] K. B. K. Teo, S. E. Rodil, J. T. H. Tsai, A. C. Ferrari, J. Robertson, and W. I. Milne, “Effect of graphitic inclusions on the optical gap of tetrahedral amorphous carbon films,” *J. Appl. Phys.*, vol. 89, no. 7, pp. 3706–3710, 2001, doi: 10.1063/1.1351863.
- [73] S. Xu, L. K. Cheah, and B. K. Tay, “Spectroscopic ellipsometry studies of tetrahedral amorphous carbon prepared by filtered cathodic vacuum arc technique,” *Thin Solid Films*, vol. 312, pp. 160–169, 1998.
- [74] A. C. Ferrari, S. E. Rodil, J. Robertson, and W. I. Milne, “Is stress necessary to stabilise  $sp^3$  bonding in diamond-like carbon?,” *Diam. Relat. Mater.*, vol. 11, no. 3–6, pp. 994–999, 2002, doi: 10.1016/S0925-9635(01)00705-1.

- [75] A. C. Ferrari and J. Robertson, “Resonant Raman spectroscopy of disordered, amorphous, and diamondlike carbon,” *Phys. Rev. B - Condens. Matter Mater. Phys.*, vol. 64, no. 7, pp. 1–13, 2001, doi: 10.1103/PhysRevB.64.075414.
- [76] N. A. Marks, D. R. McKenzie, B. A. Pailthorpe, M. Bernasconi, and M. Parrinello, “Microscopic Structure of Tetrahedral Amorphous Carbon,” *Phys. Rev. Lett.*, vol. 76, no. 5, pp. 768–771, 1996, doi: 10.1103/PhysRevLett.76.768.
- [77] Y. Lifshitz *et al.*, “Growth mechanisms of DLC films from C<sup>+</sup> ions: experimental studies,” *Diam. Relat. Mater.*, vol. 4, no. 4, pp. 318–323, 1995, doi: 10.1016/0925-9635(94)05205-0.
- [78] Y. Lifshitz *et al.*, “Optical and photoemission studies of DLC films prepared with a systematic variation of the sp<sup>3</sup>:sp<sup>2</sup> composition,” *Diam. Relat. Mater.*, vol. 6, no. 5–7, pp. 687–693, 1997, doi: 10.1016/S0925-9635(96)00696-6.
- [79] R. Locher, C. Wild, and P. Koidl, “Direct ion-beam deposition of amorphous hydrogenated carbon films,” *Surf. Coatings Technol.*, vol. 47, no. 1–3, pp. 426–432, 1991, doi: 10.1016/0257-8972(91)90308-J.
- [80] D. R. McKenzie, D. Muller, and B. A. Pailthorpe, “Compressive-stress-induced formation of thin-film tetrahedral amorphous carbon,” *Phys. Rev. Lett.*, vol. 67, no. 6, pp. 773–776, 1991, doi: 10.1103/PhysRevLett.67.773.
- [81] A. Erdemir and C. Donnet, “Tribology of diamond-like carbon films: Recent progress and future prospects,” *J. Phys. D. Appl. Phys.*, vol. 39, no. 18, 2006, doi: 10.1088/0022-3727/39/18/R01.
- [82] J. Robertson, “Mechanical properties and coordinations of amorphous carbons,” *Phys. Rev. Lett.*, vol. 68, no. 2, pp. 220–223, 1992, doi: 10.1103/PhysRevLett.68.220.
- [83] Sam Zhang, *Thin Films and Coatings: Toughening and Toughness Characterization*. Oakville, Canada: Apple Academic Press Inc., 2015.
- [84] G. M. Pharr *et al.*, “Hardness, elastic modulus, and structure of very hard carbon films produced by cathodic-arc deposition with substrate pulse biasing,” *Appl. Phys. Lett.*, vol. 779, no. 1996, p. 779, 1995, doi: 10.1063/1.116530.
- [85] A. C. Ferrari, J. Robertson, M. G. Beghi, C. E. Bottani, R. Ferulano, and R. Pastorelli, “Elastic constants of tetrahedral amorphous carbon films by surface Brillouin scattering,” *Appl. Phys. Lett.*, vol. 75, no. 13, pp. 1893–1895, 1999,



doi: 10.1063/1.124863.

- [86] S. Xu, D. Flynn, B. K. Tay, S. Praver, and K. W. Nugent, "Mechanical properties and Raman spectra of tetrahedral amorphous carbon films with high sp<sup>3</sup> fraction deposited using a filtered cathodic arc," *Philos. Mag. B*, vol. 76, no. 3, pp. 37–41, 1997.
- [87] B. Schultrich, H. Scheibe, D. Drescher, and H. Ziegele, "Deposition of superhard amorphous carbon films by pulsed vacuum arc deposition," *Surf. Coat. Technol.*, vol. 98, no. 1–3, pp. 1097–1101, 1998, doi: 10.1016/S0257-8972(97)00386-1.
- [88] D. H. Buckley, "TRIBOLOGICAL PROPERTIES OF SURFACES," *Thin Solid Films*, vol. 53, pp. 271–283, 1978.
- [89] J. Robertson, "Diamond-Like Carbon Films, Properties and Applications," in *Comprehensive Hard Materials*, vol. 3, Vinod K. Sarin, Ed. Elsevier Ltd, 2014, pp. 101–139.
- [90] J. Koskinen *et al.*, "Microstructural changes in DLC films due to tribological contact," *Surf. Coatings Technol.*, vol. 109, pp. 385–390, 1998.
- [91] T. Roch, V. Weihnacht, H. Scheibe, A. Roch, and A. F. Lasagni, "Direct Laser Interference Patterning of tetrahedral amorphous carbon films for tribological applications," *Diam. Relat. Mater.*, vol. 33, pp. 20–26, 2013, doi: 10.1016/j.diamond.2012.12.002.
- [92] X. Chen, Z. Peng, X. Yu, Z. Fu, W. Yue, and C. Wang, "Microstructure and tribological performance of self-lubricating diamond/tetrahedral amorphous carbon composite film," *Appl. Surf. Sci.*, vol. 257, no. 8, pp. 3180–3186, 2011, doi: 10.1016/j.apsusc.2010.10.136.
- [93] J. Oksanen *et al.*, "Tribology International Tribological properties of laser-textured and ta-C coated surfaces with burnished WS 2 at elevated temperatures," *Tribology Int.*, vol. 70, pp. 94–103, 2014, doi: 10.1016/j.triboint.2013.09.005.
- [94] Y. C. Ean, Y.-J. Jang, J.-K. Kim, W. L. Y. Hsien, N. J. Siambun, and S.-S. Kim, "Effect of Substrate Bias on the Tribological Behavior of ta-C Coating Prepared by Filtered Cathodic Vacuum Arc," *Int. J. Precis. Eng. Manuf.*, vol. 18, no. 5, pp. 779–787, 2017, doi: DOI: 10.1007/s12541-017-0093-5.



- [95] T. Aizawa, E. Masaki, and Y. Sugita, "Complete ashing of used DLC coating for reuse of the end-milling tools," *Manuf. Lett.*, vol. 2, no. 1, pp. 1–3, 2014, doi: 10.1016/j.mfglet.2013.10.006.
- [96] W. M. Silva, L. M. Jesus, J. R. Carneiro, P. S. Souza, P. S. Martins, and V. J. Trava-Airoldi, "Performance of carbide tools coated with DLC in the drilling of SAE 323 aluminum alloy," *Surf. Coatings Technol.*, vol. 284, pp. 404–409, 2015, doi: 10.1016/j.surfcoat.2015.09.061.
- [97] P. Baowan, C. Saikaew, and A. Wisitsoraat, "Influence of helix angle on tool performances of TiAlN- and DLC-coated carbide end mills for dry side milling of stainless steel," *Int. J. Adv. Manuf. Technol.*, vol. 90, no. 9–12, pp. 3085–3097, 2017, doi: 10.1007/s00170-016-9601-5.
- [98] N. Nemati, O. V Penkov, and D. Kim, "Superior surface protection governed by optimized interface characteristics in WC/DLC multilayer coating," *Surf. Coat. Technol.*, vol. 385, p. 125446, 2020, doi: 10.1016/j.surfcoat.2020.125446.
- [99] A. Misra, J. P. Hirth, and R. G. Hoagland, "Length-scale-dependent deformation mechanisms in incoherent metallic multilayered composites," *Acta Mater.*, vol. 53, no. 18, pp. 4817–4824, 2005, doi: 10.1016/j.actamat.2005.06.025.
- [100] M. Kot, L. Major, and J. Lackner, "The tribological phenomena of a new type of TiN/a-C: H multilayer coatings," *Mater. Des.*, vol. 51, no. April, pp. 280–286, 2013, doi: 10.1016/j.matdes.2013.04.008.
- [101] L. Liu *et al.*, "Improved interfacial adhesion between TiAlN/DLC multilayered coatings by controlling the morphology via bias," *Surf. Coatings Technol.*, vol. 331, no. July, pp. 15–20, 2017, doi: 10.1016/j.surfcoat.2017.10.029.
- [102] Y. Lin, Z. Zhou, and K. Y. Li, "Improved wear resistance at high contact stresses of hydrogen-free diamond-like carbon coatings by carbon/carbon multilayer architecture," *Appl. Surf. Sci.*, vol. 477, pp. 137–146, 2019, doi: 10.1016/j.apsusc.2017.11.118.
- [103] A. Anders, "Time-dependence of ion charge state distributions of vacuum arcs: An interpretation involving atoms and charge exchange collisions," *IEEE*

- Trans. Plasma Sci.*, vol. 33, no. 1 II, pp. 205–209, 2005, doi: 10.1109/TPS.2004.841804.
- [104] I. G. Brown, “Vacuum arc ion sources,” *Rev. Sci. Instrum.*, vol. 65, no. 10, pp. 3061–3081, 1994, doi: 10.1063/1.1144756.
- [105] André Anders and G. Y. Yushkov, “Ion flux from vacuum arc cathode spots in the absence and presence of a magnetic field,” *J. Appl. Phys.*, vol. 91, no. May, p. 4824, 2002, doi: 10.1063/1.1459619.
- [106] E. Hantzsche, “Two-Dimensional Models of Expanding Vacuum Arc Plasmas,” *IEEE Trans. Plasma Sci.*, vol. 23, no. 6, pp. 893–898, 1995.
- [107] C. Wieckert, “A Multicomponent Theory of the Cathodic Plasma Jet in Vacuum Arcs,” *Contrib. to Plasma Phys.*, vol. 27, no. 5, pp. 309–330, 1987.
- [108] J. E. Daalder, “Components of cathode erosion in vacuum arcs,” *J. Phys. D Appl. Phys.*, vol. 9, pp. 2379–2395, 1976.
- [109] D. M. Sanders and A. Anders, “Review of Cathodic Arc Deposition Technology at the Start of the New Millennium,” *Surf. Coatings Technol.*, vol. 133, pp. 78–90, 2000, doi: 10.1016/S0257-8972(00)00879-3.
- [110] K. Miernik and J. Walkowicz, “Spatial distribution of microdroplets generated in the cathode spots of vacuum arcs,” *Surf. Coatings Technol.*, vol. 125, pp. 161–166, 2000.
- [111] C. Technology, “The ion current density and spectroscopic study in a straight magnetic filtering arc deposition system,” *Surf. Coatings Technol.*, vol. 95, pp. 201–206, 1997.
- [112] A. Anders, “Approaches to rid cathodic arc plasmas of macro- and nanoparticles: A review,” *Surf. Coatings Technol.*, vol. 120–121, pp. 319–330, 1999, doi: 10.1016/S0257-8972(99)00460-0.
- [113] J. Storer, J. E. Galvin, and I. G. Brown, “Transport of vacuum arc plasma through straight and curved magnetic ducts,” *J. Appl. Phys.*, vol. 66, no. 11, pp. 5245–5250, 1989, doi: 10.1063/1.343711.
- [114] M. M. M. Bilek, D. R. McKenzie, Y. Yin, M. U. Chhowalla, and W. I. Milne, “Interactions of the directed plasma from a cathodic arc with electrodes and magnetic fields,” *IEEE Trans. Plasma Sci.*, vol. 24, no. 5, pp. 1291–1298, 1996, doi: 10.1109/27.538803.

- [115] A. Anders, S. Anders, and I. G. Brown, "Transport of vacuum arc plasmas through magnetic macroparticle filters," *Plasma Sources Sci. Technol.*, vol. 4, no. 1, pp. 1–12, 1995, doi: 10.1088/0963-0252/4/1/001.
- [116] André Anders, "Macroparticle Filters," in *Cathodic Arcs*, Newyok, NY: Springer, 2008, pp. 299–362.
- [117] J. Koskinen, A. Anttila, and J. P. Hirvonen, "Diamond-like carbon coatings by arc-discharge methods," *Surf. Coatings Technol.*, vol. 47, no. 1–3, pp. 180–187, 1991, doi: 10.1016/0257-8972(91)90280-A.
- [118] M. Hakovirta, J. Salo, A. Anttila, and R. Lappalainen, "Graphite particles in the diamond-like a-C films prepared with the pulsed arc-discharge method," *Diam. Relat. Mater.*, vol. 4, no. 12, pp. 1335–1339, 1995, doi: 10.1016/0925-9635(95)00313-4.
- [119] S. Anders, A. Anders, M. R. Dickinson, R. A. MacGill, and I. G. Brown, "S-shaped magnetic macroparticle filter for cathodic arc deposition," *IEEE Trans. Plasma Sci.*, vol. 25, no. 4, pp. 670–674, 1997, doi: 10.1109/27.640683.
- [120] M. M. M. Bilek and I. G. Brown, "Deposition probe technique for the determination of film thickness uniformity," *Rev. Sci. Instrum.*, vol. 69, no. 9, pp. 3353–3356, 2010, doi: 10.1063/1.1149100.
- [121] B. Petereit, P. Siemroth, H. Schneider, and H. Hilgers, "High current filtered arc deposition for ultra thin carbon overcoats on magnetic hard disks and read-write heads," *Surf. Coatings Technol.*, vol. 175, pp. 648–650, 2003, doi: 10.1016/S0257-8972.
- [122] P. Siemroth, J. Berthold, B. Petereit, H. Schneider, and H. Hilgers, "A new generation of filtered arc sources for ultrathin top coats on magnetic hard disks," *Surf. Coat. Technol.*, vol. 189, pp. 684–690, 2004, doi: 10.1016/j.surfcoat.2004.07.004.
- [123] T. Witke, T. Schuelke, B. Schultrich, P. Siemroth, and J. Vetter, "Comparison of filtered high-current pulsed arc deposition ( $\phi$ /HCA) with conventional vacuum arc methods," *Surf. Coatings Technol.*, vol. 126, pp. 81–88, 2000.
- [124] Thomas Schulke, A. Anders, and P. Siemroth, "Macroparticle Filtering of High-Current Vacuum Arc Plasmas," *IEEE Trans. Plasma Sci.*, vol. 25, no. 4, pp. 660–664, 1997.

- [125] H. Takikawa and H. Tanoue, "Review of cathodic arc deposition for preparing droplet-free thin films," *IEEE Trans. Plasma Sci.*, vol. 234, no. 4, pp. 992–999, 2007, doi: 10.1109/DEIV.2006.357354.
- [126] H. Fukui, J. Okida, N. Omori, H. Moriguchi, and K. Tsuda, "Cutting performance of DLC coated tools in dry machining aluminum alloys," *Surf. Coatings Technol.*, vol. 187, no. 1, pp. 70–76, 2004, doi: 10.1016/j.surfcoat.2004.01.014.
- [127] N. Miyakawa, S. Minamisawa, H. Takikawa, and T. Sakakibara, "Physical-chemical hybrid deposition of DLC film on rubber by T-shape filtered-arc-deposition," *Vacuum*, vol. 73, no. 3–4, pp. 611–617, 2004, doi: 10.1016/j.vacuum.2003.12.079.
- [128] H. Takikawa, N. Miyakawa, S. Minamisawa, and T. Sakakibara, "Fabrication of diamond-like carbon film on rubber by T-shape filtered-arc-deposition under the influence of various ambient gases," *Thin Solid Films*, vol. 457, no. 1, pp. 143–150, 2004, doi: 10.1016/j.tsf.2003.12.029.
- [129] H. Hikokasa, T. Iwasaki, H. Takikawa, T. Sakakibara, H. Hasegawa, and N. Tsuji, "Development of X-shape filtered arc deposition apparatus for thick ta-C film coating," *IEEJ Trans. Fundam. Mater.*, vol. 126, no. 8, pp. 757–762, 2006, doi: 10.1541/ieejfms.126.757.
- [130] H. Hikosaka, Y. Iwasaki, H. Tanoue, H. Takikawa, T. Sakakibara, and H. Hasegawa, "Development of X-shape filtered arc deposition (X-FAD) apparatus and DLC/Cr film preparation," in *Proceedings - International Symposium on Discharges and Electrical Insulation in Vacuum, ISDEIV*, 2006, vol. 2, pp. 620–623, doi: 10.1109/DEIV.2006.357378.
- [131] H. Takikawa, K. Izumi, R. Miyano, and T. Sakakibara, "DLC thin film preparation by cathodic arc deposition with a super droplet-free system," *Surf. Coatings Technol.*, vol. 163–164, pp. 368–373, 2003, doi: 10.1016/S0257-8972(02)00629-1.
- [132] Y. Iwasaki, S. Minamisawa, H. Takikawa, T. Sakakibara, and H. Hasegawa, "Influence of duct bias on deposition rate of DLC film in T-shape filtered arc deposition," *Vacuum*, vol. 80, no. 11–12, pp. 1266–1271, 2006, doi: 10.1016/j.vacuum.2006.01.060.

- [133] N. Instruments, “PXI NI PXI-8108 User Manual,” no. March. 2010, [Online]. Available: <http://www.ni.com/pdf/manuals/372561e.pdf>.
- [134] Artisan Technology Group, “NI PXI-8108 2.53 GHz Dual-Core Embedded Controller.” <https://www.artisanng.com/TestMeasurement/87275-1/National-Instruments-PXI-8108-2-53-GHz-Dual-Core-Embedded-Controller>.
- [135] NATIONAL INSTRUMENT, “DEVICE SPECIFICATIONS NI PXI-2565 16-SPST Power Relay Module.” NATIONAL INSTRUMENT, [Online]. Available: [ni.com](http://ni.com).
- [136] Artisan Technology Group, “NI PXI-2565 16-Channel High Power General Purpose Relay.” <https://www.artisanng.com/TestMeasurement/75737-4/National-Instruments-PXI-2565-16-Channel-High-Power-General-Purpose-Relay>.
- [137] “DEVICE SPECIFICATIONS NI 6251 M Series Data Acquisition:16 AI, 1.25 MS/s, 24 DIO, 2 AO The.” NATIONAL INSTRUMENT, pp. 1–26.
- [138] G. Bräuer, “Magnetron Sputtering,” in *Comprehensive Materials Processing*, vol. 4, 2014, pp. 57–73.
- [139] J. Schein *et al.*, “Low Mass Vacuum Arc Thruster System for Station Keeping Missions,” 2001.
- [140] A. Anders, J. Schein, and N. Qi, “Pulsed vacuum-arc ion source operated with a ‘triggerless’ arc initiation method,” *Rev. Sci. Instrum.*, vol. 71, no. 2 II, pp. 827–829, 2000, doi: 10.1063/1.1150305.
- [141] A. Anders, I. G. Brown, R. A. MacGill, and M. R. Dickinson, “‘Triggerless’ triggering of vacuum arcs,” *J. Phys. D. Appl. Phys.*, vol. 31, no. 5, pp. 584–587, 1998, doi: 10.1088/0022-3727/31/5/015.
- [142] Gennady A. Mesyats and Dimitri I. Proskurovsky, “Pulsed Electrical Discharge in Vacuum,” in *Contributions to Plasma Physics*, 1st ed., Springer Berlin, Heidelberg, 1990.
- [143] H. Lux *et al.*, “The role of substrate temperature and magnetic filtering for DLC by cathodic arc evaporation,” *Coatings*, vol. 9, no. 5. 2019, doi: 10.3390/COATINGS9050345.
- [144] W.-Y. Lee, Y.-J. Jang, T. Tokoroyama, M. Murashima, and N. Umehara, “Effect of defects on wear behavior in ta-C coating prepared by filtered

- cathodic vacuum arc deposition,” *Diam. Relat. Mater.*, vol. 105, p. 107789, 2020.
- [145] D. M. Sanders and A. Anders, “Review of cathodic arc deposition technology at the start of the new millennium,” *Surf. Coatings Technol.*, vol. 133–134, pp. 78–90, 2000.
- [146] Wikipedia, “Pulsed forming network.” [https://en.wikipedia.org/wiki/Pulse-forming\\_network](https://en.wikipedia.org/wiki/Pulse-forming_network).
- [147] General Atomics, “Pulse Forming Networks.” <https://www.ga.com/capacitors/pulse-forming-networks>.
- [148] T. Abe and K. Oyama, “Langmuir probe,” in *An Introduction to Space Instrumentation*, K. Oyama and C. Z. Cheng, Eds. 2013, pp. 63–75.
- [149] L. Conde, “An introduction to Langmuir probe diagnostics of plasmas.” E.T.S. Ingenieros Aeronáuticos, Spain, 2011.
- [150] Francis F. Chen, *Plasma Physics and Controlled Fusion*, 2<sup>nd</sup> ed. Newyok: Springer, 2006.
- [151] A. Anders and E. Oks, “Charge-state-resolved ion energy distribution functions of cathodic vacuum arcs: A study involving the plasma potential and biased plasmas,” *J. Appl. Phys.*, vol. 101, no. 4, 2007, doi: 10.1063/1.2561226.
- [152] A. Anders, N. Pasaja, S. H. N. Lim, T. C. Petersen, and V. J. Keast, “Plasma biasing to control the growth conditions of diamond-like carbon André,” *Surf. Coat. Technol.*, vol. 201, no. 8, pp. 4628–4632, 2007.
- [153] B. Schultrich, “Structure and Characterization of Vacuum Arc Deposited Carbon Films—A Critical Overview,” *Coatings*, vol. 12, no. 2, p. 109, 2022, doi: 10.3390/coatings12020109.
- [154] E. A. Edelberg, A. Perry, N. Benjamin, and E. S. Aydil, “Compact floating ion energy analyzer for measuring energy distributions of ions bombarding radio-frequency biased electrode surfaces,” *Rev. Sci. Instrum.*, vol. 70, no. 6, pp. 2689–2698, 1999, doi: 10.1063/1.1149829.
- [155] V. M. Bardakov, S. D. Ivanov, A. V. Kazantsev, and N. A. Strokin, “Peculiarities of measuring ion energy distribution in plasma with a retarding field analyzer,” *Rev. Sci. Instrum.*, vol. 86, no. 5, 2015, doi: 10.1063/1.4920998.



- [156] D. Gahan *et al.*, “Ion energy distribution measurements in rf and pulsed dc plasma discharges,” *Plasma Sources Sci. Technol.*, vol. 21, no. 2, 2012, doi: 10.1088/0963-0252/21/2/024004.
- [157] S. Sharma *et al.*, “Measurement of deposition rate and ion energy distribution in a pulsed dc magnetron sputtering system using a retarding field analyzer with embedded quartz crystal microbalance,” *Rev. Sci. Instrum.*, vol. 87, no. 4, 2016, doi: 10.1063/1.4946788.
- [158] R. A. Pitts *et al.*, “Retarding field energy analyzer for the JET plasma boundary,” *Rev. Sci. Instrum.*, vol. 74, no. 11, pp. 4644–4657, 2003, doi: 10.1063/1.1619554.
- [159] R. Goldston and P. Rutherford, *Introduction to Plasma Physics*. IOP Publishing Ltd., 1995.
- [160] F. F. Chen, *Introduction to Plasma Physics and Controlled Fusion. Volume 1: Plasma Physics*, 2<sup>nd</sup> ed. Springer, 1984.
- [161] N. T. Do, V. H. Dinh, L. Van Lich, H. H. Dang-Thi, and T. G. Nguyen, “Effects of substrate bias voltage on structure of diamond-like carbon films on AISI 316L stainless steel: A molecular dynamics simulation study,” *Materials (Basel)*, vol. 14, no. 17, 2021, doi: 10.3390/ma14174925.
- [162] N. Win Khun, A. Neville, I. Koley, and H. Zhao, “Effects of substrate bias on tribological properties of diamondlike carbon thin films deposited via microwave-excited plasma-enhanced chemical vapor deposition,” *J. Tribol.*, vol. 138, no. 3, 2016, doi: 10.1115/1.4031995.
- [163] D. Sheeja, B. K. Tay, S. P. Lau, and X. Shi, “Tribological properties and adhesive strength of DLC coatings prepared under different substrate bias voltages,” *Wear*, vol. 249, no. 5–6, pp. 433–439, 2001, doi: 10.1016/S0043-1648(01)00541-5.
- [164] J. Zhu, J. Han, X. Han, H. I. Schlaberg, and J. Wang, “sp<sup>3</sup>-rich deposition conditions and growth mechanism of tetrahedral amorphous carbon films deposited using filtered arc,” *J. Appl. Phys.*, vol. 104, no. 1, pp. 0–9, 2008, doi: 10.1063/1.2951588.
- [165] X. L. Peng, Z. H. Barber, and T. W. Clyne, “Surface roughness of diamond-like carbon films prepared using various techniques,” *Surf. Coatings Technol.*,



- vol. 138, pp. 23–32, 2001, doi: 10.1088/1009-0630/8/6/17.
- [166] A. C. Ferrari and J. Robertson, “Interpretation of Raman spectra of disordered and amorphous carbon,” vol. 61, no. 20, pp. 95–107, 2000.
- [167] J. Schwan, S. Ulrich, V. Batori, and H. Ehrhardt, “Raman Spectroscopy on Amorphous Carbon Films,” *J. Appl. Phys.*, vol. 80, pp. 440–447, 1996, doi: 10.1063/1.362745.
- [168] A. C. Ferrari *et al.*, “Density,  $sp^3$  fraction, and cross-sectional structure of amorphous carbon films determined by x-ray reflectivity and electron energy-loss spectroscopy,” *Phys. Rev. B*, vol. 62, no. 16, pp. 11089–11103, 2000, doi: 10.1103/PhysRevB.62.11089.
- [169] T. Koehler, T. Frauenheim, and G. Jungnickel, “Stability, chemical bonding and vibrational properties of amorphous carbon at different mass density,” *Phys. Rev. B*, vol. 52, no. 16, pp. 11837–11844, 1995, doi: 10.1557/proc-383-437.
- [170] D. Bociaga *et al.*, “Surface characteristics and biological evaluation of Si-DLC coatings fabricated using magnetron sputtering method on Ti6Al7Nb substrate,” *Nanomaterials*, vol. 9, no. 6, 2019, doi: 10.3390/nano9060812.
- [171] J. Etula, N. Wester, S. Sainio, T. Laurila, and J. Koskinen, “Characterization and electrochemical properties of iron-doped tetrahedral amorphous carbon (ta-C) thin films,” *RSC Adv.*, vol. 8, no. 46, pp. 26356–26363, 2018, doi: 10.1039/c8ra04719g.
- [172] T. Chunjaemsri, N. Chanlek, H. Nakajima, and S. Rujirawat, “Synchrotron-based NEXAFS analysis of thermal-treated diamond-like carbon films,” *Radiat. Phys. Chem.*, no. April, pp. 1–4, 2019, doi: 10.1016/j.radphyschem.2019.04.021.
- [173] S. S. Roy, R. Mccann, P. Papakonstantinou, P. Maguire, and J. A. Mclaughlin, “The structure of amorphous carbon nitride films using a combined study of NEXAFS, XPS and Raman spectroscopies,” *Thin Solid Films*, vol. 482, pp. 145–150, 2005, doi: 10.1016/j.tsf.2004.11.132.
- [174] K. A. H. Al Mahmud, M. Varman, M. A. Kalam, H. H. Masjuki, H. M. Mobarak, and N. W. M. Zulkifli, “Tribological characteristics of amorphous hydrogenated (a-C: H) and tetrahedral (ta-C) diamond-like carbon coating at

- different test temperatures in the presence of commercial lubricating oil,” *Surf. Coatings Technol.*, vol. 245, pp. 133–147, 2014, doi: 10.1016/j.surfcoat.2014.02.052.
- [175] C. K. Park, S. M. Chang, H. S. Uhm, S. H. Seo, and J. S. Park, “XPS and XRR studies on microstructures and interfaces of DLC films deposited by FCVA method,” *Thin Solid Films*, vol. 420–421, pp. 235–240, 2002, doi: 10.1016/S0040-6090(02)00750-2.
- [176] N. Dwivedi, S. Kumar, H. K. Malik, Govind, C. M. S. Rauthan, and O. S. Panwar, “Correlation of  $sp^3$  and  $sp^2$  fraction of carbon with electrical, optical and nano-mechanical properties of argon-diluted diamond-like carbon films,” *Appl. Surf. Sci.*, vol. 257, no. 15, pp. 6804–6810, 2011, doi: 10.1016/j.apsusc.2011.02.134.
- [177] C. Donnet and A. Erdemir, “Tribology of Diamond-like Carbon Films,” *Mater. Today*, vol. 11, no. 4, p. 58, 2008, doi: 10.1016/s1369-7021(08)70060-9.
- [178] A. Leyland and A. Matthews, “On the significance of the H/E ratio in wear control: A nanocomposite coating approach to optimised tribological behaviour,” *Wear*, vol. 246, no. 1–2, pp. 1–11, 2000, doi: 10.1016/S0043-1648(00)00488-9.
- [179] J. B. Cai, X. L. Wang, W. Q. Bai, D. H. Wang, C. D. Gu, and J. P. Tu, “Microstructure, mechanical and tribological properties Of A-C/A-C:Ti nanomultilayer film,” *Surf. Coatings Technol.*, vol. 232, pp. 403–411, 2013, doi: 10.1016/j.surfcoat.2013.05.042.
- [180] Sam Zhang, *Thin Films and Coatings: Toughening and Toughness Characterization*. Oakville, Canada: Apple Academic Press Inc., 2015.
- [181] J. Il Kim, J. Kim, D. H. Kim, Y. J. Jang, and N. Umehara, “Improved wear imbalance with multilayered nanocomposite nanocrystalline Cu and tetrahedral amorphous carbon coating,” *Ceram. Int.*, vol. 47, no. 18, pp. 25664–25673, 2021, doi: 10.1016/j.ceramint.2021.05.292.
- [182] Y. J. Jang, J. I Kim, W. Y. Lee, and J. Kim, “Tribological properties of multilayer tetrahedral amorphous carbon coatings deposited by filtered cathodic vacuum arc deposition,” *Friction*, vol. 9, no. 5, pp. 1292–1302, 2021, doi: 10.1007/s40544-020-0476-y.

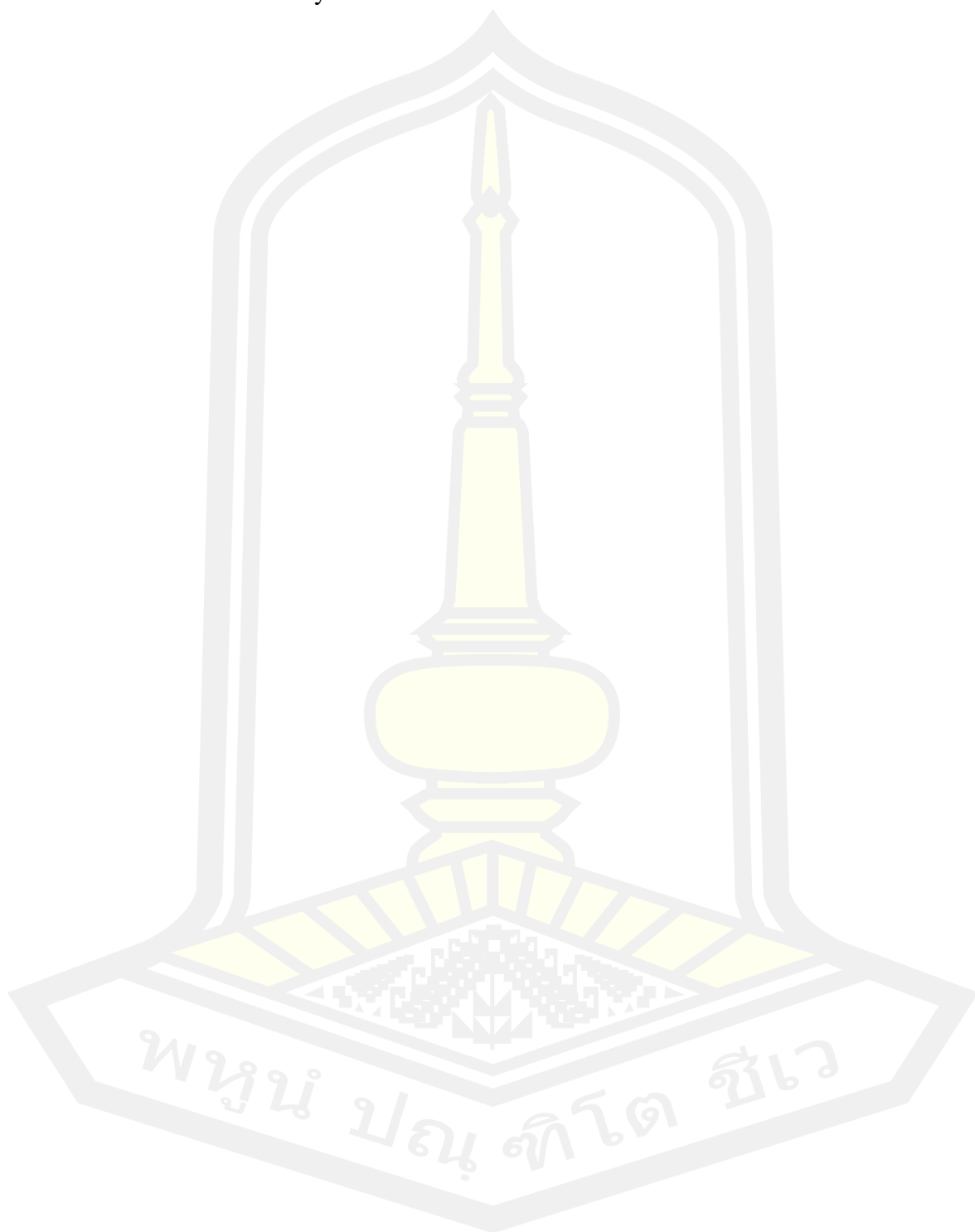
- [183] G. P. Lopinski, V. I. Merkulov, and J. S. Lannin, "Vibrational states of tetrahedral amorphous carbon," *Appl. Phys. Lett.*, vol. 69, no. 22, pp. 3348–3350, 1996, doi: 10.1063/1.117302.
- [184] F. Papa, D. Monaghan, R. Brown, V. Bellido-gonzalez, and I. Sorzabal, "Circular Ion Sources for pre-treatment, etching and ion assistance." Gencoa.
- [185] "Thin film and components for sputter deposition, process control and plasma treatment." Gencoa.
- [186] V. Dudnikov and A. Westner, "Ion source with closed drift anode layer plasma acceleration," *Rev. Sci. Instrum.*, vol. 73, no. 2, pp. 729–731, 2002, doi: 10.1063/1.1431703.
- [187] P. Li, F. Zhang, S. Geng, J. Zhao, and D. Tang, "Three-dimensional Particle-In-Cell simulation of ion characteristics in anode layer ion source," *Surf. Coat. Technol.*, vol. 365, pp. 102–108, 2019, doi: 10.1016/j.surfcoat.2018.08.059.
- [188] S. F. Geng, D. L. Tang, C. X. Wang, X. M. Qiu, and P. K. Chu, "Concentrated ion beam emitted from an enlarged cylindrical-anode-layer Hall plasma accelerator and mechanism," *J. Appl. Phys.*, vol. 113, p. 043302, 2013, doi: 10.1063/1.4788697.
- [189] G. D. Alton, "SOURCES OF LOW-CHARGE-STATE POSITIVE-ION BEAMS," in *Atomic, Molecular, and Optical Physics: Charged Particles*, F.B. dunning and Randall G. Hulet, Eds. Academic Press, 1995, pp. 69–168.
- [190] S. I. R. Torab, "Ion Beam Source Construction and Applications," Cairo, 2011.
- [191] G. Shamuilov *et al.*, "Child-Langmuir law for photoinjectors," *Appl. Phys. Lett.*, vol. 113, p. 204103, 2018, doi: 10.1063/1.5063888.
- [192] M. Kahn *et al.*, "Structural and mechanical properties of diamond-like carbon films deposited by an anode layer source," *Thin Solid Films*, vol. 517, pp. 6502–6507, 2009, doi: 10.1016/j.tsf.2009.03.213.
- [193] C. Casiraghi, A. C. Ferrari, and J. Robertson, "Raman spectroscopy of hydrogenated amorphous carbons," *Phys. Rev. B*, vol. 72, p. 085401, 2005, doi: 10.1103/PhysRevB.72.085401.
- [194] A. C. Ferrari and J. Robertson, "Raman spectroscopy of amorphous, nanostructured, diamond-like carbon, and nanodiamond," *Phil. Trans. R. Soc. Lond. A*, vol. 362, pp. 2477–2512, 2004, doi: 10.1098/rsta.2004.1452.

- [195] C. Vivensang, G. Turban, E. Anger, and A. Gicquel, "Reactive ion etching of diamond and diamond-like carbon films," *Diam. Relat. Mater.*, vol. 3, pp. 645–649, 1994.
- [196] F. C. Tai, S. C. Lee, C. H. Wei, and S. L. Tyan, "Correlation between I D/I G Ratio from Visible Raman Spectra and  $sp^2/sp^3$  Ratio from XPS Spectra of Annealed Hydrogenated DLC Film," *Mater. Trans.*, vol. 47, no. 7, pp. 1847–1852, 2006, doi: 10.2320/matertrans.47.1847.
- [197] J. F. Zhao, P. Lemoine, Z. H. Liu, J. P. Quinn, P. Maguire, and J. A. McLaughlin, "A study of microstructure and nanomechanical properties of silicon incorporated DLC films deposited on silicon substrates," *Diam. Relat. Mater.*, vol. 10, pp. 1070–1075, 2001.
- [198] K. W. Nugent *et al.*, "SLATED Systematic variation of the Raman spectra of DLC films as a function of  $sp^2:sp^3$  composition," *Diam. Relat. Mater.*, vol. 5, pp. 433–438, 1996.
- [199] X. B. Yan, T. Xu, S. R. Yang, H. W. Liu, and Q. J. Xue, "Characterization of hydrogenated diamond-like carbon films electrochemically deposited on a silicon substrate," *J. Phys. D Appl. Phys.*, vol. 37, pp. 2416–2424, 2004, doi: 10.1088/0022-3727/37/17/012.
- [200] R. M. Dey, M. Pandey, D. Bhattacharyya, D. S. Patil, and S. K. Kulkarni, "Diamond like carbon coatings deposited by microwave plasma CVD: XPS and ellipsometric studies," *Bull. Mater. Sci.*, vol. 30, no. 6, pp. 541–546, 2007.
- [201] Y. Lu *et al.*, "Pulsed laser deposition of the protective and Anti-reflective DLC film," *Infrared Phys. Technol.*, vol. 119, p. 103949, 2021, doi: <https://doi.org/10.1016/j.infrared.2021.103949>.
- [202] A. Mateen *et al.*, "Effects of ion flux density and energy on the composition of TiNx thin films prepared by magnetron sputtering with an anode layer ion source," *Surf. Coat. Technol.*, vol. 365, pp. 58–64, 2019, doi: 10.1016/j.surfcoat.2018.05.091.
- [203] P. P. Murmu *et al.*, "A novel radial anode layer ion source for inner wall pipe coating and materials modification — Hydrogenated diamond-like carbon coatings from butane gas," *Rev. Sci. Instrum.*, vol. 85, p. 085118, 2014, doi: 10.1063/1.4892813.

- [204] F. Ferreira, R. Serra, J. C. Oliveira, and A. Cavaleiro, “Effect of peak target power on the properties of Cr thin films sputtered by HiPIMS in deep oscillation magnetron sputtering (DOMS) mode,” *Surf. Coat. Technol.*, vol. 258, pp. 249–256, 2014, doi: 10.1016/j.surfcoat.2014.09.020.
- [205] D. V Sidelev *et al.*, “Deposition of Cr films by hot target magnetron sputtering on biased substrates,” *Surf. Coat. Technol.*, vol. 350, pp. 560–568, 2018, doi: 10.1016/j.surfcoat.2018.07.047.
- [206] Q. Xie *et al.*, “Effect of substrate bias current on structure and properties of CrN<sub>x</sub> films deposited by plasma enhanced magnetron sputtering,” *Surf. Coat. Technol.*, vol. 365, pp. 134–142, 2019, doi: 10.1016/j.surfcoat.2018.06.090.
- [207] Y. Lv, L. Ji, X. Liu, H. Li, H. Zhou, and J. Chen, “Influence of substrate bias voltage on structure and properties of the CrAlN films deposited by unbalanced magnetron sputtering,” *Appl. Surf. Sci.*, vol. 258, pp. 3864–3870, 2012, doi: 10.1016/j.apsusc.2011.12.048.
- [208] C. Kuo, C. Lin, Y. Lin, and J. Chang, “Effects of cathode voltage pulse width in high power impulse magnetron sputtering on the deposited chromium thin films,” *Coatings*, vol. 10, p. 542, 2020.
- [209] R. Machunze, A. P. Ehiasarian, F. D. Tichelaar, and G. C. A. M. Janssen, “Stress and texture in HIPIMS TiN thin films,” *Thin Solid Films*, vol. 518, no. 5, pp. 1561–1565, 2009, doi: 10.1016/j.tsf.2009.09.069.
- [210] D. Gall *et al.*, “Pathways of atomistic processes on TiN (001) and (111) surfaces during film growth: an ab initio study,” *J. Appl. Phys.*, vol. 93, no. 11, p. 9086, 2012, doi: 10.1063/1.1567797.
- [211] H. Elmkhah, F. Attarzadeh, A. Fattah-alhosseini, and K. H. Kim, “Microstructural and electrochemical comparison between TiN coatings deposited through HIPIMS and DCMS techniques,” *J. Alloys Compd.*, vol. 735, pp. 422–429, 2018, doi: 10.1016/j.jallcom.2017.11.162.
- [212] J. Alami, Z. Maric, H. Busch, F. Klein, U. Grabowy, and M. Kopnarski, “Enhanced ionization sputtering: A concept for superior industrial coatings,” *Surf. Coat. Technol.*, 2013, doi: 10.1016/j.surfcoat.2013.11.040.
- [213] S. Mahieu and D. Depla, “Reactive sputter deposition of TiN layers: modelling the growth by characterization,” *J. Phys. D Appl. Phys.*, vol. 42, p. 053002,

- 2009, doi: 10.1088/0022-3727/42/5/053002.
- [214] M. S. Kabir, Z. Zhou, and Z. Xie, “Designing multilayer diamond like carbon coatings for improved mechanical properties,” *J. Mater. Sci. & Technol.*, vol. 65, pp. 108–117, 2021, doi: 10.1016/j.jmst.2020.04.077.
- [215] Z. Xu, Y. J. Zheng, F. Jiang, Y. X. Leng, H. Sun, and N. Huang, “Applied Surface Science The microstructure and mechanical properties of multilayer diamond-like carbon films with different modulation ratios,” *Appl. Surf. Sci.*, vol. 264, pp. 207–212, 2013, doi: 10.1016/j.apsusc.2012.10.003.
- [216] J. Zhang, X. Yu, X. Zhao, and L. Zhang, “Influences of interfacial carbonization on the structure and mechanical properties of multilayered Cr-containing diamond-like carbon films,” *J. Phys. Chem. C*, vol. 121, pp. 6781–6787, 2017, doi: 10.1021/acs.jpcc.7b00436.
- [217] C. Q. Guo, Z. L. Pei, D. Fan, J. Gong, and C. Sun, “Microstructure and tribomechanical properties of (Cr, N)-DLC/DLC multi-layer films deposited by a combination of filtered and direct cathodic vacuum arcs,” *Diam. Relat. Mater.*, vol. 60, pp. 66–74, 2015, doi: 10.1016/j.diamond.2015.10.019.
- [218] Z. Xu, H. Sun, Y. X. Leng, X. Li, W. Yang, and N. Huang, “Effect of modulation periods on the microstructure and mechanical properties of DLC/TiC multilayer films deposited by filtered cathodic vacuum arc method,” *Appl. Surf. Sci.*, vol. 328, pp. 319–324, 2014, doi: 10.1016/j.apsusc.2014.12.041.
- [219] L. Wang, Y. Liu, H. Chen, and M. Wang, “Modification Methods of Diamond like Carbon Coating and the Performance in Machining Applications: A Review,” *Coatings*, vol. 12, p. 224, 2022.
- [220] A. A. Voevodin and J. S. Zabinski, “Architecture of multilayer nanocomposite coatings with super-hard diamond-like carbon layers for wear protection at high contact loads,” *Wear*, vol. 204, pp. 516–527, 1997.
- [221] W. Ni *et al.*, “Effects of the ratio of hardness to Young’s modulus on the friction and wear behavior of bilayer coatings,” *Appl. Phys. Lett.*, vol. 83, no. 18, pp. 4028–4030, 2004, doi: 10.1063/1.1811377.
- [222] M. A. Caro, V. L. Deringer, J. Koskinen, T. Laurila, and G. Csányi, “Growth Mechanism and Origin of High  $sp^3$  Content in Tetrahedral Amorphous

Carbon,” *Phys. Rev. Lett.*, vol. 120, no. 16, p. 166101, 2018,  
doi: 10.1103/PhysRevLett.120.166101





## BIOGRAPHY

<b>NAME</b>	Nopphon Saowiang
<b>DATE OF BIRTH</b>	19 April 1994
<b>PLACE OF BIRTH</b>	Sisaket hospital
<b>ADDRESS</b>	128/2, Lin Fah Subdistrict, Yang Chum Noi District, Sisaket Province, 33190
<b>EDUCATION</b>	2010 Junior High School, Phakha School, Sisaket Province 2013 Senior Secondary, Satri Siriket School, Sisaket Province 2017 Bachelor of Science (B.Sc.) in Physics, Faculty of Science, Mahasarakham University 2019 Master of Science (M.Sc.) in Physics, Faculty of Science, Mahasarakham University 2022 Doctor of Philosophy of Science (Ph.D.) in Physics, Faculty of Science, Mahasarakham University
<b>Research output</b>	N. Saowiang, A. Chingsungnoen, and P. Poolcharuansin, “Influence of the Ion Flux and the Bias Voltage on Microstructure of Hydrogenated Amorphous Carbon Films Deposited by DC Magnetron Sputtering,” Burapha Science Journal, vol. 24, no. 2, pp. 835–850, 2019.

